University of Assiut

Faculty of Science

Short Range Correlations in Finite Nuclear Systems

A Thesis

Submitted to the Faculty of Science, University of Assiut

for the degree of

Doctor of Philosophy in Science (Physics)

By

Sherif Rashad Mokhtar

B. Sc. (Physics), University of Assiut

M. Sc. (Physics), University of Assiut

Supervised by

Prof. Dr.

S.A.E. Khallaf

Faculty of Science

University of Assiut, Egypt

Prof. Dr.

Giampaolo Co'

Faculty of Science

University of Lecce, Italy

Dr.

Mohamed El-Azab Farid

Faculty of Science

University of Assiut, Egypt

2002

Dedication

I dedicate this work to

My Parents whom I felt their real love in my heart when I was several thousand miles away from them. Special grateful to My Mother for all her unconditional love and support and for everything she has always done for me.

Acknowledgments

First and foremost, gratitude and most deep thanks to our creator ALLAH for always guidance and helping.

The thesis could not have been accomplished without the help of many individuals. Therefore, I would like to thank them and make a list of their contributions here, even though the list may not be complete. I apologize for any possible but unintentional omissions.

I would like to express my deep thanks to Prof. Giampaolo Co', Department of Physics, University of Lecce, Italy, for the suggestion of the subject, daily help, advice, teaching, valuable discussions, helping in programming the Fortran codes, and encouragement during the development of the work through the two years I spent in Italy and even when I came back to Egypt. I thank him not only for his knowledge and experience, but also for his patience with my most unreasonable questions and for his friendship. I look forward to a continuing relationship for many years to come.

I wish to give my wider thanks to Prof. S.A.E. Khallaf, Department of Physics, Faculty of Science, University of Assiut, Egypt, for his continuous encouragement and discussion. Also, I thank him for his careful and paternal assistance and help.

Special thanks to Dr. Mohamed El-Azab Farid, Department of Physics, Faculty of Science, University of Assiut, Egypt, for his continuous encouragement, valuable comments. He was enthusing to complete my work may be more than my enthusiasm.

Thanks to Prof. Antonio Miguel Lallena, Department of Modern Physics, University of Granada, Spain, for his valuable comments, discussions and for his remarks about the Fortran codes during his visits to University of Lecce. Also, I owe a deal to Dr. Marta Anguiano, post-doctor in Department of Physics, University of Lecce, for physics discussions and for valuable contributions during the work.

I wish to thank all staff in Department of Physics, University of Lecce, directed by Prof. Armando Blanco and in National Institute of Nuclear Physics, Lecce's section directed by Prof. Federico Cesaroni, for the good hospitality and for providing all facilities during my stay in Lecce, Italy. I am specially indebted to Mrs. Maria Concetta Gerardi, Scientific Secretary of Department of Physics, University of Lecce, who kept all the administrative work in order and always ready with kind words of encouragement.

I would like to thank the Italian Foreigner Ministry for the financial support to my scholarship during my stay in Lecce, Italy.

I would like to express appreciation to the staff of Department of Physics, Faculty of Science, University of Assiut directed by Prof. M.M. Hafez for their encouragement and facilities providing.

Sherif Rashad MOKHTAR

Publications

1. "Short-range correlations in low-lying nuclear excited states",
   S.R. Mokhtar, G. Co' and A.M. Lallena, *Phys. Rev.* **C62** (2000) 067304.

2. "Short-range correlations in semi-exclusive electron scattering experiments",
   S.R. Mokhtar, M. Anguiano, G. Co' and A.M. Lallena, *Ann. Phys.* (NY) **292** (2001) 67.

3. " Short-range correlations and meson exchange currents in photonucleon emission",
   M. Anguiano, G. Co', A.M. Lallena and S.R. Mokhtar, *Ann. Phys.* (NY) **296** (2002) 235.

Contents

Abstract

A model that treats short-range correlations in finite nuclei in case of nuclear excitations is developed. The model considers the correlations up to the first order in the number of correlation lines. The basic idea of the model consists in truncating the correlated basis function cluster expansion in order to retain only those terms containing a single scalar Jastrow type correlation line. The proper normalization of the many-body wave functions requires the evaluation of two- and three- point diagrams, the last ones are usually neglected in the literature.

The model is applied to the nuclear excitations induced by electromagnetic probes (electron and γ-photon reactions) where the nuclear responses are calculated by considering the short-range correlations acting only on the one-body operators of the external electromagnetic probes. Thus our transition matrix elements contain all correlated two- and three-point terms of the charge, magnetization and convection one-body current operators.

The electromagnetic transitions to various low-lying excited electric and magnetic states of ^{16}O, ^{40}Ca, ^{48}Ca and ^{208}Pb nuclei are calculated within our model. The collectivity of the states are tested by means of the discrete random phase approximation code. The selected states should be described well with single one-particle-one-hole $(1p-1h)$ pair or at most two $1p-1h$ pairs. The calculations by including to the mean field transitions the two-point diagrams only are unstable and give a wrong estimation of the size of the transitions. In general the effects of the

correlations are small and do not explain the required quenching factor to describe the data.

Then, the model is applied to the one nucleon emission electron scattering reaction from ^{16}O nucleus in the quasielastic region. Again the instability of including only two-point diagrams is confirmed. When all the diagrams are included the effects of short-range correlations are rather small. The final state interactions between the emitted nucleon and the residual nucleus is calculated by considering the emitted particle moving in a complex optical potential. It has been found that the largest correction to the mean field results arises from these interactions but a quenching factor is still needed.

Finally, one nucleon emission process induced by a real photon is studied with our model. The model is applied to the photoproton reaction above the giant resonance to avoid the collective states. Nucleon rescattering effects are considered as in case of electron scattering. The role of one-body currents of convection and magnetization and two-body currents due to meson exchange are investigated. We found that the photonucleon emission cross section is rather sensitive to the presence of short-range correlations at high photon energies and large values of emission angles. In this region, however, the effects of meson exchange currents are more important than those produced by short-range correlations.

Chapter 1

Introduction

A major problem in nuclear physics is to understand the structure of complex nuclei in terms of the microscopic Nucleon-Nucleon (*NN*) interaction. Even though it is commonly accepted that the Quantum Chromodynamics (QCD) is the theory describing the strong interactions, a derivation of the *NN* force in the energy regime of interest for nuclear physics is still far from being achieved.

For this reason the realistic *NN* interactions used in nuclear physics are obtained by fitting the properties of two-nucleon systems. These are the deuteron, the only bound state of two nucleons, and more than 5000 *NN* elastic scattering data. From the study of these data it turns out that the realistic *NN* interaction has a strongly repulsive core at interparticle distances smaller than 0.5 fm. The most pursued method to describe the A-body nuclear system is to solve of the many-body Schrödinger equation. The non-relativistic nuclear many-body theory has achieved many successes in describing the properties of nuclei by means of the hamiltonian:

$$H = \sum_i \frac{-\hbar^2}{2M_i}\nabla_i^2 + \sum_{i<j} v_{ij} + \sum_{i<j<k} v_{ijk} \ ,$$
$$= T + V \ , \tag{1.1}$$

where M_i is the mass of a nucleon i and T is the kinetic energy. This hamiltonian contains in addition to the two-body interaction (v_{ij}), also the three-body interaction (v_{ijk}). The three-body interaction is fixed by reproducing the triton binding energy.

Exact solutions of the Schrödinger equation with the hamiltonian (1.1) have been obtained for the few-body system within different theories: Faddeev-like [Sta91], correlated hyperspherical harmonics expansion [Kie93] and Green Function Monte Carlo (*GFMC*) [Wir00]. This latest technique has been applied to investigate light nuclei up to $A = 8$.

Since the formulation of the *GFMC* equations is independent from the number of particles composing the system, the nuclear many-body problem is in principle solved. It is ,however, easy to show that a straightforward application of the *GFMC* is strongly hindered by numerical limitations. For example, the number of spin-isospin configurations to be sampled is $\sim 10^8$ for ^{16}O and becomes $\sim 10^{27}$ for ^{40}Ca !

For medium and heavy nuclei there is no method able to solve the Schrödinger equation exactly i.e. without approximation. The simplest approximation been used to solve the many-body problem is the mean field approximation leading to the Independent Particle Model (*IPM*). In the *IPM*, the A-nucleon system is described by a nuclear hamiltonian H_o

which is a sum of single-particle hamiltonians i.e.

$$H_o = \sum_i \left[\frac{-\hbar^2}{2M_i} \nabla_i^2 + V_i \right] \tag{1.2}$$

where V_i is the single-particle potential felt by the nucleon i. In this model the eigenstates $|\Phi_0\rangle$ of the many-body Schrödinger equation is the Slater determinant composed by the eigenstates of the one-body hamiltonians. Because of the presence of the strong repulsive core, the *IPM* wave functions can not be used with realistic *NN* interactions. The results are unstable and may lead to unbound nuclei [Müt99]. The success of the *IPM* has been obtained by modifying the *NN* interaction to reproduce some properties of the nuclei under investigation. These modified interactions are called effective interactions. Bruckner G-matrix theory provides a method to derive an effective interaction starting from realistic *NN* interactions. The most commonly used residual interactions are of phenomenological type and the parameters are tuned to reproduce some properties of complex nuclei.

The *IPM* describes a nucleus as a system of nucleons moving independently in a one body potential called mean field. Thus, the *IPM* does not take into account the repulsive core of the force between two nucleons. Over many years, various theoretical techniques have been developed to correct the *IPM*. Perturbation microscopic approaches have been performed to construct perturbative corrections to the *IPM*. The difficulties related to the repulsive core of the *NN* interaction appears in the perturbation expansion terms. The use of *IPM* wave functions together with realistic interactions produces very large values of the various terms of the infinite perturbation expansions. The result is stable if all the infinite terms of the expansion are calculated, but this is exactly what a perturbative expansion wants to avoid. The problem has been tackled by working either on the *NN* interaction or on the *IPM* wave function.

The methods acting on the interaction substitute the realistic microscopic interaction between two nucleons with an effective interaction constructed to take into account the effects produced by the presence in the medium of the other nucleons. The effective interaction does not have the strong repulsion at short distances, therefore can be used together with the *IPM* wave functions in the perturbation theory. The most commonly used techniques according to this method is Brueckner Bethe Goldstone method [Bal91].

The other methods developed to solve the problem of the repulsive core are changing the *IPM* wave function basis. These methods are based upon the variational principle. It assumes that the many-body wave function is a product of a correlation function G and of a Slater determinant ground state wave function $|\Phi_0\rangle$. In the region where the repulsive core of the potential is acting, the correlation function G reduces the relative wave function of two nucleons with respect to the *IPM*. The most commonly used technique according to this method is the Correlated Basis Function theory (*CBF*) [Cla79] and it will be briefly discussed in section 2.1.1. This approach provides approximated solutions of the Schrödinger equation.

In many-body physics the word correlation indicates anything beyond the *IPM* description of the system. In nuclear physics one commonly distinguishes between long- and short-range correlations. The correlations due to the *NN* short-range repulsion are called Short-Range Correlations (*SRC*), while those related to nuclear collective phenomena are called Long-Range Correlations (*LRC*).

While the presence of collective phenomena in nuclei has been evident and known since the early time of nuclear physics, much effort has been directed to search for clear signatures of *SRC*. The best known and most dramatic effects of *SRC* is the enhancement of the nucleon momentum distribution $n(k)$ [Ari96, Fab01] at large values of the momentum k.

Unfortunately the momentum distribution is not directly observable, therefore one has to search for phenomena sensitive to it and consequently to the *SRC*. The search for these phenomena is the motivation of this work. In order to have a maximum sensitivity to the *SRC*, special care must be taken in the choice of the experimental facilities and of the kinematics. In these last few years, the experimental techniques have been improved to measure with high accuracy very small cross sections such as those of double and triple coincidence experiments (see e.g. [Ryc95a, Gar99, Ros00]).

The electromagnetic reactions (electron and γ-photon scattering from nuclei) are a powerful tool for studying the nuclear structure. This because the electromagnetic (*EM*) interaction is relatively weak with respect to the nuclear force. Thus in a perturbation expansion of the Quantum Electrodynamics (*QED*) equations, one only needs to consider the lowest order terms to obtain accurate results. Thus in the description of an electron scattering process, it is a reasonable approximation to consider only the one-photon exchange contributions and to describe the electron wave functions as plane waves, i.e. the Plane Wave Born Approximation ($PWBA$). This simplifies the form of cross section which becomes a multiplication between two tensors: the lepton and hadron tensors. The lepton tensor describes the electron and is determined by *QED*. The hadron tensor describes the target nucleus. It is therefore possible to obtain relevant information about the *SRC* of the hadron structure contained in the target response to the *EM* probe. This is a great advantage with respect to hadron scattering by nuclei, because in this last case it is very complicated to separate the nuclear structure part from the reaction mechanism.

While for real photons momentum ($\mathbf{q}$) and energy (ω) transferred to the nucleus are related by the equation $\omega - \mathbf{q}^2 = 0$, for virtual photons, i.e. in electron scattering, one has $\omega - \mathbf{q}^2 \leq 0$. This allows to vary the momentum transfer to the nucleus at a fixed value of ω (i.e. at a specific transition between nuclear states). In this way one has an additional degree of freedom to study the nuclear structure. Furthermore, electrons can interact with the nucleus by a direct coupling with its charge distribution, while real photons cannot do it.

Figure 1.1 shows the schematic representation of the nuclear response for a given momentum transfer q in the five different ω regions. In the region I, the elastic scattering peak occurs where the energy transferred to the nucleus is $\omega = 0$. This will leave the nucleus in its ground state. One can get a useful information about the ground state properties of the nucleus e.g. its size, ground state charge distribution. In the region II, one can see many peaks corresponding to the excitation of low-lying states, where the energy transferred is greater than zero but still below

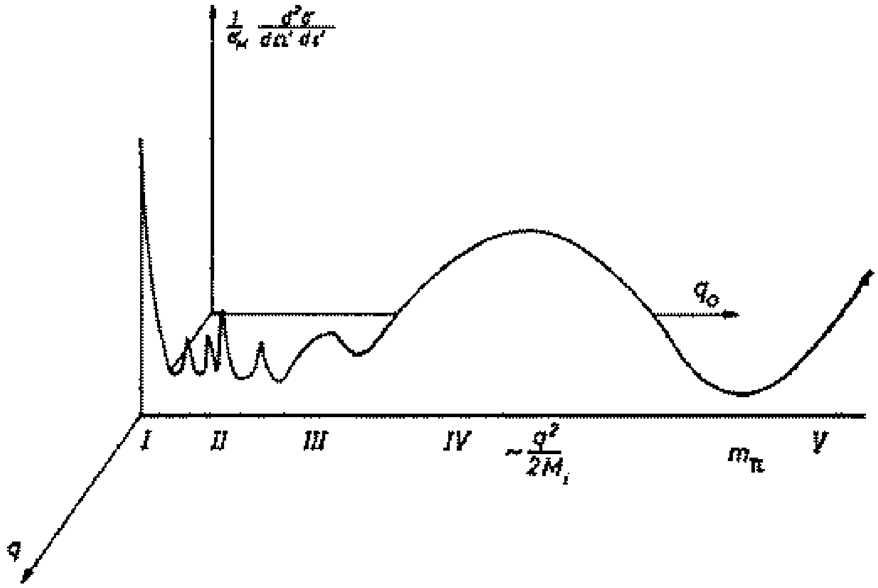

Figure 1.1: Schematic representation of the nuclear response for electron scattering at a given momentum transfer.

the particle emission threshold. The excited states of this region, are produced as a result of single one-particle-one-hole $(1p - 1h)$ transitions and/or collective ones. Region III represents the giant resonance peak in which the excitation energy ω is above the nucleon emission threshold. The nucleus is excited as a whole into the continuum with participation of a large number of nucleons and it decays mainly by emitting nucleons. With increasing the excitation energy, the quasielastic peak (denoted by region IV) occurs at about $\omega = \mathbf{q}^2/2M_i$. Its position corresponds to the elastic peak in electron scattering by a free nucleon. This means that the incident electron interacts only with the emitted nucleon and leaves the residual nucleus practically undisturbed. The peak shows a small shift in the position and a broad width due to the effect of nucleon binding and Pauli principle. In this region, the detection of the emitted nucleon in coincidence with scattered electron represents a valuable source of information on single particle properties inside the nucleus. At excitation energies larger than the pion rest mass m_π, it becomes possible to produce real pions.

We are interested here in two kinds of experiments which may serve to study the *SRC*. First inelastic electron scattering (e, e') in the low-lying excited states, where only the scattered electron is detected (inclusive experiment). This reaction refers to region II in Fig. 1.1. The second experiment is the coincidence inelastic electron (or γ) scattering $(e, e'N)$ (or (γ, N)) in quasielastic region (i.e. region IV in Fig. 1.1). The basic assumptions of this quasielastic experiment are defined as a process in which the virtual (or real) photon is absorbed by one nucleon N which is indeed detected in coincidence with the scattered electron, while the daughter nucleus is assumed not to be measured (semi-exclusive experiment).

Analysis of electromagnetic (e, e') form factors of low-lying excited states shows disagreement between theory and experiment particularly for the high spin states (see e.g. [Hyd87] for ^{16}O, [Wis85] for ^{48}Ca and [Lic79, Con92] for ^{208}Pb). These states are supposed to be composed by few $1p-1h$ configurations. Because of their relatively simple structure one expects that the *IPM* should be able to reproduce the data. It is noticed that the *IPM* correctly predicts the shape of the form factors but the predicted strength overestimates the data.

Also, the quasielastic $(e, e'N)$ and (γ, N) reactions provide new insights into the decay properties of the nucleus and, consequently, into the microscopic structure of the nuclear states. The quasielastic excitation is dominated by the single particle dynamics and then it is expected to be well described by the *IPM*. With respect to the inclusive experiments, new structure functions appear in the $(e, e'N)$ cross section which may shed new light on nuclear structure. Again, the shapes predicted by the *IPM* wave functions are in good agreement with the $(e, e'N)$ data but the strength is off (see e.g. [Ste88] for ^{12}C, [Leu94, Blo95] for ^{16}O and [Bob94] for ^{208}Pb).

From the comparison with the experiment, a quenching factor must be applied to the *IPM* results to reproduce the data. This factor, which is extracted from a fit to the data, is considered as a further spectroscopic factor. The origin of this quenching is attributed to correlations.

There have been various attempts to include the effects of correlations and solve this disagreement, but the situation has not yet been clarified. In the case of low-lying states, the first order core polarization mechanism [Ham80] produces a quenching effect, but other studies [Suz83] found this effect to be small. The quenching of the 12^- and 14^- form factors in ^{208}Pb have been explained by a Random Phase Approximation (*RPA*) plus particle vibration coupling model [Kre80], which contains the coupling of $1p-1h$ configurations with $2p-2h$ configurations. But these results have not been confirmed by a self consistent first- and second- RPA calculation [Dec81]. The influence of the Meson Exchange Currents (*MEC*) has been studied by many authors [Deh85, Kre86, Lal88]. It is found that *MEC* produce a small effect in these high spin states in the range of momentum transfer less or equal 3 fm^{-1}. In some cases, the *MEC* enhance the (e, e') form factors and, as a consequence, the quenching required becomes bigger [Ari94].

In case of $(e, e'N)$ experiment, the source of quenching has been investigated following various hypotheses: from relativistic effects [Udi93] to in medium modifications of the nucleon properties [Ste86, Ste87]. A mechanism related to the presence of *SRC* and *LRC* has been proposed [Pan84]. Correlations give rise to virtual scattering of nucleons to states of momentum larger than the Fermi momentum, producing a depletion of the normally fully occupied states in the *IPM*. Thus the correlations reduce the occupation probability of the single particle level of the hole states and produce a finite probability of occupying the particle states even when the nucleus is in its ground state [Pan84]. Various estimates of these occupation probabilities have been done both in nuclear matter [Ram89, Ben89] and in finite nuclei [Pol97, Fab01], but their values do not seem to be compatible with the empirical spectroscopic factors.

Many theoretical and experimental studies have been done to search for the effects of the *SRC* in different energies and momentum transferred for different nuclei. Müther and Dickhoff [Müt94] studied the effects of *SRC* on the p-wave single particle function in ^{16}O$(e, e'p)$ reaction. They observed that the momentum distribution for $p_{\frac{1}{2}}$ state at high momentum and low excitation energy is not very sensitive to *SRC* and may be described well by the *IPM*. While, the momentum distribution increases significantly at high momentum and excitation energies.

Bobeldijk *et al.* [Bob94] studied the effects of *SRC* and *LRC* in quasielastic $^{208}\mathrm{Pb}(e,e'p)$ reaction at high missing momentum and low excitation energy. The *SRC* have been included by extending to the nuclear system the prescription fixed in [Pan90] by using variational Monte Carlo calculations of correlated quantum drops of liquid $^{3}\mathrm{He}$. The *LRC* are included by inserting an effective mass for the nucleon in the nuclear medium [Ma91, Mah91]. They found the same marginal effect of *SRC* in the specified region. Meanwhile, the *LRC* enhanced the momentum distribution to reproduce the data at high missing momentum (still the spectroscopic factors are needed).

On the other hand, the fact that this enhancement is not observed for the light nucleus $^{16}\mathrm{O}$, in the experiment of Blomqvist *et al.* [Blo95], supports the idea that enhancement at small excitation energies may originate from *LRC* which could be sensitive to the whole nuclear system and exhibit different results for different nuclei. On contrary, the effects of *SRC* should depend on the behaviour of *NN* interaction and are not very sensitive to the global structure of the nuclear system.

The *LRC* have been studied for $^{16}\mathrm{O}(e,e'p)$ in terms of $1p-2h$ and $2p-1h$ excitations considering the residual interaction between these configurations [Ami96, Ami97]. They showed that the inclusion of *LRC* does not produce any significant enhancement in the momentum distribution for nucleon removal at high missing momentum as compared with the mean field prediction. These results encourage to make more studies in the quasielastic $(e,e'N)$ at these high excitation energies and momentum regions. These studies should be extended to cover the (γ,N) reaction at different excitation energies.

Along with the experimental studies, a precise theoretical treatment is needed to investigate the *SRC*. Direct calculations of quasielastic $(e, e'p)$ cross sections with models taking into account *SRC* show noticeable effects produced by these correlations [Giu94, Ryc95b, Ryc97, Gai00, Jan00, Ryc00], in spite of the fact that also in these cases spectroscopic factors are still needed. These calculations of the semi-exclusive cross section have been done with simplified treatments of the correlations. In some calculations only the lowest order cluster terms have been considered [Giu94, Ryc95b, Ryc97, Jan00, Ryc00]. In other calculations [Gai00] the overlap wave function, which in the mean field model corresponds to the hole single-particle wave function, has been extracted from correlated one-body density distributions evaluated with more or less sophisticated ground state calculations.

There are two weak points in these calculations. A first one concerns the inconsistency of the various inputs of the calculations. Single-particle wave functions and correlations are not linked by a unique nuclear hamiltonian as they should be. The second weak point is related to the fact that the proper normalization of the many-body wave function is not preserved.

In this work, we develop a model for nuclear excited states that considers the cluster expansions by calculating all terms related to the first order in correlation function power. In our model the normalization of the wave function is maintained, since the cluster expansion conserves the sum rules order by order [Cla79]. This is more clearly seen in the application of the model to the description of the ground state densities [Co'95, Ari97]. The second novelty with respect to other approaches is that we link the inputs of the model, single-particle wave functions and correlations, by means of the same nuclear hamiltonian.

Our aim is twofold: on one hand we want to see if there are significant effects of the *SRC* in the existing data and we like to investigate the best kinematical conditions to single out the *SRC* effects. To reach these goals, we have applied our model to calculate the nuclear responses of doubly closed shell nuclei in different excitation energy regions. The electromagnetic excitations of the (e, e') reaction for some noncollective low-lying states and of the quasielastic $(e, e'p)$ and (γ, p) reactions will be under our investigation. On the other hand, we will analyze the validity of various approximations commonly adopted in the mean field description of these processes.

In Chapter 2, a theoretical derivation of our *SRC* model is given. The application of the model in the inclusive (e, e') reaction is discussed in Chapter 3. The application in case of quasielastic semi-exclusive $(e, e'p)$ reaction is investigated in Chapter 4. In Chapter 5, the investigation is devoted to (γ, p) reaction where also the role of the *MEC* is discussed.

Chapter 2

Short-Range Correlation Model

2.1 Theoretical Framework

In this section, we will present the theoretical framework of our model which is based upon the *CBF* theory. The description of the *CBF* theory will be rather sketchy and it will emphasize the points needed to our discussion. We refer the interested reader to more detailed descriptions of the theory [Cla79, Pan79].

2.1.1 CBF Theory

The *CBF* is one of the most promising theories attacking the complicated problem of the short range repulsion in many-body systems. The *CBF* has been used not only to study the nuclear matter ground state properties [Wir88], but also dynamical quantities, as electromagnetic responses [Fan87, Fab97].

The *CBF* theory is based upon the variational principle:

$$\delta E[\Psi_0] = \delta \frac{\langle \Psi_0 | H | \Psi_0 \rangle}{\langle \Psi_0 | \Psi_0 \rangle} = 0 \ . \tag{2.1}$$

The solution of Eq. (2.1) is exactly that of the Schrödinger equation if there are no limitations on the Hilbert space spanned to search for the minimum of the energy functional. The *CBF* approach searches for the minimum within a subspace of correlated many-body ground state wave functions of the form:

$$|\Psi_0\rangle = G|\Phi_0\rangle \ , \tag{2.2}$$

where $|\Phi_0\rangle$ is a Slater determinant of single-particle wave functions and $G = G(1, 2...A)$ is a many-body correlation operator.

The most common ansatz on the correlation operator is to consider it given by a symmetrized product of two-body correlation operators F_{ij}:

$$G(1, 2...A) = \mathcal{S}\left[\prod_{i<j} F_{ij}\right] \ , \tag{2.3}$$

where $\mathcal{S}$ indicates the symmetrizer operator for noncommuting state-dependent operators appearing in F_{ij}. The two-body correlation F_{ij} reflects an operatorial structure dependence similar to that of the modern *NN* interactions [Wir95]. Nowadays, sophisticated *CBF* calculations consider F_{ij} of the form [Pan79, Wir95, Fab01]:

$$F_{ij} = \sum_{p=1,8} f^p(r_{ij}) O^p_{ij} \ . \tag{2.4}$$

In the above equation $f^p(r_{ij})$ is a scalar two-body correlation function depending on the interparticle distance $r_{ij} = |\mathbf{r}_i - \mathbf{r}_j|$ between the positions of the particles i and j. The operators O^p_{ij} are:

$$\begin{array}{ll} O^{p=1}_{ij} = 1\,, & O^{p=5}_{ij} = S_{ij}\,, \\ O^{p=2}_{ij} = (\boldsymbol{\sigma}_i \cdot \boldsymbol{\sigma}_j)\,, & O^{p=6}_{ij} = S_{ij}(\boldsymbol{\tau}_i \cdot \boldsymbol{\tau}_j)\,, \\ O^{p=3}_{ij} = (\boldsymbol{\tau}_i \cdot \boldsymbol{\tau}_j)\,, & O^{p=7}_{ij} = (\mathbf{L} \cdot \mathbf{S})_{ij}\,, \\ O^{p=4}_{ij} = (\boldsymbol{\sigma}_i \cdot \boldsymbol{\sigma}_j)(\boldsymbol{\tau}_i \cdot \boldsymbol{\tau}_j)\,, & O^{p=8}_{ij} = (\mathbf{L} \cdot \mathbf{S})_{ij}(\boldsymbol{\tau}_i \cdot \boldsymbol{\tau}_j)\,. \end{array} \tag{2.5}$$

They include central ($p = 1,\,2,\,3\,\text{and}\,4$), tensor ($p = 5, 6$) and spin-orbit ($p = 7, 8$) components, with $S_{ij} = (3\hat{\mathbf{r}}_{ij} \cdot \boldsymbol{\sigma}_i\,\hat{\mathbf{r}}_{ij} \cdot \boldsymbol{\sigma}_j - \boldsymbol{\sigma}_i \cdot \boldsymbol{\sigma}_j)$ indicating the tensor operator. At $p = 1$, Eq. (2.3) refers to purely scalar (state-independent or Jastrow [Jas55]) correlations, while the other terms represent state-dependent correlations.

In principle, the functional energy $E[\Psi_0]$ of Eq. (2.1) can be calculated for a $3A$-dimensional integral by means of Variational Monte Carlo integration techniques *VMC* [Wir91]. When A becomes very large, the required numerical efforts, for making the integrals for realistic interactions and correlations, become an impossible task.

In the *CBF* theory analyses, the various terms of the energy functional (2.1) on the basis of the number of particles are linked by dynamical correlations (our *SRC*) and statistical correlations due to the Pauli exclusion principle. This analysis is called cluster expansion and follows from the analogous statistical mechanics theory of Mayer used to study liquids.

It is possible to classify the various clusters in terms of their topological properties. It is possible to find a set of equations which can sum in closed form all the diagrams of a certain class. The set of equations obtained are called Fermi Hypernetted Chains equations (*FHNC*).

2.1.2 Cluster Expansion

In the *CBF*, $E[\Psi_0]$ is expanded in clusters defined as subsystems of the A-particle system (n-particle clusters, $n = 1, ...A$). Assuming the many-body correlation is a scalar function (Jastrow ansatz), we have:

$$G(1, 2...A) = \prod_{i<j}^{A} f(r_{ij}) \ . \tag{2.6}$$

The choice (2.6) of the correlations function leads to the following expression for the energy functional:

$$\begin{aligned} E[G\Phi_0] &= \frac{\langle\Psi_0|H_o|\Psi_0\rangle}{\langle\Psi_0|\Psi_0\rangle} = \frac{\langle\Psi_0|T+V|\Psi_0\rangle}{\langle\Psi_0|\Psi_0\rangle} \\ &= \frac{\langle\Psi_0|T|\Psi_0\rangle}{\langle\Psi_0|\Psi_0\rangle} + \frac{\langle\Phi_0|G^+VG|\Phi_0\rangle}{\langle\Phi_0|G^+G|\Phi_0\rangle} \\ &= \frac{\langle\Psi_0|T|\Psi_0\rangle}{\langle\Psi_0|\Psi_0\rangle} + \frac{\langle\Phi_0|V\prod_{i<j}^{A} f^2(r_{ij})|\Phi_0\rangle}{\langle\Phi_0|\prod_{i<j}^{A} f^2(r_{ij})|\Phi_0\rangle} \ . \end{aligned} \tag{2.7}$$

In the above equation, we considered the commutation relation between the scalar correlation function and the potential operator. To show the mechanism of the cluster expansion, we use the function $h(r_{ij}) = f^2(r_{ij}) - 1$. Then Eq. (2.7) becomes:

$$\begin{aligned} E[G\Phi_0] &= \frac{\langle\Psi_0|T|\Psi_0\rangle}{\langle\Psi_0|\Psi_0\rangle} + \\ &\frac{<\Phi_0|V[1+h(r_{12})][1+h(r_{13})].....[1+h(r_{23})]...|\Phi_0>}{<\Phi_0|[1+h(r_{12})][1+h(r_{13})].....[1+h(r_{23})]...|\Phi_0>} \\ &= \frac{\langle\Psi_0|T|\Psi_0\rangle}{\langle\Psi_0|\Psi_0\rangle} + \\ &\frac{<\Phi_0|V[1+\sum_{i<j}^{A} h(r_{ij}) + \sum_{i<j,k<l}^{A} h(r_{ij})h(r_{kl}) + ...]|\Phi_0>}{<\Phi_0|[1+\sum_{i<j}^{A} h(r_{ij}) + \sum_{i<j,k<l}^{A} h(r_{ij})h(r_{kl}) + ...]|\Phi_0>} \ . \end{aligned} \tag{2.8}$$

The simplest term is the mean value of the potential between two uncorrelated states, which is obtained by picking up all the “ones” in the various terms of Eq. (2.8). More complicated terms are obtained considering a single $h(r_{ij})$ function multiplying the “ones”. The procedure continues considering terms with two, three, etc. $h(r_{ij})$ functions. Obviously the procedure illustrated here for the potential part of the hamiltonian should be applied also to the kinetic energy part.

Each term of the cluster expansion can be expressed in a diagrammatic form. From the analysis of the various diagrams, it is possible to show that the unlinked terms are canceled by the denominator. The *FHNC* equations sum in a closed form all the nodal diagrams [Cla79, Pan79, Ros82]

With this *FHNC* computational technology the ground state properties of doubly closed shell nuclei have been studied. The energy, density and momentum distributions have been studied in ls coupling [Co'92, Co'94] with scalar correlations and semi-realistic V interactions. After that, the *FHNC* equations were generalized to the case of jj coupling with central correlations and correlations depending on the third component of the isospin [Ari96].

The inclusion of state-dependent of F_{ij} is troublesome since the non-commutativity of the correlation operators prevents the development of a complete *FHNC* theory for the correlated wave function of Eq. (2.3). Thus, an approximated treatment of the operatorial correlations called Single Operator Chain (*SOC*) has been developed [Pan79]. In a series of papers [Fab98, Fab00, Fab01], the *SOC* approximation together with a full *FHNC* treatment of the Jastrow part of the correlation provides an accurate description of finite doubly closed shell nuclei.

2.2 Ground State First Order SRC Model

The promising results of applying *CBF* and *FHNC* theories to describe the ground state nuclear systems, specially for medium and heavy nuclei, encourage us to extend them to describe nuclear excited states. Meanwhile, in addition to the known difficulties related to *FHNC* calculation of the ground state systems, further complication may appear in the extension of the theory to the nuclear excited states.

As a result of difficulties from the full *FHNC* expansions, Co' [Co'95] has developed a model, in the frame work of *CBF* and *FHNC* theories, to treat *SRC* up to the first order in the correlation. The basic idea for this model consists in retaining only the terms with a single correlation line in the cluster expansion. The truncation of the expansion simplifies the calculations and it was done in a way to conserve the normalization of the wave function. In that model, the one-body density distribution, defined as

$$\rho(\mathbf{r}_1) = \frac{A}{\langle \Psi_0 | \Psi_0 \rangle} \int d^3r_2 ..... \int d^3r_A \Psi_0^*(\mathbf{r}_1, ..., \mathbf{r}_A) \Psi_0(\mathbf{r}_1, ..., \mathbf{r}_A) \ , \quad (2.9)$$

has been evaluated by performing the cluster expansion of both numerator and denominator to eliminate the so-called unlinked diagrams [Fan74, Fan75, Fan79], and by keeping only the terms that contain single correlation function $h(r_{ij})$. The expression for the density obtained in this approximation is:

$$\begin{aligned}
\rho(\mathbf{r}_1) &= \int d^3r_2.....\int d^3r_A\ \Phi_0^*(\mathbf{r}_1,....,\mathbf{r}_A)\left[1+\sum_{i<j}^{A}h(r_{ij})\right]_L \Phi_0(\mathbf{r}_1,....,\mathbf{r}_A) \\
&= \int d^3r_2.....\int d^3r_A\ \Phi_0^*(\mathbf{r}_1,....,\mathbf{r}_A) \\
&\qquad \left[1+\sum_{i=2}^{A}h(r_{1i})+\sum_{i=2}^{A}\sum_{j>i}^{A}h(r_{ij})\right]_L \Phi_0(\mathbf{r}_1,....,\mathbf{r}_A)\,, \qquad (2.10)
\end{aligned}$$

where the subindex L indicates that only the linked diagrams have to be calculated. The so called Mayer-like diagrams representing the terms considered in the model are shown in Fig. 2.1. The explanation of the symbols shown in the figure is the following one.

1. There are two types of points:

   (i) External points, which are depicted as *white circles* to signify a functional dependence (i.e. not integrated) of the one-body density at point $\mathbf{r}_1$.

   (ii) Internal points, which are depicted as *black circles* representing integration over the full range of the (dummy) coordinate variables at points $\mathbf{r}_i$, $i = 2, ..., A$.

2. There are two types of lines, or bonds:

   (i) Dynamical Correlation lines (or simply correlation lines), which represent correlation function $h(r_{ij})$, drawn as *dashed lines* connecting the two points i and j.

   (ii) Statistical correlation lines (or exchange lines), which are drawn as *oriented lines* connecting single-particle wave functions.

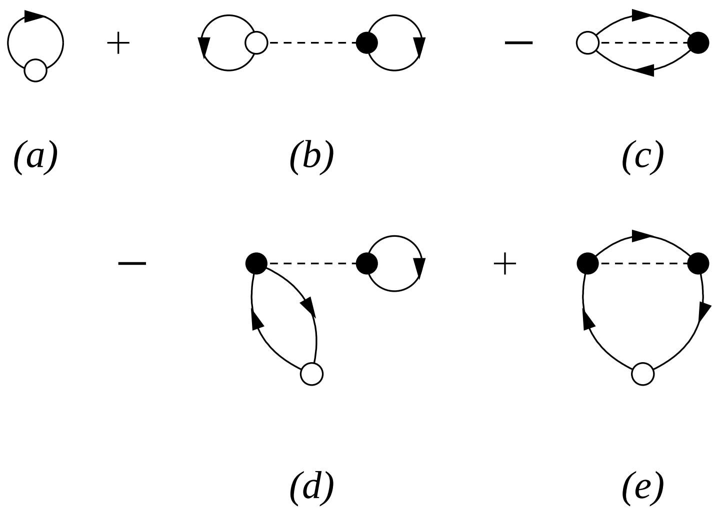

Figure 2.1: Diagrams representing the terms considered in the model for the calculation of the density distribution. The dashed lines represent the correlation function $h(r_{ij})$ and the oriented lines represent the single-particle wave functions. The white circles are the point $\mathbf{r}_1$ which is not integrated, while the black circles are the points $\mathbf{r}_i$ and $\mathbf{r}_j$ which are integrated.

3. Each *black circle* is an extremity of at least one *dashed line*.

4. The *oriented lines* form closed loops which may superimpose the *dashed lines*, as shown in diagrams (c) and (e) of Fig. 2.1.

5. No closed oriented loop may have a common point (external or internal) with another closed oriented one.

The second line of Eq. (2.10) stresses on the fact that the external point $\mathbf{r}_1$ may be one of the two correlated particles $\sum_{i=2}^{A} h(r_{1i})$, or may be not one of them $\sum_{i=2}^{A} \sum_{j>i}^{A} h(r_{ij})$. From the diagrammatic point of view, this will lead to the appearance of two- and three-point diagrams, respectively. The two-point diagrams are shown in Fig. 2.1 as (*b*) and (*c*), while three-point diagrams as (*d*) and (*e*). The diagram (*a*) represents the uncorrelated or mean field contribution of the one-body density distribution.

The density calculated is correctly normalized. This can be seen by considering that, since the uncorrelated term, corresponding to the diagram (*a*) of Fig. 2.1, is already correctly normalized, the contribution to the normalization of the other terms should be zero. In the diagrammatic picture of Fig. 2.1 the integration on $\mathbf{r}_1$ transform in black the white circle. Since in the three point diagrams (*d*) and (*e*) of the figure the white circles are not reached by the correlation line $h(r_{ij})$, the integration implies that the single-particle wave functions connected to these points should be the same. Therefore the contribution of the diagram (*d*) cancel that of the diagram (*b*) as well as the contribution of the diagram (*e*) that of the diagram (*c*).

The work has been extended [Ari97] to study the momentum distribution and the effects of the state-dependent part for the doubly closed shell nuclei. The validity of the model has been checked by comparing the density and momentum distribution results with those produced by full *FHNC* calculation. The agreement between the result of the two calculations is very good. In this investigation, the authors found that the major effects of the correlations in both density and momentum distribution are produced by the scalar part of the correlations.

2.3 First Order SRC Model for Nuclear Excitations

The description of nuclear responses to an external probe (such in case of electron scattering) is given by the linear response of many-body system to the perturbations induced by an external operator $O(\mathbf{q})$ as follows [Fan87]:

$$S(\mathbf{q},\omega) \;=\; -\frac{1}{\pi}\,\mathrm{Im}\,\mathrm{D}(\mathbf{q},\omega) \;\;, \tag{2.11}$$

where $\mathbf{q}$ and ω represent the momentum and energy transferred to the nucleus and with

$$D(\mathbf{q},\omega) \;=\; \langle\widetilde{\Psi}_0 \,|\, O^{+}(\mathbf{q})\,(H - E_0 - \omega + i\varepsilon)^{-1}\, O(\mathbf{q}) \,|\, \widetilde{\Psi}_0\rangle \;\;, \tag{2.12}$$

where H is the nuclear hamiltonian with eigenvalue E_f and E_0 for excited and ground states. The normalized ground and excited eigenstates of the hamiltonian H are:

$$|\,\widetilde{\Psi}_n\rangle \;=\; \frac{|\Psi_n\rangle}{\langle\Psi_n|\Psi_n\rangle^{\frac{1}{2}}} \;\;, \tag{2.13}$$

with $n \equiv 0$ for ground state and $n \equiv f$ for excited state.

Inserting into Eq. (2.12) a complete set of eigenvectors $|\,\widetilde{\Psi}_f\rangle$ of the hamiltonian H we obtain:

$$D(\mathbf{q},\omega) \;=\; \sum_f \frac{|\langle\widetilde{\Psi}_f \,|\, O(\mathbf{q}) \,|\, \widetilde{\Psi}_0\rangle|^2}{E_f - E_0 - \omega + i\varepsilon} \;=\; \sum_f \xi_f^{+}(\mathbf{q})\,(E_f - E_0 - \omega + i\varepsilon)^{-1}\,\xi_f(\mathbf{q}) \;\;, \tag{2.14}$$

where we have defined the transition matrix $\xi_f(\mathbf{q})$ as:

$$\xi_f(\mathbf{q}) \;=\; \frac{\langle\Psi_f|\,O(\mathbf{q})\,|\Psi_0\rangle}{\langle\Psi_f|\Psi_f\rangle^{\frac{1}{2}}\,\langle\Psi_0|\Psi_0\rangle^{\frac{1}{2}}} \;\;. \tag{2.15}$$

The description of the nuclear excited states of Eq. (2.13) is based upon the approach developed by Fantoni and Pandharipande [Fan87] and applied to nuclear matter. The basic ansatz consists in assuming that the nuclear excited states $|\Psi_f\rangle$ can be described as a product of a Slater determinant and a many-body correlation function which is the same correlation function describing the ground state:

$$|\Psi_f\rangle \;=\; G\,|\Phi_f\rangle \;\;, \tag{2.16}$$

where $|\Phi_f\rangle$ indicates a Slater determinant which differs from $|\Phi_0\rangle$ by the fact that a certain number of hole single-particle states have been substituted with particle wave functions. In our work, we consider only scalar correlation function G, Eq. (2.6), for both ground and excited states and one-body external operator $O(\mathbf{q})$.

In order to use the cluster expansion techniques it is useful to rewrite the function $\xi_f(\mathbf{q})$ as:

$$\xi_f(\mathbf{q}) \;=\; \frac{\langle\Phi_f|\,G^+\,O(\mathbf{q})\,G|\Phi_0\rangle}{\langle\Phi_0|\,G^+\,G\,|\Phi_0\rangle}\left[\frac{\langle\Phi_0|\,G^+\,G\,|\Phi_0\rangle}{\langle\Phi_f|\,G^+\,G\,|\Phi_f\rangle}\right]^{\frac{1}{2}} \;. \tag{2.17}$$

Inserting Eq. (2.6) into Eq. (2.17) and expanding the numerator and the denominator in powers of the correlation function $h(r_{ij}) = f^2(r_{ij})-1$:

$$\begin{aligned}
\xi_f(\mathbf{q}) \;&=\; \frac{\langle\Phi_f|\prod_{i<j}\,f^+(r_{ij})\,O(\mathbf{q})\,\prod_{i<j}\,f(r_{ij})\,|\Phi_0\rangle}{\langle\Phi_0|\prod_{i<j}\,f^+(r_{ij})\,\prod_{i<j}\,f(r_{ij})\,|\Phi_0\rangle} \\
&\qquad\times\left[\frac{\langle\Phi_0|\prod_{i<j}\,f^+(r_{ij})\,\prod_{i<j}\,f(r_{ij})\,|\Phi_0\rangle}{\langle\Phi_f|\prod_{i<j}\,f^+(r_{ij})\,\prod_{i<j}\,f(r_{ij})\,|\Phi_f\rangle}\right]^{\frac{1}{2}} \\
&=\; \frac{\langle\Phi_f|\,O(\mathbf{q})\,\prod_{i<j}\,(1+h(r_{ij}))\,|\Phi_0\rangle}{\langle\Phi_0|\prod_{i<j}\,(1+h(r_{ij}))\,|\Phi_0\rangle}\;\left[\frac{\langle\Phi_0|\prod_{i<j}\,(1+h(r_{ij}))\,|\Phi_0\rangle}{\langle\Phi_f|\prod_{i<j}\,(1+h(r_{ij}))\,|\Phi_f\rangle}\right]^{\frac{1}{2}},
\end{aligned} \tag{2.18}$$

where we have considered, as in case of ground state, the real scalar function $f(r_{ij})$ is commuting with the operator $O(\mathbf{q})$.

Like in the case of the density distribution, after performing the full cluster expansion of numerators and denominators to eliminate all the unlinked diagrams of the numerators with the denominators [Fan87], we retain only the terms containing a single correlation line $h(r_{ij})$. Then the transition matrix may be written as:

$$\xi_f(\mathbf{q}) \rightarrow \xi_f^1(\mathbf{q}) \;=\; \langle \Phi_f |\, O(\mathbf{q}) \sum_{i<j} (1 + h(r_{ij}))\, |\Phi_0\rangle_L \,, \tag{2.19}$$

where the subindex L indicates that only the linked diagrams are considered.

This is a generic transition matrix which can be used to calculate the excitation of the nucleus to a discrete bound level below the particle emission threshold or to calculate the transitions leading to final states with one or two particles in the continuum. In this work, we are interested to high spin low-lying excited states and with one particle in continuum where both of the two reactions may be formed by one-particle-one-hole ($1p{-}1h$) excitations. In our approach we shall consider only *OB* operators associated to the *SRC*. The expression of their Fourier transform is of the type:

$$O(\mathbf{q}) = \sum_{i=1,A} \int d^3r\, e^{-i\mathbf{q}\cdot\mathbf{r}}\, O(\mathbf{r})\delta(\mathbf{r} - \mathbf{r}_i)$$

To simplify the writing of the expectation values, here and in the following chapters, we simply write $O(\mathbf{q})$ understanding the above equation. If we label 1 to the coordinate where the external operator $O(\mathbf{q})$ is acting, we can specify the ξ^1_f in Eq. (2.19) as:

$$\begin{aligned}
\xi^1_f(\mathbf{q}) &= \xi^1_{1p1h}(\mathbf{q}; ph) \\
&= \Big[\langle \Phi_{1p1h} | \, O(\mathbf{q}) \, | \Phi_0 \rangle_L \, + \, \langle \Phi_{1p1h} | \, O(\mathbf{q}) \sum_{i>1}^{A} h(r_{1i}) \, | \Phi_0 \rangle_L \\
&\qquad + \, \langle \Phi_{1p1h} | \, O(\mathbf{q}) \sum_{1<i<k}^{A} h(r_{ik}) \, | \Phi_0 \rangle_L \Big] ,
\end{aligned} \tag{2.20}$$

The terms contributing to $\xi^1_{1p1h}(\mathbf{q})$ are presented as Mayer like diagrams in Fig. 2.2. In the diagrams, the black squares indicate the coordinates of integration points where the excitation one-body operator $O(\mathbf{q})$ is acting (labeled with 1 in Eq. (2.20)), while the black dots indicate integration points to the other coordinates. The dashed and oriented lines have the same meaning as in Fig. 2.1. We consider that the wave functions $|\Phi\rangle$ are entering to a point, while the wave functions $\langle\Phi|$ are exiting from it. The letters i, k indicate generic single-particle hole wave functions below the Fermi surface and imply a summation over them. We indicate with p and h the particle and hole single-particle wave functions containing the quantum numbers defining the asymptotics of the many-body final state $|\Psi_f\rangle$.

The truncation of any infinite series is always a delicate operation because a wrong choice of the terms retained can produce equations which do not conserve the properties of the system under investigation. Thus, in constructing the model we have been interested to preserve the normalization of the wave function. This has been obtained by considering that the terms which contribute to the transition matrix $\xi^1_{1p1h}(\mathbf{q})$ of Eq. (2.20) should provide the normalization condition of the density if the density

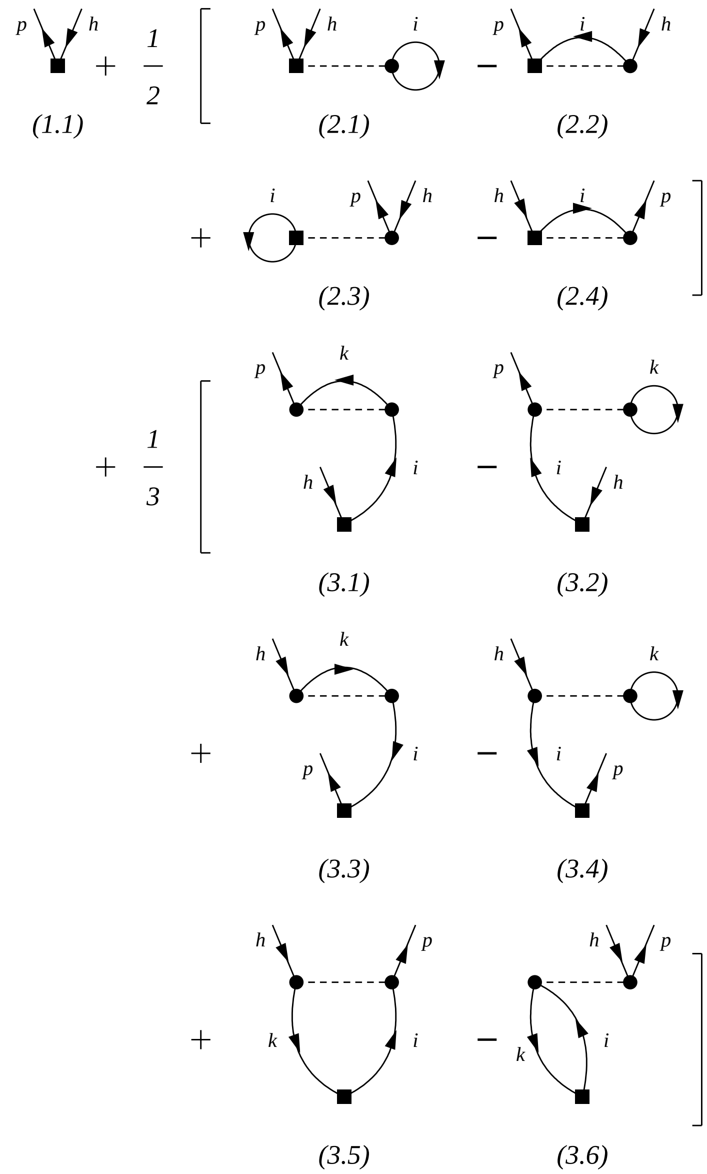

Figure 2.2: Diagrams considered in the calculation of the $(1p-1h)$ excitations. The symbols have the same meaning of those in Fig. 2.1. The black squares represent the point where the external field is acting on. The letters i, k indicate the generic summed hole wave functions. The letters h and p are the survived hole and particle wave functions, respectively.

operator is used and in the limit for $q \to 0$ and $p \to h$. In this sense, one can reconstruct the diagrams of Fig. 2.1 by closing the particle and hole lines in Fig. 2.2 and considering that in the three-point diagrams the $q \to 0$ limit implies that the wave functions linked to the black squares should be equal because of the orthonormality of the set of single-particle wave functions.

Therefore, the presence of two-point diagrams (where the excitation operator is acting on one of the two correlated particles) and three-point diagrams (where the excitation operator is acting on particles different than the correlated pair) is necessary to have a correct normalization of the many-body wave function. On the contrary, the density distribution is not conserved in other calculations [Giu91, Giu94, Ryc95b, Ryc97, Jan00, Ryc00], where the expansion adopted is truncated at the second order but it is based on the number of particles of the cluster and not on the powers of $h(r_{ij})$.

The validity of our truncation scheme has been tested for the charge operator [Ama98, Ama99a], by comparing the nuclear matter charge responses calculated with this model with those obtained with the *FHNC* procedure in the inclusive quasielastic region. The excellent agreement between the full calculation and the truncated model has been obtained because we have included in the truncated model, in order to have a correctly normalized many-body wave function, both two- and three- point diagrams. The result encouraged to extend the model to the current operators.

2.4 Electromagnetic Excitations

In this section, we shall give the mathematical derivation of the matrix elements of Eq. (2.20) needed to evaluate the electromagnetic hadron responses. We work in *PWBA*, or one-photon exchange approximation. In this framework, the cross sections can be written as a sum of terms where the leptonic variables are factorized with respect to the hadronic responses.

2.4.1 Nuclear EM Currents

The first step to give the explicit formula of transition matrix elements of Eq. (2.20) is to define the external operator $O(\mathbf{q})$. Let us begin by considering electron-nucleus scattering [Cio80, Bof93]. The initial and final electron four- vector are described as $k \equiv (\epsilon, \mathbf{k})$ and $k' \equiv (\epsilon', \mathbf{k}')$, respectively. In the process a virtual (or real) photon with four-momentum $q_\mu \equiv (\omega, \mathbf{q}) = k - k'$ is transferred to the nucleus. The basic theoretical quantity required to describe the nuclear part of the reaction induced by the electromagnetic probe is the four-vector nuclear electromagnetic current amplitude $J_\mu(\mathbf{q}) \equiv (\rho(\mathbf{q}), \mathbf{J}(\mathbf{q}))$:

$$J_\mu(\mathbf{q}) = \int \mathrm{d}^3r \; e^{i\mathbf{q}\cdot\mathbf{r}} \langle \Psi_f | J_\mu(\mathbf{r}) | \Psi_0 \rangle \ , \tag{2.21}$$

which is the Fourier transformation of the four-vector nuclear charge-current operator $J_\mu(\mathbf{r}) \equiv (\rho(\mathbf{r}), \mathbf{J}(\mathbf{r}))$ taken between the ground and final states of the target nucleus. The three-vector current operator $\mathbf{J}(\mathbf{r})$ is the sum of convection $\mathbf{J}^{\mathrm{C}}(\mathbf{r})$ and magnetization $\mathbf{J}^{\mathrm{M}}(\mathbf{r})$ currents.

Current conservation implies that for a particular choice of the quantization axis ($z \parallel \mathbf{q}$), the nuclear electromagnetic current can be described by three components with respect to the direction of $\mathbf{q}$: one longitudinal generated by the charge operator $\rho(\mathbf{q})$ and two transverse ones $J_\pm(\mathbf{q})$ generated by the current operator. By choosing the spherical coordinates, the two transverse components are [Cio80, Bof93]:

$$J_\pm(\mathbf{q}) = \mp\frac{1}{\sqrt{2}}\left(J_x(\mathbf{q}) \pm iJ_y(\mathbf{q})\right) \quad . \tag{2.22}$$

Thus, our external operator $O(\mathbf{q})$ is the Fourier transforms of the charge operator in case of longitudinal contribution:

$$O(\mathbf{q}) \;\rightarrow\; \rho(\mathbf{q}) \;=\; \int \mathrm{d}^3r \; e^{i\mathbf{q}\cdot\mathbf{r}} \, \rho(\mathbf{r}) \, , \tag{2.23}$$

with

$$\rho(\mathbf{r}) \;=\; \sum_{k=1}^{A} \frac{1+\tau_k^3}{2} \, \delta(\mathbf{r}-\mathbf{r}_k) \, , \tag{2.24}$$

and it is the Fourier transforms of the current operator in case of transverse contribution:

$$O_\pm(\mathbf{q}) \;\rightarrow\; \mathbf{J}_\pm(\mathbf{q}) = \left[\mathbf{J}^{\mathrm{C}}(\mathbf{q}) + \mathbf{J}^{\mathrm{M}}(\mathbf{q})\right]_\pm \;=\; \int \mathrm{d}^3r \; e^{i\mathbf{q}\cdot\mathbf{r}} \; \left[\mathbf{J}^{\mathrm{C}}(\mathbf{r}) + \mathbf{J}^{\mathrm{M}}(\mathbf{r})\right]_\pm \, , \tag{2.25}$$

with

$$\mathbf{J}^{\mathrm{C}}(\mathbf{r}) \;=\; \sum_{k=1}^{A} \frac{-i}{2M_k} \, \frac{1+\tau_k^3}{2} \; \left[\delta(\mathbf{r}-\mathbf{r}_k)\, \nabla_k \;+\; \nabla_k \, \delta(\mathbf{r}-\mathbf{r}_k)\right] , \tag{2.26}$$

and

$$\mathbf{J}^{\mathrm{M}}(\mathbf{r}) \;=\; \sum_{k=1}^{A} \frac{1}{2M_k} \left(\mu^{\mathrm{P}}\frac{1+\tau_k^3}{2} + \mu^{\mathrm{N}}\frac{1-\tau_k^3}{2}\right) \, \nabla_k \times \delta(\mathbf{r}-\mathbf{r}_k)\, \boldsymbol{\sigma}_k \, . \tag{2.27}$$

In the previous equations M_k indicates the rest mass of k–th nucleon, μ^{P} and μ^{N} the anomalous magnetic moment of the proton and the neutron respectively, $\boldsymbol{\sigma}_k$ the Pauli spin matrix of the k–th nucleon and $\tau_k^3 = 1$ (-1) for protons (neutrons).

2.4.2 Reduced Matrix Elements

We restrict our study to the investigation of doubly closed shell nuclei with initial and final states defined as:

$$
\begin{aligned}
|\Psi_0\rangle \;\rightarrow\; |00,+1\rangle \;&=\; G\,|\Phi;00,+1\rangle\,, \qquad (2.28)\\
|\Psi_f\rangle \;\rightarrow\; |JM,\Pi;p,h\rangle \;&=\; G\,|\Phi;JM,\Pi;p,h\rangle\,. \qquad (2.29)
\end{aligned}
$$

where G is the two body scalar correlation function given by Eq. (2.6). Now, our generic external one-body operator $O(\mathbf{q}) \rightarrow O_\eta(\mathbf{q})$ has three different forms, one for the charge $\eta = 0$ and the other two for the transverse components $\eta = \pm 1$. By considering the nuclear transition between states with good angular momentum defined in the above equations, one can rewrite the matrix elements of Eq. (2.20) in the form:

$$
\begin{aligned}
\xi^1_{f,\eta}(\mathbf{q}) \;&=\; \xi^1_{J,M,\Pi,\eta}(\mathbf{q};ph)\\
&=\; \Big[\langle\Phi;J,M,\Pi;p,h|\,O_\eta(\mathbf{q})\,|\Phi;00,+1\rangle_L\\
&\quad+\langle\Phi;J,M,\Pi;p,h|\,O_\eta(\mathbf{q})\,\sum_{i>1}^{A} h(r_{1i})\,|\Phi;00,+1\rangle_L\\
&\quad+\langle\Phi;J,M,\Pi;p,h|\,O_\eta(\mathbf{q})\,\sum_{1<i<k}^{A} h(r_{ik})\,|\Phi;00,+1\rangle_L\Big]. \qquad (2.30)
\end{aligned}
$$

Since we describe the nuclear transition between states with good angular momentum, it is convenient to make multipole expansions of the operators given by Eqs. (2.23) and (2.25) by expanding the plane wave appearing in these equations as:

$$e^{i\mathbf{q}\cdot\mathbf{r}} = 4\pi \sum_{\lambda=0}^{\infty} \sum_{\nu=-\lambda}^{\lambda} i^{\lambda} j_{\lambda}(qr) Y_{\lambda\nu}(\hat{\mathbf{r}}) Y^{*}_{\lambda\nu}(\hat{\mathbf{q}}) \ , \tag{2.31}$$

where we have indicated with $\hat{\mathbf{r}}$ the angles θ_r and ϕ_r and $\hat{\mathbf{q}}$ the angles θ_q and ϕ_q, characterizing the vectors $\mathbf{r}$ and $\mathbf{q}$ in polar coordinates, respectively and with $j_\lambda(qr)$ the spherical Bessel functions with $q \equiv |\mathbf{q}|$.

After making the multipole expansion, we have for the charge, the Coulomb operator $M_{\lambda\nu}(q)$ with natural parity $\Pi = (-1)^\lambda$, defined as:

$$M_{\lambda\nu}(q) \ = \ \int \mathrm{d}^3 r \, j_\lambda(qr) \, Y_{\lambda\nu}(\hat{\mathbf{r}}) \, \rho(\mathbf{r}) \ , \tag{2.32}$$

For the current we should distinguish between the transverse electric excitations $T^{\mathrm{E}}_{\lambda\nu}(q)$, with natural parity $\Pi = (-1)^\lambda$, and the transverse magnetic excitations $T^{\mathrm{M}}_{\lambda\nu}(q)$, with unnatural parity $\Pi = (-1)^{\lambda+1}$:

$$T^{\mathrm{E}}_{\lambda\nu}(q) \ = \ \frac{1}{q} \int \mathrm{d}^3 r \ \{\nabla \times [j_\lambda(qr) \, \mathbf{Y}^{\nu}_{\lambda\lambda}(\hat{\mathbf{r}})]\} \cdot \mathbf{J}(\mathbf{r}) \ , \tag{2.33}$$

and

$$T^{\mathrm{M}}_{\lambda\nu}(q) \ = \ \int \mathrm{d}^3 r \, j_\lambda(qr) \, \mathbf{Y}^{\nu}_{\lambda\lambda}(\hat{\mathbf{r}}) \cdot \mathbf{J}(\mathbf{r}) \ , \tag{2.34}$$

where we have used the symbol $\mathbf{Y}^{M}_{LJ}$ to indicate the vector spherical harmonics [Edm57]:

$$\mathbf{Y}^{M}_{LJ}(\hat{\mathbf{r}}) = \sum_{\mu\eta} < L\mu 1\eta | JM > Y_{L,\mu}(\hat{\mathbf{r}}) \, e_\eta$$

By substituting the above equations into Eq. (2.30) and using the Wigner-Eckart theorem (to extract the dependence on magnetic quantum numbers from the matrix element) and the properties of the 3j symbols, one can get $J = \lambda$ and $M = \nu = \eta$. Then, we can rewrite Eq. (2.30) in terms of reduced matrix elements:

$$\begin{aligned}
\xi^{1}_{f,\eta}(\mathbf{q}) &= i^{J}\sqrt{2\pi}\,\xi^{1}_{J,\Pi,\eta}(\mathbf{q};ph) \\
&= i^{J}\sqrt{2\pi}\Big[\langle\Phi;J,\Pi;p,h\|\,O_{J(\eta)}(\mathbf{q})\,\|\Phi;0,+1\rangle_{L} \\
&\quad +\ \langle\Phi;J,\Pi;p,h\|\,O_{J(\eta)}(\mathbf{q})\,\sum_{i>1}^{A}h(r_{1i})\,\|\Phi;0,+1\rangle_{L} \\
&\quad +\ \langle\Phi;J,\Pi;p,h\|\,O_{J(\eta)}(\mathbf{q})\,\sum_{1<i<k}^{A}h(r_{ik})\,\|\Phi;0,+1\rangle_{L}\Big], \qquad (2.35)
\end{aligned}$$

where we have defined the multipole expanded operators $O_{J(\eta)}(\mathbf{q})$ as:

$$O_{J(\eta)}(\mathbf{q}) = \begin{cases} \sqrt{2}M_{J(0)}(q) & \text{if } \eta = 0 \\ T^{\mathrm{E}}_{J(\pm1)}(q) + \eta T^{\mathrm{M}}_{J(\pm1)}(q) & \text{if } \eta = \pm1 \end{cases} . \qquad (2.36)$$

We insert η in Eqs. (2.35) and (2.36) to distinguish between charge and transverse operators while the reduced matrix itself does not depend on the magnetic quantum number η.

The many-body wave functions $|\Phi;J,M,\Pi;p,h\rangle$ and $|\Phi;00,+1\rangle$ are Slater determinant of single-particle wave functions of the form:

$$\begin{aligned}
\phi_k(\mathbf{r}) &\equiv |r;l_k\tfrac{1}{2}j_k m_k\rangle \qquad (2.37) \\
&= R^{t}_{n_k l_k j_k}(r)\sum_{\mu_k s}\langle l_k\mu_k\tfrac{1}{2}s|j_k m_k\rangle\,Y_{l_k\mu_k}(\hat{\mathbf{r}})\,\chi_s\,\chi_t\ , \qquad (2.38)
\end{aligned}$$

where χ_s and χ_t are the spin and isospin wave functions, respectively.

By using the orthonormality of the single-particle basis, we rewrite the reduced transition matrix elements of Eq. (2.35) as sums over one-body matrix elements:

$$
\begin{aligned}
\xi^1_{f,\eta}(\mathbf{q}) &= \sum_{ph} i^J \sqrt{2\pi}\, \xi^1_{J,\Pi,\eta}(\mathbf{q}; ph) \\
&= \sum_{ph} i^J \sqrt{2\pi} \Big[\langle p \| \, O_{J(\eta)}(\mathbf{q}) \, \| h \rangle_L + \sum_{i>1}^{A} \langle p, i \| \, O_{J(\eta)}(\mathbf{q}) \, h(r_{1i}) \, \| h, i \rangle_L \\
&\quad + \sum_{1<i<k}^{A} \langle p, i, k \| \, O_{J(\eta)}(\mathbf{q}) \, h(r_{ik}) \, \| h, i, k \rangle_L \Big] \;, \qquad (2.39)
\end{aligned}
$$

where the summation over all possible $1p - 1h$ for the exited state $|f\rangle$ is understood. For simplicity, we indicate the single-particle wave functions for particle and hole states using the letters p, h, i and k. Here the sums of the i and k indices are running on all the hole single particle wave functions. The subindeces $1, 2, 3$ of the correlation function $h(r_{ij})$ are associated to the radial coordinates of the first wave function, where also $O_{J(\eta)}(\mathbf{q})$ is acting, the second and the third one respectively. We have indicated only the direct matrix elements in the second and third term of the equation, but we calculate all the exchange diagrams, as it is shown in Fig. 2.2.

The multipole expanded one-body operators $O_{J(\eta)}(\mathbf{q})$ given by Eq. (2.36) are calculated by inserting the expressions (2.24), (2.26) and (2.27) into Eqs. (2.32), (2.33) and (2.34). The final calculation for the electromagnetic excitation of the two- and three- point reduced matrix elements given by Eq. (2.39), are shown in Appendix A, where the explicit operators for the charge and transverse current, Eqs. (2.32), (2.33) and (2.34) are inserted.

To keep it general, we will calculate the reduced matrix element terms of Eq. (2.39) using a generic operator. Generally, one may write the resulting multipole expanded one-body operator $O_{JM}(\mathbf{q})$ as the product of a term depending on q and on the modulus of $\mathbf{r}_1$ times a term depending only on the angular coordinates. In our case, we will work with reduced operator $O_{J(M)}(\mathbf{q})$ where there is no dependence of the magnetic quantum number

$$O_{J(M)}(\mathbf{q}) \equiv F_J(qr_1)\mathcal{O}_J(\hat{\mathbf{r}}_1) \ . \tag{2.40}$$

We will work with the conventions of Edmonds [Edm57] to indicate the 3j, 6j and 9j symbols. The calculations of the reduced matrix elements are carried out by performing a multipole expansion of the correlation function $h(r_{ij})$:

$$\begin{aligned} h(r_{ij}) &= h(r_i, r_j, \cos\theta_{ij}) = \sum_{L=0}^{\infty} h_L(r_i, r_j)\, P_L(\cos\theta_{ij}) \\ &= \frac{4\pi}{\widehat{L}^2} \sum_{L=0}^{\infty} h_L(r_i, r_j) \sum_{N=-L}^{L} Y^*_{LN}(\hat{\mathbf{r}}_i)\, Y_{LN}(\hat{\mathbf{r}}_j) \ , \end{aligned} \tag{2.41}$$

where P_L are the Legendre polynomials and we have used the notation $\widehat{\alpha} = \sqrt{2\alpha+1}$. Because of the completeness and the orthogonality of the Legendre polynomials, the $h_L(r_i, r_j)$ terms can be evaluated as:

$$h_L(r_i, r_j) = \frac{2L+1}{2} \int_{-1}^{1} \mathrm{d}(\cos\theta_{ij})\, P_L(\cos\theta_{ij})\, h(r_i, r_j, \cos\theta_{ij}) \ . \tag{2.42}$$

By inserting the generic operator of Eq. (2.40) into the first term of Eq. (2.39), we obtain the contribution of uncorrelated mean field:

$$\begin{aligned} D_1 &= \langle \phi_p(r_1) \| F_J(qr_1) \mathcal{O}_J(\hat{\mathbf{r}}_1) \| \phi_h(r_1) \rangle \\ &= \int \mathrm{d}^3 r_1 \, \phi_p^*(r_1) \, F_J(qr_1) \, \mathcal{O}_J(\hat{\mathbf{r}}_1) \, \phi_h(r_1) \\ &= \omega_{ph}^J \int \mathrm{d}r_1 \, r_1^2 \, R_p^*(r_1) \, F_J(qr_1) \, R_h(r_1) \ , \end{aligned} \tag{2.43}$$

where we have defined:

$$\omega_{\alpha\beta}^J = \langle \alpha \, \| \, \mathcal{O}_J(\hat{\mathbf{r}}_1) \, \| \, \beta \rangle \ , \tag{2.44}$$

where $\alpha \equiv l_\alpha \frac{1}{2} j_\alpha$ and $\beta \equiv l_\beta \frac{1}{2} j_\beta$ represent the angular momentum quantum numbers of the single-particle wave functions. The first line of Eq. (2.43) represent the contribution of the one-point diagram labeled as (1.1) in Fig. 2.2, while we have obtained the second line by separating the radial and angular dependence of the of the operator and wave functions.

The contribution of correlation is included into the two- and three-point diagrams represented by the second and third terms of Eq. (2.39). To obtain the contribution of the two-point diagrams, we insert the generic operator of Eq. (2.40) into the second term of Eq. (2.39). According to our model this will lead to four different diagrams. The First two-point diagram is given by:

$$D_{2.1} = \langle \phi_p(r_1) \, \phi_i(r_2) \| F_J(qr_1) \, \mathcal{O}_J(\hat{\mathbf{r}}_1) \, h(r_{12}) \| \phi_h(r_1) \, \phi_i(r_2) \rangle \ . \tag{2.45}$$

Eq. (2.45) represents the contribution of the first term of the two-point diagrams labeled as (2.1) in Fig. 2.2. By inserting the expansion of the correlation function of Eq. (2.41) and after separation of the angular and radial dependence, one can get:

$$D_{2.1} = 4\pi\, \omega^J_{ph} \int \mathrm{d}r_1\, r_1^2\, R^*_p(r_1)\, F_J(qr_1)\, R_h(r_1)\, \mathcal{H}^{[\rho]}_0(r_1) \;\; , \tag{2.46}$$

with

$$\mathcal{H}^{[\rho]}_0(r_1) \;=\; \frac{1}{4\pi} \sum_i \widehat{j}_i^{\,2}\, \mathcal{H}^{ii}_0(r_1) \;=\; \int \mathrm{d}r_2\, r_2^2\, h_0(r_1, r_2)\, \rho(r_2) \;\; , \tag{2.47}$$

where

$$\rho(r) \;=\; \frac{1}{4\pi} \sum_i \widehat{j}_i^{\,2}\, |R_i(r)|^2 \;\; , \tag{2.48}$$

is the nuclear density. In the same way, one can calculate the contribution of the other three terms of the two-point diagrams as:

$$\begin{aligned} D_{2.2} \;&=\; 4\pi\, (-1)^{j_p+j_h} \sum_{iLK} \delta_{t_i,t_h}\, (-1)^K\, \frac{\widehat{K}}{\widehat{L}^2}\, \gamma^L_{ih} \left\{ \begin{array}{ccc} L & K & J \\ j_p & j_h & j_i \end{array} \right\} \\ &\quad \times \omega^{LJ;K}_{pi} \int \mathrm{d}r_1\, r_1^2\, R^*_p(r_1)\, F_J(qr_1) R_i(r_1)\, \mathcal{H}^{[ih]}_L(r_1) \;\; , \end{aligned} \tag{2.49}$$

$$\begin{aligned} D_{2.3} \;&=\; 4\pi\, \delta_{t_p,t_h}\, (-1)^J\, \frac{1}{\widehat{J}^3}\, \gamma^J_{ph} \sum_i \widehat{j}_i\, \omega^{JJ;0}_{ii} \\ &\quad \times \int \mathrm{d}r_1\, r_1^2\, R^*_i(r_1)\, F_J(qr_1) R_i(r_1)\, \mathcal{H}^{[ph]}_J(r_1) \;\; , \end{aligned} \tag{2.50}$$

$$\begin{aligned} D_{2.4} \;&=\; 4\pi\, (-1)^{j_p+j_h+J} \sum_{iLK} \delta_{t_i,t_p}\, (-1)^L\, \frac{\widehat{K}}{\widehat{L}^2}\, \gamma^L_{pi} \left\{ \begin{array}{ccc} L & K & J \\ j_h & j_p & j_i \end{array} \right\} \\ &\quad \times \omega^{LJ;K}_{ih} \int \mathrm{d}r_1\, r_1^2\, R^*_i(r_1)\, F_J(qr_1)\, R_h(r_1)\, \mathcal{H}^{[pi]}_L(r_1) \;\; . \end{aligned} \tag{2.51}$$

In the previous equations, we have separated the angular dependence of two coordinates $\hat{\mathbf{r}}_1$ and $\hat{\mathbf{r}}_2$ in two different matrix elements $\omega^{LJ;K}_{\alpha\beta}$ and $\gamma^{\lambda}_{\alpha\beta}$, respectively. Also, we have used the property:

$$\mathcal{O}_J(\hat{\mathbf{r}})\, Y^*_{LN}(\hat{\mathbf{r}}) = \sum_K (-1)^{J-L} \widehat{K} \begin{pmatrix} J & L & K \\ 0 & -N & N \end{pmatrix} [\mathcal{O}_J \otimes Y^*_L(\hat{\mathbf{r}})]^K_{-N} \ , \tag{2.52}$$

to deal with the product of two angular terms at the same angular coordinate $\hat{\mathbf{r}}_1$. The definition of $\omega^{LJ;K}_{\alpha\beta}$ is:

$$\omega^{LJ;K}_{\alpha\beta} \ = \ \langle \alpha \| \left[\mathcal{O}_J(\hat{\mathbf{r}}_1) \otimes Y_L(\hat{\mathbf{r}}_1) \right]^K \| \beta \rangle \ , \tag{2.53}$$

and we will define $\gamma^\lambda_{\alpha\beta}$ at a generic angular coordinate $\hat{\mathbf{r}}$ because it will be used at different angular coordinates in the next equations:

$$\begin{aligned} \gamma^\lambda_{\alpha\beta} \ &= \ \langle l_\alpha \frac{1}{2} j_\alpha \| Y_\lambda(\hat{\mathbf{r}}) \| l_\beta \frac{1}{2} j_\beta \rangle \\ &= \ \frac{1}{\sqrt{4\pi}} (-1)^{j_\beta+\lambda-\frac{1}{2}} \, \xi(l_\alpha + l_\beta + \lambda) \, \widehat{j}_\alpha \widehat{j}_\beta \widehat{\lambda} \begin{pmatrix} j_\alpha & j_\beta & \lambda \\ \frac{1}{2} & -\frac{1}{2} & 0 \end{pmatrix} , \end{aligned} \tag{2.54}$$

with $\xi(l_\alpha + l_\beta + \lambda)$=1 if $l_\alpha + l_\beta + \lambda$ is even and $\xi(l_\alpha + l_\beta + \lambda)$=0 otherwise. The integral is:

$$\mathcal{H}^{[\alpha\beta]}_L(r_1) \ = \ \int \mathrm{d}r_2\, r_2^2\, R^*_\alpha(r_2)\, h_L(r_1, r_2)\, R_\beta(r_2) \ . \tag{2.55}$$

For the three-point diagrams we have obtained the following expressions:

$$\begin{aligned} D_{3.1} \ &= \ \sum_{ikL} \delta_{t_k,t_p}\, \delta_{t_i,t_p}\, \delta_{j_i,j_p}\, \xi(l_p + l_k + L)\, \xi(l_p + l_i)\, \widehat{j}^2_k \begin{pmatrix} j_p & j_k & L \\ \frac{1}{2} & -\frac{1}{2} & 0 \end{pmatrix}^2 \\ &\times \omega^J_{ih} \int \mathrm{d}r_1\, r_1^2\, R^*_i(r_1)\, F_J(qr_1)\, R_h(r_1)\, \mathcal{J}^{[pk];[ki]}_L \ , \end{aligned} \tag{2.56}$$

$$
\begin{aligned}
D_{3.2} &= 4\pi \sum_{i} \delta_{t_i,t_p}\, \delta_{j_i,j_p}\, \xi(l_p+l_i) \\
&\times \omega^J_{ih} \int \mathrm{d}r_1\, r_1^2\, R^*_i(r_1)\, F_J(qr_1)\, R_h(r_1)\, \mathcal{J}_0^{[pi];[\rho]}\,, \qquad (2.57)
\end{aligned}
$$

$$
\begin{aligned}
D_{3.3} &= \sum_{ikL} \delta_{t_i,t_h}\, \delta_{t_k,t_h}\, \delta_{j_k,j_h}\, \xi(l_i+l_h+L)\, \xi(l_k+l_h)\, \widehat{j}_i^2 \begin{pmatrix} j_i & j_h & L \\ \frac{1}{2} & -\frac{1}{2} & 0 \end{pmatrix}^2 \\
&\times \omega^J_{pk} \int \mathrm{d}r_1\, r_1^2\, R^*_p(r_1)\, F_J(qr_1)\, R_k(r_1)\, \mathcal{J}_L^{[ih];[ki]}\ , \qquad (2.58)
\end{aligned}
$$

$$
\begin{aligned}
D_{3.4} &= 4\pi \sum_{i} \delta_{t_i,t_h}\, \delta_{j_i,j_h}\, \xi(l_i+l_h) \\
&\times \omega^J_{pi} \int \mathrm{d}r_1\, r_1^2\, R^*_p(r_1)\, F_J(qr_1)\, R_i(r_1) \mathcal{J}_0^{[ih];[\rho]}\,, \qquad (2.59)
\end{aligned}
$$

$$
\begin{aligned}
D_{3.5} &= 4\pi\, (-1)^J \sum_{ikL} \delta_{t_i,t_p}\, \delta_{t_k,t_h}\, (-1)^{j_i+j_k+L}\, \frac{1}{\widehat{L}^2}\, \gamma^L_{pi}\, \gamma^L_{kh} \begin{Bmatrix} j_p & j_h & J \\ j_k & j_i & L \end{Bmatrix} \\
&\times \omega^J_{ik} \int \mathrm{d}r_1\, r_1^2\, R^*_i(r_1)\, F_J(qr_1)\, R_k(r_1) \mathcal{J}_L^{[pi];[kh]}\ , \qquad (2.60)
\end{aligned}
$$

$$
\begin{aligned}
D_{3.6} &= 4\pi\, \delta_{t_p,t_h}\, \gamma^J_{ph}\, \frac{1}{\widehat{J}^4} \sum_{ik} \delta_{t_i,t_k}\, \gamma^J_{ik} \\
&\times \omega^J_{ik} \int \mathrm{d}r_1\, r_1^2\, R^*_i(r_1)\, F_J(qr_1) R_k(r_1)\, \mathcal{J}_J^{[ph];[ki]}\ . \qquad (2.61)
\end{aligned}
$$

In these equations we have introduced the radial integrations as:

$$
\mathcal{J}_L^{[\alpha\beta];[\gamma\delta]} = \int \mathrm{d}r_2\, r_2^2\, R^*_\alpha(r_2)\, R_\beta(r_2)\, \mathcal{H}_L^{[\gamma\delta]}(r_2)\ , \qquad (2.62)
$$

with

$$
\mathcal{H}_L^{[\alpha\beta]}(r_2) = \int \mathrm{d}r_3\, r_3^2\, R^*_\alpha(r_3)\, h_L(r_2,r_3)\, R_\beta(r_3)\ , \qquad (2.63)
$$

and

$$
\mathcal{J}_0^{[\alpha\beta];[\rho]} = \int \mathrm{d}r_2\, r_2^2\, R^*_\alpha(r_2)\, R_\beta(r_2)\, \mathcal{H}_0^{[\rho]}(r_2)\ , \qquad (2.64)
$$

with

$$\mathcal{H}_0^{[\rho]}(r_2) \;=\; \frac{1}{4\pi}\sum_i \widehat{\jmath}_i^{\,2}\,\mathcal{H}_0^{ii}(r_2) \;=\; \int \mathrm{d}r_3\, r_3^2\, h_0(r_2, r_3)\, \rho(r_3) \;\; . \tag{2.65}$$

By inserting into the above equations the electromagnetic charge and transverse operators, Eqs. (2.32), (2.33) and (2.34), instead of the generic one, we will get the final reduced matrix elements for the transition caused by the electromagnetic probe (see Appendix A for details).

It is worth stressing that most cluster expansion techniques to calculate the electromagnetic response of nuclei refer to the inclusive case [Pan79, Fan87] and even in case of semi-exclusive reaction the application of the technique was done without caring of the proper normalization of the many-body wave function [Giu91, Giu94, Ryc95b, Ryc97, Jan00, Ryc00].

Our first order *SRC* reduced matrix elements may bridge the gap between the ground state many-body calculations and electromagnetic nuclear responses. We have already said that the validity of the model has been tested in nuclear matter by comparing the results with those obtained by a calculation that considers all the cluster terms [Ama98]. The agreement between the two results is excellent, showing that the first order approximation is reliable and the normalization of the wave function is maintained. In our calculations our inputs, i.e. single-particle wave functions and correlations, are related by the same nuclear hamiltonian. They are taken from *FHNC* calculations of the ground state of closed shell nuclei obtained by minimizing the hamiltonian expectation value evaluated with realistic and semi-realistic nucleon-nucleon potentials [Ari96, Fab00].

The model has been developed by Co' and Lallena [Co'01] for quasielastic inclusive reactions. We will try to extend the work for different excitation energy regions (e.g. discrete low-lying excited states and quasielastic semi-exclusive reactions), with including all correlated terms for the charge, magnetization and convection current operators.

Chapter 3

SRC in Low-Lying Nuclear Excited States

Overview

A brief review of the inclusive (e, e') cross section for inelastic electron scattering leading to the excitation of a discrete bound state below the particle emission threshold is given. We work in natural units ($\hbar = c = 1, e^2 = 1/137.04$) and employ the conventions of Bjorken and Drell [Bjo64]. As we stated in the introduction, we work in the framework of the one-photon exchange approximation or first order $PWBA$ for the electron wave functions as shown diagrammatically in Fig. 3.1. Higher order terms containing more than one photon are suppressed because of the weakness of the electromagnetic coupling constant. The nuclear current is calculated in the Impulse Approximation IA, i.e. it is given by the sum of the currents induced by the individual nucleons.

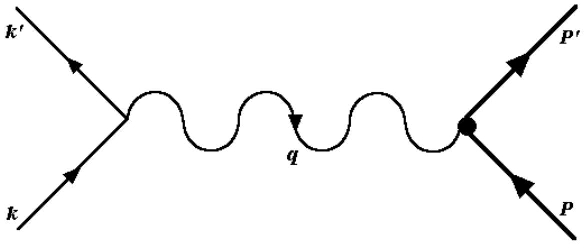

Figure 3.1: Inelastic (e, e') electron scattering in the one-photon exchange.

3.1 The Inclusive Scattering Process

In our approach the electron wave functions are plane wave solutions of the Dirac equation. In the process we want to describe, the electron is scattered through an angle θ from an initial state $k \equiv (\epsilon, \mathbf{k})$ to the final state $k' \equiv (\epsilon', \mathbf{k}')$. In this process, a single virtual photon with four-momentum $q_\mu \equiv (\omega, \mathbf{q}) = k - k'$ is exchanged with the nuclear target. The nucleus makes a transition from an initial state $|\Psi_0\rangle$ with four momentum P to a final state $|\Psi_f\rangle$ with $P' = P - q_\mu$. We consider the electron energies are large enough so that all terms depending upon the electron rest mass are neglected. If both of the incident electron beam and the target nucleus are unpolarized and only the scattered electron is observed (inclusive experiment), the *PWBA* differential cross section in the laboratory frame is given by [For66, Don75]:

$$\frac{\mathrm{d}\sigma}{\mathrm{d}\Omega} = Z^2 \sigma_M \left[v_L R_L(\mathbf{q}, \omega) + v_T R_T(\mathbf{q}, \omega) \right] \tag{3.1}$$

where we indicate with Z the nuclear charge and with σ_M the Mott cross section:

$$\sigma_M = \left(\frac{e^2 \cos(\theta/2)}{2\epsilon \sin^2(\theta/2)} \right)^2 . \tag{3.2}$$

As shown in Eq. (3.1), the cross section is decomposed into longitudinal (Coulomb) R_L and transverse (electric and magnetic) R_T hadronic terms, multiplied by corresponding leptonic factors v that come from the leptonic tensor and depend only from kinematic variables:

$$v_L = \left(\frac{q_\mu^2}{\mathbf{q}^2}\right)^2 , \tag{3.3}$$

$$v_T = \tan^2\frac{\theta}{2} - \frac{1}{2}\frac{q_\mu^2}{\mathbf{q}^2} . \tag{3.4}$$

The functions R_L and R_T represent longitudinal and transverse dynamic structure functions, respectively, or response functions that contain all the information on the distribution of the nuclear electromagnetic current density.

Eq. (3.1) describes the inclusive inelastic electron scattering differential cross section in the general situation where the responses depend on both $q \equiv |\mathbf{q}|$ and ω. In case of inelastic scattering to discrete nuclear level, the energy transfer ω can assume only specific values and equals to the nuclear excitation energy $E_f - E_0$ between the final and initial eigenstates. Electron scattering experiments in this region consist in selecting the excited state with the energy transfer and changing the momentum transfer. Because of the similarity with the elastic scattering processes it is common practice to follow the elastic scattering nomenclature and to speak about form factors, instead that response functions. The process is described by making a multipole expansion of the virtual photon Eq. (2.31). The multipolarity of the transition leads to longitudinal (Coulomb) multipole transition $C\lambda$ and transverse electric and magnetic multipole transitions $E\lambda$ and $M\lambda$, respectively, while the angular momentum λ of the virtual photon determines the multipolarity of the transitions. Thus, the response functions can be written in terms of longitudinal $F_L(q)$ and transverse electric $F_T^{\mathrm{E}}(q)$ and magnetic $F_T^{\mathrm{M}}(q)$ form factors as follow:

$$
\begin{aligned}
R_L(q,\omega) &= |F_L(q)|^2\,\delta(E_f - E_0 - \omega) && (3.5)\\
R_T(q,\omega) &= |F_T(q)|^2\,\delta(E_f - E_0 - \omega) \\
&= \left[|F_T^{\mathrm{E}}(q)|^2 + |F_T^{\mathrm{M}}(q)|^2\right]\,\delta(E_f - E_0 - \omega)\,, && (3.6)
\end{aligned}
$$

where the longitudinal form factor and the transverse electric and magnetic form factors are simple Fourier Bessel transforms of the nuclear charge and current densities given by Eqs. (2.23) and (2.25), respectively. Thus, we can express the form factors as:

$$
\begin{aligned}
|F_L(q)|^2 &= \sum \langle\Psi_0|\rho^\dagger(\mathbf{q})|\Psi_f\rangle\langle\Psi_f|\rho(\mathbf{q})|\Psi_0\rangle\,, && (3.7)\\
|F_T(q)|^2 &= \sum \langle\Psi_0|J_-^\dagger(\mathbf{q})|\Psi_f\rangle\langle\Psi_f|J_-(\mathbf{q})|\Psi_0\rangle \\
&\qquad + \langle\Psi_0|J_+^\dagger(\mathbf{q})|\Psi_f\rangle\langle\Psi_f|J_+(\mathbf{q})|\Psi_0\rangle\,, && (3.8)
\end{aligned}
$$

where the sum is performed over the average initial spin substates and over the final spin substates (unpolarized cross section). Considering the nuclear transition between states with good initial $|\Psi_0\rangle \rightarrow |J_0M_0,\Pi_0\rangle$ and final $|\Psi_f\rangle \rightarrow |J_fM_f,\Pi_f\rangle$ angular momentum and using the multipole expansion of the plane wave of Eq. (2.31), the form factors may be written after applying the Wigner-Eckart theorem as:

$$
|F_L(q)|^2 = \frac{4\pi}{Z^2}\frac{1}{2J_0+1}\sum_{\lambda=0}^{\infty}|\langle J_f\|M_\lambda(q)\|J_0\rangle|^2 \qquad (3.9)
$$

$$|F_T(q)|^2 = \frac{4\pi}{Z^2}\frac{1}{2J_0+1} \times \sum_{\lambda=1}^{\infty}\left[|\langle J_f\|T_\lambda^{\mathrm{E}}(q)\|J_0\rangle|^2 + |\langle J_f\|T_\lambda^{\mathrm{M}}(q)\|J_0\rangle|^2\right], \quad (3.10)$$

where $M_\lambda(q)$, $T_\lambda^{\mathrm{E}}(q)$ and $T_\lambda^{\mathrm{M}}(q)$ are the Coulomb, electric and magnetic operators given by Eqs. (2.32), (2.33) and (2.34), respectively. Thus the cross section may be expressed directly in terms of Coulomb $(C0, C1, ...)$, electric $(E1, E2, ...)$ and magnetic $(M1, M2, ...)$ multipole matrix elements.

We restrict our study for doubly closed shell nuclei, i.e. spin zero nuclei, with initial and final states given by Eqs. (2.28) and (2.29) where $J_0 = 0$ and $J_f = J$. Then as a result of selection rules, the sums of Eqs. (3.9) and (3.10) will include only the single multipole term $\lambda = J$. Eqs. (3.9) and (3.10) may be written as:

$$|F_L(q)|^2 = \frac{4\pi}{Z^2}|\langle J\|M_J(q)\|0\rangle|^2 \quad (3.11)$$

$$|F_T(q)|^2 = \frac{4\pi}{Z^2}\left[|\langle J\|T_J^{\mathrm{E}}(q)\|0\rangle|^2 + |\langle J\|T_J^{\mathrm{M}}(q)\|0\rangle|^2\right]. \quad (3.12)$$

The multipole expansions of Eqs. (3.11) and (3.12) require a model for the nuclear final excitation modes $|JM, \Pi_f\rangle$. In the next section, we briefly give the nuclear model that used in our calculations.

3.2 Nuclear Model

The bound low-lying nuclear excited states can be of collective type or characterized by a single-particle transition. From the microscopic point of view, the collective bound states are built up the excitation of many particle-hole pairs. They are the most extensively studied, because they are the strongest states in scattering experiments. The second type of bound states (non collective states) are the particle-hole states. These are characterized by the fact that only a few particle-hole pairs contribute to the excitation. In the extreme single particle model, this sort of transitions will be entirely due to a single transition of one-particle-one-hole $1p-1h$ pair.

The aim of our work is to study the effects of *SRC* and the dominant region of their presence. As a result of complicated structure of the collective states, it is not easy to disentangle the effects of *SRC* from other nuclear phenomena. In the present work, we look for simply non collective excited states (high spin states and stretched states that are formed with the maximal angular momentum for the particle-hole coupling) to better disentangle the effects of *SRC*. We study the degree of collectivity of the excited states by using the *RPA* where the *RPA* is the most successful approximation scheme to describe nuclear excitations.

3.2.1 Collective Excitations

The collective excitations are produced by the part of interaction neglected in the *IPM* and they are commonly described by effective theories, i.e. theories which use effective interactions. One of these theories is the *RPA* that describes excited states in terms of linear combinations of particle-hole pairs. These linear combinations are very complicated for the strongly collective low spin states while they are supposed to be very weak for high spin states. The *RPA* excited state $|\Psi_n(RPA)\rangle$ can be expressed as [Fet71]:

$$|\Psi_n(RPA)\rangle \to |JM,\Pi;p,h\rangle_{RPA} = Q_n^\dagger|\Psi_0(RPA)\rangle\,, \tag{3.13}$$

and satisfies Schrödinger equation $H|\Psi_n(RPA)\rangle = E_n|\Psi_0(RPA)\rangle$ with $H = H_o + V_{res}$. In the *RPA* the creation operator $Q_n^\dagger$ is defined as:

$$Q_n^\dagger = \sum_{ph} X_{ph}^{(n)} a_p^\dagger a_h - Y_{ph}^{(n)} a_h^\dagger a_p\,, \tag{3.14}$$

where $a^\dagger$ and a are single-particle creation and annihilation operators, respectively. The *RPA* ground state $|\Psi_0(RPA)\rangle \to |00,+1\rangle_{RPA}$ is now defined via the condition:

$$Q_n|\Psi_0(RPA)\rangle = 0\,. \tag{3.15}$$

The $X_{ph}^{(n)}$ and $Y_{ph}^{(n)}$ amplitudes are real and they are obtained by solving the *RPA* secular equations [Fet71]. The values of these amplitudes depend on the residual effective interaction whose role has been studied in many works [Lal88, Co'90, Hin92, Ari94].

The particle-hole residual interaction can be written as the sum of terms with different spin, isospin dependence by conserving the symmetry properties that the nuclear force should satisfy. We use two different residual interactions based on the Landau-Migdal theory of finite Fermi systems [Mig67, Spe77]. The first one is a zero-range density dependent interaction:

$$\begin{aligned} V_{res}^\delta &= F_0^{ph}(\mathbf{r}_1,\mathbf{r}_2) \\ &= C_0\,[f_0(\rho) + f_0'\boldsymbol{\tau}_1\cdot\boldsymbol{\tau}_2 + g_0\boldsymbol{\sigma}_1\cdot\boldsymbol{\sigma}_2 + g_0'\boldsymbol{\sigma}_1\cdot\boldsymbol{\sigma}_2\,\boldsymbol{\tau}_1\cdot\boldsymbol{\tau}_2]\,\delta(\mathbf{r}_1-\mathbf{r}_2)\,, \end{aligned} \tag{3.16}$$

with

$$
\begin{aligned}
f_0(\rho) &= f_0^{\rm ext} + \left(f_0^{\rm int} - f_0^{\rm ext}\right)\rho(r)\,, &(3.17)\\
\rho(r) &= (1+\exp[(r-R)/a])^{-1}\,, &(3.18)
\end{aligned}
$$

where R and a are the radius and the diffuseness parameter of the nuclear charge distribution. The dimensionless force parameters f_0, f_0', g_0 and g_0' are chosen in a way to reproduce the energies of some well known collective states of the nucleon under investigation. The parameter C_0 is the inverse of the density of states N_0 at the Fermi surface,

$$
C_0 = N_0^{-1} = \frac{\pi^2\hbar}{k_f m}\,, \tag{3.19}
$$

where k_f is the Fermi momentum.

In the second residual interaction, we add to the Landau-Migdal force V_{res}^{δ} the one-pion ($\pi-$) V_π and one-rho ($\rho-$) V_ρ exchange contribution. This modification includes a tensor term in the interaction which is very important for the description of the magnetic states. By summing the zero-range Landau-Migdal force to the $\pi-$ and $\rho-$ potential, we have the so called Jülich-Stony Brook interaction [Spe80]:

$$
V_{res}^{\delta+\pi+\rho} = V_{res}^{\delta} + V_\pi + V_\rho\,. \tag{3.20}
$$

The transition matrix element for the transition from the RPA ground state to RPA excited state can be calculated for any generic one-body external operator $O_{JM}(q)$. By using the Wigner-Eckart theorem and the orthonormality of the single-particle wave function of Eq. (2.38), the reduced matrix element for this transition can be expressed as [Fet71, Kre86]:

$$\langle J \| O_J(q) \| 0 \rangle = \sum_{ph} \left[X_{ph}^{(J)} + (-1)^J Y_{ph}^{(J)} \right] \langle p \| O_J(q) \| h \rangle \tag{3.21}$$

where $p \equiv l_p \frac{1}{2} j_p$ and $h \equiv l_h \frac{1}{2} j_h$ are the angular momentum quantum numbers of the single-particle wave functions for particle and hole states, respectively. Details about the calculation of the reduced matrix elements between the single-particle states can be found elsewhere [Kre86].

The *RPA* theory is formulated without considering the *SRC*. This means that all the calculations are done with uncorrelated single-particle states, corresponding to the one-point diagram (1.1) in Fig. 2.2. Thus the explicit expressions of the single particle reduced transition matrix elements $\langle p \| O_J(q) \| h \rangle$ of Eq. (3.21) for the different electro-magnetic operators are given in Appendix A by Eqs. (A.5) for the longitudinal transitions, (A.25) and (A.42) for electric transition and (A.66) and (A.81) for magnetic transitions.

3.2.2 Non Collective Excitations

We have already stated that, in order to study the *SRC* effects, we are interested in the non collective excited states characterized by one (single) or at most two $1p-1h$ pairs. We evaluate the degree of collectivity of the various excited states by means of discrete *RPA* calculations using the two interactions described above.

In our study we consider those states having a single $1p-1h$ pair with X amplitude value larger than 0.9 in both calculations. In addition, in our analysis we consider those states dominated by two $1p-1h$ pairs where for these excited states we suppose that their mean field wave functions could be described as a linear combination of the two $1p-1h$ pairs.

By using the definition of excited state wave function given by Eqs. (2.16) and (2.29) of Chapter 2, the correlated excited state wave function for the single $1p-1h$ pair transition is given by:

$$\begin{aligned} |\Psi_f\rangle &= G\,|\Phi_{1p1h}\rangle \\ &= G\,|JM,\Pi;p,h\rangle\,, \end{aligned} \tag{3.22}$$

and for the two $1p-1h$ pairs transition as:

$$\begin{aligned} |\Psi_f\rangle &= G\,|\Phi_{1p1h}\rangle_2 \\ &= G\,\left[X_{ph}\,|JM,\Pi;p,h\rangle + X_{p'h'}\,|JM,\Pi;p',h'\rangle\right]\,, \end{aligned} \tag{3.23}$$

where $|\Phi_{1p1h}\rangle$ and $|\Phi_{1p1h}\rangle_2$ are the Slater determinant of the uncorrelated single-particle wave functions for the single and two $1p-1h$ excitations, respectively. In this second case the X_{ph} amplitudes are normalized as:

$$X_{ph}^2 + X_{p'h'}^2 = 1. \tag{3.24}$$

Following the procedures presented in Chapter 2 which lead to Eq. (2.39), the correlated reduced matrix element for the transition by generic one-body external operator $O_{JM}(q)$ is given by:

$$\begin{aligned} \langle J\|O_J(q)\|0\rangle &= \langle p\|\,O_J(\mathbf{q})\,\|h\rangle_L + \sum_{i>1}^{A}\langle p,i\|\,O_J(\mathbf{q})\,h(r_{1i})\,\|h,i\rangle_L \\ &\quad + \sum_{1<i<k}^{A}\langle p,i,k\|\,O_J(\mathbf{q})\,h(r_{ik})\,\|h,i,k\rangle_L\,, \end{aligned} \tag{3.25}$$

where single-particle reduced matrix elements for uncorrelated one-point diagram $\langle p \| \, O_J(\mathbf{q}) \, \| h \rangle_L$, two-point diagrams $\langle p, i \| \, O_J(\mathbf{q}) \, h(r_{1i}) \, \| h, i \rangle_L$ and three-point diagrams $\langle p, i, k \| \, O_J(\mathbf{q}) \, h(r_{ik}) \, \| h, i, k \rangle_L$ are given in Appendix A for the different electro-magnetic operators.

3.3 Specific Applications

Our *SRC* model is applied to investigate specific doubly closed shell nuclei. This ensures that the systems under investigation have a spherical symmetry. This symmetry simplify the expression of the *RPA* secular equation which we solve to identify the degree of collectivity of the states under investigation.

Specifically, we apply our *SRC* model to study ^{16}O, ^{40}Ca, ^{48}Ca and ^{208}Pb closed shell nuclei. These nuclei have been widely investigated from both theoretical and experimental point of view. On one hand, this allows us to set the parameters of our input by reproducing the single particle energies and rms radii. On the other hand, we can compare our results with those of the other theories and with the experimental data.

The ^{48}Ca and ^{208}Pb are the lightest and heaviest doubly closed shell stable nuclei with neutron excess. The fact that the number of neutrons differs from the number of protons has the consequence that proton and neutron degrees of freedom are largely decoupled in the low-lying excitations of these nuclei. For this reason it is possible to identify certain transitions as being predominantly due to proton or neutron excitations as single $1p - 1h$ pair. Furthermore for the lightest doubly closed shell

^{16}O nucleus, there are also available $(e, e'p)$ and (γ, p) data that we can use to extend our studies at quasielastic region as it will be shown in the next chapters.

We calculate the electron excitations form factors and our results are compared with the experimental data of various high spin and stretched low-lying states in ^{16}O [Hyd87], ^{40}Ca [Wil87], ^{48}Ca [Wis85] and ^{208}Pb [Lic79, Con92] nuclei. The simplicity of the structure of these states permits the investigation of deviations from standard *IPM* results.

For magnetic excitations the comparison is done with the transverse form factor which can be unambiguously obtained for each cross section value. In the electric excitations, both longitudinal and transverse form factors contribute. Their extraction from the cross section data requires at least two measurements done at the same value of the momentum transfer $\mathbf{q}$ and for different scattering angles. Because of the difficulties related to this procedure [Co'87], for some electric states we prefer to compare our calculations directly to the cross sections.

The first input, required by our calculations, is the set of single-particle wave functions. The single-particle basis is generated by a spherical mean field potential of Woods-Saxon type:

$$V(r) = -\left[V_0 + V_{LS}\left(\frac{\hbar}{m_\pi c}\right)^2 \mathbf{L}\cdot\boldsymbol{\sigma}\frac{1}{r}\frac{\mathrm{d}}{\mathrm{d}r}\right] f(r,R,a) + V_C(r)\,, \qquad (3.26)$$

with

$$f(r,R,a) = \left(1 + \exp\left[\frac{(r-R)}{a}\right]\right)^{-1}\,, \qquad (3.27)$$

where m_π is the pion mass and $V_C(r)$ is the Coulomb potential generated by a uniform charge distribution of radius R_C. The parameters of the

Table 3.1: Parameters of the Woods-Saxon potentials used to generate the set of single-particle wave functions for the doubly closed shell nuclei under investigation. The parameters are taken from the work of Arias *et al.* [Ari96] and references there in. We indicate with π and ν proton and neutron states, respectively.

		^{16}O	^{40}Ca	^{48}Ca	^{208}Pb
π	V_0 [MeV]	52.5	57.5	59.5	60.40
	V_{LS} [MeV]	7.0	11.11	8.55	6.75
	R [fm]	3.2	4.1	4.36	7.46
	a [fm]	0.53	0.53	0.53	0.79
ν	V_0 [MeV]	52.5	55.0	50.0	44.32
	V_{LS} [MeV]	6.54	8.5	7.74	6.08
	R [fm]	3.2	4.1	4.36	7.46
	a [fm]	0.53	0.53	0.53	0.66

potential are shown in Tab. 3.1 for nuclei under investigation. Those parameters are taken from the work of Arias *et al.* [Ari96] and references there in. The parameters are adjusted to fit the experimentally known energies near the Fermi surface and the rms charge radius of nuclei under investigation.

We have to emphasize that the two-body scalar correlation function $f(r)$, the other input of our model, depends on the single-particle waves since they should be linked by the same many-body hamiltonian. In the theoretical framework of the *CBF* theory both inputs have been fixed by minimizing of the ground state energy functional for a given microscopic many-body hamiltonian.

In our calculations, the single-particle wave functions, generated with Woods-Saxon parameters given in Tab. 3.1, are linked with a purely scalar correlation function $f(r)$. The *NN* interaction used in the minimization procedure is the semi realistic $S3$ interaction of Afnan and Tang [Afn68]. In the work of Arias *et al.* [Ari96] the energy minimum was obtained by changing only the correlation function $f(r)$ while the Woods-Saxon parameters have been kept fixed.

We show in Fig. 3.2, as an example, different types of correlation function $f(r)$ in case of ^{16}O. In that figure, two types of correlation functions are obtained with the $S3$ semi realistic interaction. The dashed line, labeled as G correlation, shows the results of gaussian parameterization of the equation $f(r) = 1 - A\exp(-Br^2)$ with two free parameters A and B. The solid line, labeled as $S3$ correlation, shows the results of the Euler minimization procedure. For the sake of comparison, we show as dotted line, labeled as $V8$ correlation, the result of scalar part of the state dependent correlation function of Fabrocini *et al.* [Fab00]. Their correlation function was produced by more realistic interaction called V8' interaction which is a reduction of the Argonne V18 interaction [Wir95]. It should be noticed that the $V8$ correlation function is not linked to our single-particle basis where the energy minimum was obtained with different sets of Woods-Saxon parameters. Although the inconsistency of the inputs, we shall use the results of $V8$ correlation function together with our sets of Woods-Saxon parameters given in Tab. 3.1. This will give us the opportunity to test the need of relating both inputs.

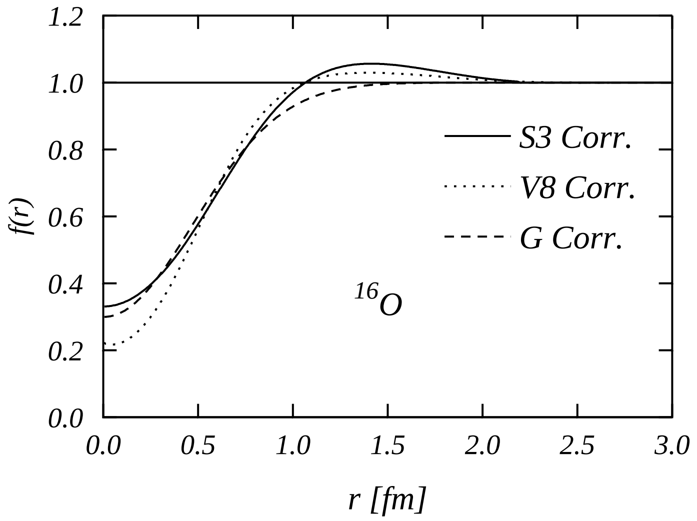

Figure 3.2: Correlation functions used in our calculations for ^{16}O nucleus. The solid and dashed lines refer to the $CBF - FHNC$ calculations of Arias *et al.* [Ari96] with $S3$ semi realistic interaction. The solid line, labeled as $S3$, has been produced by the Euler minimization procedure while the dashed line, labeled as G, by a gaussian correlation function $f(r) = 1 - A \exp(-Br^2)$ with $A = 0.7$ and $B = 2.3$ fm^{-2}. The dotted line, labeled as $V8$, represents the correlation function of the work of Fabrocini *et al.* [Fab00] where a more realistic nucleon-nucleon interaction has been used.

To complete the information on the input, we present in Tab. 3.2 some energies of single-particle states below the Fermi level (hole-states h) and some energies of single-particle states above Fermi level (particle-states p) for ^{16}O, ^{48}Ca and ^{48}Ca nuclei. The E_{WS} energies are obtained using the parameterization of the mean field potential of Woods-Saxon given in Tab. 3.1. Also, in Tab. 3.2, we show the available experimental energies $E_{exp.}$.

As suggested by Rinker and Speth [Rin78], in the actual RPA calcula-

Table 3.2: Single-particle energies in MeV of states near Fermi level.

		π		ν	
		$E_{exp.}$	E_{WS}	$E_{exp.}$	E_{WS}
^{16}O					
h-states	$1s_{1/2}$	–	−29.90	–	−33.98
	$1p_{3/2}$	−18.40	−16.92	−21.80	−20.52
	$1p_{1/2}$	−12.10	−12.74	−15.70	−16.63
p-states	$1d_{5/2}$	−0.60	−3.76	−4.14	−6.84
	$2s_{1/2}$	−0.10	−0.89	−3.27	−3.90
^{40}Ca					
h-states	$1d_{5/2}$	−14.70	−16.19	−18.20	−21.37
	$2s_{1/2}$	−10.3	−10.30	−21.60	−16.42
	$1d_{3/2}$	−8.30	−8.71	−15.60	−15.70
p-states	$1f_{7/2}$		−5.31		−9.76
	$2p_{3/2}$		0.53		−4.85
	$1f_{5/2}$		6.25		−0.82
	$2p_{1/2}$		3.61		−2.29
^{48}Ca					
h-states	$1d_{5/2}$		−20.50		−20.11
	$2s_{1/2}$	−15.81	−15.43	−12.55	−15.66
	$1d_{3/2}$	−16.17	−15.65	−12.53	−15.59
	$1f_{7/2}$			−9.95	−9.52
p-states	$1f_{7/2}$	−9.63	−9.49		
	$2p_{3/2}$	−6.54	−3.80	−5.14	−4.88
	$1f_{5/2}$	−5.82	−1.45	−1.56	−2.17
	$2p_{1/2}$	−6.11	−1.21	−3.12	−2.70
	$1g_{9/2}$		1.96	−1.13	1.32

tions, the experimental single particle energies are used wherever possible while for the remaining states not shown in Tab. 3.2 we take the E_{WS} energies. For ^{208}Pb nucleus we used the set of single-particle states given in Tab. 2 of Rinker and Speth. [Rin78] which are produced by the same Woods-Saxon parameters considered in our calculations and take into account the available experimental single-particle energies.

3.3.1 Testing the Collectivity of the Nuclear Excited States

We have already mentioned that the range of applicability of our model is limited to those kinematic situations where the effects of the collective excitations can be neglected. The collectivity of the selected excited states is studied by analyzing the discrete RPA results that obtained with the two previously mentioned residual interactions V_{res}^{δ} and $V_{res}^{\delta+\pi+\rho}$. We find that most of states under investigation are not sensitive to the change of the residual interaction. This means that for these states, the form factors of Eqs. (3.11) and (3.12) are not affected by the tensor part of the residual interaction. However, we find few states very sensitive to the inclusion of the tensor part of the residual interaction. Henceforth we shall discuss only the results of the $V_{res}^{\delta+\pi+\rho}$ and we shall refer to V_{res}^{δ} interaction if it gives different results.

The single-particle basis, used in the RPA calculation, is generated by the Woods-Saxon potential given in Tab. 3.1. The stability of the RPA results is reached by including the configuration space of the single-particle states up to 3 major shells above the Fermi level. This corresponds to a configuration space composed by 32 single-particle states for ^{16}O and 44 for ^{40}Ca and ^{48}Ca nuclei. In case of ^{208}Pb, the configuration space is increased, as shown in the work of Co' and Lallena [Co'90], to include 4 shells above the Fermi level corresponding to 100 single-particle states. Increasing the configuration space is important to include the maximum degree of mixing of the $1p-1h$ components. The stability of the RPA results has been tested by repeating the calculations with larger configuration space, e.g. including 44 single-particle states for ^{16}O and 58 for ^{48}Ca. We did not find visible difference with the results obtained with the smaller space configuration.

In the following, we shall show the calculated electro-excitation form factors in the framework of the $1p-1h$ RPA calculations.

3.3.1.1 RPA for ^{16}O Nucleus

For ^{16}O nucleus, we investigate the $J^\pi = 4^-$ magnetic excited state, $M4$, at the excitation energy $E_x = 18.98$ MeV [Hyd87]. The RPA calculations with $V_{res}^{\delta+\pi+\rho}$ show that the dominant $1p-1h$ components are $\nu 1d_{5/2}1p_{3/2}^{-1}$ and $\pi 1d_{5/2}1p_{3/2}^{-1}$. In Tab. 3.3 we show the largest X amplitudes for the $1p-1h$ pairs of our RPA calculations. In this table Q indicates the quenching needed to bring the calculated form factor $|F|^2_{th.}$ and the experimental data $|F|^2_{exp.}$ into agreement. The χ^2 value is evaluated after applying the quenching factor to the theoretical calculation to fit number of experimental data $N_{exp.}$ associated with error $\Delta|F|^2_{exp.}$, where:

$$\chi^2 = \frac{1}{N_{exp.}} \sum_{i=1}^{N_{exp.}} \left[\frac{|F|^2_{th.} - |F|^2_{exp.}}{\Delta|F|^2_{exp.}} \right]^2 . \tag{3.28}$$

Table 3.3: X amplitudes for 4^- state in ^{16}O [Hyd87]. The results are obtained in the framework of $1p-1h$ excitations of *RPA* with $V_{res}^{\delta+\pi+\rho}$ interaction, the Y amplitudes are not tabulated.

J^π	E_x MeV	highest $1p-1h$	$V_{res}^{\delta+\pi+\rho}$ X	Q	χ^2
4^-	18.98	$\pi 1d_{5/2}1p_{3/2}^{-1}$	$+0.7025$	0.66	28.26
		$\nu 1d_{5/2}1p_{3/2}^{-1}$	-0.7084		

As a result of strong mixing between the two $1p-1h$ pairs, we consider the uncorrelated *IPM* excited state wave function composed by two $1p-1h$ pairs corresponding to the wave function $|\Phi_{1p1h}\rangle_2$ of Eq. (3.23). The X_{ph} amplitude of the first $\nu 1d_{5/2}1p_{3/2}^{-1}$ pair of the wave function $|\Phi_{1p1h}\rangle_2$ is taken from the *RPA* calculation. The $X_{p'h'}$ amplitude of the second $\pi 1d_{5/2}1p_{3/2}^{-1}$ pair is fixed by means of the normalization condition Eq. (3.24).

In Fig. 3.3 the dotted line shows the calculated transverse form factors for the *RPA* calculation, and the solid line the *IPM* calculation. The label IPM_2 in the figure indicates that the state is composed by two $1p-1h$ pairs. Henceforth, we shall label the *IPM* results in the figures as IPM_1 when the excited state is composed by single $1p-1h$ pair and as IPM_2 in case if the excited state is composed by two $1p-1h$ pairs. From that figure, one can notice that the two curves are overlapped. This means that the non dominant $1p-1h$ components of the *RPA* do not affect

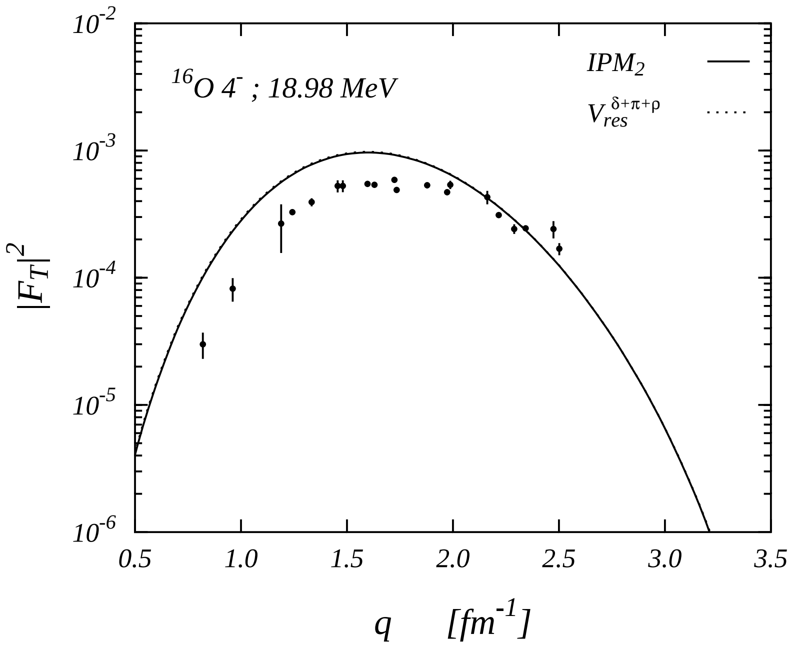

Figure 3.3: Transverse form factor for the 4^- state in ^{16}O at 18.98 MeV. The results of *IPM* (solid line) and *RPA* (dotted line) are compared with the data of Ref. [Hyd87].

the calculated form factor and we can safely assume that the state is constructed only by the above mentioned couple of $1p-1h$ pairs.

3.3.1.2 RPA for ^{40}Ca Nucleus

We investigated the inelastic electron scattering on ^{40}Ca nucleus at the excitation energy range $7.5 < E_x < 8.5$. According to the experiment of Williamson *et al.* [Wil87], four states ($J^\pi = 2^-, 3^-, 4^-, 5^-$) are expected at $E_x = 8.424, 7.695, 7.659, 8.551$ MeV, respectively. These states are dominated by $1p-1h$ configuration of $1f_{7/2}1d^{-1}_{3/2}$. In Tab. 3.4 we show the largest $1p-1h$ X amplitudes of RPA calculations with $V_{res}^{\delta+\pi+\rho}$ for both of

Table 3.4: X amplitudes for magnetic $2^-, 4^-$ and electric $3^-, 5^-$ states in ^{40}Ca [Wil87]. The results are obtained in the framework $1p-1h$ excitations of RPA with $V_{res}^{\delta+\pi+\rho}$ interaction, the Y amplitudes are not tabulated.

J^π	E_x MeV	$V_{res}^{\delta+\pi+\rho}$ highest $1p-1h$	X	Q_T	χ^2	Q_L	χ^2
2^-	8.424	$\pi 1f_{7/2} 1d_{3/2}^{-1}$	+0.6264	0.19	7.16		
		$\nu 1f_{7/2} 1d_{3/2}^{-1}$	−0.6072				
4^-	7.659	$\pi 1f_{7/2} 1d_{3/2}^{-1}$	−0.8720	2.10	0.95		
		$\nu 1f_{7/2} 1d_{3/2}^{-1}$	−0.4495				
3^-	7.695	$\pi 1f_{7/2} 1d_{3/2}^{-1}$	+0.8176	0.62	19.68	0.63	3.78
		$\nu 1f_{7/2} 1d_{3/2}^{-1}$	−0.4450				
5^-	8.551	$\pi 1f_{7/2} 1d_{3/2}^{-1}$	−0.6373	0.25	79.55	0.38	4.69
		$\nu 1f_{7/2} 1d_{3/2}^{-1}$	+0.7279				

electric $J^\pi = 3^-, 5^-$ and magnetic $J^\pi = 2^-, 4^-$ states under investigation. The quenching factors Q_T and Q_L for transverse and longitudinal data, respectively, are given with their χ^2 values.

In the RPA calculations there is no single $1p-1h$ pair with X amplitude greater than 0.9. Thus we consider that the uncorrelated IPM wave function for those excited states are composed by two $1p-1h$ pairs where the X_{ph} and $X_{p'h'}$ amplitudes for each excited state are fixed as in the ^{16}O case.

As shown in Fig. 3.4, the simple uncorrelated *IPM* calculations, solid lines, usually overestimate the data, while the *RPA* results, dotted lines describe the data more satisfactory than *IPM* results. These states show a large degree of collectivity and the minor *RPA* components play an important role.

3.3.1.3 RPA for ^{48}Ca Nucleus

The ^{48}Ca nucleus has been studied extensively by experimentalists since it is the lightest doubly magic nucleus with neutron excess. Wise *et al.* [Wis85] performed inelastic electron scattering from ^{48}Ca. In their experiment, they considerably increased the information about the magnetic and electric states up to 10 MeV excitation. From their work, we have selected some of magnetic and electric high spin states that may be described in terms of few $1p-1h$ pairs. The ^{48}Ca excited states have been widely studied in the framework of the *RPA* formalism [Ama92a, Ama92b, Ama93a, Ari94].

In our investigation we find that the *RPA* results for the states $J^\pi = 2^-$ and 4^- are rather sensitive to the changes of the residual interaction. While states with $J^\pi = 6^-, 8^-, 3^+$ and 5^+ are not so sensitive. So, for the first two states we show the results of both residual interactions. Tab. 3.5 shows the largest X amplitudes for the $1p-1h$ pairs of our *RPA* calculations with both $V_{res}^{\delta+\pi+\rho}$ and V_{res}^{δ} residual interactions.

The form factors corresponding to both residual interactions are shown by the dotted lines of Fig. 3.5. The results obtained with the V_{res}^{δ} residual interaction predicts shape and size of the form factors better than the

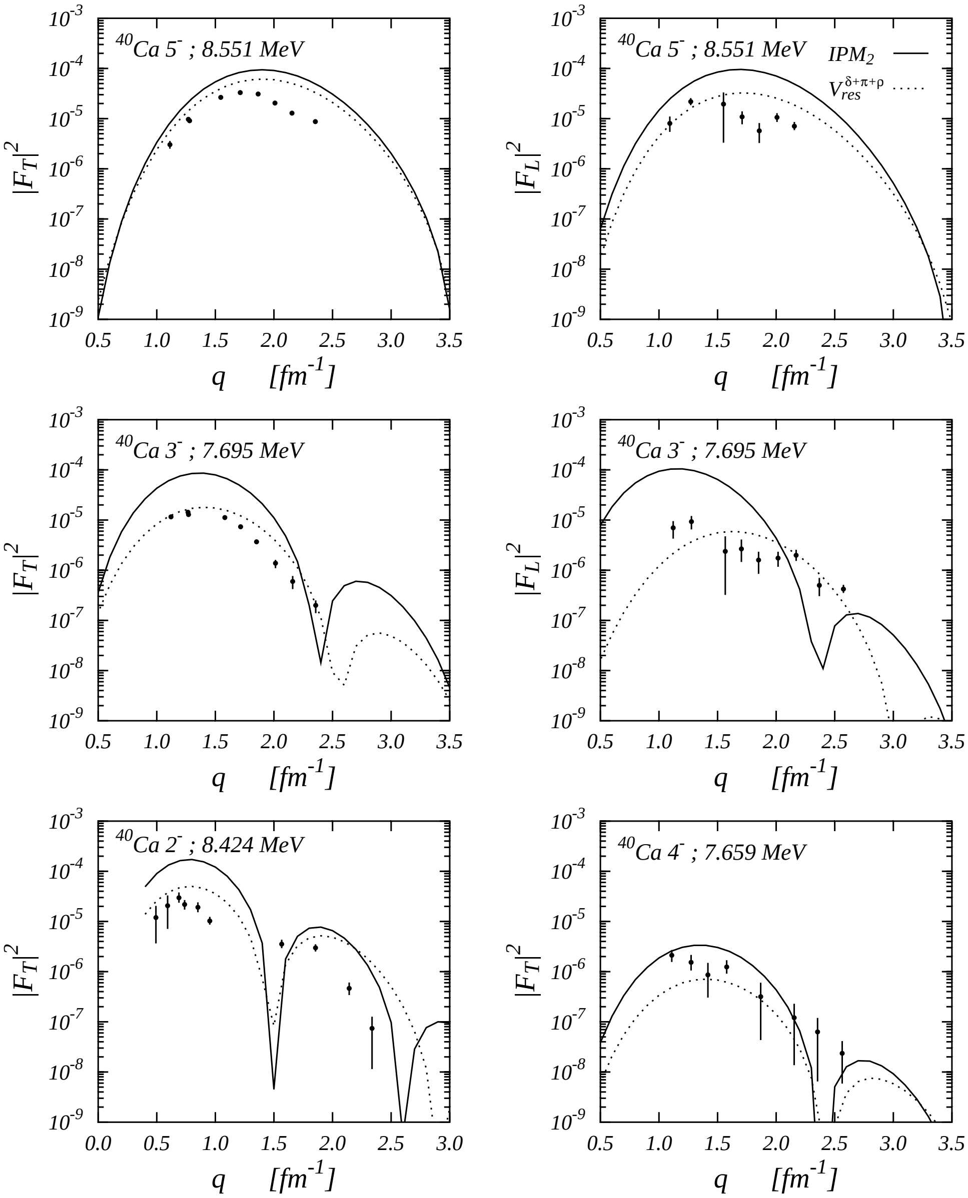

Figure 3.4: Transverse $|F_T(q)|^2$ and longitudinal $|F_L(q)|^2$ form factors for excited states in ^{40}Ca at excitation energy range $7.5 < E_x < 8.5$. The results of *IPM* (solid lines) and *RPA* (dotted lines) are compared with the data of Ref. [Wil87].

Table 3.5: X amplitudes for magnetic $2^-, 4^-$ in ^{48}Ca [Wis85]. The results are obtained in the framework of $1p-1h$ excitation of RPA with $V_{res}^{\delta+\pi+\rho}$ and V_{res}^{δ} interactions, the Y amplitudes are not tabulated.

$V_{res}^{\delta+\pi+\rho}$ highest $1p-1h$	X	Q	χ^2	V_{res}^{δ} highest $1p-1h$	X	Q	χ^2
			2^- at $E_x = 6.893$ MeV				
$\pi 1f_{7/2}1d_{3/2}^{-1}$	-0.6139	1.14	9.06	$\pi 1f_{7/2}1d_{3/2}^{-1}$	-0.9278	1.10	3.54
$\nu 2p_{3/2}1d_{3/2}^{-1}$	$+0.5611$			$\pi 1f_{7/2}1d_{5/2}^{-1}$	-0.3261		
			4^- at $E_x = 6.105$ MeV				
$\pi 1f_{7/2}1d_{3/2}^{-1}$	-0.8435	1.46	58.79	$\pi 1f_{7/2}2s_{1/2}^{-1}$	-0.7520	0.91	8.84
$\pi 1f_{7/2}2s_{1/2}^{-1}$	-0.5178			$\pi 1f_{7/2}1d_{3/2}^{-1}$	-0.6544		

$V_{res}^{\delta+\pi+\rho}$. The reason of this failure of the $V_{res}^{\delta+\pi+\rho}$ may be attributed to the strength of the tensor part of the residual interaction which may be too strong. There are studies suggesting that the nuclear medium reduces the strength of the tensor force [Ama92b, Hin92, Lal93, Ari94]. This investigation is not in the aims of our work, therefore for these states we shall use the results obtained by V_{res}^{δ} residual interaction only to build the uncorrelated *IPM* wave functions.

According to the results of V_{res}^{δ} interaction, see Tab. 3.5, we consider the uncorrelated *IPM* wave function for 2^- state composed by single $1p-1h$ pair where the X amplitude for that state is greater than 0.9. For the 4^- state, the *IPM* wave function is composed by $\pi 1f_{7/2}2s_{1/2}^{-1}$ and $\pi 1f_{7/2}1d_{3/2}^{-1}$ with X_{ph} and $X_{p'h'}$ amplitudes fixed with Eq. (3.24). The

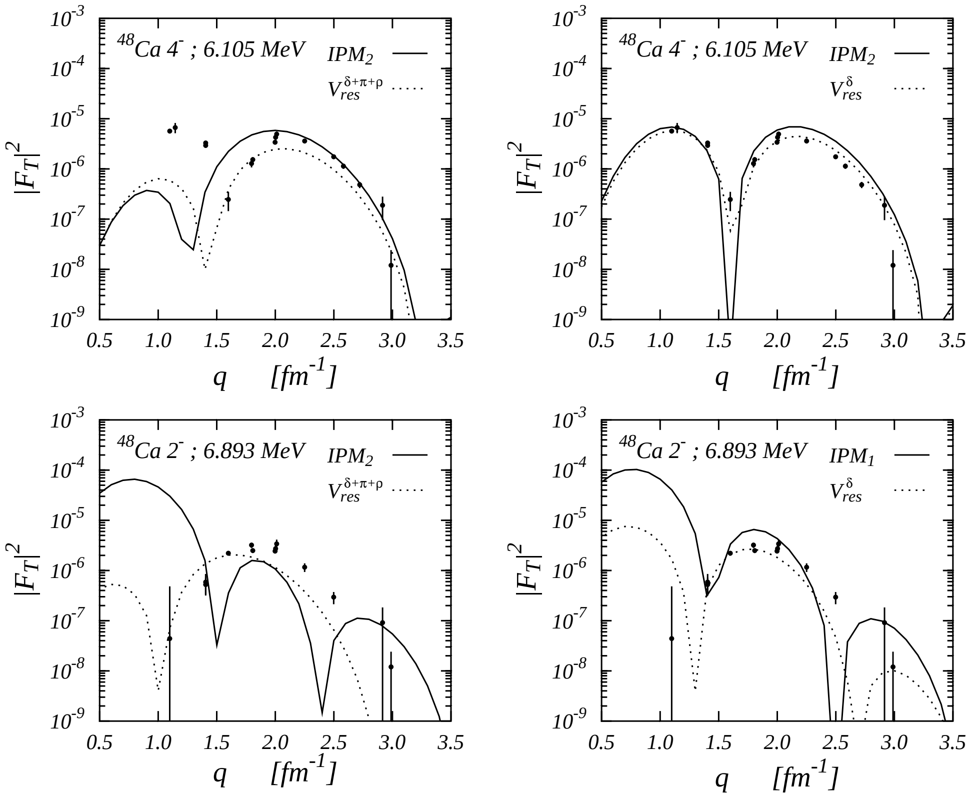

Figure 3.5: Transverse form factors for 2^- and 4^- states in ^{48}Ca with two different residual interactions. The results of *IPM* (solid lines) and *RPA* (dotted lines) are compared with the data of Wise *et al.* [Wis85].

corresponding (e, e') form factors are shown in Fig. 3.5 as solid lines.

For other magnetic states under investigation $6^-, 8^-, 3^+$ and 5^+, we obtain similar results for both residual interactions. Thus, in Tab. 3.6 we present the X amplitudes obtained with $V_{res}^{\delta+\pi+\rho}$ residual interaction only. We consider the uncorrelated *IPM* wave functions for these states with single $1p-1h$ pair that appear in *RPA* results with X amplitudes larger than 0.9. In Fig. 3.6 the obtained form factors are shown for both *RPA* and *IPM* calculations with dotted and solid lines, respectively. The results for both calculations are very similar and this confirms the consideration that these states are built by a single $1p-1h$ pair.

For the selected electric states 5_1^- at $E_x = 5.726$ MeV and 5_2^- at $E_x = 8.804$ MeV, the highest X amplitudes are shown in Tab. 3.6. For those two states, we consider the uncorrelated *IPM* wave functions as a combination between the two $1p-1h$ pairs tabulated in the table, where the X_{ph} parameters is fixed according to Eq. (3.23). The cross sections for 5_1^- and 5_2^- divided by the Mott cross section σ_M are calculated at the scattering angle $\theta = 160^o$ and are shown in the upper panels of Fig. 3.6 for both *RPA* and *IPM* calculations. As shown from the figure, both the *RPA* and *IPM* results have the same shape of the distribution but *RPA* does much better in predicting the size. However, we have ignored the non dominant components in the *IPM* calculations which still affect the transition strength at these excitations.

3.3.1.4 RPA for ^{208}Pb Nucleus

The ^{208}Pb nucleus has been the subject of several (e, e') experimental and theoretical studies. From the experimental point of view the investigation of the high spin states has been limited by the lack of the energy resolution. Lichtenstadt *et al.* [Lic79] observed high spin magnetic $14^-, 12^-$ and electric $12^+, 10^+$ states. With increasing resolution, Connelly *et al.* [Con92] measured the high spin magnetic states $11^+, 10^-, 9^+$ in addition to the confirmation of previously measured magnetic $14^-, 12^-$ and electric 12^+ states.

Table 3.6: X amplitudes for magnetic $6^-, 8^-, 3^+$ and 5^+ and electric 5_1^- and 5_2^- states in ^{48}Ca [Wis85]. The results are obtained in the framework of $1p-1h$ excitations of RPA with $V_{res}^{\delta+\pi+\rho}$ interaction, the Y amplitudes are not tabulated.

J^π	E_x MeV	$V_{res}^{\delta+\pi+\rho}$ highest $1p-1h$	X	Q	χ^2
6^-	8.557	$\pi 1f_{7/2}1d_{5/2}^{-1}$	-0.9702	0.07	2.72
		$\nu 2d_{5/2}1f_{7/2}^{-1}$	$+0.2008$		
8^-	9.276	$\nu 1g_{9/2}1f_{7/2}^{-1}$	$+0.9988$	0.22	6.28
		$\nu 1h_{11/2}1d_{5/2}^{-1}$	$+0.0463$		
3^+	4.608	$\nu 2p_{3/2}1f_{7/2}^{-1}$	$+0.9811$	0.51	3.54
		$\nu 2p_{1/2}1f_{7/2}^{-1}$	-0.1933		
5^+	5.147	$\nu 2p_{3/2}1f_{7/2}^{-1}$	$+0.9974$	0.47	10.18
		$\nu 1g_{9/2}2s_{1/2}^{-1}$	-0.0818		
5_1^-	5.726	$\pi 1f_{7/2}1d_{3/2}^{-1}$	-0.8259	0.97	3.92
		$\nu 1g_{9/2}1f_{7/2}^{-1}$	-0.4727		
5_2^-	8.804	$\nu 1g_{9/2}1f_{7/2}^{-1}$	-0.8242	0.65	6.01
		$\pi 1f_{7/2}1d_{3/2}^{-1}$	$+0.5100$		

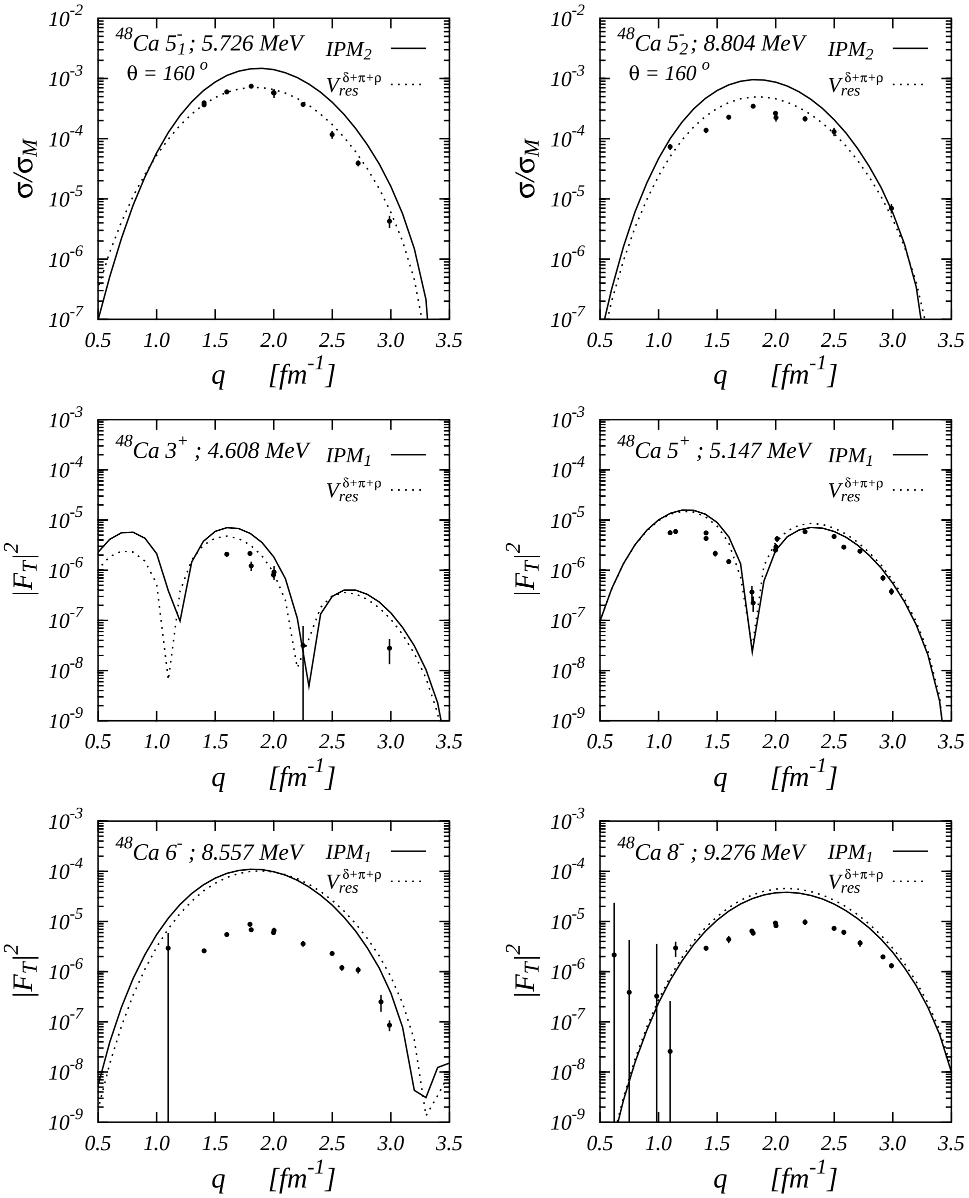

Figure 3.6: The lower panels are the transverse form factors for high spin magnetic excited states $6^-, 8^-, 3^+, 5^+$ in ^{48}Ca. The upper panels are the cross sections divided by the Mott cross section σ_M for electric states 5^-_1 and 5^-_2 in ^{48}Ca. The results of *IPM* (solid lines) and *RPA* (dotted lines) are compared with the data of Wise *et al.* [Wis85].

Our *RPA* calculations show that some magnetic states are sensitive to the choice of the residual interaction. These are the states assigned as $J^\pi = 10_1^-$ at $E_x = 6.283$ MeV, 12_1^- at 6.437 MeV and 9_2^+ at 5.26 MeV. Other magnetic states with $J^\pi = 10_2^-, 12_2^-, 14^-, 9_1^+, 11_1^+$ and 11_2^+ at $E_x = 6.884, 7.064, 6.745, 5.01, 5.291$ and 5.86 MeV, respectively, give similar results for both interactions. Thus we shall show the *RPA* results of both $V_{res}^{\delta+\pi+\rho}$ and V_{res}^{δ} residual interactions for the states $10_1^-, 12_1^-$ and 9_2^+, while for the other states we shall present the *RPA* results of $V_{res}^{\delta+\pi+\rho}$.

In Fig. 3.7 we show, as dotted lines, the calculated *RPA* form factors for both residual interactions for the states $10_1^-, 12_1^-$ and 9_2^+. The left panels represent the results of $V_{res}^{\delta+\pi+\rho}$ interaction and the right ones those of V_{res}^{δ}. The largest X amplitudes for both interactions are shown in Tab. 3.7. The two states with negative parity 10_1^- and 12_1^- are dominated by the neutronic $1p-1h$ transition of $\nu 1j_{15/2}1i_{13/2}^{-1}$ with amplitude greater than 0.9 for both residual interactions. In the *IPM* calculations, we consider that these states are composed by this single neutronic transition. As a result, we plot, as solid lines, the same *IPM* results for 10_1^-, panels (a) and (b) and for 12_1^- panels (c) and (d) of Fig. 3.7.

In case of the positive parity state 9_2^+ the $V_{res}^{\delta+\pi+\rho}$ gives wrong mixing and with amplitude for the highest $1p-1h$ component $\pi 1h_{9/2}1h_{11/2}^{-1}$ smaller than 0.9, while the V_{res}^{δ} gives this protonic transition with amplitude higher than 0.9 and even a better description to the data. In the *IPM* calculations we describe this state in two different ways. In a first calculation we consider the state as composed by two $1p-1h$ pairs with the largest X amplitude taken from $V_{res}^{\delta+\pi+\rho}$ and the second amplitude

Table 3.7: X amplitudes for magnetic $10_1^-, 12_1^-$ and 9_2^+ states in ^{208}Pb [Con92]. The results are obtained in the framework of $1p-1h$ excitations of *RPA* with $V_{res}^{\delta+\pi+\rho}$ and V_{res}^{δ} interactions, the Y amplitudes are not tabulated.

$V_{res}^{\delta+\pi+\rho}$				V_{res}^{δ}			
highest $1p-1h$	X	Q	χ^2	highest $1p-1h$	X	Q	χ^2
10_1^- at $E_x = 6.283$ MeV							
$\nu 1j_{15/2}1i_{13/2}^{-1}$	-0.9924	0.28	0.93	$\nu 1j_{15/2}1i_{13/2}^{-1}$	$+0.9844$	0.96	1.18
$\pi 1i_{13/2}1h_{11/2}^{-1}$	$+0.1116$			$\pi 1i_{13/2}1h_{11/2}^{-1}$	$+0.1679$		
12_1^- at $E_x = 6.437$ MeV							
$\nu 1j_{15/2}1i_{13/2}^{-1}$	-0.9811	0.41	2.70	$\nu 1j_{15/2}1i_{13/2}^{-1}$	-0.9753	2.45	5.28
$\pi 1i_{13/2}1h_{11/2}^{-1}$	$+0.1907$			$\pi 1i_{13/2}1h_{11/2}^{-1}$	-0.2199		
9_2^+ at $E_x = 5.260$ MeV							
$\pi 1h_{9/2}1h_{11/2}^{-1}$	-0.8580	3.12	7.69	$\pi 1h_{9/2}1h_{11/2}^{-1}$	-0.9928	1.17	2.19
$\nu 1j_{15/2}2f_{5/2}^{-1}$	-0.4163			$\nu 1i_{11/2}1i_{13/2}^{-1}$	-0.1091		

fixed through Eq. (3.24). The result of this calculation is shown as solid line in panel (e) of Fig. 3.7. In a the second calculation, we consider this state composed by a single $1p-1h$ pair as suggested by the results of V_{res}^{δ} interaction. The result is shown by the solid line in panel (f) of Fig. 3.7. Also, here the uncorrelated *IPM* result as suggested by the V_{res}^{δ} residual interaction gives better description to the data.

For the other magnetic states we present only the *RPA* results with the $V_{res}^{\delta+\pi+\rho}$ residual interaction since the second residual interaction gives

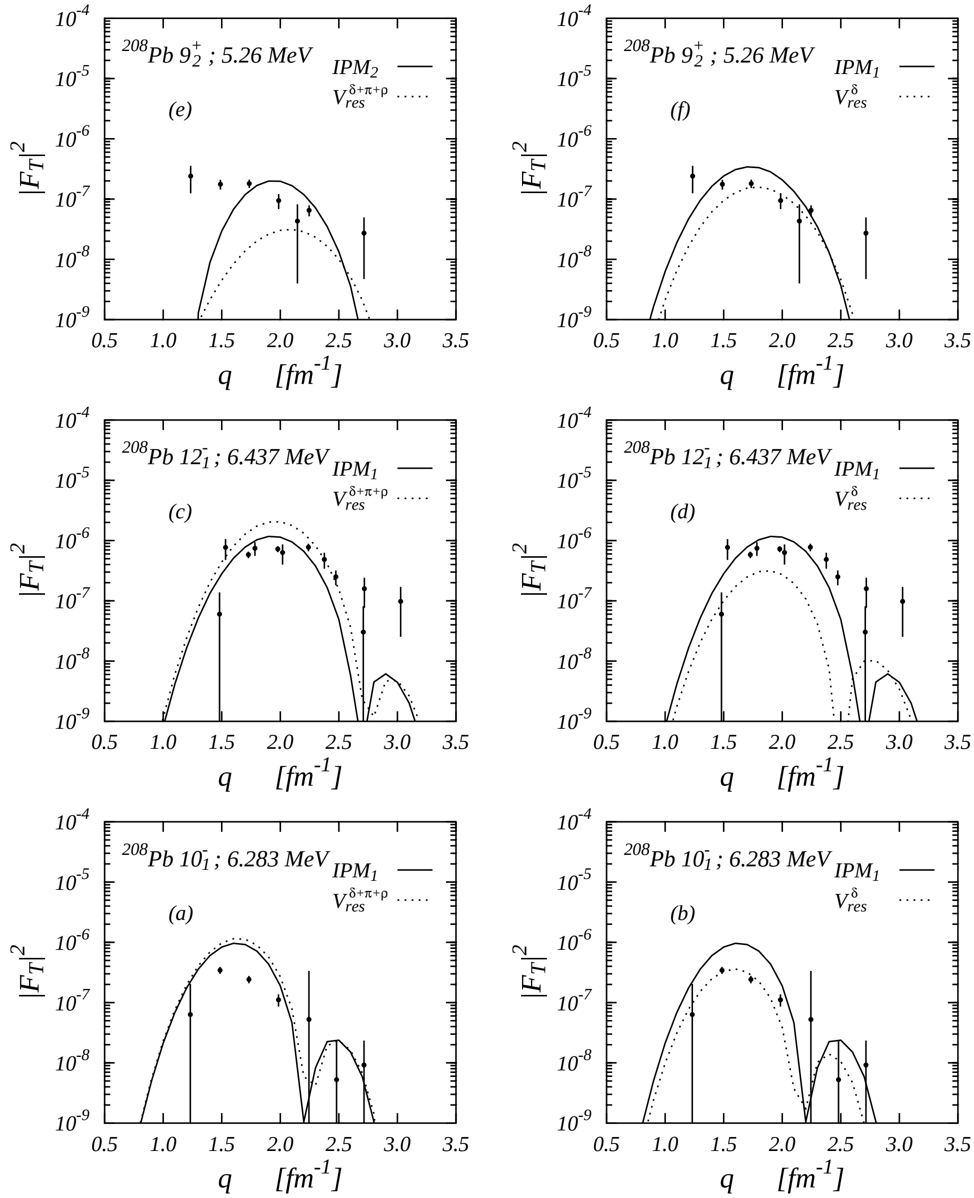

Figure 3.7: Transverse form factors for high spin magnetic excited states $10_1^-, 12_1^-$ and 9_2^+ in ^{208}Pb. The *RPA* calculations are done with two residual interactions: $V_{res}^{\delta+\pi+\rho}$ (left panels) and V_{res}^{δ} (right panels). The results of *IPM* (solid lines) and *RPA* (dotted lines) are compared with the data of Ref. [Con92].

rather similar results. Tab. 3.8 shows the largest X amplitudes produced by the $V_{res}^{\delta+\pi+\rho}$ interaction. The dominant $1p-1h$ component for each state has X amplitude greater than 0.95, thus those states are supposed to be well described as a single $1p-1h$ pair. In Fig. 3.8 we compare the *RPA* results obtained with the $V_{res}^{\delta+\pi+\rho}$ interaction, dotted lines, with the *IPM* results, solid lines. For the states $10_2^-, 12_2^-, 14^-$ and 11_1^+ the two calculations produce very similar results indicating that in this case the role of the residual interaction is very weak. The 9_1^+ and 11_2^+ states have slightly different results for *RPA* and *IPM* calculations.

In addition to the magnetic high spin states, we investigated some electric high spin states. The states observed with the largest angular momentum are the 10^+ and 12^+ states. Lichtenstadt *et al.* [Lic79] observed four excited states assigned as $J^\pi = 10^+$ and one state as $J^\pi = 12^+$. The first three 10^+ states at excitation energies 4.89, 5.07 and 5.54 MeV are composed by a strong mixing between four $1p-1h$ pairs. The 10^+ and 12^+ states at 5.92 and 6.01 MeV, respectively, are almost pure single $1p-1h$ pair, the $\nu 1i_{11/2}1i_{13/2}^{-1}$ transition. Thus, we restrict our investigation to these last electric states.

For those two electric states, the *RPA* calculations with both residual interactions give rather similar results for both interactions, thus we present here the results with $V_{res}^{\delta+\pi+\rho}$ only. Tab. 3.9 shows the largest X amplitudes for both states 10^+ and 12^+ together with the quenching factors needed to bring the calculated cross sections in agreement with the experimental data. The quenching factors are shown at two different electron scattering angels $\theta = 90^o$ and 160^o. The dotted lines in pan-

Table 3.8: X amplitudes for magnetic $10^-_2, 12^-_2, 14^-, 9^+_1, 11^+_1$ and 11^+_2 states in ^{208}Pb [Con92]. The results have been obtained in the framework of $1p-1h$ excitations of RPA with $V_{res}^{\delta+\pi+\rho}$ interaction, the Y amplitudes have not been tabulated.

J^π	E_x MeV	$V_{res}^{\delta+\pi+\rho}$ highest $1p-1h$	X	Q	χ^2
10^-_2	6.884	$\pi 1i_{13/2}1h^{-1}_{11/2}$	-0.9852	0.45	6.18
		$\nu 1i_{11/2}1h^{-1}_{9/2}$	-0.1098		
12^-_2	7.064	$\pi 1i_{13/2}1h^{-1}_{11/2}$	-0.9801	0.33	6.34
		$\nu 1j_{15/2}1i^{-1}_{13/2}$	-0.1888		
14^-	6.745	$\nu 1j_{15/2}1i^{-1}_{13/2}$	-1.0002	0.36	5.53
		$\nu 1k_{17/2}1h^{-1}_{11/2}$	-0.0494		
9^+_1	5.010	$\nu 2g_{9/2}1i^{-1}_{13/2}$	-0.9566	0.57	14.31
		$\nu 1j_{15/2}3p^{-1}_{3/2}$	$+0.2006$		
11^+_1	5.291	$\nu 2g_{9/2}1i^{-1}_{13/2}$	-0.9884	0.27	4.69
		$\nu 1j_{17/2}2f^{-1}_{7/2}$	-0.1332		
11^+_2	5.860	$\nu 1i_{11/2}1i^{-1}_{13/2}$	$+0.9953$	0.35	6.49
		$\nu 2g_{9/2}1i^{-1}_{13/2}$	-0.0786		

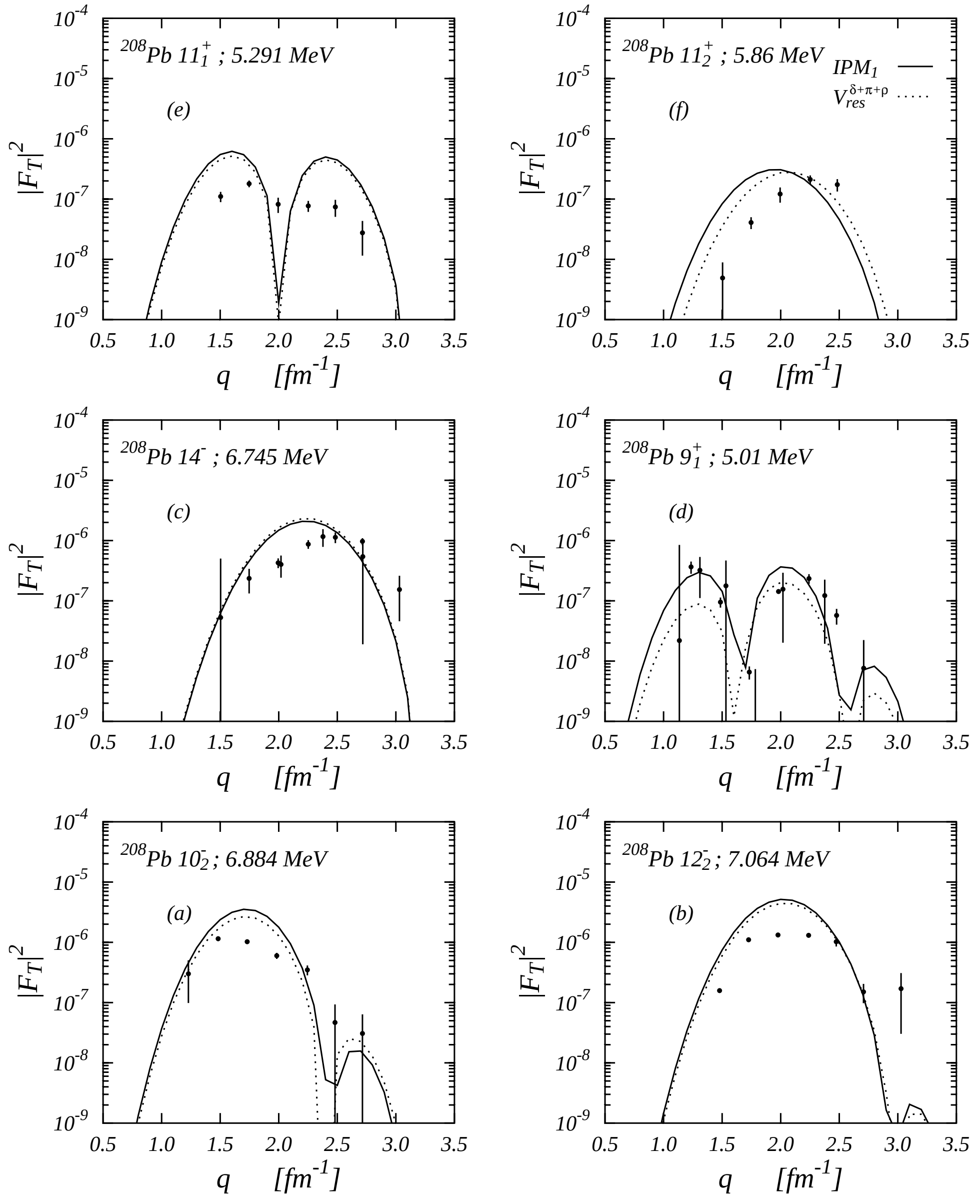

Figure 3.8: Transverse form factors for high spin magnetic excited states $10_2^-, 12_2^-, 14^-, 9_1^+, 11_1^+$ and 11_2^+ in ^{208}Pb. The *RPA* calculations are done with $V_{res}^{\delta+\pi+\rho}$ residual interaction. The *IPM* calculations are performed with single $1p-1h$ for all shown states, labeled as IPM_1. The results of IPM_1 (solid lines) and *RPA* (dotted lines) are compared with the data of Connelly *et al.* [Con92].

Table 3.9: X amplitudes for electric 10^+ and 12^+ states in ^{208}Pb [Lic79]. The results are obtained in the framework of $1p-1h$ excitations of *RPA* with $V_{res}^{\delta+\pi+\rho}$ interaction, the Y amplitudes are not tabulated.

J^π	E_x MeV	highest $1p-1h$	$V_{res}^{\delta+\pi+\rho}$ X	$\theta=90^o$ Q	$\theta=90^o$ χ^2	$\theta=160^o$ Q	$\theta=160^o$ χ^2
10^+	5.92	$\nu 1i_{11/2}1i^{-1}_{13/2}$	+0.8038	0.16	10.49	0.38	9.92
		$\pi 1h_{9/2}1h^{-1}_{11/2}$	−0.5830				
12^+	6.10	$\nu 1i_{11/2}1i^{-1}_{13/2}$	+0.9874	0.94	7.57	0.77	12.60
		$\nu 1j_{15/2}1h^{-1}_{9/2}$	+0.1510				

els (a) and (c) of Fig. 3.9 represent the *RPA* calculations with $V_{res}^{\delta+\pi+\rho}$ interaction.

We consider the 10^+ state composed by two $1p-1h$ pairs as suggested by our *RPA* calculation. The solid line in the panel (a) of Fig. 3.9 shows the result of this calculation. Lichtenstadt *et al.* [Lic79] suggested in their study that the main $1p-1h$ transition $\nu 1i_{11/2}1i^{-1}_{13/2}$ should contribute with amplitude greater than 0.9. Thus we repeated the *IPM* calculation by considering only this $1p-1h$ contribution. The result of this calculation is shown, as solid line, in panel (b) of Fig. 3.9. In case of 12^+ state, the *RPA* calculation show that the $\nu 1i_{11/2}1i^{-1}_{13/2}$ pair has amplitude greater than 0.9, thus we consider that state composed by single $1p-1h$ pair and the corresponding cross section is shown as solid line in panel (c) of Fig. 3.9.

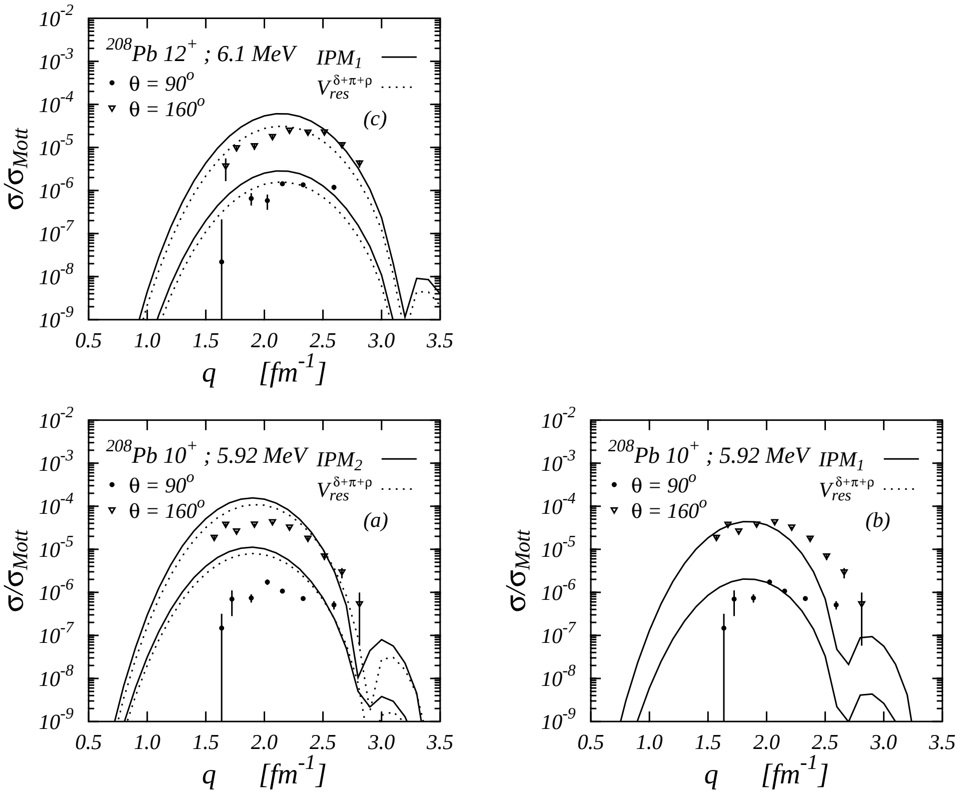

Figure 3.9: Cross section divided by the Mott cross section σ_M for the electric 10^+ and 12^+ states in ^{208}Pb. The dotted lines represent *RPA* calculations with $V_{res}^{\delta+\pi+\rho}$ interaction and the solid lines the *IPM* calculations at two different electron scattering angles $\theta = 90^o$ and 160^o. The results are compared with the experimental data of Lichtenstadt *et al.* [Lic79].

3.3.2 SRC Model

The study presented in the previous section has been used to select those excited states with scarce collectivity in order to apply to them our *SRC* model. The $1p - 1h$ pairs, and their amplitudes, used to build the wave functions of each excited state we have considered, are shown in Tabs. 3.10 and 3.11. We have to refer that the tabulated X_{ph} amplitudes in those tables are the same amplitudes that used to build the uncorrelated *IPM* results in the previous section.

The results of our calculations are summarized in the last columns of Tabs. 3.10 and 3.11, where the quenching factors Q and the χ^2 values are tabulated in case of *IPM* and correlated calculations. In those tables we show only the results of using the gaussian correlation function, labeled as G correlation in the tables. Also, the tabulated quenching factors Q in case of gaussian correlation are applied to the full correlated gaussian results, i.e. by adding to the *IPM* mean field calculation all two-point and three-point diagrams of Fig. 2.2. The quenching factors Q for the uncorrelated *IPM* and correlated calculations and the χ^2 per datum are compared. The values of the χ^2 are evaluated after the application of the quenching factors.

By looking to the quenching factors and to the χ^2, we noticed that the *SRC* do not substantially change the *IPM* results neither in the shape nor in the size. The size of the *SRC* effect is rather small. The direction of the effect is quite controversial. Sometime there is a lowering of the *IPM* results, other times an increase. It is also difficult to state if the

Table 3.10: Excited states calculated and their quenching factors. We indicate the excitation energy E_x, the quenching factors Q and the χ^2 for the results of *IPM* and full correlation function of the gaussian type. For the electric states of 5_1^- and 5_2^- ^{48}Ca nucleus we show the quenching on the full cross section, and we indicate the scattering angle were the cross section has been measured. For the electric states of 3^- and 5^- in ^{40}Ca nucleus the data have been analyzed [Wil87] by separating them into longitudinal and transverse responses, as we show them in Figs. 3.4 and 3.10, but here we show the quenching factor for the transverse response only where the longitudinal response gives the same effect.

	J^π	E_x (MeV)	$1p-1h$ pairs	X_{ph}	*IPM*		G Corr.	
					Q	χ^2	Q	χ^2
^{16}O	4^-	18.98	$\pi 1d_{5/2}1p_{3/2}^{-1}$	$+0.7058$	0.67	27.36	0.66	35.07
			$\nu 1d_{5/2}1p_{3/2}^{-1}$	-0.7084				
^{40}Ca	2^-	8.424	$\pi 1f_{7/2}1d_{3/2}^{-1}$	$+0.7946$	0.11	4.50	0.11	4.34
			$\nu 1f_{7/2}1d_{3/2}^{-1}$	-0.6072				
	4^-	7.659	$\pi 1f_{7/2}1d_{3/2}^{-1}$	-0.8720	0.48	0.81	0.45	0.81
			$\nu 1f_{7/2}1d_{3/2}^{-1}$	-0.4895				
	3^-	7.695	$\pi 1f_{7/2}1d_{3/2}^{-1}$	$+0.8176$	0.16	4.54	0.18	2.87
			$\nu 1f_{7/2}1d_{3/2}^{-1}$	-0.5757				
	5^-	8.551	$\pi 1f_{7/2}1d_{3/2}^{-1}$	-0.6857	0.17	70.66	0.22	44.94
			$\nu 1f_{7/2}1d_{3/2}^{-1}$	$+0.7279$				
^{48}Ca	2^-	6.893	$\pi 1f_{7/2}2s_{1/2}^{-1}$	$+1.0000$	0.52	5.00	0.53	5.02
	4^-	6.105	$\pi 1f_{7/2}2s_{1/2}^{-1}$	-0.7520	0.61	16.95	0.61	16.98
			$\pi 1f_{7/2}1d_{3/2}^{-1}$	-0.6591				
	6^-	8.557	$\pi 1f_{7/2}1d_{5/2}^{-1}$	$+1.0000$	0.06	6.99	0.06	8.67
	8^-	9.276	$\nu 1g_{9/2}1f_{7/2}^{-1}$	$+1.0000$	0.26	6.39	0.25	7.94
	3^+	4.608	$\nu 2p_{3/2}1f_{7/2}^{-1}$	$+1.0000$	0.32	1.93	0.34	2.26
	5^+	5.147	$\nu 2p_{3/2}1f_{7/2}^{-1}$	$+1.0000$	0.42	20.77	0.43	19.83
$\theta = 160^o$	5_1^-	5.726	$\pi 1f_{7/2}1d_{3/2}^{-1}$	-0.8259	0.48	15.67	0.52	6.92
			$\nu 1g_{9/2}1f_{7/2}^{-1}$	-0.5639				
	5_2^-	8.804	$\pi 1f_{7/2}1d_{3/2}^{-1}$	$+0.5663$	0.34	7.11	0.37	8.01
			$\nu 1g_{9/2}1f_{7/2}^{-1}$	$+0.8242$				

Table 3.11: The same as Tab. 3.10 but for magnetic and electric excited states in ^{208}Pb nucleus. The experimental points are taken from the work of Connelly *et al.* [Con92] for the magnetic states and Lichtenstadt *et al.* [Lic79] for the electric states.

	J^π	E_x (MeV)	$1p-1h$ pairs	X_{ph}	*IPM* Q	*IPM* χ^2	G Corr. Q	G Corr. χ^2
^{208}Pb	9_1^+	5.010	$\nu 2g_{9/2}1i_{13/2}^{-1}$	+1.0000	0.38	5.92	0.37	7.17
	9_2^+	5.260	$\pi 1h_{9/2}1h_{11/2}^{-1}$	+1.0000	0.59	2.09	0.59	2.10
	11_1^+	5.291	$\nu 2g_{9/2}1i_{13/2}^{-1}$	+1.0000	0.23	4.39	0.23	4.49
	11_2^+	5.860	$\nu 1i_{11/2}1i_{13/2}^{-1}$	+1.0000	0.17	10.61	0.17	10.61
	10_1^-	6.283	$\nu 1j_{15/2}1i_{13/2}^{-1}$	+1.0000	0.34	9.12	0.34	9.29
	10_2^-	6.884	$\pi 1i_{13/2}1h_{11/2}^{-1}$	+1.0000	0.33	6.05	0.33	6.05
	12_1^-	6.437	$\nu 1j_{15/2}1i_{13/2}^{-1}$	+1.0000	0.70	3.35	0.68	3.57
	12_2^-	7.064	$\pi 1i_{13/2}1h_{11/2}^{-1}$	+1.0000	0.28	7.64	0.27	8.85
	14^-	6.745	$\nu 1j_{15/2}1i_{13/2}^{-1}$	+1.0000	0.39	5.53	0.39	5.53
$\theta = 90^o$	10^+	5.920	$\nu 1i_{11/2}1i_{13/2}^{-1}$	+1.0000	0.63	18.90	0.69	20.63
$\theta = 160^o$	10^+	5.920	$\nu 1i_{11/2}1i_{13/2}^{-1}$	+1.0000	0.88	28.91	0.95	32.15
$\theta = 90^o$	12^+	6.100	$\nu 1i_{11/2}1i_{13/2}^{-1}$	+1.0000	0.52	7.55	0.57	8.76
$\theta = 160^o$	12^+	6.100	$\nu 1i_{11/2}1i_{13/2}^{-1}$	+1.0000	0.39	12.70	0.42	14.84

inclusion of the *SRC* improves the agreement with the data. There are various situations where the effect of the *SRC* on specific excited state is opposite to the effect on other state even in the same nucleus.

For the sake of discussion of our findings, we show in Figs. 3.10, 3.11 and 3.12 some excited states in ^{40}Ca, ^{48}Ca and ^{208}Pb nuclei. In the 4^- state of ^{40}Ca, the correlations slightly enhance the value of the maximum at $q = 1.3$ fm^{-1} as shown in panel (b) of Fig. 3.10. This implies a smaller Q for the correlated calculation, as shown in Tab. 3.10 where the quenching factor decreased from 0.48 for the *IPM* calculation to 0.45 to the correlated one. After the Q factor is applied both calculations have the same value of χ^2 indicating that the correlations slightly affect the shape of the transition.

A different example is the cross sections calculated for the 5_1^- and 5_2^- in ^{48}Ca (see panels (e) and (f) of Fig. 3.11) and 10^+ and 12^+ in ^{208}Pb (see panels (e) and (f) of Fig. 3.12). In that case the correlation lowers the maximum of the distribution. This produces a small increase of Q where the difference in the lowering produced by the correlation, i.e. the ratio between dashed and solid lines, is within 1%. Even after the Q factor has been applied the agreement with the data is rather poor, as the high values of the χ^2 indicate for 5_2^- in ^{48}Ca and 10^+ and 12^+ in ^{208}Pb (see Tabs. 3.10 and 3.11).

Since the main difference between our *SRC* model and other models one can find in the literature is the presence of the three-point diagrams, we have investigated their role. We have also investigated the sensitivity of the results to different types of correlation function by using the three

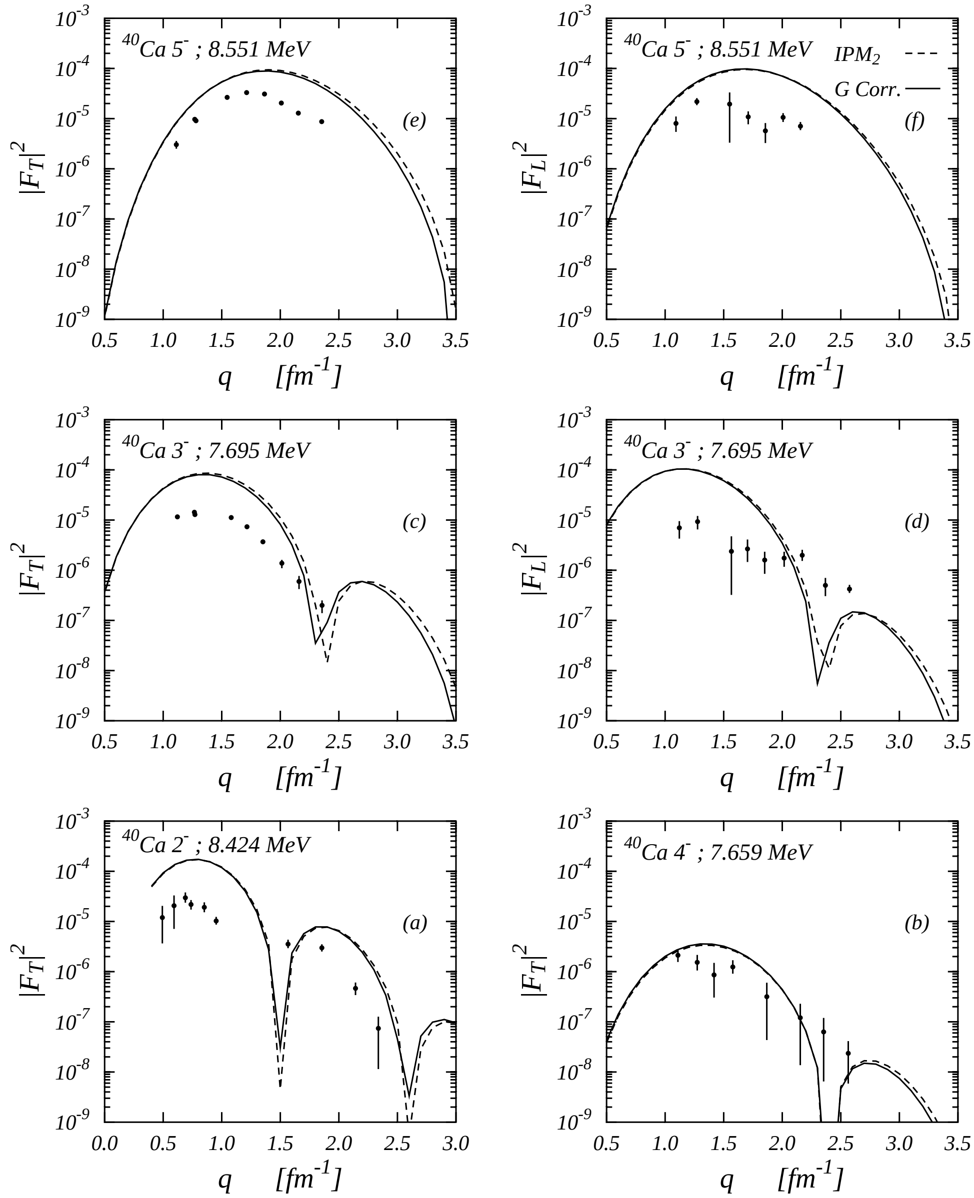

Figure 3.10: Transverse and longitudinal form factors for excited states in ^{40}Ca at excitation energy range $7.5 < E_x < 8.5$. The results of *IPM* (dashed lines) and full gaussian G correlation of our *SRC* model (solid lines) are compared with the data of Williamson *et al.* [Wil87].

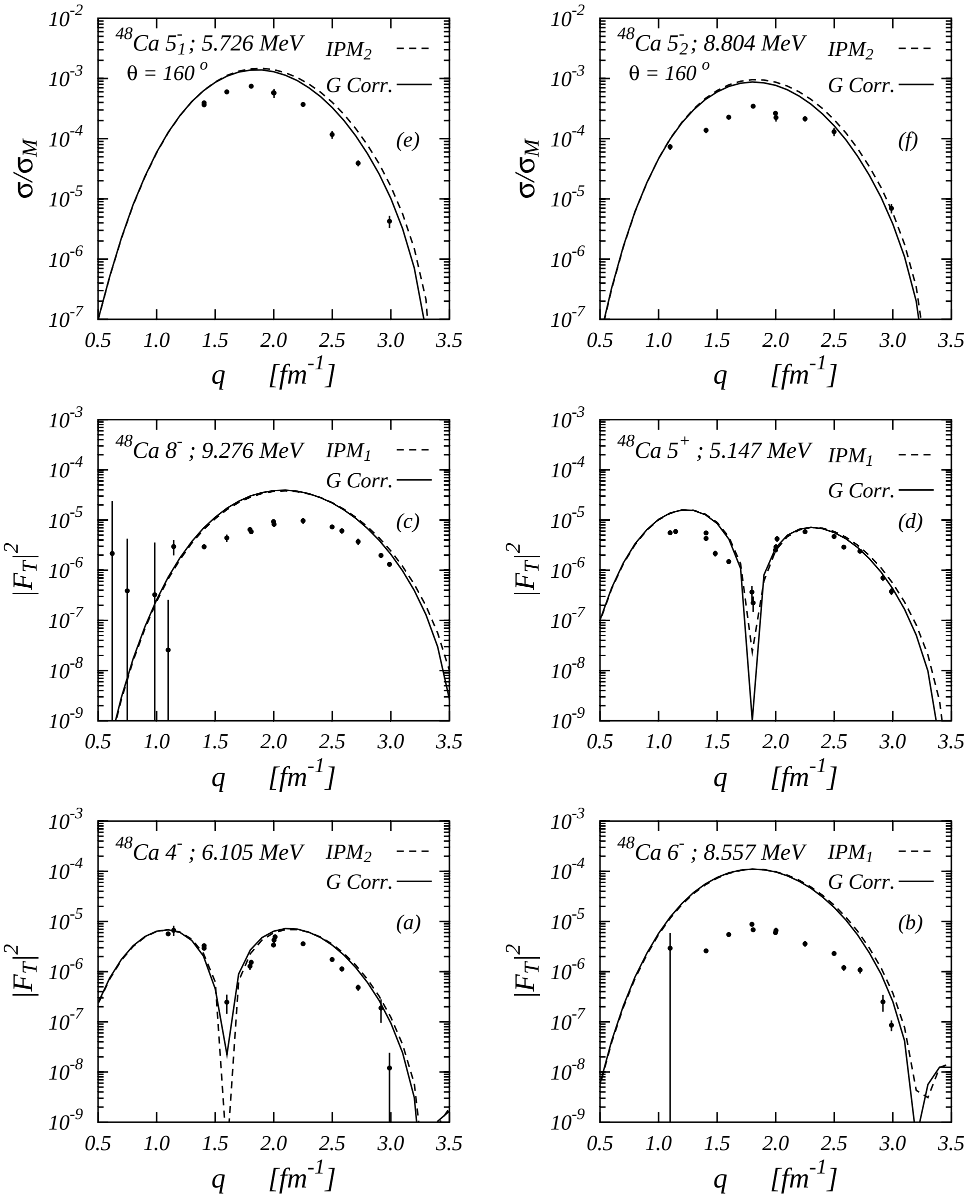

Figure 3.11: The lower panels are the transverse form factors for some high spin magnetic excited states in ^{48}Ca. The upper panels are the cross sections divided by the Mott cross section σ_M for electric states 5^-_1 and 5^-_2 in ^{48}Ca. The results of *IPM* (dashed lines) and full gaussian G correlation of our *SRC* model (solid lines) are compared with the data of Wise *et al.* [Wis85].

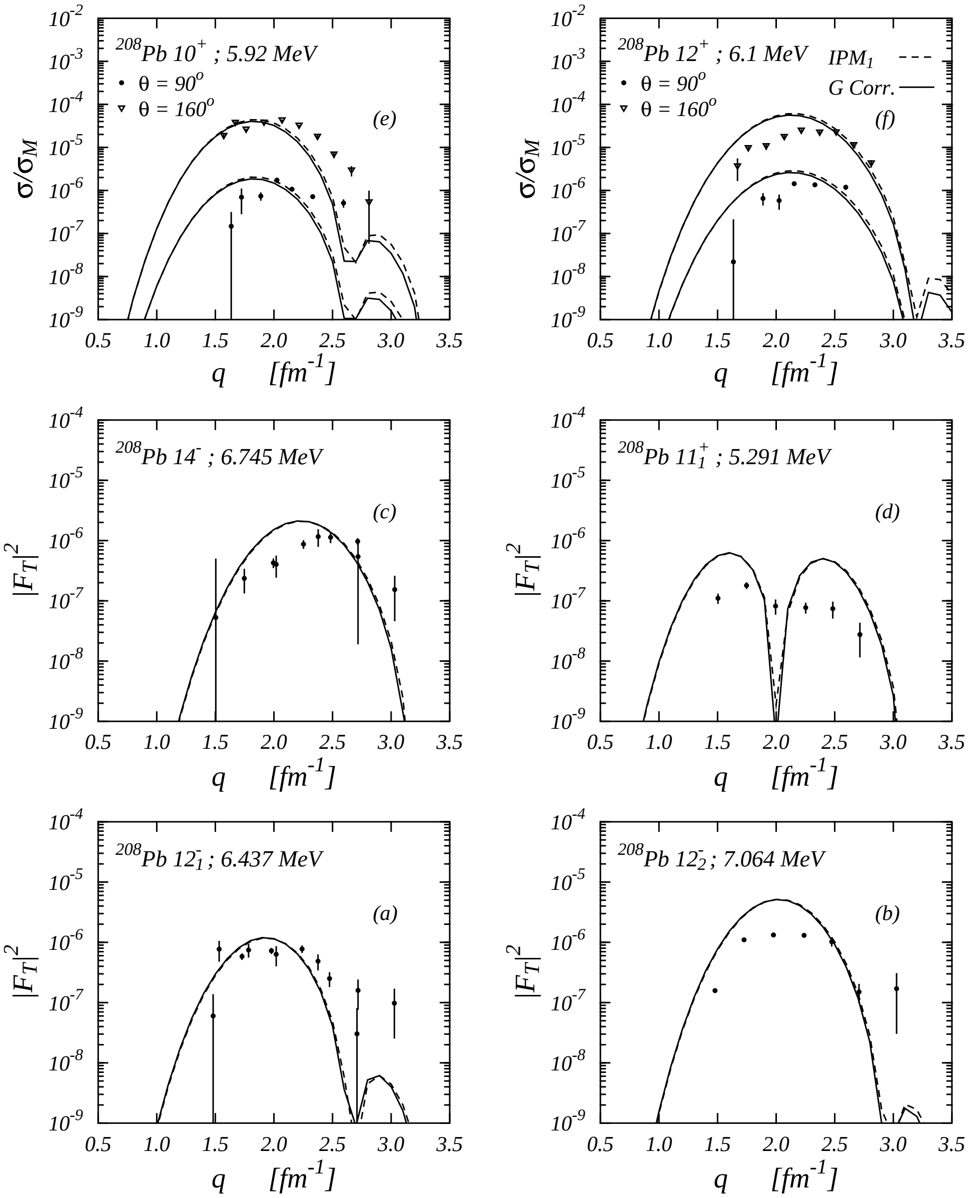

Figure 3.12: The lower panels are the transverse form factors for some high spin magnetic excited states in ^{208}Pb. The upper panels are the cross sections divided by the Mott cross section σ_M for electric states 10^+ and 12^+ in ^{208}Pb. The results of *IPM* (dashed lines) full gaussian G correlation of our *SRC* model (solid lines) are compared with the data of Connelly *et al.* [Con92].

different types of correlation function, G, $V8$ and $S3$, shown in Fig. 3.2.

We present here the results obtained for the magnetic excited state 4^- at 18.98 MeV in ^{16}O. The same investigation done for other excited states in all nuclei under study showed analogous results. Fig. 3.13 shows the effect of inclusion the two- and three-point diagrams for the three correlation functions, G, $V8$ and $S3$. In that figure, the dotted lines represent the uncorrelated *IPM* results, the dashed lines are obtained by adding only the two-point diagrams to the mean field calculations, and the solid lines are obtained within the complete *SRC* model. As we already mentioned, the effects of the correlations are very small. Thus in the left panels of Fig. 3.13 we show the form factors in linear scale to allow better identification of the correlations effects consisting in a more or less pronounced modification of the maximum of the distributions.

For all correlation function types, it can be noticed that the effect of including the three-point diagrams has opposite sign with respect to that of the two-point diagrams. The three-point diagrams almost cancel the effect produced by the two-point diagrams. For example, in case of gaussian correlation, the effect of adding the two-point diagrams is a lowering of the curve, while by adding the three-point diagrams the curve is enhanced again to almost level the uncorrelated results as shown in panel (a) of Fig. 3.13. The situation is inverted in case of $S3$ correlation where the effect of adding the two-point diagrams is an enhancement of the curve while by adding the three-point diagrams the curve is again lowered to meet the uncorrelated results as shown in panel (e) in Fig. 3.13.

Therefore the full correlation form factors, solid lines, are approxi-

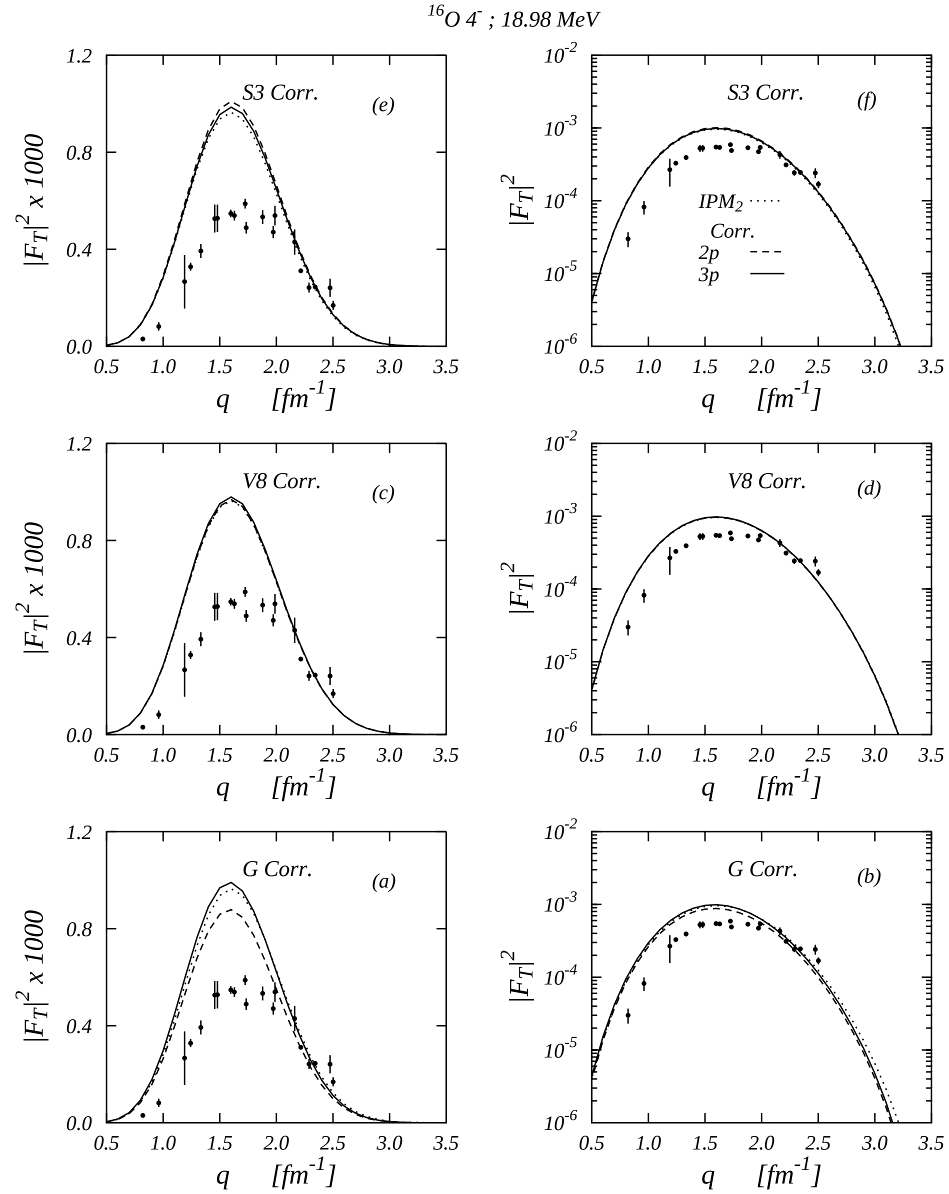

Figure 3.13: Transverse form factor for the 4^- state in ^{16}O [Hyd87]. The form factor is calculated with three different types of correlation function, gaussian G, $V8$ and $S3$ correlations. The dotted lines show the IPM results (labeled as IPM_2), the dashed lines are obtained with the inclusion of the two-point diagrams of Fig. 2.2 (labeled as $2p$) and the solid lines are obtained considering all diagrams of that figure where the three-point diagrams are included (labeled as $3p$).

Table 3.12: Comparison between the quenching factor Q and χ^2 values for the 4^- state at $E_x = 18.98$ Mev in ^{16}O. The comparison is done between the *IPM* results and the results of the three different types of correlation function: gaussian G, $V8$ and $S3$. The *IPM* wave function for the state is taken as suggested by the *RPA* results of Tab. 3.3 where the X_{ph} amplitudes are fixed through Eq. (3.23) as follow: $|4^-\rangle = +0.7058\,|\pi 1d_{5/2}1p^{-1}_{3/2} > -\ 0.7084\,|\nu 1d_{5/2}1p^{-1}_{3/2} >$

IPM		G Corr.		$V8$ Corr.		$S3$ Corr.	
Q	χ^2	Q	χ^2	Q	χ^2	Q	χ^2
0.67	27.36	0.66	35.07	0.66	28.17	0.65	25.56

mately overlapped with the mean field calculations, dotted lines. The stability of the full correlation with different types of correlation function is understood as a result of using a correctly normalized many-body wave function which should include two- and three-point diagrams as we discussed in Chapter 2.

In Tab. 3.12, the quenching factor Q and χ^2 values for the full correlated form factor of 4^- state in ^{16}O for each type of correlation are compared with uncorrelated *IPM* results. The full correlations slightly enhance the value of the maximum of the distribution. This enhancement is not equal for all types of correlation as it can be noticed in case of gaussian G and $S3$ correlations as shown in panel (a) and (e) of Fig. 3.13, respectively. This enhancement implies a smaller Q for the correlated calculation as shown in Tab. 3.12.

3.4 Conclusions

In this chapter we have studied the effects of short-range correlations on the inclusive (e, e') process for some high spin electric and magnetic low-lying nuclear exited states. Our *SRC* model has been applied to investigate ^{16}O, ^{40}Ca, ^{48}Ca and ^{208}Pb nuclei.

Before applying our *SRC* model, we have tested the degree of collectivity for the states under investigations by means of discrete *RPA* code using two different residual interactions. Then we have selected the magnetic and electric high spin states that can be described in terms of single or two $1p - 1h$ pairs to apply our *SRC* model on these states.

Three different scalar correlation functions have been used to investigate the short-range correlations effects. The correlation functions G and $S3$ have been linked with the single-particle basis with the same semi realistic $S3$ interaction of Afnan and Tang [Afn68] as shown by the work of Arias *et al.* [Ari96]. We have also used the third correlation function $V8$ that not linked to our single-particle basis with the same hamiltonian to test the effect of the consistency of the inputs.

From what we have presented it appears evident that the correlation effects are very small and can not be considered relevant to improve the description of the experimental data. Also, we found that the effects of correlations did not change by using correlation function that are not linked with the mean field produced by our single-particle basis. The size of these effects is in agreement with the results of microscopic nuclear matter calculations done within the *CBF* theory and using the *FHNC* re-summation techniques [Ben90] which find occupation numbers very close to those of the *IPM*.

It is possible that some of the correlation components we have neglected, especially the tensor terms, could produce noticeable effects, as indicated by Fabrocini [Fab97]. On the other hand, microscopic calculations in both infinite systems [Wir88] and finite nuclei [Fab00], show that the scalar term is by far the largest one in the correlation. Furthermore, a study of the ground state charge and momentum distributions of doubly closed shell nuclei [Ari97] indicate the small influence of these state dependent terms.

Our results in *RPA* calculations have shown that the presence of the mixing between $1p-1h$ pairs can heavily modify the size and sometimes even the shape of the form factor. This feature can be seen directly by comparing the quenching factor needed in cases of *RPA*, *IPM* and *SRC* results. The *RPA* results one can find in literature [Lal88, Co'90, Hin92, Ari94] have shown the same outcome. For this reason we think that the origin of the quenching factor should be searched by looking with more detail to the coupling of the single-particle excitations with the collective modes of the nucleus.

Chapter 4

SRC in Semi-Exclusive Electron Scattering

Overview

Semi-exclusive inelastic reactions are produced when one or more nucleons are knocked-out from the target nucleus and are detected in coincidence with the scattered electron, while the residual nucleus remains undetected. The simplest case of semi-exclusive reaction is one-nucleon knockout. The Feynman diagram corresponding to the kinematic variables of the first order $PWBA$ (one-photon exchange) process is shown in Fig. 4.1. In this situation, the four-momenta of the incident and scattered electrons and of the emitted nucleon are measured, so that k, k' and p are known. Additionally the residual nucleus is left in its ground state or in an excited state.

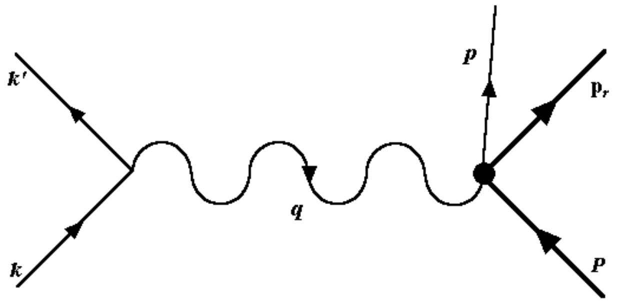

Figure 4.1: The Feynman diagram for inelastic $(e, e'N)$ electron scattering with one nucleon (proton) knockout in the one-photon exchange.

4.1 The Quasielastic $(e, e'N)$ Scattering Process

Here we work in the quasielastic region where the nuclear excitations are dominated by $1p - 1h$ dynamics. Semi-exclusive quasielastic electron reactions have been the subject of several review articles [For67, Fru84, Bof93, Kel96], we briefly recall the expressions of the coincidence $(e, e'N)$ cross section used in our calculations.

4.1.1 Framework

As we mentioned in the previous chapter, we consider the general formalism for the scattering of unpolarized electrons from an unpolarized target nucleus, we work in natural units ($\hbar = c = 1, e^2 = 1/137.04$) and employ the conventions of Bjorken and Drell [Bjo64]. The initial and final electron four vectors are respectively $k \equiv (\epsilon, \mathbf{k})$ and $k' \equiv (\epsilon', \mathbf{k}')$, and we use the symbol $q_\mu \equiv (\omega, \mathbf{q}) = k - k'$ to indicate the four momentum transfer, corresponding to $\omega = \epsilon - \epsilon'$ and three momentum transfer $\mathbf{q} = \mathbf{k} - \mathbf{k}'$.

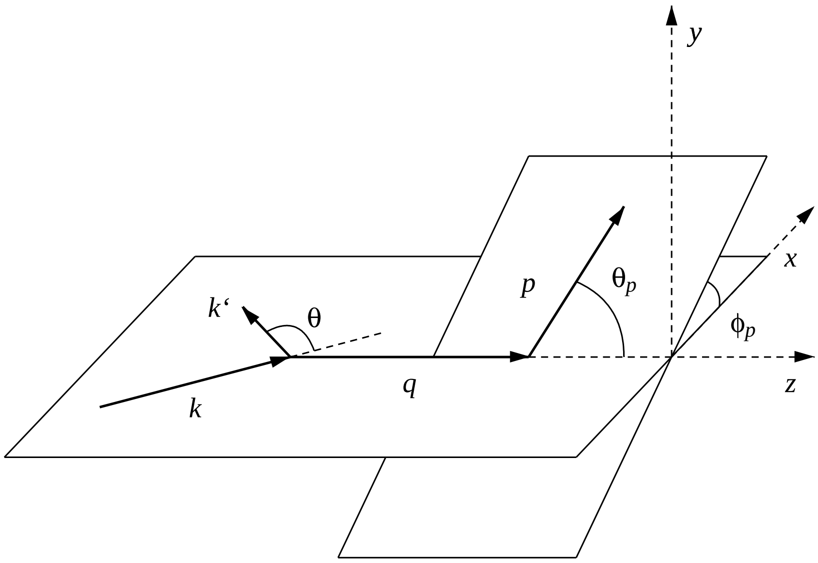

Figure 4.2: Reference system used in our calculations for $(e, e'N)$ reaction.

Note that $q_\mu^2 = \omega^2 - \mathbf{q}^2 \leq 0$. The four momentum of the emitted proton is $p \equiv (\epsilon_p, \mathbf{p})$. The reference system, shown in Fig. 4.2, is defined following the commonly used prescriptions. The scattering plane is defined by the electron vectors $\mathbf{k}$ and $\mathbf{k}'$, and the reaction plane is similarly defined by $\mathbf{q}$ and $\mathbf{p}$. The angle of the scattered electron is θ and the angle between the scattering and reaction planes is given by ϕ_p. The quantization axis is taken along the direction of $\mathbf{q}$ and the angles θ_p and ϕ_p define the direction of the emitted proton. The two planes coincide when $\phi_p = 0^0$ or 180^0 which is referred to as "in-plane" kinematics and the condition $\theta_p = 0^0$ is referred to as "parallel" kinematics (i.e. the detected proton emerges parallel to $\mathbf{q}$).

The four momentum of the target nucleus is P while the recoiling nucleus has four momentum P'. The three momentum of the recoil nucleus is $\mathbf{p}_r$. Since the absorbed three momentum of the virtual photon $\mathbf{q}$ and the three momentum of the detected proton $\mathbf{p}$ are measured, one can always calculate the missing three momentum $\mathbf{p}_m$ by applying conservation of three momentum at the reaction vertex:

$$\mathbf{p}_m = \mathbf{q} - \mathbf{p} \tag{4.1}$$

which is the recoil three momentum of the residual nucleus, i.e. $\mathbf{p}_m = \mathbf{p}_r$. Note that some authors, e.g. [Kel96], use the opposite sign convention ($\mathbf{p}_m = -\mathbf{p}_r$). The missing energy is then calculated from:

$$E_m = \omega - T_p - T_{A-1}\,, \tag{4.2}$$

where T_p is the kinetic energy of the outgoing proton and T_{A-1} the kinetic energy of the recoiling nucleus.

4.1.2 The $(e, e'N)$ Cross Section in the PWBA

In our calculations, we derive the cross section by adopting the commonly used assumptions [For67, Die75, Kle83]: (a) the electron wave functions are plane wave solutions of the Dirac equation; (b) only one photon is exchanged between the electron and the nucleus; (c) all the terms depending upon the electron rest mass are neglected; and (d) the initial hadronic nuclear system $|\Psi_0\rangle$ is described with good angular momenta i.e. $|\Psi_0\rangle \rightarrow |J_0 M_0, \Pi_0\rangle$ while the final hadronic state $|\Psi_f\rangle$ corresponds asymptotically to a knocked-out proton with energy ϵ_p, momentum $\mathbf{p}$ and with unobserved spin projection σ, together with an undetected rest nucleus with angular momentum j_h and its projection on the quantization axis m_h, i.e. $|\Psi_f\rangle \rightarrow |\mathbf{p}\sigma; j_h m_h\rangle$. With these approximations, in the $PWBA$ we can express the differential cross section of $(e, e'N)$ reaction in the form:

$$\frac{d^5\sigma}{d\epsilon' d\Omega_e d\Omega_p} = \frac{\sigma_M K}{(2\pi)^3} \left(v_L w_L + v_T w_T + v_{TL} w_{TL} + v_{TT} w_{TT}\right) , \qquad (4.3)$$

where σ_M is defined by Eq. (3.2). Since we describe the emitted particle, with mass M_p, within the non relativistic kinematics, we obtain $K = |\mathbf{p}|M_p$. The leptonic factors v_L and v_T are defined by Eqs. (3.3) and (3.4) while the leptonic factors v_{TL} and v_{TT} have the form:

$$v_{TL} = \frac{q_\mu^2}{\sqrt{2}\mathbf{q}^2} \left(\tan^2\frac{\theta}{2} - \frac{q_\mu^2}{\mathbf{q}^2}\right)^{\frac{1}{2}} , \qquad (4.4)$$

$$v_{TT} = \frac{1}{2}\frac{q_\mu^2}{\mathbf{q}^2} . \qquad (4.5)$$

The information about the nuclear structure is included in the four independent response functions w that are related to matrix elements of various components of the nuclear current $J_\mu(\mathbf{q}) \equiv (\rho(\mathbf{q}), \mathbf{J}(\mathbf{q}))$. Because of the current conservation, only three components of the current four-vector are independent, as shown in Sec. 2.4.1. We choose the charge $\rho(\mathbf{q})$ (longitudinal) and the two transverse $J_\pm(\mathbf{q})$ components in spherical coordinates. Thus, we can express the responses w as:

$$w_L = \sum \langle\Psi_i|\rho^\dagger(\mathbf{q})|\Psi_f\rangle\langle\Psi_f|\rho(\mathbf{q})|\Psi_i\rangle , \qquad (4.6)$$

$$
\begin{aligned}
w_T &= \sum \langle\Psi_i|J_-^\dagger(\mathbf{q})|\Psi_f\rangle\langle\Psi_f|J_-(\mathbf{q})|\Psi_i\rangle \\
&\quad + \langle\Psi_i|J_+^\dagger(\mathbf{q})|\Psi_f\rangle\langle\Psi_f|J_+(\mathbf{q})|\Psi_i\rangle\,, && (4.7) \\
w_{TL} &= \sum 2Re\Big(\langle\Psi_i|\rho^\dagger(\mathbf{q})|\Psi_f\rangle\langle\Psi_f|J_-(\mathbf{q})|\Psi_i\rangle \\
&\quad - \langle\Psi_i|\rho^\dagger(\mathbf{q})|\Psi_f\rangle\langle\Psi_i|J_+^\dagger(\mathbf{q})|\Psi_f\rangle\Big)\,, && (4.8) \\
w_{TT} &= \sum 2Re\left(\langle\Psi_i|J_+^\dagger(\mathbf{q})|\Psi_f\rangle\langle\Psi_f|J_-(\mathbf{q})|\Psi_i\rangle\right)\,. && (4.9)
\end{aligned}
$$

In the previous equations, we sum over the undetected polarizations of the final particles, i.e. the sum on the projection of angular momenta of the spin of the emitted proton σ and of the residual nucleus m_h is understood. The response functions w_L and w_T are due to the longitudinal and the transverse components of the current, respectively. The response function w_{TL} is due to the interference of the transverse and the longitudinal components of the current and w_{TT} is due to the interference of the two transverse components. With respect to the inclusive experiments we have here two additional responses w_{TL} and w_{TT} arising from the interference between various terms of the four-current. These terms do not contribute in the inclusive case, since the transition is between two nuclear states with definite angular momentum. This symmetry cancel the interference terms between electromagnetic operators with different z-axis components.

4.1.3 The Plane Wave Impulse Approximation

In the *PWIA* the $(e, e'N)$ cross section is derived using the following further assumptions:

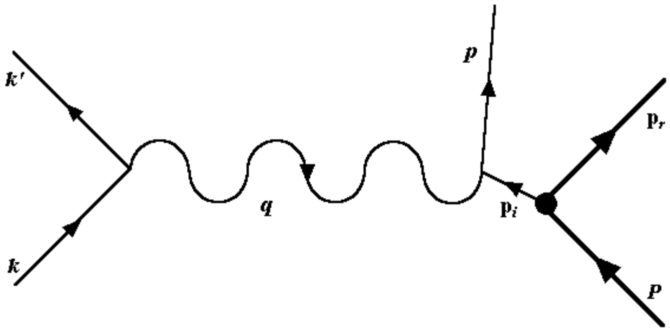

Figure 4.3: $(e, e'N)$ reaction in the $PWIA$.

1. The virtual photon interacts with a single nucleon in the nucleus.

2. The struck nucleon leaves the nucleus without any further interactions with the residual nucleus and the knocked-out proton may be represented by a plane wave (i.e. no Final State Interactions (*FSI*)).

3. The knocked-out nucleon is the one detected in the experiment.

4. The nucleus can be described by the *IPM*.

A diagram of the $(e, e'N)$ process in the $PWIA$ is shown in Fig. 4.3. Applying conservation of the three momentum to the photon-proton vertex, the initial proton three momentum $\mathbf{p}_i$, i.e. the momentum of the proton before being emitted, is given by:

$$\mathbf{p}_i = \mathbf{p} - \mathbf{q} \tag{4.10}$$

Comparing to Eq. (4.1), the initial proton momentum is related to the missing momentum, $\mathbf{p}_m$, by:

$$\mathbf{p}_i = -\mathbf{p}_m \, . \tag{4.11}$$

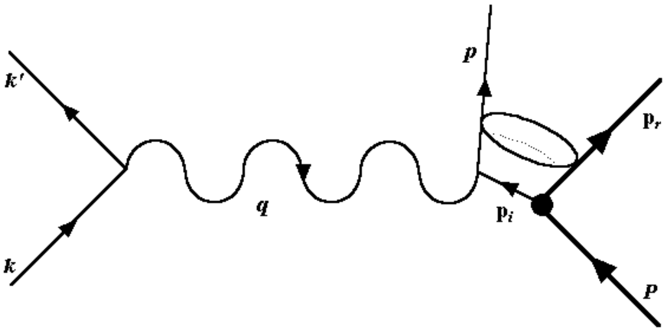

Figure 4.4: $(e, e'N)$ reaction in the $DWIA$.

By measuring the missing momentum in the $(e, e'N)$ experiment, one can therefore determine the initial momentum that the struck proton had inside the nucleus before the scattering occurred.

4.1.4 The Distorted Wave Impulse Approximation

Of all the assumptions made within the $PWIA$ framework, the second one is the least likely to be valid, since the ejected nucleon interacts with the residual nucleus via the strong interaction. The Distorted Wave Impulse Approximation ($DWIA$) takes these *FSI* into account, while at the same time maintaining the other three assumptions. Fig. 4.4 shows the diagram for the $DWIA$.

The main effect of the *FSI* felt by the ejected proton is a reduction of the cross section. This reduction is related to the fact that the interaction of the struck nucleon with the other nucleons may remove this nucleon from the single-nucleon emission channel and populate other channels like deuteron, alpha particles emission etc. Thus in the $DWIA$, the attenuation of the *FSI* is usually described using a complex optical potential in which the ejected proton is moving. The optical potentials are obtained from fits to elastic proton scattering data, and the imaginary part of these potentials accounts for the loss of flux produced by transitions to channels other than the elastic one. A description of the optical potential formalism and a detailed comparison of several widely used optical potentials may be found in [Kel96].

4.2 Nuclear Model

As we mentioned, the nuclear final state $|\Psi_f\rangle$ is described in the asymptotic region as the product of the wave function of the emitted proton $\phi(\mathbf{p}\cdot\mathbf{r})\chi_\sigma$, where $\mathbf{p}$ is its momentum, and that of the rest nucleus: $\Psi(\mathbf{r}_1...\mathbf{r}_{A-1};\epsilon_h;j_h,m_h)$. We indicate with j_h the angular momentum of the rest nucleus and we define $\epsilon_h=\epsilon_p-\omega$. In a strict independent particle model these quantities correspond to the angular momentum and energy of the hole state, respectively. We perform a multipole expansion of $|\Psi_f\rangle$ to express it in terms of eigenstates of the total angular momentum of the A nucleon system:

$$\begin{aligned}|\Psi_f\rangle &= \frac{4\pi}{|\mathbf{p}|}\sum_{l_p\mu_p}\sum_{j_pm_p}\sum_{JM,\Pi} i^{l_p}Y^*_{l_p\mu_p}(\widehat{\mathbf{p}})\langle l_p\mu_p\frac{1}{2}\sigma|j_pm_p\rangle \\ &\quad \langle j_pm_pj_hm_h|JM\rangle|\Psi;JM,\Pi;(l_pj_pm_p\epsilon_p,l_hj_hm_h\epsilon_h)\rangle \\ &\equiv \frac{4\pi}{|\mathbf{p}|}\sum_{p}\sum_{JM,\Pi} i^{l_p}Y^*_{l_p\mu_p}(\widehat{\mathbf{p}})\langle l_p\mu_p\frac{1}{2}\sigma|j_pm_p\rangle \\ &\quad \langle j_pm_pj_hm_h|JM\rangle\ \frac{|JM,\Pi;p,h\rangle}{\langle JM,\Pi;p,h|JM,\Pi;p,h\rangle^{\frac{1}{2}}}\,. \end{aligned} \tag{4.12}$$

In the above equations the state $|\Psi;JM,\Pi;(l_pj_pm_p\epsilon_p,l_hj_hm_h\epsilon_h)\rangle$ represents the excited state of the system with A nucleons with total angular momentum J projection M, parity Π, having a particle in the continuum wave characterized by orbital and total angular momentum l_p and j_p with projection m_p and energy ϵ_p, and a residual nucleus with hole quantum numbers l_h j_h, m_h and ϵ_h. We indicate with $Y_{l\mu}$ the spherical harmonics and with the symbol $\langle l_a m_a l_b m_b | JM \rangle$ the Clebsch-Gordan coefficients [Edm57]. In the last expression, the nuclear excited state is given in terms of unnormalized many-body wave function $|JM, \Pi; p, h\rangle$

In our model, the nuclear final state with total angular momentum J is described as a superposition of all possible one-particle one-hole transitions allowed by the angular momentum selection rules. Within this approximation, the knowledge of the energy and of the momentum of the emitted proton determines the quantum numbers of the hole state of the residual nucleus. Then the summation on the hole states drops and we sum only over the possible particle states in the continuum. We define the sum over p as a summation over the l_p, μ_p, j_p and m_p quantum numbers.

From the equations (4.6)-(4.9) defining the w factors, one can see that the basic ingredients to be calculated are the transition matrix elements from the ground state to the excited state of the nuclear system induced by a one body operator. We write the transition matrix elements as:

$$
\begin{aligned}
\langle \Psi_f | O_\eta(\mathbf{q}) | \Psi_i \rangle &= \frac{4\pi}{|\mathbf{p}|} \sum_p \sum_{J,M,\Pi} (-i)^{l_p} Y_{l_p \mu_p}(\widehat{\mathbf{p}}) \langle l_p \mu_p \frac{1}{2} \sigma | j_p m_p \rangle \langle j_p m_p j_h m_h | JM \rangle \\
&\quad \frac{\langle JM, \Pi; p, h | O_\eta(\mathbf{q}) | 00, +1 \rangle}{\langle JM, \Pi; p, h | JM, \Pi; p, h \rangle^{\frac{1}{2}} \langle 00, +1 | 00, +1 \rangle^{\frac{1}{2}}} \\
&\equiv \frac{4\pi}{|\mathbf{p}|} \sum_p \sum_{J,M,\Pi} \mathcal{A}(p, h; J, M, \Pi)\ \xi_{J,M,\Pi,\eta}(\mathbf{q}; p, h)\,, \qquad (4.13)
\end{aligned}
$$

where $|00,+1\rangle$ is the unnormalized ground state which, for the nuclei we shall consider, has zero angular momentum and positive parity. We include all the geometric part of the expression in the symbol

$$\mathcal{A}(p,h;J,M,\Pi) = (-i)^{l_p} Y_{l_p\mu_p}(\widehat{\mathbf{p}}) \langle l_p\mu_p\frac{1}{2}\sigma|j_pm_p\rangle\langle j_pm_pj_hm_h|JM\rangle\ , \quad (4.14)$$

and we indicate with $O_\eta(\mathbf{q})$ the generic one-body operator inducing the transition. For $\eta = 0$ this is the charge operator, while for $\eta = \pm 1$ the two transverse components of Eq. (2.22) are considered.

As we mentioned in previous chapters, in our *SRC* nuclear model we consider doubly closed shell nuclei with initial and final states defined as shown in Eqs. (2.28) and (2.29). Here the excited wave function $|\Phi;JM,\Pi;ph\rangle$ indicates a Slater determinant describing the mean field wave function in a pure independent particle model where the hole function h is substituted with the continuum particle function p. With respect to a pure *IPM*, the novelty of our *SRC* is the presence of the correlation function G for both ground and excited states. In our calculations, we restricted ourselves to the use of purely scalar (Jastrow) correlation function leading to the adopted ansatz on the correlation function G as given by Eq. (2.6).

To exploit cluster expansion techniques it is convenient to rewrite the transition matrix $\xi_{J,M,\Pi,\eta}(\mathbf{q};p,h)$ in Eq. (4.13) as:

$$\begin{aligned}\xi_{J,M,\Pi,\eta}(\mathbf{q};p,h) \quad &= \quad \frac{\langle JM,\Pi;p,h|O_\eta(\mathbf{q})|00,+1\rangle}{\langle 00,+1|00,+1\rangle} \\ &\qquad \times \left[\frac{\langle 00,+1|00,+1\rangle}{\langle JM,\Pi;p,h|JM,\Pi;p,h\rangle}\right]^{\frac{1}{2}}\ . \end{aligned} \quad (4.15)$$

We apply the same technique given in Sec. 2.3: (a) the unlinked diagrams are eliminated by expanding both numerator and denominator in power of the short-range correlation function $h(r_{ij}) = f^2(r_{ij}) - 1$, (b) we retain only the terms containing a single correlation line of $h(r_{ij})$. By labeling with 1 the coordinate where the external operator $O_\eta(\mathbf{q})$ is acting, we can specify the ξ of Eq. (4.15) as:

$$\begin{aligned}
\xi_{J,M,\Pi,\eta}(\mathbf{q};p,h) \quad \longrightarrow & \quad \xi^1_{J,M,\Pi,\eta}(\mathbf{q};p,h) \\
= & \quad \langle\Phi; JM,\Pi;p,h|\, O_\eta(\mathbf{q})\, |\Phi;00,+1\rangle \\
& + \langle\Phi; JM,\Pi;p,h|\, O_\eta(\mathbf{q}) \sum_{i>1}^{A} h(r_{1i})\, |\Phi;00,+1\rangle_L \\
& + \langle\Phi; JM,\Pi;p,h|\, O_\eta(\mathbf{q}) \sum_{1<i<k}^{A} h(r_{ik})\, |\Phi;00,+1\rangle_L \,.
\end{aligned} \tag{4.16}$$

The above expression shows that our model generates, in addition to the uncorrelated transitions represented in Fig. 2.2 by the one-point diagram (1.1), also two- and three-point diagrams. The presence of these last diagrams is necessary to have the correct normalization of the many-body wave function, as we discussed before.

Substituting Eq. (4.16) into Eq. (4.13) and following Sec. 2.4 where the explicit forms of the external operator $O_\eta(\mathbf{q})$ are inserted, we rewrite Eq. (4.13) as:

$$
\begin{aligned}
\langle\Psi_f|O_\eta(\mathbf{q})|\Psi_i\rangle &= \frac{4\pi\sqrt{2\pi}}{|\mathbf{p}|}\sum_p\sum_{J,\Pi}(-i)^{-J}\mathcal{A}(p,h;J,-\eta,\Pi) \\
&\quad\times\Big[\langle p||\,O_{J(\eta)}(\mathbf{q})\,||h\rangle + \sum_{i>1}^{A}\langle p,i||\,O_{J(\eta)}(\mathbf{q})\,h(r_{1i})\,||h,i\rangle \\
&\quad+\sum_{1<i<k}^{A}\langle p,i,k||\,O_{J(\eta)}(\mathbf{q})\,h(r_{ik})\,||h,i,k\rangle\Big] \\
&= \frac{4\pi\sqrt{2\pi}}{|\mathbf{p}|}\sum_{ph}\sum_{J,\Pi}(-i)^{-J}\mathcal{A}(p,h;J,-\eta,\Pi)\;\xi^1_{J,\Pi,\eta}(\mathbf{q};p,h)\,,
\end{aligned}
\tag{4.17}
$$

where $O_{J(\eta)}(\mathbf{q})$ is defined by Eq.(2.36) and $\xi^1_{J,\Pi,\eta}(\mathbf{q};p,h)$ is the sum of the reduced matrix elements corresponding to the one-, two- and three-points diagrams of Fig. 2.2. The derivation of these matrices are given in Appendix A for the different electro-magnetic operators.

Now all the ingredients to calculate the responses w and then the cross section are available. The information on the angular distribution of the emitted particle is fully contained in the spherical harmonics of Eq. (4.14), which has to be squared to calculate the response. We have to deal with a geometrical term of the type:

$$
\begin{aligned}
&\Big((-i)^{-J'}\mathcal{A}(p',h';J',-\eta',\Pi')\Big)^*\;\Big((-i)^{-J}\mathcal{A}(p,h;J,-\eta,\Pi)\Big) = \\
&= \;\langle l'_p(-m_h-\eta'-\sigma)\frac{1}{2}\sigma|j'_p(-m_h-\eta')\rangle\langle j'_p(-m_h-\eta')j_hm_h|J'-\eta'\rangle \\
&\qquad\langle l_p(-m_h-\eta-\sigma)\frac{1}{2}\sigma|j_p(-m_h-\eta)\rangle\langle j_p(-m_h-\eta)j_hm_h|J-\eta\rangle \\
&\qquad(-i)^{l_p-l'_p-J+J'}Y_{l_p,(-m_h-\eta-\sigma)}(\widehat{\mathbf{p}})Y^*_{l'_p,(-m_h-\eta'-\sigma)}(\widehat{\mathbf{p}})\,.
\end{aligned}
\tag{4.18}
$$

This expression arises because the angular momentum of the hole j_h , its z axis projection m_h, and σ the third component of the spin of the emitted particle, are good quantum numbers of the hadronic final state. The above equation shows that the dependence from the angle ϕ_p between the scattering plane and the plane where the momentum of the emitted particle is lying, is present only when $\eta \neq \eta'$, i.e. only in the interference terms tl and tt in Eq. (4.3). The dependence of ϕ_p can explicitly be extracted and we can rewrite the cross section expression as:

$$\begin{aligned} \frac{d^5\sigma}{d\epsilon' d\Omega_e d\Omega_p} &= \frac{\sigma_M K}{(2\pi)^3}\Big[v_L W_{0,0} + v_T (W_{+1,+1} + W_{-1,-1}) \\ &\quad + 2 v_{TL} Re(W_{-1,0} - W_{+1,0}) \cos\phi_p \\ &\quad + 2 v_{TT} Re(W_{+1,-1}) \cos 2\phi_p \Big], \end{aligned} \tag{4.19}$$

where the W functions are defined as:

$$\begin{aligned} W_{\eta\eta'} &= \frac{32\pi^3}{|\mathbf{p}|^2} \sum_{\sigma m_h} \sum_{J\Pi l_p j_p} \sum_{J'\Pi' l'_p j'_p} (-i)^{l_p - l'_p - J + J'} (-1)^{\eta - \eta'} \\ &\quad \langle l_p(-m_h - \eta - \sigma)\frac{1}{2}\sigma | j_p(-m_h - \eta)\rangle \langle j_p(-m_h - \eta) j_h m_h | J - \eta\rangle \\ &\quad \langle l'_p(-m_h - \eta' - \sigma)\frac{1}{2}\sigma | j'_p(-m_h - \eta')\rangle \langle j'_p(-m_h - \eta') j_h m_h | J' - \eta'\rangle \\ &\quad \left[\frac{(l_p + m_h + \eta + \sigma)!}{(l_p - m_h - \eta - \sigma)!} \frac{(l'_p + m_h + \eta' + \sigma)!}{(l'_p - m_h - \eta' - \sigma)!}\right]^{\frac{1}{2}} \left[\frac{2l_p + 1}{4\pi}\right]^{\frac{1}{2}} \left[\frac{2l'_p + 1}{4\pi}\right]^{\frac{1}{2}} \\ &\quad P_{l_p}^{-m_h - \eta - \sigma}(\cos\theta_p)\; P_{l'_p}^{-m_h - \eta' - \sigma}(\cos\theta_p) \\ &\quad \xi^1_{J,\Pi,\eta}(\mathbf{q}; p, h)\; \xi^{1\dagger}_{J',\Pi',\eta'}(\mathbf{q}; p', h)\,. \end{aligned} \tag{4.20}$$

In the literature the expression of the cross section of Eq. (4.19) is written as:

$$\begin{aligned}\frac{d^5\sigma}{d\epsilon' d\Omega_e d\Omega_p} &= \frac{\sigma_M K}{(2\pi)^3}\left[v_L W_L + v_T W_T\right. \\ &\qquad \left. + v_{TL} W_{TL}\cos\phi_p + v_{TT} W_{TT}\cos 2\phi_p\right], \qquad (4.21)\end{aligned}$$

where we define the charge response $W_L \equiv W_{0,0}$, the transverse response $W_T \equiv W_{+1,+1} + W_{-1,-1}$, the interference of transverse and longitudinal response $W_{TL} \equiv 2Re(W_{-1,0} - W_{0,+1})$ and the interference of the two transverse components response $W_{TT} \equiv 2Re(W_{-1,+1})$. In general, the responses W_L, W_T, W_{TL} and W_{TT} are functions of variables ω, q_μ^2, θ_p and p.

4.3 Kinematic Conditions

In this section the kinematic conditions commonly used in the quasielastic $(e, e'N)$ experiments are briefly discussed. In the $(e, e'N)$ experiments the cross section is usually expressed as a function of the initial nucleon three momentum defined as:

$$\begin{aligned}p_i \equiv |\mathbf{p}_i| &= |\mathbf{p} - \mathbf{q}| \\ &= \sqrt{|\mathbf{p}|^2 + |\mathbf{q}|^2 - 2|\mathbf{p}||\mathbf{q}|\cos\theta_p}\,. \qquad (4.22)\end{aligned}$$

This equation shows that the scattering angles θ and θ_p, as defined in Fig. 4.2, are not uniquely determined for a certain choice of p_i. Consequently there is a freedom in the choice of kinematics employed in the experiment. Two kinematic conditions are commonly used in the quasielastic $(e, e'p)$ experiments: “parallel” and “perpendicular” kinematics. Both terms refer to “in-plane” kinematics where the escaping proton is detected in the scattering plane ($\phi_p = 0^0$ or 180^0).

In parallel kinematics, the knocked-out proton is detected in the same direction as the transferred momentum $\mathbf{q}$ such that $\theta_p = 0^0$. Keeping constant the momentum $|\mathbf{p}|$ and the kinetic energy T_p of the emitted proton, the initial momentum of the emitted proton p_i is varied by changing $\mathbf{q}$, i.e. by varying either the energy of the electron beam or the electron scattering angle θ where $|\mathbf{q}| = \sqrt{|\mathbf{k}|^2 + |\mathbf{k}'|^2 - 2|\mathbf{k}||\mathbf{k}'|\cos\theta}$. In this situation p_i is parallel or antiparallel to $\mathbf{q}$ ($p_i \parallel \mathbf{q}$) depends on the projection of the initial proton momentum along the direction of the momentum transfer. That means that the same value of p_i is obtained for two values of $\mathbf{q}$ defining two opposite directions of p_i. In our work, we adopt the convention that the positive (negative) values of p_i are associated with the condition $|\mathbf{p}| > |\mathbf{q}|$ ($|\mathbf{p}| < |\mathbf{q}|$), see panels ($a$) and ($b$) of Fig. 4.5.

In perpendicular kinematics, both the four momentum transfer $(\omega, \mathbf{q})$ and the momentum $|\mathbf{p}|$ of the emitted proton are kept constant. Note that by keeping $\mathbf{q}$ and ω constant through the experiment the electron scattering angle θ does not need to be changed. The initial momentum of the emitted proton p_i is varied by changing the angle θ_p between $\mathbf{q}$ and $\mathbf{p}$. It is customary to choose $|\mathbf{q}| = |\mathbf{p}|$ for perpendicular kinematics, so $p_i = 0$ is obtained at $\theta_p = 0^0$. For that kinematic sittings where $|\mathbf{q}| = |\mathbf{p}|$, both $\mathbf{q}$ and $\mathbf{p}$ are usually large enough for the relevant range of p_i to be covered with relatively small θ_p angles. This setting yields p_i close to being perpendicular to $\mathbf{q}$ on either side of $\mathbf{q}$ ($\mathbf{q} \perp p_i$). Panels (c) and (d) of Fig. 4.5 illustrates these kinematic conditions. The same value of the

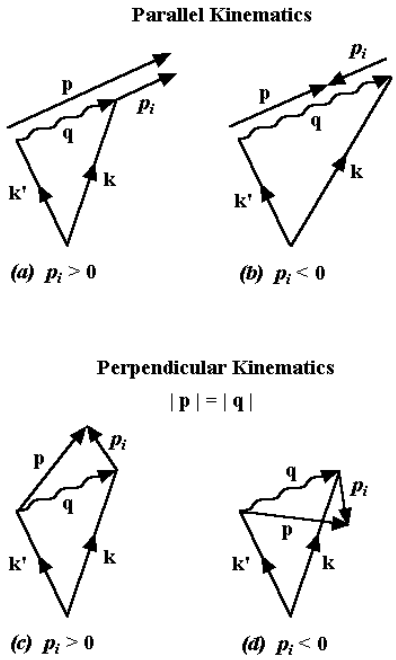

Figure 4.5: A schematic representation of parallel (upper) and perpendicular (lower) kinematics.

magnitude of the p_i is obtained for two different values of θ_p, that define two opposite directions for p_i. In what follows we assign a positive value of p_i when the proton is escaping in the half-plane which is bordered by the z-axis and lies on the side of initial electron beam direction. For our conventions of Fig. 4.2, this means that p_i is positive for $\phi_p = 0^0$ and negative for $\phi_p = 180^0$.

4.4 The Off-Shell Electron-Proton Cross Section

The quasielastic experimental $(e, e'p)$ cross section in impulse approximation ($PWIA$ or $DWIA$) is usually given in a factorized form as follows:

$$\frac{d^5\sigma}{d\epsilon' d\Omega_e d\Omega_p} = K\sigma_{ep}S\,, \tag{4.23}$$

where K is the kinematical factor defined in Eq. (4.3), σ_{ep} is the elastic electron-proton scattering amplitude and S is called the proton spectral function. The spectral function corresponds to the probability for finding in the target nucleus a proton of momentum $p_i = -\mathbf{p}_m$ and separation energy E_m. In case of $PWIA$ the undistorted spectral function would depend only on E_m and $\mathbf{p}_m$, i.e. $S \equiv S(E_m, \mathbf{p}_m)$. While in case of $DWIA$, the FSI between the ejectile and the residual nucleus make the distorted spectral function depends upon the ejectile momentum $\mathbf{p}$ in addition to the previous parameters, i.e. $S \equiv S(E_m, \mathbf{p}_m, \mathbf{p})$. In the relativistic impulse approximation approach one essentially replaces σ_{ep} by the elastic scattering amplitude between free relativistic particles. But, due to the binding energy of the nucleus the initial proton is off the mass shell. In other words, the energy of the initial proton ϵ_i which would be obtained from the conservation of energy $\epsilon_i = \epsilon_p - \omega$ does not match with the momentum $\mathbf{p}_i$ defined by Eq. (4.10), that is $\epsilon_i^2 \neq |\mathbf{p}_i|^2 + M^2$, where M is the rest mass of the proton. It introduces some ambiguities in the relativistic estimation of σ_{ep}. In order to reduce off-shell ambiguities certain physical requirements can be imposed. In the spirit of the impulse approximation, the off-shell electron-proton cross section σ_{ep}, which has been widely used in the analysis of the experiments, was proposed by de Forest [For83].

Since the experimentalists prefer to present their data in terms of reduced cross section ρ by dividing the differential cross section of Eq. (4.23) by $K\,\sigma_{ep}$, the theoretical reduced cross section must be obtained from an unfactorized calculation by using the same prescription. Thus in our calculations we compute the reduced cross section by dividing Eqs. (4.19) and (4.21) by $K\,\sigma_{ep}^{cc1}$ as follows:

$$\rho = \frac{1}{K\,\sigma_{ep}^{cc1}} \frac{d^5\sigma}{d\epsilon' d\Omega_e d\Omega_p}\,, \tag{4.24}$$

where σ_{ep}^{cc1} is the de Forest prescription for σ_{ep}.

4.5 Specific Applications

We apply our *SRC* model to the investigation of the $^{16}\mathrm{O}(e,e'p)^{15}\mathrm{N}$ reaction in the quasielastic region. The motivations of the choice of $^{16}\mathrm{O}$ nucleus have been already outlined in Sec. 3.3. It is a sufficiently light nucleus such that the plane wave description of the electron wave functions is still valid [Giu87, Slu97]. Also, it is a lightest spherical doubly-closed shell nucleus and the symmetries implied simplify the treatment of the shell and finite size effects. These are also the reasons why this nucleus has been investigated with fully microscopic calculations [Ari96, Fab00].

The work of Arias *et al.* [Ari96] and Fabrocini *et al.* [Fab00] provide us the needed link between the inputs of our calculations where the single-particle bases and the correlation functions should be linked together with the same many body hamiltonians. As we stated in Sec. 3.3, we consider the $S3$ and the scalar part of $V8$ correlation functions. The two correlation functions are shown in Fig. 3.2 for ^{16}O nucleus. In the calculation of Chapter 3, we generated the single-particle basis of ^{16}O nucleus using one set of Woods-Saxon parameters given in Tab. 3.1. That set of parameters is linked to the calculations of $S3$ correlation function only while we used the same set with the $V8$ correlation to test the effect of inconsistency between our inputs. Here, we generate the single-particle basis by two sets of Woods-Saxon parameters. The first one, linked to the $S3$ correlation function, is given in Tab. 3.1. The second set, linked to the $V8$ correlation function, is shown in Tab. 4.1. For sake of completeness, we show in Tab. 4.2 the energies of single-particle states below the Fermi level (hole-states h) and some energies of single-particle states above Fermi level (particle-states p) for ^{16}O using the Woods-Saxon parameters given in Tab. 4.1. These energies can be compared with the experimental energies and the energies of the other set of Woods-Saxon parameters shown in Tab. 3.2. Henceforth we shall label with $S3$ all the results obtained with the single-particle wave functions generated with parameters shown in Tab. 3.1 and linked to the $S3$ correlation function, and we shall label with $V8$ all the results obtained with the single-particle wave functions generated with parameters shown in Tab. 4.1 and linked to the $V8$ correlation function. Note that we do not present the results of the gaussian correlation function G because it gives similar results as those obtained with the $S3$ input.

Table 4.1: Parameters of the Woods-Saxon potentials used to generate the set of single-particle wave functions for ^{16}O nucleus that linked to $V8$ correlation function. The parameters are taken from the work of Fabrocini *et al.* [Fab00].

	V_0 [MeV]	V_{LS} [MeV]	R [fm]	a [fm]
π	53.0	0.0	3.45	0.7
ν	53.0	0.0	3.45	0.7

In our model the single-particle bound wave functions and negative energies are obtained using the mean field potentials of Woods-Saxon type previously mentioned, i.e. using both $S3$ parameters given in Tab. 3.1 and $V8$ parameter given in Tab. 4.1. If not specifically mentioned our results are obtained by using the same mean field for bound states and for the emitted proton wave function with positive energies. In Sec. 4.5.2 we shall investigate the effect of using different mean fields for hole and particle states as it is commonly done in the investigation of $(e, e'N)$ data.

Our calculations are done in both perpendicular and parallel kinematics. As we stated in Sec. 4.3, in the perpendicular kinematics the value of the momentum transfer $|\mathbf{q}|$ is kept fixed and the changes of p_i of Eq. (4.10) are obtained by changing the detection angle θ_p. This is, for us, the easiest case to calculate and to investigate, even though all the four response functions $W_{\eta\eta'}$ contribute. In the parallel kinematics, the momentum transfer $|\mathbf{q}|$ and the momentum of the emitted proton $|\mathbf{p}|$ are kept in the same direction and the missing momentum is changed by

Table 4.2: Single-particle energies of states near Fermi level of ^{16}O nucleus using Woods-Saxon parameters given in Tab. 4.1.

		π	ν
		E_{WS} [MeV]	
h-states	$1s_{1/2}$	-30.72	-34.54
	$1p_{3/2}$	-17.58	-21.05
	$1p_{1/2}$	-17.58	-21.05
p-states	$1d_{5/2}$	-4.41	-7.47
	$2s_{1/2}$	-4.47	-7.43

changing the values of $|\mathbf{q}|$. In this case the interference responses, those with $\eta \neq \eta'$ do not contribute [Co'85].

Since in $(e, e'p)$ processes the number of variables into play is relatively large and for the purpose of theoretical investigation of the cross section and responses, we have mainly done our investigation at fixed kinematical conditions that cover most of experiments found in literatures. Throughout all of our theoretical investigation we keep the value of the energy transfer fixed at $\omega = \epsilon_i - \epsilon_f = 128$ MeV, and the value of the momentum of the emitted proton fixed at $|\mathbf{p}|= 444$ MeV/c, knocked out from the $1p_{1/2}$ level. In perpendicular kinematics the scattering angle was fixed to set $|\mathbf{q}| = |\mathbf{p}|$. The kinematical conditions just described cover the experimental kinematics of $^{16}\mathrm{O}(e, e'p)^{15}\mathrm{N}$ in both perpendicular experiment of Bernheim *et al.* [Ber82] and in the parallel one of Leuschner *et al.* [Leu94].

In the calculation of the responses, Eq. (4.20), and of the cross section, Eq. (4.21), the sum over multipoles J are infinite. In practice we sum all multipoles until the final results are stable. In our work, we tested the convergence of the multipole expansion by calculating the cross section for various values of J. In Fig. 4.6 we show, for example, the mean filed cross sections calculated up to $J = 5$ as dashed doubly dotted lines, $J = 10$ as dashed dotted lines, $J = 12$ as dashed lines, $J = 15$ as dotted lines and $J = 20$ as solid lines. We should recall that we define p_i in Eq. (4.22), also we consider the values of p_i to be positive when $\phi_p = 0^0$ and negative when $\phi_p = 180^0$ in case of perpendicular kinematics while in case of parallel kinematics $p_i > 0$ when $|\mathbf{p}| > |\mathbf{q}|$ and $p_i < 0$ when $|\mathbf{p}| < |\mathbf{q}|$. The left panels of the figure, i.e. (a) and (c), show the perpendicular kinematics results with both $S3$ and $V8$ mean field potentials, respectively. The right ones correspond to the parallel kinematics. It is clear that the convergence of parallel results is reached with number of multipoles smaller than in case of perpendicular results. In parallel kinematics it is enough to include multipoles up to $J = 12$ where the curves with highest summation of J are almost overlapped in panels (b) and (d) of Fig. 4.6. While in perpendicular kinematics we have to sum up to $J = 15$.

In Fig. 4.7 we show the convergence for the responses W_L, W_T, W_{TL} and W_{TT} as a function of initial momentum p_i in perpendicular kinematics. Again the convergence of each individual response is reached at $J = 15$. In all of the calculations that follow we include multipoles up to $J = 20$ in both parallel and perpendicular kinematics.

The cross section is obtained by summing the contributions of all the responses. From Eq. (4.21) one can observe that in case of perpendicular

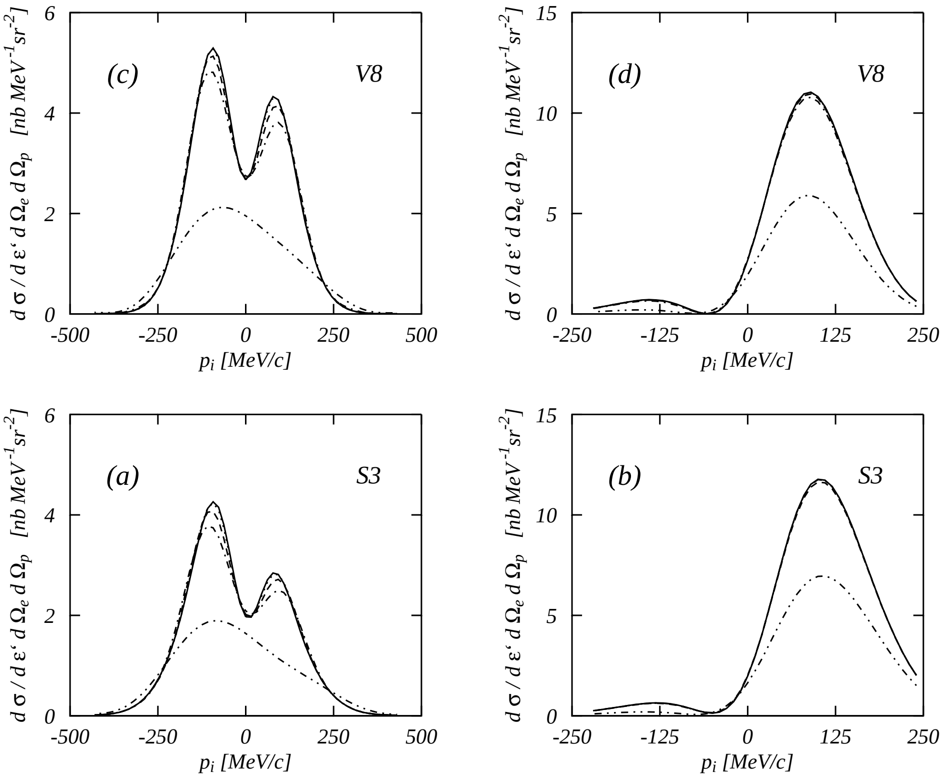

Figure 4.6: Mean field cross sections as a function of the proton initial momentum for the ^{16}O$(e, e'p)^{15}$N process. The proton is emitted from the $1p_{1/2}$ level. The left panels are obtained in perpendicular kinematics while the other ones correspond to parallel kinematics. The labels $S3$ and $V8$ refer to the two different inputs as discussed in the text. The dashed doubly dotted, dashed dotted, dashed, dotted and solid lines represent summation of multipoles up to $J = 5$, $J = 10$, $J = 12$, $J = 15$ and $J = 20$, respectively.

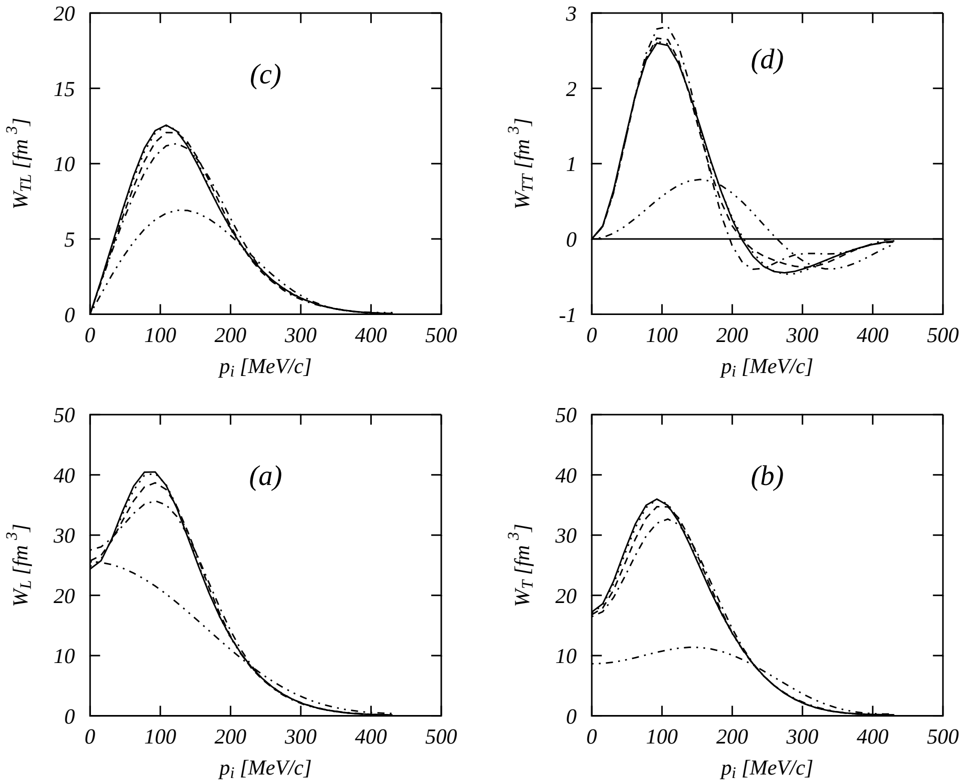

Figure 4.7: The $S3$ mean field responses in perpendicular kinematics. The Kinematical conditions and the meaning of the lines are the same of Fig. 4.6.

kinematics, the W_{TL} responses is added for positive values of p_i and subtracted for the negative ones, and this generates the asymmetry in the perpendicular cross sections of Fig. 4.6.

4.5.1 General Features of the Results of SRC Model

In this section we discuss the general features of the results of our SRC model. In Fig. 4.8 we present the cross sections for the kinematics described above as a function of p_i. In Fig. 4.8, the left panels show the perpendicular kinematics results while the right ones correspond to the parallel kinematics. The solid lines are obtained considering the complete *SRC* model. Since the main novelty of our calculations is the presence of the three-point diagrams, we shall discuss with some detail their role. For this reason we show with dashed lines the results obtained by adding to the mean field only those terms coming from the two-point diagrams. The dotted lines, that are almost exactly overlapped to the solid ones, show the mean field results.

The first remark we can make is that the effect of the correlations is very small, as we found in the inclusive case of low-lying nuclear excited states in Chapter 3 and as it has been found in the work of Co' and Lallena [Co'01] for the inclusive quasielastic reactions. As we already found in Sec. 3.3.2 and pointed out in literature [Co'95, Ari97, Co'01], the three-point diagrams reduce the effect produced by the two-point diagrams whatever it is. This is the consequence of the requirement of the conservation of the number of particles.

In order to emphasize the effect of the correlations we present in Fig. 4.9 the same results in terms of difference between the correlated cross sections and the uncorrelated ones. In order to have a relative measure of the effect we divide these differences by the maximum values of the uncorrelated cross sections. Henceforth we shall call these results normalized differences.

The effect of the two-point diagrams is rather different for the $S3$ and $V8$ calculations. In the former case is positive, the mean field cross

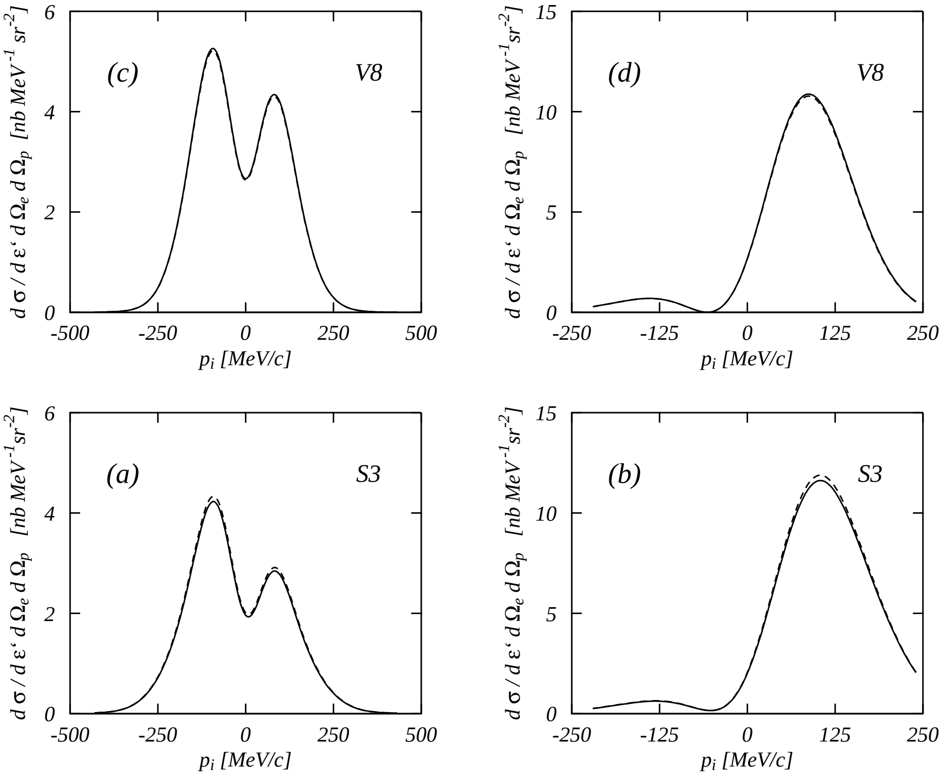

Figure 4.8: Cross sections as a function of the proton initial momentum for the ^{16}O$(e, e'p)^{15}$N process. The proton is emitted from the $1p_{1/2}$ level. The left panels are obtained in perpendicular kinematics while the other ones correspond to parallel kinematics. The labels $S3$ and $V8$ refer to the two different inputs as discussed in the text. The solid lines represent the results obtained with our complete SRC model, while the dashed ones are obtained leaving out the three-point diagrams of Fig. 2.2. The dotted lines, almost exactly overlapped to the solid ones, are the mean field results.

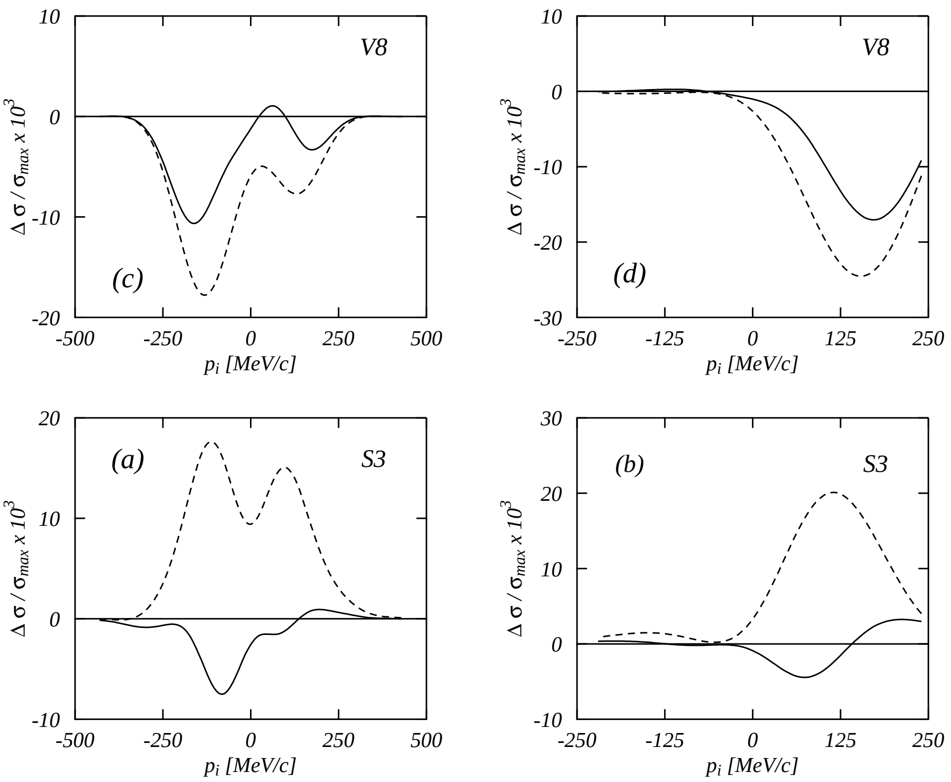

Figure 4.9: Normalized differences between the correlated and uncorrelated cross sections of Fig. 4.8. These are the differences between the cross sections divided by the maximum values of the uncorrelated cross sections. The dashed lines represent the two-point diagrams results while the solid lines those obtained with the full calculations. The left panels show the perpendicular kinematics results and the right panels the parallel ones.

section is increased by the correlations, while it is negative in the latter case. It is interesting to notice that the final result is rather similar in both cases as one would expect given the strong similarity of the two correlation functions used.

The effect of the correlations on the individual responses calculated in perpendicular kinematics is shown in Fig. 4.10. We should first notice that the charge response W_L and the transverse response W_T are much larger than the interference responses W_{TL} and W_{TT} as one can see in Fig. 4.7. In the charge response W_L the various terms of the correlations behave like the full cross sections, the final results being a lowering of the mean field response. This is not the case for the W_T response, showing an increase of the mean field results. This effect has been discussed in detail in work of Co' and Lallena [Co'01] where it has been shown that it is related to the absence of the diagram (2.3) of Fig. 2.2 in the longitudinal response.

In what refers to the interference responses, the behaviour of W_{TL} is similar to that of W_L. In W_{TT} the correlations increases the mean field responses. In this last response the three-point diagrams appear to be very sensitive to the input, their contribution is negligible for $V8$ calculation and noticeable for the $S3$ ones.

In order to study the dependence of the correlation on the momentum transfer, we calculate the $(e, e'p)$ cross sections in perpendicular kinematics for different values of $|\mathbf{q}|$. In all the calculations we fix the momentum of the emitted proton such as $|\mathbf{p}| = |\mathbf{q}|$. Results obtained for four different values of $|\mathbf{q}|$ are shown in Fig. 4.11 as normalized difference. Like in the

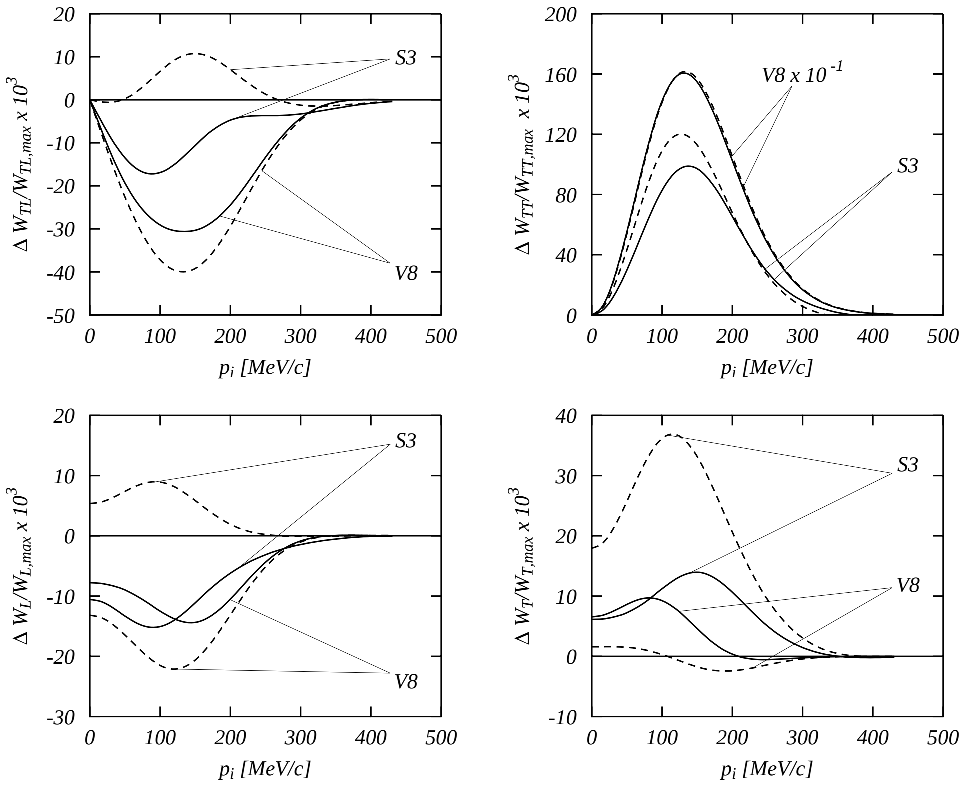

Figure 4.10: Normalized differences between correlated and uncorrelated response functions in the perpendicular kinematics for the calculations of Fig. 4.8. The differences are divided by the maximum value of the uncorrelated responses. The solid lines represent the results of the complete calculations of our *SRC* model and the dashed ones those obtained using the two-point diagrams only.

previous figures the dashed lines show the results obtained by adding to the mean field calculation the two-point diagrams only, while the solid lines show the results of the full calculation where also the three-point diagrams are added. The shape of the lines is slightly modified at different values of $|\mathbf{q}|$, but the order of magnitude of the effect is almost the same. It is interesting to notice that the cancellation of the two-point diagrams effects produced by the inclusion of the three-point terms generates results rather independent from the correlation function.

The possible changes of the correlation effects depending upon the hole wave function have been studied. As example we show in Figs. 4.12 and 4.13 the cross sections, and the normalized differences, obtained for the emission of the $1p_{3/2}$ and $1s_{1/2}$ protons under the same perpendicular kinematics of Fig. 4.8. While for the $1p_{3/2}$ case the shapes of the cross sections are noticeably similar to those previously shown of $1p_{1/2}$, the curves obtained for the $1s_{1/2}$ proton are rather different. The small differences in the radial shapes of the two p hole wave functions do not modify sensitively the behaviour of the cross section. On the other hand, the big difference in the s wave cross section is due to the different radial shape of the hole wave function. In spite of this the behaviour of the correlation effects is analogous in all the cases we consider. The calculations done with two-point diagrams show noticeable sensitivity to the change of the correlation, while, when the three-point diagrams are added all the results are similar and almost independent from the correlation function.

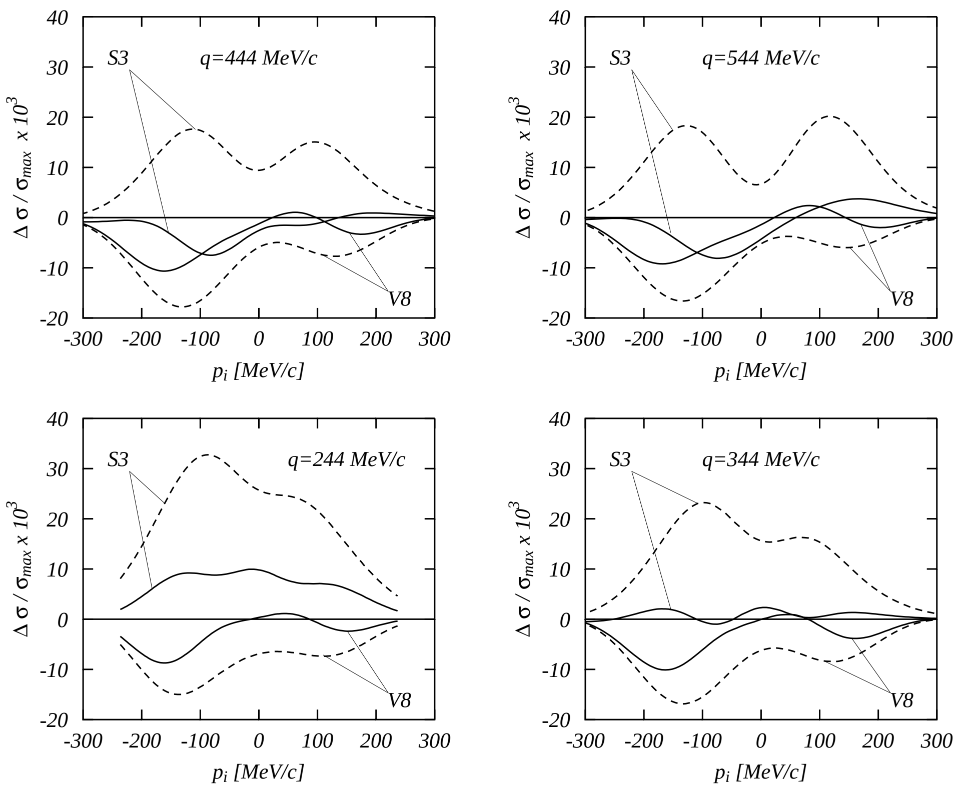

Figure 4.11: Normalized differences between correlated and uncorrelated cross sections calculated in perpendicular kinematics for different values of the momentum transfer $q \equiv |\mathbf{q}|$. Like in the previous figures the dashed lines refer to the two-point diagrams calculations while the solid lines show the results of the full calculation.

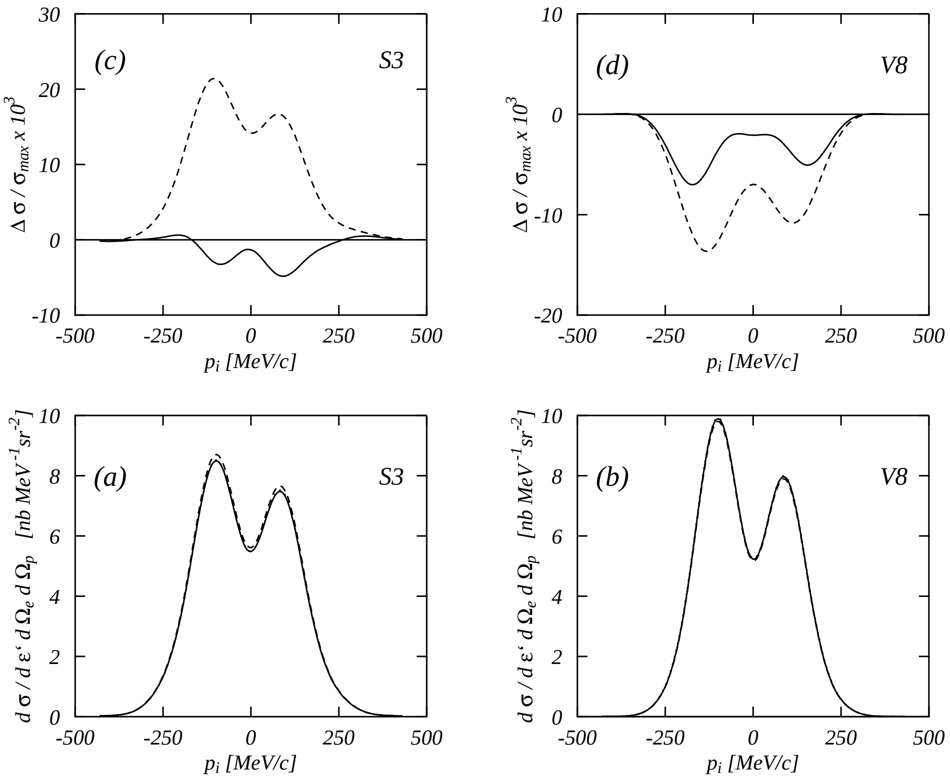

Figure 4.12: Cross sections for the emission of the $1p_{3/2}$ proton in perpendicular kinematics for the $S3$ and $V8$ input parameters. The dotted lines show the uncorrelated result, the dashed lines the results obtained adding the two-point diagrams and the solid lines the result of the complete calculation. In the panels (a) and (b) we show the cross sections while in the panels (c) and (d) the normalized differences between correlated and uncorrelated cross sections.

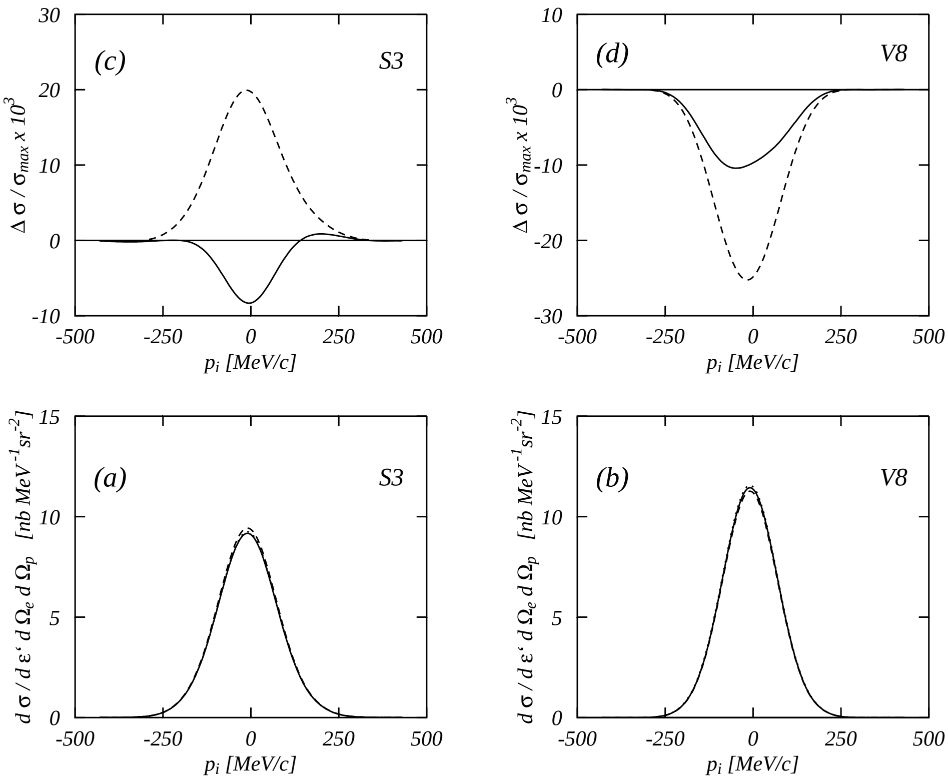

Figure 4.13: The same as the previous figure for the emission of the $1s_{1/2}$ proton.

4.5.2 Orthogonality and Consistency of the Input

In the analysis of the $(e, e'p)$ experiments it is a common practice to solve the single particle Schrödinger equation using a real mean field potential to describe the hole wave function while the particle wave function is described by solving the Schrödinger equation using a complex optical potential. The parameters of this potential are fixed to fit the proton elastic scattering from the rest nucleus. This procedure, adopted to take into account the *FSI* of the emitted proton with the rest nucleus, produces a non orthogonality between particle and hole single-particle wave functions. The effects of this procedure on the $(e, e'p)$ cross section have been thoroughly studied in Ref. [Bof82] where it has been shown that they are negligible for the typical kinematics used in the experiments.

We investigate the non orthogonality effects when correlations are included in the calculations. In our derivation of the transition matrix elements the orthogonality of the single-particle wave functions is essential. On the other hand, since we use central potentials, only the radial parts of the wave functions change, therefore all the angular momentum algebra is still valid. This means that the non orthogonality is present only between single-particle wave functions having the same angular momentum but different number of nodes in the radial part.

We have done two calculations where the particle wave functions are evaluated with a different mean field with respect to the hole wave functions. In the first one the particle mean field was set to zero; therefore the emitted particle wave function was described as plane wave. This kind of calculation is commonly referred as $PWIA$. In the second type of calculation we use the optical potential of Schwandt *et al.* [Sch82] with the parameterization adapted for ^{16}O as what was done by Leuschner *et al.* [Leu94].

We show in Fig. 4.14 the cross sections calculated with the $S3$ and $V8$ inputs for the same perpendicular kinematics conditions used in Fig. 4.8. The panels (a) and (b) show the $PWIA$ results, while the other two panels those obtained with the optical potential of Schwandt *et al.* [Sch82]. A comparison with the results of Fig. 4.8 show that the $PWIA$ cross sections are slightly larger than the original ones, while the cross sections obtained with the optical potential are smaller. It is interesting to notice that the $PWIA$ results have a minimum for $p_i = 0$ which is exactly zero, as expected, because in this approximation the cross section is related to the Fourier transform of the hole wave function.

In both kinds of calculations the effect of the correlations is very small and to emphasize it we show in Fig. 4.15 the normalized differences. The behaviour of the various terms is similar to that shown in Fig. 4.9. The results obtained with the two-point terms are rather different when calculated with $S3$ and $V8$ inputs. When also the three-point diagrams are included they become similar. Clearly the effects of the non orthogonality of the basis are negligible on the correlations. We obtain similar results also in parallel kinematics.

A comparison between the three calculations done in perpendicular kinematics show that the shapes of the results obtained in $PWIA$ and with the optical potential are rather similar and quite different from the

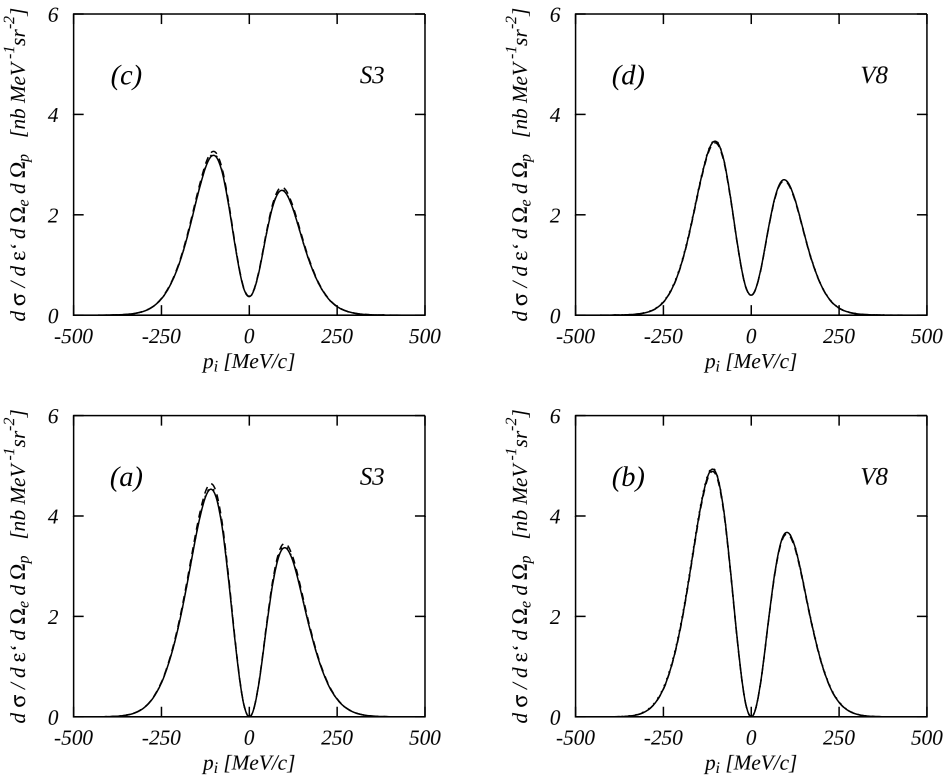

Figure 4.14: Cross sections calculated in perpendicular kinematics under the same conditions of Fig. 4.8 with different mean field potentials for the particle wave functions. In panel (a) and (b) the results obtained in Plane Wave Impulse Approximations are presented. In the panels (c) and (d) those obtained the optical potential of Schwandt *et al.* [Sch82]. The meaning of the line is the same as in Fig. 4.8.

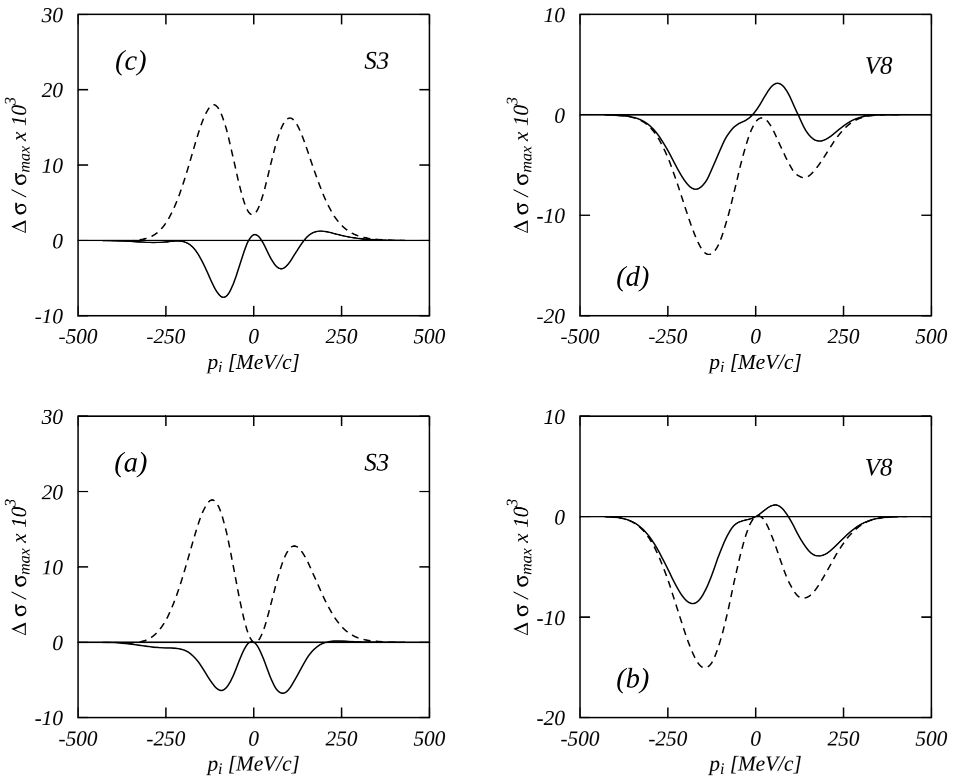

Figure 4.15: Normalized differences between the cross sections presented in Fig. 4.14. The meaning of the lines is the same as in Fig. 4.9.

results obtained with the same real potential used for the hole states. This arises because the real part of the Scwhandt potential is quite weak, -28.359 MeV, against the about -50 MeV of the potential used in our $V8$ and $S3$ calculations. The effect of the optical potential is to conserve the $PWIA$ shapes but to lower the values of the cross section. This second effect is obtained because of the presence of the imaginary part of the potential.

We have already stressed that our inputs are taken from microscopic $FHNC$ calculations where, for a given hamiltonian, the energy mean value has been minimized by varying both mean field and correlation function. This consistency of the input is not usually respected in $(e, e'p)$ calculations with short-range correlations, where mean field and correlation functions are taken form different sources.

We tested the need of relating mean field and correlation functions by interchanging them in our inputs. This means that we make calculations using the $S3$ mean field potential together with the $V8$ correlation functions, and vice versa. The results of these calculations are shown in Fig. 4.16 as normalized differences and are compared in each panel with the results of Fig. 4.9. Also in this figure the need of including three-point diagrams for the reasons already mentioned becomes evident. The final results seems to be rather independent from the mean field used. On the other hand, the quantity shown is defined to minimize the effects of the mean field and enhance those of the correlations.

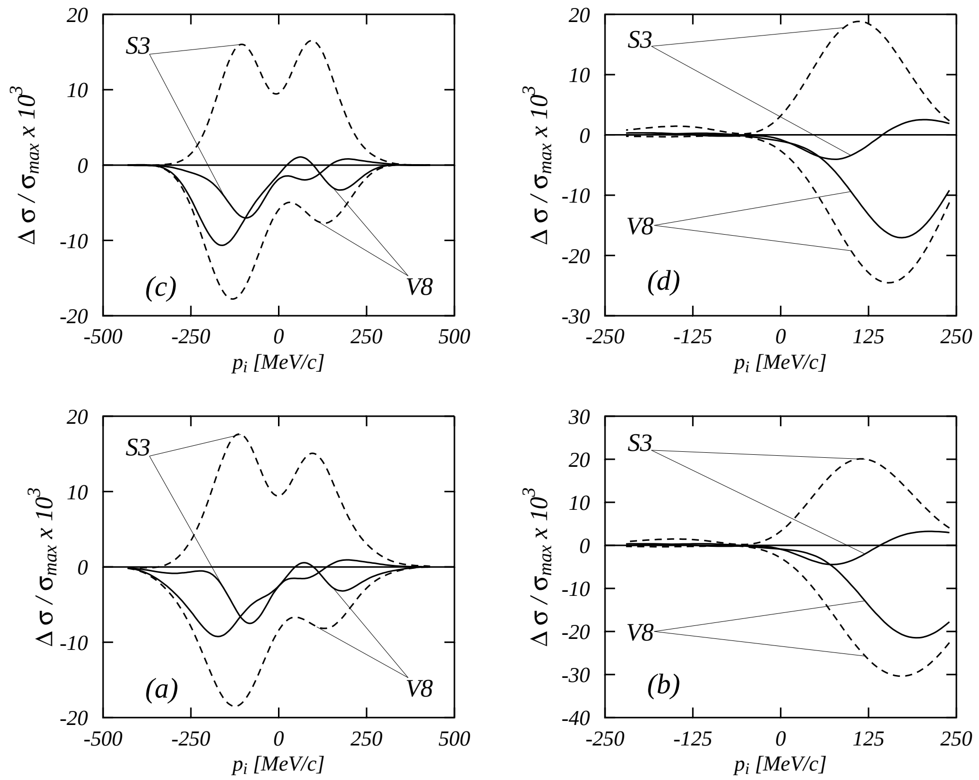

Figure 4.16: Normalized differences between cross sections calculated with the same mean field potential but with different correlation functions. In the panels (a) and (b) the $S3$ mean field is used, while in the panels (c) and (d) the $V8$ mean field was considered. The $S3$ and $V8$ labels indicate the correlation function used. The calculations of the (a) and (c) panels are done in perpendicular kinematics and those of the (b) and (d) panels in parallel kinematics. As usual the dashed lines refer to calculations with two-point diagrams while the solid lines represent the complete calculations.

4.5.3 Comparison With Other Approaches

In this section we shall try to make a comparison between our *SRC* approach model and other models that handle short-range correlations in electron scattering. Depending upon the methodology used to attack the problem we classify these models into two categories. A first kind of calculations [Jan00, Ryc00] uses an approach similar to our but the evaluation of the diagrams remains restricted to the so-called single pair approximation. This approximation implies that only those two-point diagrams where the knocked out particle is directly connected to the electromagnetic operators are considered. In our classification scheme these are the diagrams (2.1) and (2.2) of Fig. 2.2, even though the exchange diagram (2.2) is not always considered.

The second category of calculations [Ami97, Pol97, Gai00] is based upon the idea of the spectral function [Fru84, Bof96]. The basic hypothesis is that the nuclear finite state wave function can be separated in terms of emitted particle wave function and spectral function which is related to the overlap between the wave function of the target nucleus and that of the A-1 nucleons system. Spectral functions used in the evaluation of $(e, e'p)$, and also $(e, e'2N)$, cross sections have been calculated in various manners. In some case the Brueckner G-matrix theory has been used [Ami97], in others they have been obtained from a variational Monte Carlo calculations [Lap99]. In the work of Gaidarov *et al.* [Gai00] the spectral functions have been obtained using the asymptotic properties of the one-body density matrices obtained from microscopic theories. A precise comparison with our approach is rather difficult since the spectral functions include high order correlation terms which we do not consider. It remains however the fact that also this approach consider only those diagrams where the emitted particle is directly connected to the electromagnetic operators. In our approach this could be translated by saying that in addition to the diagrams (2.1) and (2.2), already mentioned, also the diagrams (3.3) and (3.4) are considered.

In order to mimic the other approaches, we repeat the calculations of Fig. 4.8 without those diagrams where the particle is not directly connected to the electromagnetic operators. In these calculations the 1/2 and 1/3 terms multiplying the two- and three-point diagrams respectively are set to 1, as it is done in the literature. The results of these calculations are presented in Fig. 4.17 as normalized differences. The solid lines show the results of the complete calculations, those of Fig. 4.8. The dotted lines are obtained by using the diagram (2.1) only, the dashed dotted lines are obtained by adding also the diagram (2.2) and the dashed lines by adding the diagrams (3.3) and (3.4).

It is clear from the figure that the inclusion of the diagrams (3.3) and (3.4) changes radically the effect of the correlations, modifying shapes and signs. The final result in the case of $S3$ is rather similar to that of the complete calculation, but for the $V8$ input there is a noticeable difference. This instability of these results shows, in a clear manner, the need of including all the terms of the expansion.

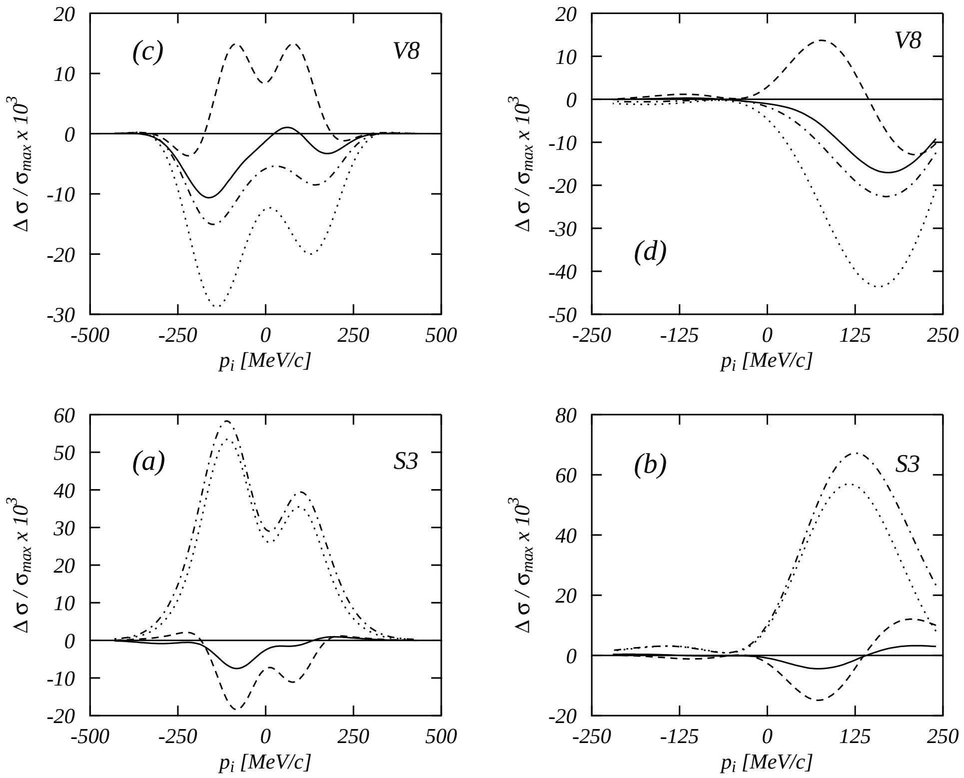

Figure 4.17: Normalized differences between correlated and uncorrelated cross sections. The solid lines represents the complete calculations, the dotted lines are evaluated by adding to the mean field the contribution of the diagram (2.1) of Fig. 2.2, the dashed dotted lines, the contribution of the diagrams (2.1) and (2.2) and the dashed lines, the diagrams (2.1), (2.2), (3.4) and (3.5).

4.5.4 Comparison With Experimental Data

In this section we compare the results of our calculations with some quasielastic $(e,e'p)$ experimental data available on ^{16}O target. In the literature these data are presented in terms of reduced cross section that is obtained from Eq. (4.24) where the cross section is divided by the electron-proton cross section σ_{ep} and by the kinematic factor K of Eq. (4.3). In our calculations, we used the σ_{ep}^{cc1} which is the prescription of de Forest [For83] for the σ_{ep}.

In Fig. 4.18 we make the comparison with the $1p_{1/2}$ proton emission data of Bernheim *et al.* [Ber82] measured in perpendicular kinematics. The solid lines represent the complete calculations of Fig. 4.8, where all the diagrams are considered and the same mean field potential for both particles and hole is used. In the panels (a) and (b) the results for the $S3$ and $V8$ inputs are shown respectively. In the panels (c) and (d) the same curves are multiplied by a reduction factors to improve the agreement with the experimental data. These factors are 0.5 for the $S3$ result and 0.4 for the $V8$ one. Even after quenching the curves the agreement with the data is rather poor.

The dashed lines of the figure are obtained by changing the particle mean field with the optical potential of Schwandt *et al.* [Sch82], in the parameterization of Leuschner *et al.* [Leu94]. Also in this case a quenching of the curves is necessary, and the final results, shown in the two upper panels, are obtained multiplying by 0.68 and 0.6 the $S3$ and $V8$ results respectively. The dashed curves show a better agreement with the

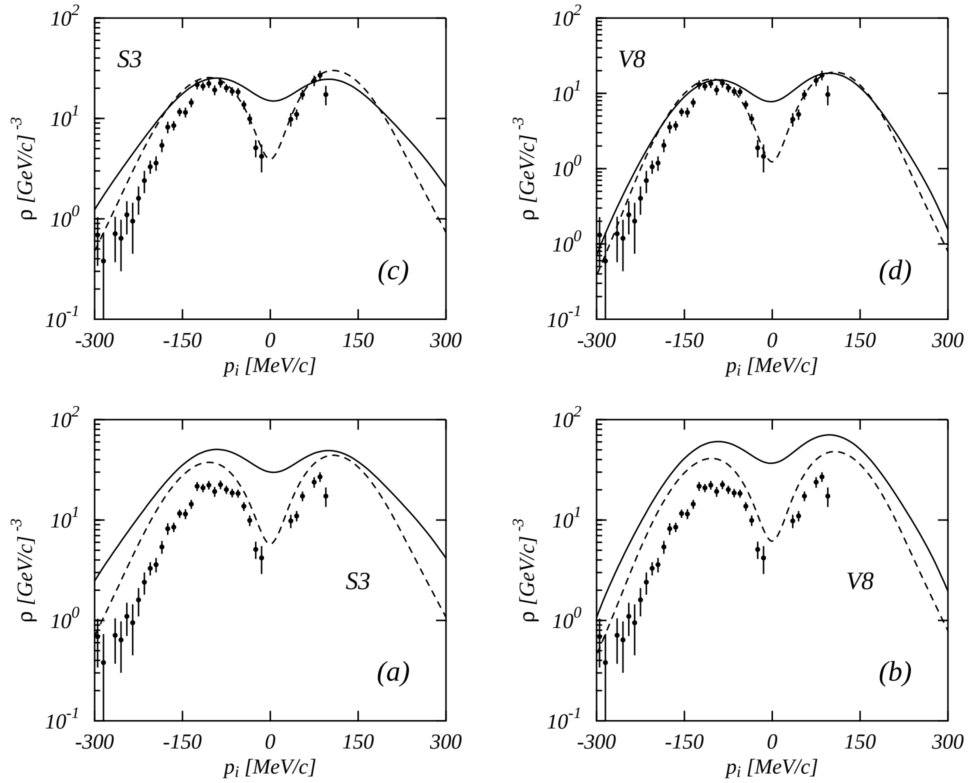

Figure 4.18: Reduced cross section compared with the experimental data of Saclay [Ber82]. The solid lines are obtained from the complete calculations of Fig. 4.8 in perpendicular kinematics. The dashed lines are calculated with the optical potential of Schwandt *et al.* [Sch82]. In the panels (c) and (d) the curves of the lower panels are multiplied by reduction factors to reproduce the data (see text).

experimental data.

An analogous situation is found in Fig. 4.19 where the comparison is done with the data of Leuschner *et al.* [Leu94], again for the emission of the $1p_{1/2}$ proton but measured in parallel kinematics. The meaning of the curves is the same of the previous figure, and in this case we used for all the curves the same quenching factor of 0.8.

The results presented in Fig. 4.18 and 4.19 clearly show that the fully consistent calculations are unable to reproduce the data. Not only in terms of magnitude, but the obtained results are qualitative different with respect to the data distribution. The mean fields fixed by the minimization process in the work of Arias *et al.* [Ari96] and Fabrocini *et al.* [Fab00] are too strong to describe properly the motion of the emitted particle in the continuum as we are already observed. The shift of the minimum of the reduced response with respect to $p_i = 0$ in parallel kinematics is an effect produced by the distortion potential.

In Figs. 4.20 and 4.21, we compare the results of our calculations with the experimental values of the electromagnetic responses given in the work of Spaltro *et al.* [Spa93]. The responses of their work have been measured in perpendicular kinematics at ω = 100 MeV, and $\mathbf{q}$ = 460 MeV/c. Our calculations have been done with the Scwhandt *et al.* optical potential [Sch82] and using the $S3$ input for Fig. 4.20 and $V8$ one for Fig. 4.21. The meaning of the various lines is that of Fig. 4.8: dotted lines mean field results, dashed lines obtained with the inclusion of the two-points diagrams, solid lines the complete calculations. All the lines are multiplied by a reduction factor of 0.7. The effect of the short range

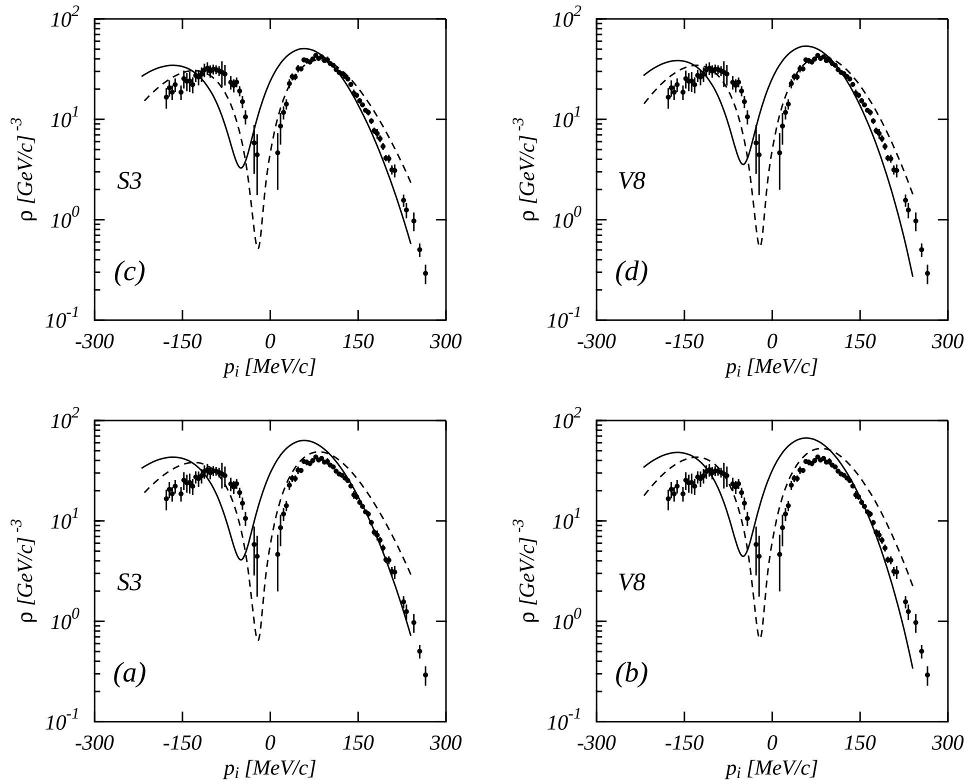

Figure 4.19: Reduced cross sections compared with the experimental data of Nikhef [Leu94]. The solid lines are obtained from the complete calculations of Fig 4.8 in parallel kinematics. The dashed lines are calculated with the optical potential of Schwandt *et al.* [Sch82]. In the panels (c) and (d) the curves of the lower panels are multiplied by a common reduction factors of 0.8 .

correlations is very small. One can clearly identify the increase of the responses, in case of $S3$, produced by the inclusion of only the two-point diagrams, but the final results is essentially back to mean field result. The calculation done with the $V8$ input produce analogous results, with the obvious difference in the two-point calculations. The same data have been studied by Amaro *et al.* [Ama99b] where it has been shown that the effects of the Meson Exchange Current are larger than those we find for the short-range correlations.

4.6 Conclusions

In this chapter we have studied the effects of short-range correlations on the one-nucleon emission processes induced by electromagnetic probes. We have applied our SRC to the $^{16}\mathrm{O}(e,e'p)^{15}\mathrm{N}$ reaction for the perpendicular and parallel kinematics of the Saclay [Ber82] and NIKHEF [Leu94] experiments.

In the kinematic conditions investigated, the effects of the short-range correlations are extremely small as compared to the mean field results. They are within the accuracy of the experimental data and the uncertainty on the theoretical inputs.

The two correlation functions used in our calculations are rather similar, therefore we expect them to produce similar effects on the mean field results. This does not happens if only two-point diagrams are included. The $S3$ increases the mean field responses, and cross sections, while the $V8$ lowers their values. The effects of the correlations become similar

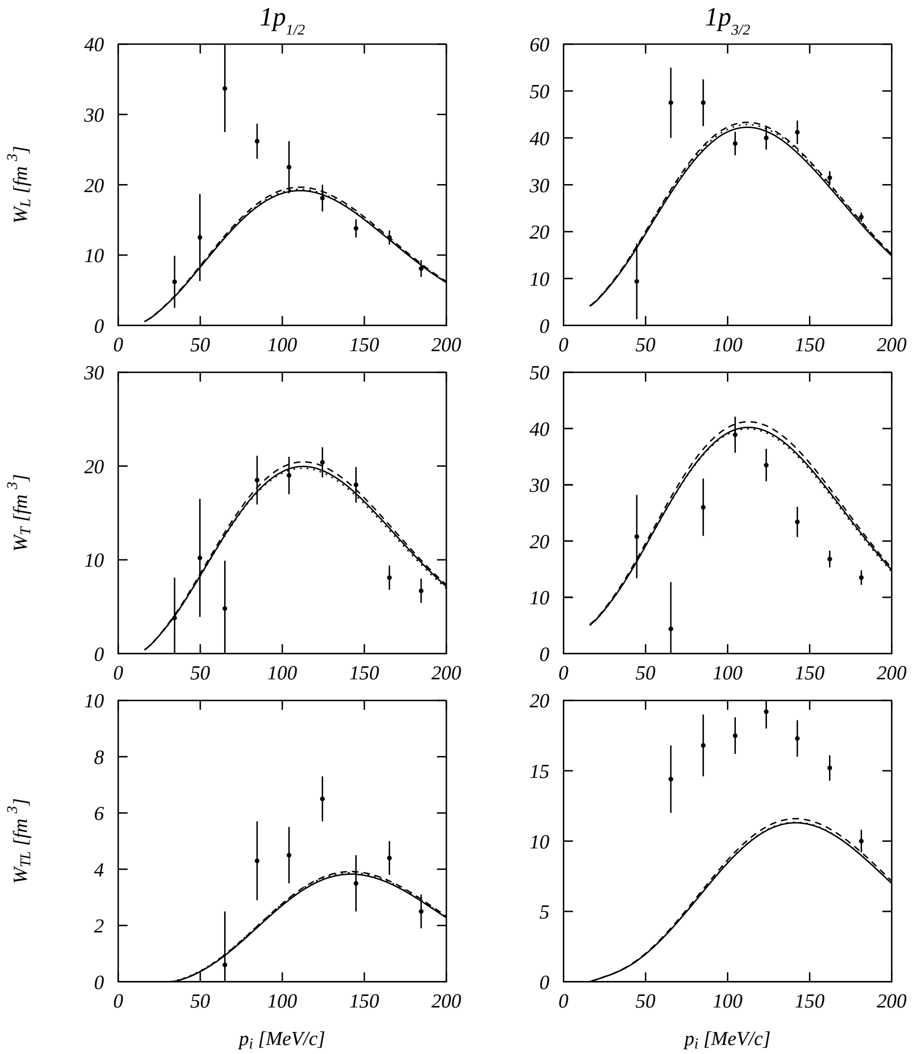

Figure 4.20: Response functions compared with the experimental data of Spaltro *et al.* [Spa93]. Our calculations are done with the $S3$ input and using the optical potential of Scwhandt *et al.* [Sch82]. The solid lines show the results of the complete calculations, the dashed ones those obtained with the two-point diagrams, and the dotted lines (overlapped to the solid ones), the mean filed results. The panel labelled W_L shows actually $W_L + \frac{1}{2}\frac{\mathbf{q}^2}{\mathbf{q}^2-\omega^2}W_{TT}$. The contribution of W_{TT} is in any case small. The response W_{TL} is multiplied by $1/\sqrt{2}$ in order to agree with the response experimentally separated. All the curves are multiplied by a 0.7 factor.

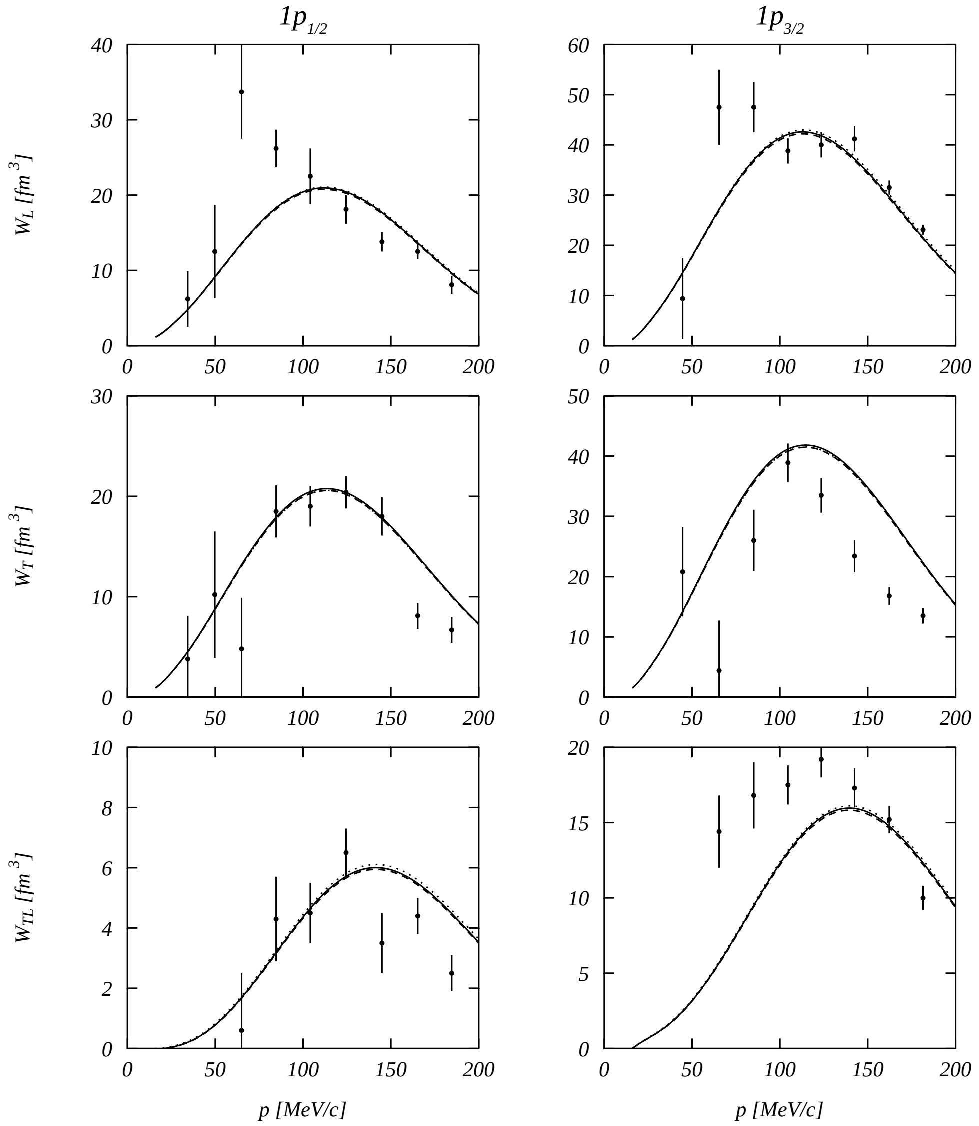

Figure 4.21: The same as Fig. 4.20 but for $V8$ input. All the curves are multiplied by a 0.4 factor.

when the three-point diagrams are included. The detailed study of the separated responses shows that the three-point diagrams reduce the effect produced by the two-point diagrams alone, whatever they are. This fact is a consequence of the need of the three-point diagrams to ensure the proper normalization of the wave function. This results is almost independent from the momentum transfer or from the hole wave function.

We have been concerned about the consistency of the input, and we have calculated cross sections with different mean fields describing the emitted particle, and we have also interchanged correlation functions and mean field in our inputs. We did not find significant changes on the effects of the correlations saying that these effects are rather independent from the chosen mean field.

We have tried to compare our short-range correlation model with other approaches one finds in the literature. In these approaches only those diagrams where the emitted particle is directly connected to the one-body electromagnetic operator are considered. We have done calculations where only these diagrams have been considered, and we found a strong dependence of the results on the number of diagrams included, showing big instabilities to small changes of the input. The situation is rather complicated by the fact that in these approaches the particle wave function is usually described as moving in a optical potential. Therefore it is not clear whether the diagrams we have explicitly calculated are effectively considered by the optical potential.

The comparison with the experimental data [Ber82, Leu94, Spa93], shows that the short-range correlation effects do not significantly improve the agreement with the data. The spectroscopic factor is still needed to reproduce the data.

Chapter 5

SRC and MEC in Photonucleon Emission

Overview

In this chapter the one-nucleon knock-out processes induced by real photon are studied by considering short-range correlation effects. Since, the exclusive (γ, N) reaction is also induced by the *EM* interaction, it is of interest to compare its results with exclusive quasielastic $(e, e'N)$ reaction. In the photon case, $\omega = |\mathbf{q}|$ and the mismatch between the momentum transfer and the momentum of the knocked-out nucleon is quit large. Thus, if the reaction proceeds through Direct Knock-Out (*DKO*) process where the photon interacts with a single nucleon, one probes the high momentum tail of the single-particle wave function of the initially bound nucleon before being emitted. Thus, photon-induced nucleon emission appears of particular interest for our purpose, since the cross section is expected to be very sensitive to effects of the *SRC*.

5.1 The Quasifree (γ, N) Scattering Process

5.1.1 Theoretical Framework

Our model is based in the framework of *DKO* model where the virtual or real photon couples to a single (quasifree) nucleon in the nucleus which is subsequently emitted. In the *DKO* model, the virtual or real photon interacts with the nucleon through One-Body (*OB*) operators and the *OB* currents is calculated in the *IA*. Our model is developed with the aim to improve the mean field *IPM* picture by including the *SRC* effects. The presence in the nucleus of collective phenomena is not considered in our model. For this reason, the range of applicability of our model is limited to those kinematic situations where the effects of the collective excitations can be neglected.

In the previous chapter, the model was applied to $(e, e'p)$ reaction in the quasielastic region where the *DKO* model works remarkably well [Fru84, Ama98, Co'98, Co'01]. It has been verified [Co'88] that in this region collective excitations described in terms of continuum *RPA* are negligible. The effect of these excitations becomes smaller with increasing the value of the momentum transferred to the nucleus. As we found in Chapter 4, the major effect modifying the *IPM* responses is that of the *FSI* between the emitted nucleon and the rest nucleus. These *FSI* effects can be accounted for by using an optical potential.

Our model has been applied in Chapter 3 to study the excitation of low-lying states. Also in this case we excluded collective excitations and we studied data at the momentum transfer above 300 MeV/c, quite far from the $\omega = |\mathbf{q}|$ condition of the photon point.

The electron scattering kinematics ensuring the dominance of the single-particle excitations are not achievable with real photons. At low photon energy, around the giant dipole resonance, the collective excitations of the nucleus are expected to be dominant and they should be progressively diminish in importance with increasing photon energy. The photon excitation of doubly closed shell nuclei has been widely studied with self-consistent continuum *RPA* with Skyrme interactions, first by the Bologna group [Cav82, Cav84, Sar93] and later by the Gent group [Ryc87a, Ryc87b, Ryc88]. Furthermore, in the literature it is well known that continuum *RPA* calculations successfully describe photon reactions even at energies above the giant resonance region [Gia85]. Thus it is necessary to study the importance of the collective excitation modes in photonuclear reactions.

In the recent work of our group [Ang02], the applicability of the *DKO* model has been tested by using the Fourier Bessel continuum *RPA* theory [Har82] with two types of effective forces: a zero-range Landau-Migdal interaction and the finite range polarization potential [Pin88]. It has been concluded for the photoproton reaction at photon energies above the giant dipole resonance that the effects of *RPA* are negligible and the *RPA* cross section is essentially that of the mean field *IPM* with *OB* currents.

The above conclusion seems consistent with the findings of many authors [Fin77, Bof81] where it has been concluded in their work that the *DKO* model, with *OB* currents and rescattering *FSI* process with the rest nucleus, is the dominant mechanism describing (γ, p) reaction for photon energies above the giant resonance and below pion photoproduction, i.e. for energy range between 60-100 MeV. The apparent success of the *OB* picture in explaining the (γ, p) reaction above the giant resonance is questionable when it comes to reproduce the (γ, p) data at photon energies higher than around 100 MeV and at backward angles, where the momentum mismatch is very large. At these energies and angles, we are probing the high momentum components in the single-particle wave function where the corrections due to the correlations between nucleons is expected to be in its maximum strength and beyond the pictures of mean field *IPM* and *OB*. Also, at these higher energies we are close from the threshold of pion photoproduction where Two-Body (*TB*) process such as those involving *MEC* are expected to be important or even dominant. Even in the energy range 60-100 MeV, the *OB* picture fails to reproduce the (γ, n) reactions while models that involving *MEC* are able to reproduce the data [Cav84, Ryc88]. Some authors [Ire94, Mil95, Mor95] claim that even for (γ, p) reaction in the photon energy range 60-100 MeV, the contribution of *MEC* must be the main mechanism responsible for the observed cross section.

From what we have summarized above, it is necessary before investigating the effects of *SRC* to include other effects arising from the multi-hadron currents related to the *MEC*. Therefore in this chapter the cross section of the exclusive (γ, p) reaction is calculated by considering that the photoabsorption occurs through both *OB* and *TB* currents.

5.1.2 The (γ, N) Cross Section in the PWBA

In this section we briefly recall the expressions used to evaluate the cross section for the nucleon emission induced by the absorption of a real photon. Detailed derivations of these expressions can be found in review articles and books [Gia85, Bof96]. The treatment presented in Secs. 4.1.2 and 4.2 can be applied also to exclusive (γ, N) reaction.

In contrast to the case of virtual photon where the pure longitudinal and transverse responses plus the two interference responses occur, for real photon there is only the pure transverse response. Thus the basic quantity to calculate is the transverse transition amplitude given by Eq. (4.7) where only the transverse components of the current $J_{\pm}$ of Eq. (2.22) appear. In case of photonuclear reactions the energy and the modulus of the momentum transferred, $q \equiv |\mathbf{q}|$, are equal, i.e. $\omega = q$. This is not the case in processes involving electron scattering where one has: $\epsilon - \epsilon' \leq q \leq \epsilon + \epsilon'$.

The nuclear initial state is characterized by the total angular momentum and parity of the system. Since we restrict our calculations to doubly closed shell nuclei we immediately consider that the nuclear ground state has zero angular momentum and positive parity $|\Psi_0\rangle \equiv |J_0 M_0, \Pi_0\rangle = |00, +1\rangle$. In processes where the emitted nucleon is detected, the nuclear final state can be described by Eq. (4.12). Following the treatment given in Sec. 4.2 we express the transverse response W_T as:

$$
\begin{aligned}
W_T \;=\; & \frac{32\pi^3}{|\mathbf{p}|^2} \sum_{\sigma m_h} \sum_{J\Pi l_p j_p} \sum_{J'\Pi' l'_p j'_p} \sum_{\eta\pm1} (-i)^{l_p - l'_p - J + J'} \\
& \langle l_p \mu_p \frac{1}{2}\sigma | j_p m_p \rangle \langle j_p m_p j_h m_h | J - \eta \rangle \langle l'_p \mu_p \frac{1}{2}\sigma | j'_p m'_p \rangle \langle j'_p m_p j_h m_h | J' - \eta \rangle \\
& \left[\frac{(l_p + m_h + \eta + \sigma)!}{(l_p - m_h - \eta - \sigma)!} \frac{(l'_p + m_h + \eta + \sigma)!}{(l'_p - m_h - \eta - \sigma)!} \right]^{\frac{1}{2}} \left[\frac{2l_p + 1}{4\pi} \right]^{\frac{1}{2}} \left[\frac{2l'_p + 1}{4\pi} \right]^{\frac{1}{2}} \\
& P^{\mu_p}_{l_p}(\cos\theta_p)\; P^{\mu_p}_{l'_p}(\cos\theta_p)\; \xi^{1}_{J,\Pi,\eta}(\mathbf{q}; p, h)\; \xi^{1\dagger}_{J',\Pi',\eta}(\mathbf{q}; p', h)\,. \qquad (5.1)
\end{aligned}
$$

With the above definitions the cross section describing the nucleon emission induced by the absorption of a real photon can be written as [Gia85]:

$$
\frac{d\sigma}{d\Omega_p} = \frac{2\pi^2 e^2}{\omega} \frac{K}{(2\pi)^3} W_T\,, \qquad (5.2)
$$

where the kinematic factor K is defined in Eq. (4.3).

In Eq. (5.1), $\xi^{1}_{J,\Pi,\eta}(\mathbf{q}; p, h)$ represents the reduced transition matrix element. In photonuclear reactions the transitions should be induced by current operator only $\mathbf{J}(\mathbf{r})$ where the charge operator does not contribute. Therefor as shown in Sec. 2.4, the multipole expanded generic operator $O_{J(\eta)}(\mathbf{q})$ is conveniently described by appropriate sum of the electromagnetic operators $T^{\mathrm{E}}_{JM}(q)$ and $T^{\mathrm{M}}_{JM}(q)$ generating respectively electric and magnetic excitations and is given by the second term of Eq. (2.36).

In our model, the *SRC* act only on the one-body current operators, i.e. by considering $\mathbf{J}(\mathbf{r}) = \mathbf{J}^{\mathrm{OB}}(\mathbf{r})$. The one-body currents are the sum of the convection $\mathbf{J}^{\mathrm{C}}(\mathbf{r})$ and magnetization $\mathbf{J}^{\mathrm{M}}(\mathbf{r})$ currents where both currents are defined by Eqs. (2.26) and (2.27), respectively. This procedure corresponds to the quasifree *DKO* considered in Sec. 2.4.1 and applied in Chapters 3 and 4.

According to our *SRC* model, the $\xi^1_{J,\Pi,\eta}(\mathbf{q};p,h)$ is defined as given in Eq. (4.17) as:

$$\begin{aligned}\xi^1_{J,\Pi,\eta}(\mathbf{q};p,h) \quad &= \quad \langle p||\, O_{J(\eta)}(\mathbf{q})\,||h\rangle \,+\, \sum_{i>1}^{A} \langle p,i||\, O_{J(\eta)}(\mathbf{q})\, h(r_{1i})\,||h,i\rangle \\ &\quad + \sum_{1<i<k}^{A} \langle p,i,k||\, O_{J(\eta)}(\mathbf{q})\, h(r_{ik})\,||h,i,k\rangle\,. \qquad (5.3)\end{aligned}$$

The various terms generated by the above expression are shown as Mayer-like diagrams in Fig. 2.2. The first term of Eq. (5.3) is the *IPM* contribution and it corresponds to the one-point diagram (1.1) of Fig. 2.2. The other two terms of the equation are represented by the two- and three-point diagrams. The presence of these last diagrams is necessary to have the correct normalization of the many-body wave function, as discussed in Chapter 2.

In our calculations we have also considered the *MEC* but only in the *IPM*, i.e. by neglecting the last two terms of Eq. (5.3). Thus we suppose that the electromagnetic current operator $\mathbf{J}(\mathbf{r})$ is composed by the sum of one-body current operator $\mathbf{J}^{\mathrm{OB}}(\mathbf{r})$ and two-body current operator $\mathbf{J}^{\mathrm{TB}}(\mathbf{r})$. Thus we have:

$$\mathbf{J}(\mathbf{r}) = \mathbf{J}^{\mathrm{OB}}(\mathbf{r}) + \mathbf{J}^{\mathrm{TB}}(\mathbf{r})\,. \qquad (5.4)$$

The two-body $\mathbf{J}^{\mathrm{TB}}(\mathbf{r})$ currents can be constructed in a non-relativistic approach to interacting nucleon-meson-Δ systems [Ris84]. To give the expressions of the *MEC* it is convenient to define the function $\mathcal{H}(\mathbf{r})$ as the

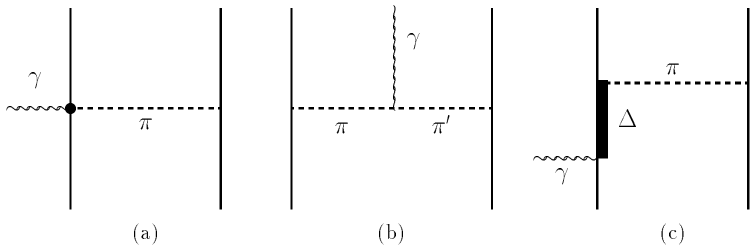

Figure 5.1: Feynman diagrams of the three MEC operators we consider: (a) seagull, (b) pionic and (c) Δ-isobar.

Fourier transform of the dynamical pion propagator [Ama93b, Ama94]:

$$\mathcal{H}(\mathbf{r}-\mathbf{r}_l) = \int \frac{\mathrm{d}^3k}{(2\pi)^3}\,\frac{F_{\pi\mathrm{N}}(k,\varepsilon)\,\mathrm{e}^{i\mathbf{k}\cdot(\mathbf{r}-\mathbf{r}_l)}}{k^2+m_\pi^2-\varepsilon^2}\,, \tag{5.5}$$

where we indicate with $F_{\pi\mathrm{N}}$ the pion–nucleon form factor and with $\varepsilon = (\Delta E)_l$ the energy of the exchanged pion, of mass m_π obtained as the difference between the energies of the final and initial single particle states of the l-th nucleon.

In our work we take into account only one-pion exchange, and then the two-body currents are the sum of three types of *MEC*: the seagull $\mathbf{J}^{\mathrm{S}}$, the pionic $\mathbf{J}^{\pi}$ and the virtual Δ excitation $\mathbf{J}^{\Delta}$. The three types of *MEC* are represented by the Feynman diagrams of Fig. 5.1. They are the seagull (a), the pionic (b) and the virtual Δ excitation (c). The expressions of the seagull, pionic and Δ-isobar currents in momentum space are given by [Ama93b, Ama94]:

$$\mathbf{J}^{\mathrm{S}}(\mathbf{q},\omega) \;=\; 4\pi\frac{f_\pi^2}{m_\pi^2}\,F_{\mathrm{S}}(q,\omega)\sum_{\substack{k,l=1\\k\neq l}}^{A}\left[\boldsymbol{\tau}_k\times\boldsymbol{\tau}_l\right]_3\mathrm{e}^{i\mathbf{q}\cdot\mathbf{r}_k}\boldsymbol{\sigma}_k\,\boldsymbol{\sigma}_l\cdot\nabla_k\mathcal{H}(\mathbf{r}_k-\mathbf{r}_l)\,, \tag{5.6}$$

$$
\begin{aligned}
\mathbf{J}^{\pi}(\mathbf{q},\omega) &= -4\pi\frac{f_\pi^2}{m_\pi^2}\,F_\pi(q,\omega)\sum_{\substack{k,l=1\\k\neq l}}^{A}[\boldsymbol{\sigma}_k\times\boldsymbol{\tau}_l]_3\int \mathrm{d}^3r\,\mathrm{e}^{i\mathbf{q}\cdot\mathbf{r}} \\
&\times\boldsymbol{\sigma}_k\cdot\nabla\mathcal{H}(\mathbf{r}-\mathbf{r}_k)\,\nabla\left[\boldsymbol{\sigma}_l\cdot\nabla\mathcal{H}(\mathbf{r}-\mathbf{r}_l)\right]\,, \qquad (5.7)
\end{aligned}
$$

and

$$
\begin{aligned}
\mathbf{J}^{\Delta}(\mathbf{q},\omega) &= -iC_\Delta F_\Delta(q,\omega)\sum_{\substack{k,l=1\\k\neq l}}^{A}\mathrm{e}^{i\mathbf{q}\cdot\mathbf{r}_k}\mathbf{q} \\
&\times\Big\{[\boldsymbol{\tau}_k\times\boldsymbol{\tau}_l]_3\;\boldsymbol{\sigma}_k\times\nabla_k\boldsymbol{\sigma}_l\cdot\nabla_k\mathcal{H}(\mathbf{r}_k-\mathbf{r}_l) \\
&\quad-\;4\tau_l^3\nabla_k\boldsymbol{\sigma}_l\cdot\nabla_k\mathcal{H}(\mathbf{r}_k-\mathbf{r}_l)\Big\}\,. \qquad (5.8)
\end{aligned}
$$

In the above equations $f_\pi = 0.079$ is the effective pion-nucleon coupling constant and

$$C_\Delta = 4\pi\frac{f_\pi^2}{m_\pi^2}\frac{4}{25M(M_\Delta - M)}\,, \qquad (5.9)$$

with M_Δ the Δ mass. We indicate with the symbols F_π, F_Δ the electromagnetic form factors of the pion and the of the Δ and with F_S the electric isovector nucleon form factor. To be consistent with the one-body currents we use the following expressions for F_S and F_π:

$$
\begin{aligned}
F_{\mathrm{S}} &= G_{\mathrm{E}}^{\mathrm{P}} - G_{\mathrm{E}}^{\mathrm{N}}, \qquad (5.10)\\
F_\pi &= F_{\pi\gamma} = \frac{1}{1+(q^2-\omega^2)/m_\rho^2}\,, \qquad (5.11)
\end{aligned}
$$

where m_ρ is the mass of the ρ-meson.

The situation is more complicated for the Δ current since the electromagnetic form factor F_Δ, and the constant C_Δ are model dependent.

The major uncertainty is related to C_Δ, but a discussion of this problem is beyond the aim of the present work. The expression (5.9) of C_Δ that we choose is widely used in the literature [Ris84]. For the form factor F_Δ, following the static quark model, we use:

$$F_\Delta = 2G_{\mathrm{M}}^{V} = G_{\mathrm{M}}^{\mathrm{P}} - G_{\mathrm{M}}^{\mathrm{N}}. \tag{5.12}$$

Finally, we would like to comment on the pion-nucleon form factor

$$F_{\pi\mathrm{N}}(k,\varepsilon) = \frac{\Lambda^2 - m_\pi^2}{\Lambda^2 + k^2 - \varepsilon^2} \tag{5.13}$$

included in the expression (5.5) of the pion propagator. It has verified [Ama93b] that, in the quasi-elastic peak region, for the values of Λ commonly accepted ($\sim$ 1 GeV), the results are very close to those obtained considering simply $F_{\pi\mathrm{N}} = 1$, which is the value we adopt. Details about the calculation of the reduced matrix elements between the single-particle states in case of the above two-body currents can be found elsewhere [Ama93b, Ama94].

5.2 Specific Applications

The nuclear model above presented is applied to describe photonuclear exclusive (γ, p) reaction from the ^{16}O nucleus, where the residual nucleus is left in its ground state (γ, p_0) or a low-lying excited state. We perform our calculations over wide range of photon energies from 60 MeV to 196 MeV. The motivations of the choice of the ^{16}O nucleus have already been outlined in Secs. 3.3 and 4.5. Our theoretical treatment for the *SRC* has been done for ^{16}O in case of inclusive quasielastic electron scattering [Co'01] and also our model has been applied for exclusive quasielastic electron scattering experiments as shown in Chapter 4. The comparison of calculations with consistent theoretical ingredients and constrained parameters for both $(e, e'p)$ and (γ, p) cross sections can enable us to check in comparison with data the consistency of the theoretical description of the two reactions. Obviously the formalism could be applied to study any other doubly closed shell nucleus.

By keeping the consistency between $(e, e'p)$ and (γ, p) in mind, we restrict our selves to generate the bound single-particle basis wave functions by only one set of mean field potential of Woods-Saxon. In our calculations we generate the single-particle wave functions by Woods-Saxon parameters that given in Tab. 3.1 and linked to semi realistic $S3$ correlation function of Afnan and Tang [Afn68] through the *FHNC* calculations by minimizing the ground state expectation value of the hamiltonian [Ari96]. In order to take into account *FSI*, the emitted particle and continuum single-particle wave functions are calculated by solving Schrödinger equation by using a complex energy dependent optical potential of Schwandt *et al.* [Sch82] that was fitted proton elastic scattering data.

The usual treatment in the photonuclear processes in the energy range starting from the particle emission threshold up to 60 MeV the sum of multipoles in Eq. (5.1) can be restricted to electric multipoles with $J = 2$, i.e. with including only 1^- and 2^+. The importance of higher multipoles in the photoproton reaction due to mainly the interference effects with 1^- and 2^+ should be considered [Ryc87b]. Clearly with increasing photon energies and at large values of emission angles, where the momentum mismatch increases, the need of higher multipoles is evident. In our calculations, we insert all the electric and magnetic multipoles up to $J = 12$. This last requirement was necessary to ensure the numerical stability at high momentum mismatch.

5.2.1 Testing the DKO Model

In this section we test the validity of the *DKO* model and the importance of the *FSI* to the (γ, p) reaction. We have already mentioned the relevance of the *FSI* in the description of the quasielastic electron scattering data. In treating $(e, e'p)$ reactions we chose the approach of the Pavia group [Bof82, Bof93, Bof96] which takes into account the *FSI* by describing the emitted nucleon as moving in an optical potential. We have adopted the same strategy also in the (γ, p) reaction. In this type of calculations the single-particle basis is not any more orthonormal since particle and hole wave functions are described by two different mean fields. This problem has been investigated in Refs. [Bof82, Bof84] where it has been found that the effects of the non orthogonality of the basis are not important under the kinematic conditions of interest. Also, the problem has been discussed in Sec. 4.5.2 to test the effects of non orthogonality when correlations are included. It is concluded that the effects of the non orthogonality of the basis are negligible on the correlations.

The angular distributions of the $^{16}\mathrm{O}(\gamma, p_0)^{15}\mathrm{N}$ cross sections calculated at photon energies of 60, 80, 100 and 196 MeV by using different potentials are compared in Fig. 5.2 with the experimental data of references [Fin77, Sme93, Mil95, Ada88], respectively. All the curves represent calculations of mean field *IPM* with *OB* currents only. The solid lines are obtained when the particle wave functions are evaluated using energy dependent optical potential of Schwandt *et al.* [Sch82]. The dashed lines are obtained by using, for the particle states, purely real Woods-Saxon potential with parameters given in Tab. 3.1 and used to generate the hole wave functions. The dotted lines are obtained by setting the particle mean field to zero. As expected, the dotted lines showing the $PWIA$ results are above the experimental data. The results of dashed lines do not reproduce the shape of the angular distributions nor its size where they are always smaller than the data. In this case, the depth of the real part of the potential is the deepest one among those we have used. The results shown by the solid lines, where obtained by using a potential whose real part becomes gradually shallower with increasing the photon energy, have the same order of magnitude of the data. It is clear that with increasing photon energy or at backward angles the *DKO* model fails to reproduce the data even with including *FSI*.

Thus, as in the electron scattering case, we found that the largest correction to the naive mean field model arises from the rescattering of the emitted proton. Therefore an investigation of the photoproton emission cross sections above the giant resonance can be done by using the *DKO* model with *FSI* described by an optical potential taken from proton elastic scattering.

Henceforth we shall investigate the proton emission cross sections by using the *DKO* with the energy dependent optical potential of Schwandt

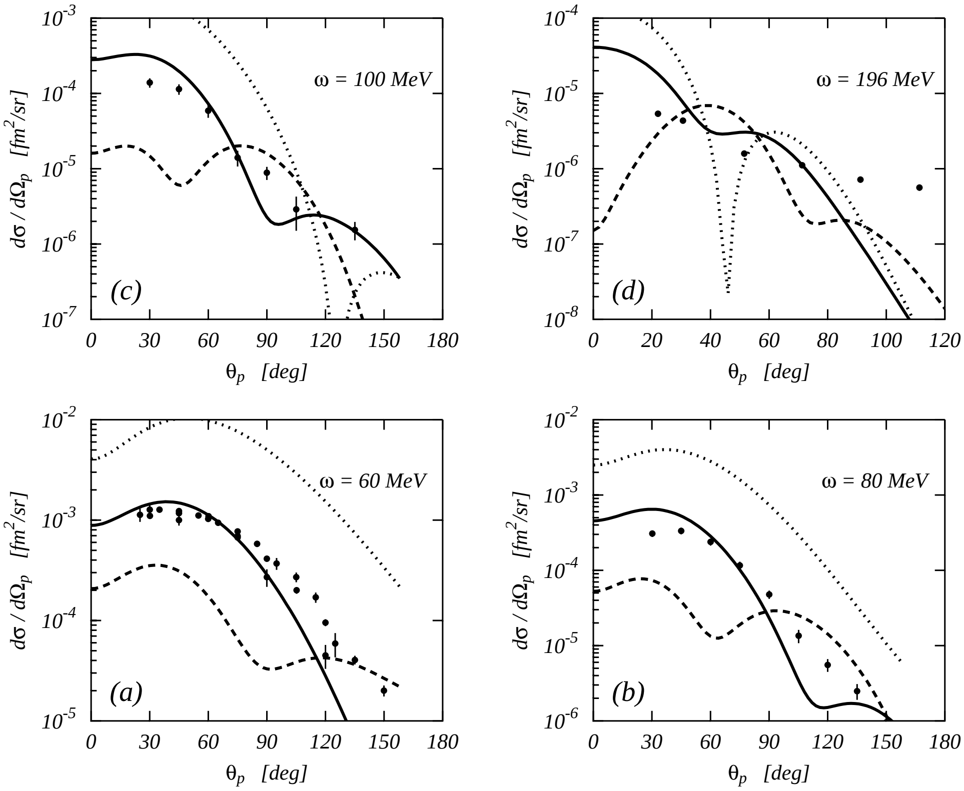

Figure 5.2: Cross sections of the ^{16}O$(\gamma, p_0)^{15}$N reaction for various energies of the photon. The solid lines are obtained using, for the particle states, the energy dependent optical potential of Schwandt *et al.* [Sch82], the dashed lines with the real potential of reference [Ari96] also used for the hole states, and the dotted lines are obtained in $PWIA$. The experimental data at different photon energies are taken from references as follow: 60 MeV [Fin77, Sme93, Mil95], 80 MeV [Fin77], 100 MeV [Fin77] and 196 MeV [Ada88].

et al. [Sch82].

5.2.2 The EM Currents

The effects of the *SRC* we aim to disentangle, are certainly small as compared to the total size of the cross section. It is therefore mandatory to control all the approximations of our model, to be sure that the size of the effects we found do not fall within the uncertainty of our theoretical hypotheses. In this subsection we discuss those hypotheses related to the treatment of the electromagnetic currents.

The *OB* magnetization current, Eq. (2.27), is usually neglected in the study of photonuclear reactions [Gia85, Ryc88, Sar93], but we studied its relevance. The ratios between the transverse responses, Eq. (5.1), calculated using only the convection or the magnetization current and the responses obtained with the full *OB* currents are shown in Fig. 5.3.

The panel (a) of the figure show that at the photon point ($q = \omega$) the contribution of the convection current is larger than that of the magnetization current. With the increase of the momentum transfer, the relative importance of the two currents is interchanged. In the quasielastic regime the magnetic current dominates as it is well known [Ama01]. Even at the photon point the relative importance of the magnetization current increases with increasing energy. This trend which is shown in the panel (b) of the figure where the relative ratios calculated at the photon points are given as function of the excitation energy. Thus since we are investigating photonuclear reaction at high photon energy we have to include the explicit expression of the magnetization current in our calculations in

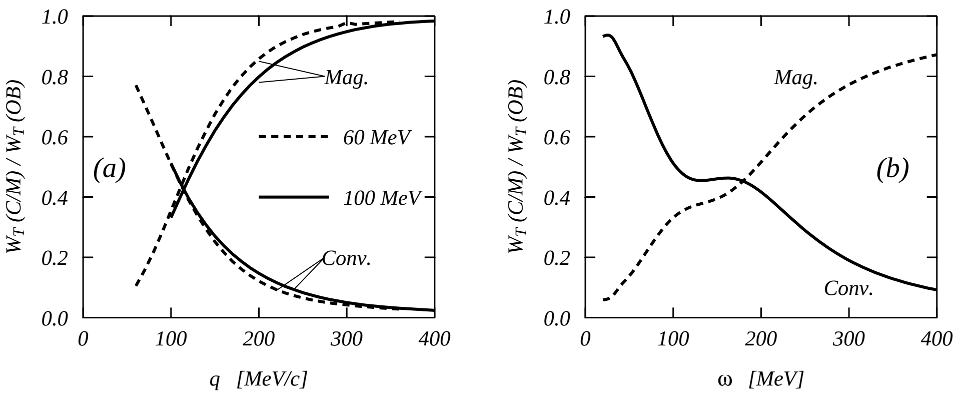

Figure 5.3: Ratio between transverse responses calculated by using only convection or magnetization current on the full OB currents response. In the panel (a) the excitation energies are fixed and the momentum transfer q is changed. In the panel (b) the ratios are calculated at the photon point for various values of the excitation energy.

addition to the explicit expression of convection current.

As we discussed in Sec. 5.1.1, the effects of the MEC on the photonuclear reactions are estimated to be very important. In order to investigate the effects of the MEC and the role of each seagull, pionic and Δ-isobar currents, we show in Fig. 5.4 the normalized differences defined as:

$$\Delta W_T = \frac{W_T(OB + MEC) - W_T(OB)}{W_T(OB)} \tag{5.14}$$

where we indicate with $OB + MEC$ the responses obtained by adding the various MEC terms to the OB currents. In the panel (a) of the figure the normalized differences calculated at the photon point are shown as a function of the excitation energy. In the panel (b) as a function of the momentum transfer for fixed excitation energy.

The results presented in Fig. 5.4 shows that the inclusion of the seag-

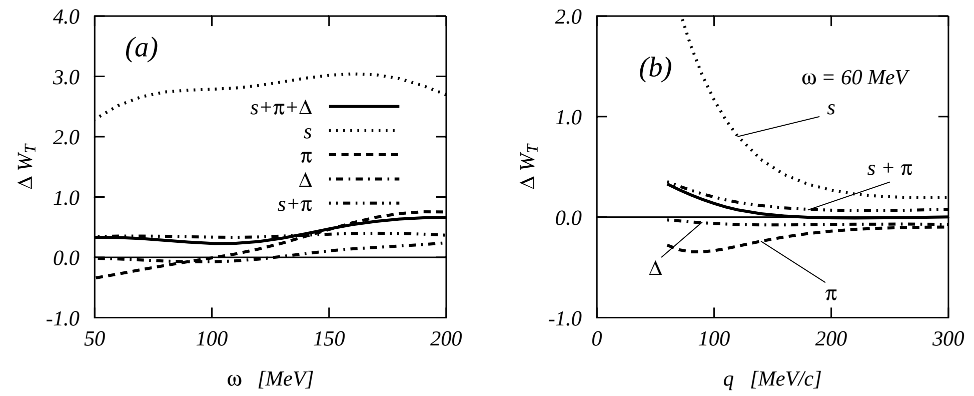

Figure 5.4: Normalized differences, Eq. (5.14), obtained by adding to the *OB* currents the various *MEC* terms indicated in the figure: dotted lines are *OB*+seagull, labeled (s), dashed lines are *OB*+pionic, labeled (π), dashed doubly dotted lines are *OB*+seagull+pionic, labeled (s + π) and dashed dotted lines are *OB*+Δ, labeled (Δ). The thick solid lines show the results obtained with the inclusion of all the *MEC* currents to the *OB* currents and labeled as (s+π+Δ). In the panel (a) the normalized differences are calculated at the photon point, in the panel (b) at fixed excitation energy ω as a function of the momentum transfer q.

ull term only in addition to the *OB* currents, as it is done for example in the work of Benenti *et al.* [Ben94] and Gaidarov *et al.* [Gai00], largely overestimates the role of the *MEC* as shown by dotted lines in the figure. Adding the pionic current alone slightly reduces the *OB* response at energies smaller than 100 MeV, and it slightly increases it at larger values as shown by dotted lines. Although the contribution of the pionic current alone is small, the sum of both seagull and pionic currents to the *OB* currents quenches the effect of seagull current as shown by dashed doubly dotted lines. The presence of destructive interference between seagull and pionic currents is well known in the studies of the quasielastic peak

[Ama93b, Ord81].

The contribution of the Δ current is relatively small as shown by dashed dotted lines. We should remark that we consider only the virtual excitation of Δ, and do not include the pion production channel which implies the real delta excitation. This channel is open above $\omega = 140$ MeV.

Panel (b) shows that at the photon point the contribution of the seagull term is relatively larger than at higher q values. The pionic terms reduces the *OB* response for all q values. The interference between these two terms is the dominant contribution since the Δ current is negligible. The solid line shows that the inclusion of all the *MEC* diagrams produces relatively small variations on the *OB* currents. The photon point is the place where the *MEC* effects are largest, on a relative scale. It is worth to notice that the relative difference becomes smaller with increasing momentum transfer. Thus in quasielastic $(e, e'p)$ reaction in Chapter 4 we ignored their effects. Also, we give in Sec. 5.2.5 the results of $(e, e'p)$ with including *MEC* to assure its negligible effect in quasielastic region.

In Fig. 5.5 we compare the angular distributions of the $^{16}\mathrm{O}(\gamma, p_0)^{15}\mathrm{N}$ cross sections calculated for various photon energies. The calculations have been done with the optical potential and the thin solid lines represent the results obtained with the *OB* currents only. The other lines are obtained by adding the various *MEC* terms where the meaning of the lines is similar to that of Fig. 5.4. The contribution of the seagull current (dotted lines) noticeably increases the cross section, but the effect of the pionic current (dashed lines) goes in the opposite direction. When both

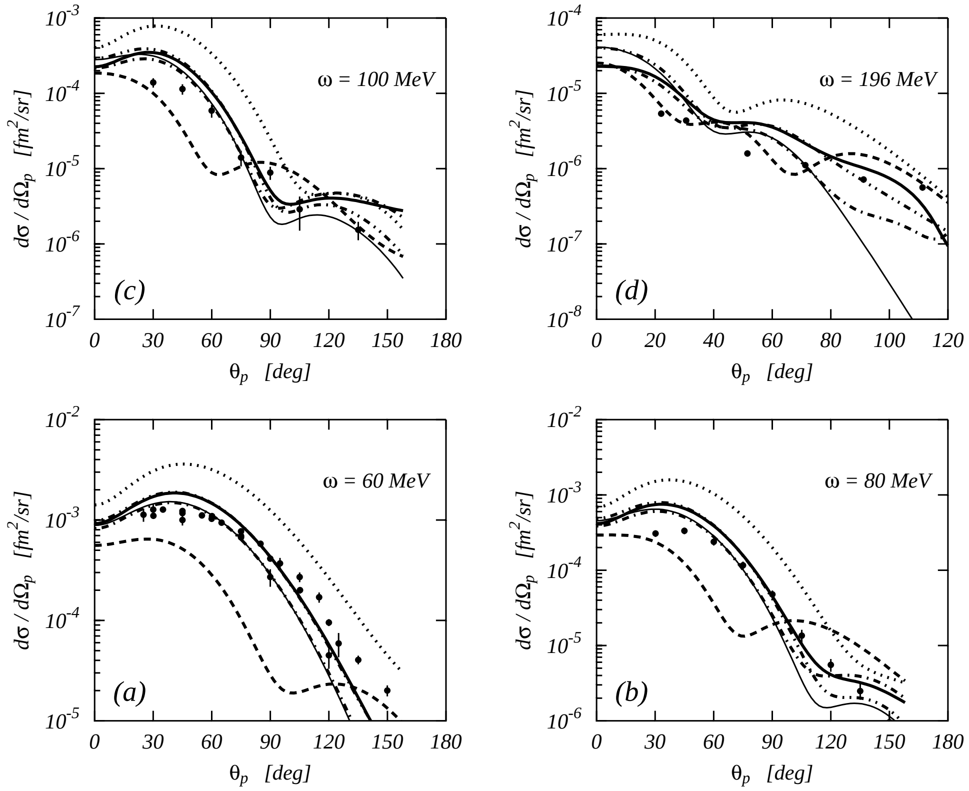

Figure 5.5: Angular distribution of the ^{16}O$(\gamma, p_0)^{15}$N cross section for various energies of the photon. The thin solid lines show the OB results, the other lines have the same meaning of those in Fig. 5.4. Data as in Fig. 5.2.

currents are considered (dashed doubly dotted lines), the results are only slightly above the OB ones. The excitation of the virtual Δ (dashed dotted lines) is not important but for high values of θ_p and at high photon energies. The total results (thick solid lines) are slightly above the OB ones, the differences become larger at high values of θ_p.

The results obtained with the OB currents only (thin solid lines) steeply decrease with increasing θ_p. At high θ_p values the inclusion of seagull and pionic currents pushes up the cross section by an order of magnitude.

5.2.3 The Results of SRC Model

As a result of expected sensitivity of the results to correlations, we investigate the effects of *SRC* by evaluating the (γ, p) cross sections with three different correlation functions. As we already mentioned, all the calculations are done with the same hole single-particle basis that generated by the set of Woods-Saxon parameters given in Tab. 3.1. In our calculations, we consider two types of correlation functions linked to our basis through the $S3$ interaction according to the work of Arias *et al.* [Ari96]: a first one has been obtained with the Euler procedure, labelled $S3$ in our calculations and a second one of gaussian type, labelled G. For sake of comparison we also use the scalar part of the state dependent correlation function taken from [Fab00], labelled $V8$. The three correlation functions are shown in Fig. 3.2 for ^{16}O nucleus.

Since the novelty of our approach is the inclusion of the three-point diagrams we have to study the importance of these terms in case of (γ, p) as we have done for the (e, e') and the $(e, e'p)$ reactions in Chapters 3 and 4, respectively. In Fig. 5.6 we show the normalized difference of Eq. (5.14) evaluated by adding to the *OB* terms the correlated two- and three-point diagrams instead of the *MEC*. The solid lines are obtained by considering all the diagrams of Fig. 2.2 and the dashed lines by adding to the *IPM* response the two-point diagrams only.

These results agree with our findings for inclusive (e, e') low-lying nu-

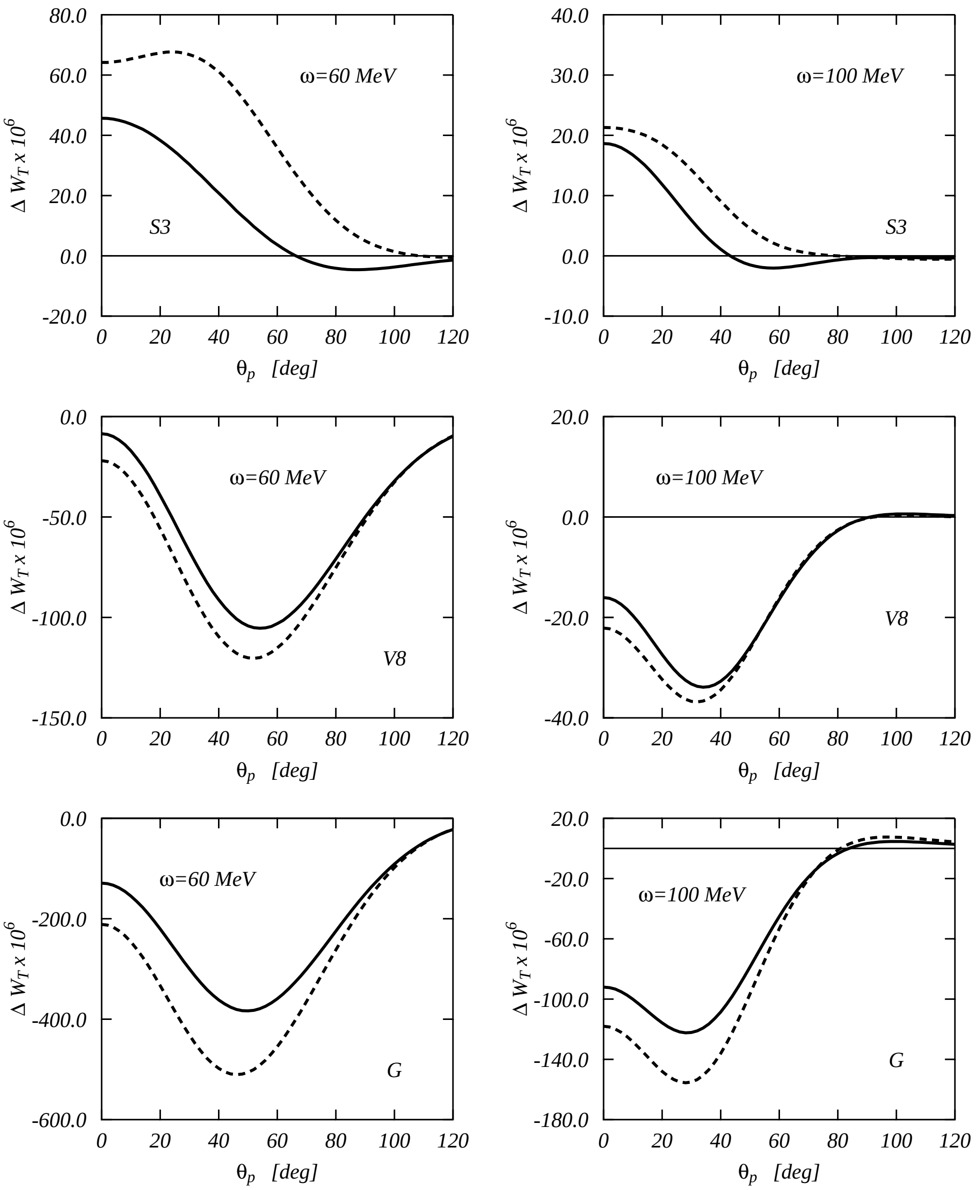

Figure 5.6: Normalized difference between correlated and uncorrelated responses. The dashed lines are calculated with two-point diagrams only, the solid lines with both two- and three-point diagrams.

clear excited states in Chapter 3 and for exclusive $(e, e'p)$ quasielastic in Chapter 4 and with findings of Co' and Lallena [Co'01] for the inclusive (e, e') quasielastic reaction. The effect of the two-point diagrams, whatever it is, is lowered by the inclusion of the three-point terms. It is interesting to notice that the effect of the $S3$ correlation is smaller than that of the other two correlations and it has opposite sign.

The angular distributions of the $^{16}\mathrm{O}(\gamma, p_0)^{15}\mathrm{N}$ cross sections calculated for different photon energies are shown in Fig. 5.7. The thin solid lines show the pure *IPM* results with *OB* currents. The other lines represent the results of the full calculations of the *SRC* of our model, i.e. they have been obtained by adding to the *IPM* with *OB* all two- and three-point diagrams of Fig. 2.2. The thicker solid, dashed and dotted lines are obtained by including the contribution of the $S3$, $V8$ and gaussian correlations respectively. In this case the results are very sensitive to the correlation as expected in photonuclear reactions. Therefore the three correlations produce rather different effects.

The sensitivity of the results to the correlation is larger than in the case of electron scattering. The source of this relatively high sensitivity are investigated by calculating the (e, e') quasielastic electromagnetic responses at fixed excitation energy (ω=100 MeV) for various values of the momentum transfer. The results of these calculations are shown in Fig. 5.8. All the results shown in the left panels are obtained by using the $S3$ correlation while those of the right panels with the gaussian correlation. The (a) and (f) panels show the longitudinal responses, not present in reactions with real photons. The solid lines are the *IPM* responses and

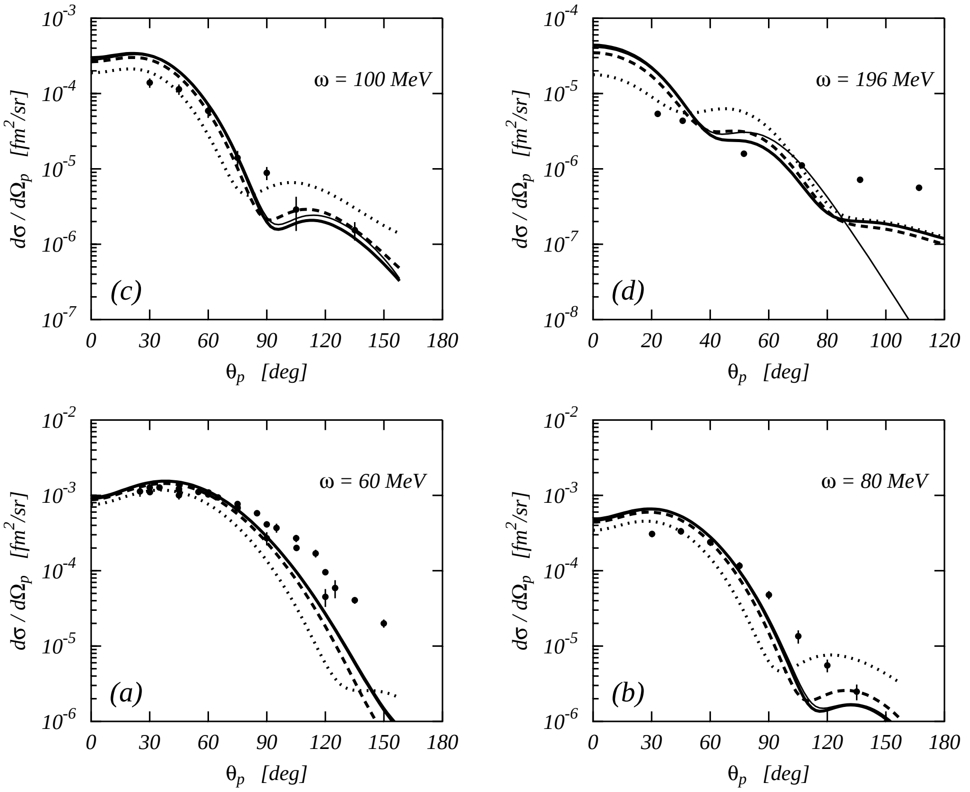

Figure 5.7: Angular distributions calculated with the inclusion of the *SRC*. The thin solid lines are the *IPM* results, the thick solid lines show the results obtained with the $S3$ correlation, the dashed lines with the $V8$ correlation function and the dotted lines with the gaussian G correlation function.

the dashed lines are obtained by adding the correlations. Referring to Fig. 2.2 the solid lines are obtained using only the diagram (1.1) and the dashed lines all the diagrams of the figure. In addition to these lines we show the responses calculated without the OB terms. This means that we used all the diagrams labelled 2 and 3 in Fig. 2.2 and we eliminated the contribution of the (1.1) diagram. The results of these calculations are shown by the dotted lines. The analogous results for the transverse responses are shown in the panels (c) and (h) of the figure. To emphasize the difference between the various responses in the panels (b),(d),(g) and (i) we show the normalized differences.

As expected, for all the momentum transfer values calculated, the OB responses are order of magnitude larger than the responses obtained only with the correlation terms. Also the qualitative behaviour of the responses as a function of q is quite different. While the OB responses increase by more than two order of magnitude with increasing q the change of the correlated responses is much more limited. The consequence of this fact is that, relatively speaking, at the photon point IPM and correlated responses are closer in magnitude than at higher q. For this reason the photon cross sections are relatively more sensitive to the SRC than the electron scattering processes. The comparison between the normalized differences, shown in the (b),(d),(g) and (i) panels, is a measure of the importance of the interference effects between OB and correlation transition amplitudes. As expected the most important part of the correlation effects is due to these interference terms.

The observation of the angular distributions of Fig. 5.7 shows that at

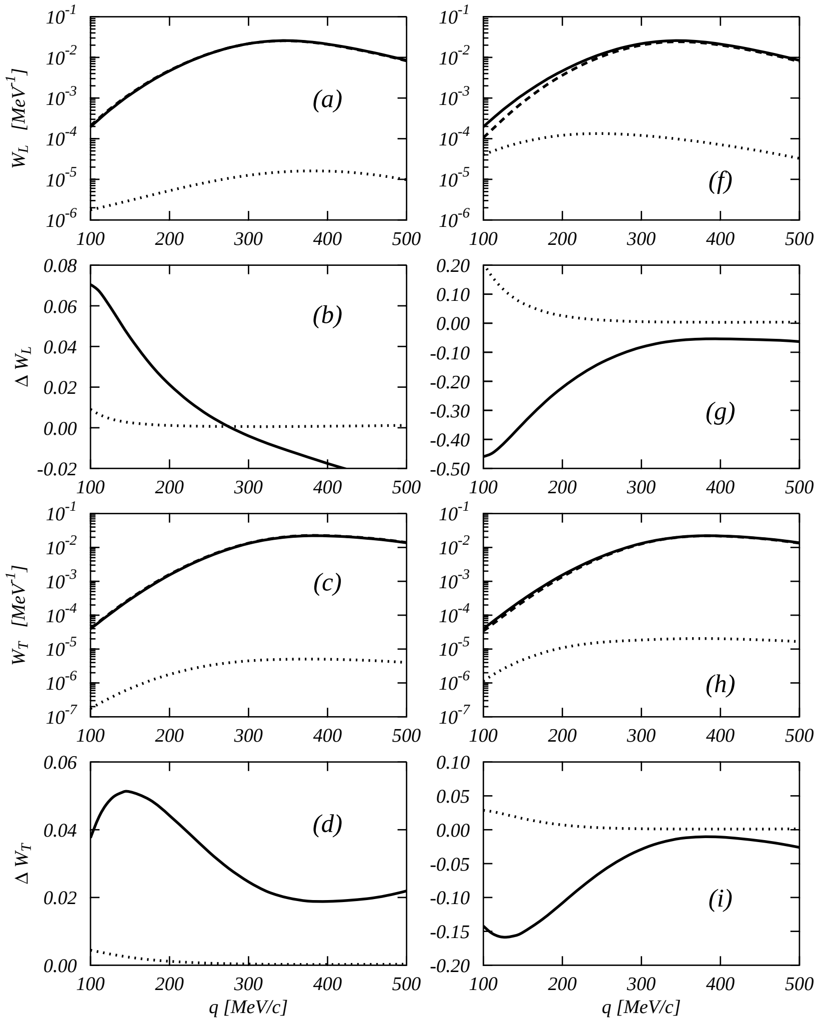

Figure 5.8: Inclusive responses and normalized ratios (see text) as a function of the momentum transverse at $\omega = 100$ MeV. The left panels refer to the $S3$ correlation, the right ones to the gaussian correlations, the (a),(b),(f),(g) panels to the longitudinal response (not present in photonuclear processes) and the other ones to the transverse response. The solid lines of the panels (a),(c),(f),(h) are the OB responses the dashed ones the OB+correlations responses and the dotted lines the responses obtained only with the correlation terms. The solid lines of the panels (b),(d),(g),(i) show the difference between OB and OB+correlation responses normalized to the OB response. The dotted lines the ratio between the purely correlated responses and the OB responses.

high values of the photon energy the correlation effects show up at large scattering angle. The *IPM* cross sections are almost overlapped to the thick solid lines in Fig. 5.7. At 196 MeV the *IPM* cross sections show a fast decrease for large nucleon emission angles while the correlated cross sections indicates a less rapid fall. This behaviour remember us with the increase of ground state momentum distribution at high momentum values when it is calculated with *SRC* with respect to the calculations of *IPM* [Ari97, Cio91, Fab01]. In effect, by transforming the value of the emission angle θ_p in the value of the momentum of the target nucleon p_i, it is possible to verify that the values of p_i probed go from 400 to 700 MeV/c. This is the interval where the correlated nucleon momentum distributions start to differ from that obtained with the *IPM*.

5.2.4 Comparison with Data

The results we have so far obtained are summarized in the figures 5.9 and 5.10 to discuss their comparison with the data. The thin solid lines are calculated within the simple *IPM* by using *OB* currents only. The dotted lines show the results obtained by adding the $S3$ *SRC* obtained with the Euler procedure. The inclusion of the *MEC* produces the dashed lines. Finally the thick solid lines are obtained by including both *SRC* and *MEC*. Our calculations overestimate the data at small emission angles. This is more evident in Fig. 5.9 but also in Fig. 5.10 at $\omega = 196$ MeV where more data are available. The shape of the data at high energy values is reproduced only because of the inclusion of *SRC* and *MEC*. It is evident that the *MEC* contributions are larger than those of the *SRC*.

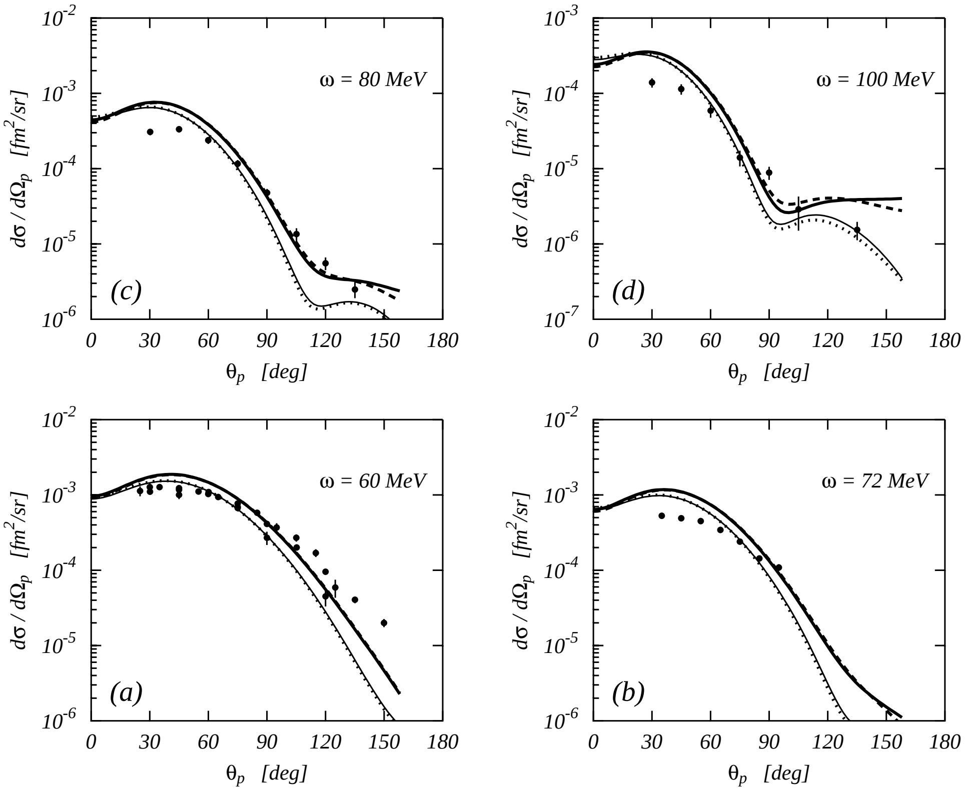

Figure 5.9: Angular distributions of the $^{16}O(\gamma, p_0)^{15}N$ cross sections. The thin solid lines are calculated in the *IPM* by using *OB* currents only. The dotted lines include the effects of the $S3$ correlation to the *OB*. The dashed lines include the effects of *MEC* to the *OB* and the thick solid lines all the effects. The experimental data as in Fig. 5.2 and the data at 72 MeV is taken from the work of Miller *et al.* [Mil95].

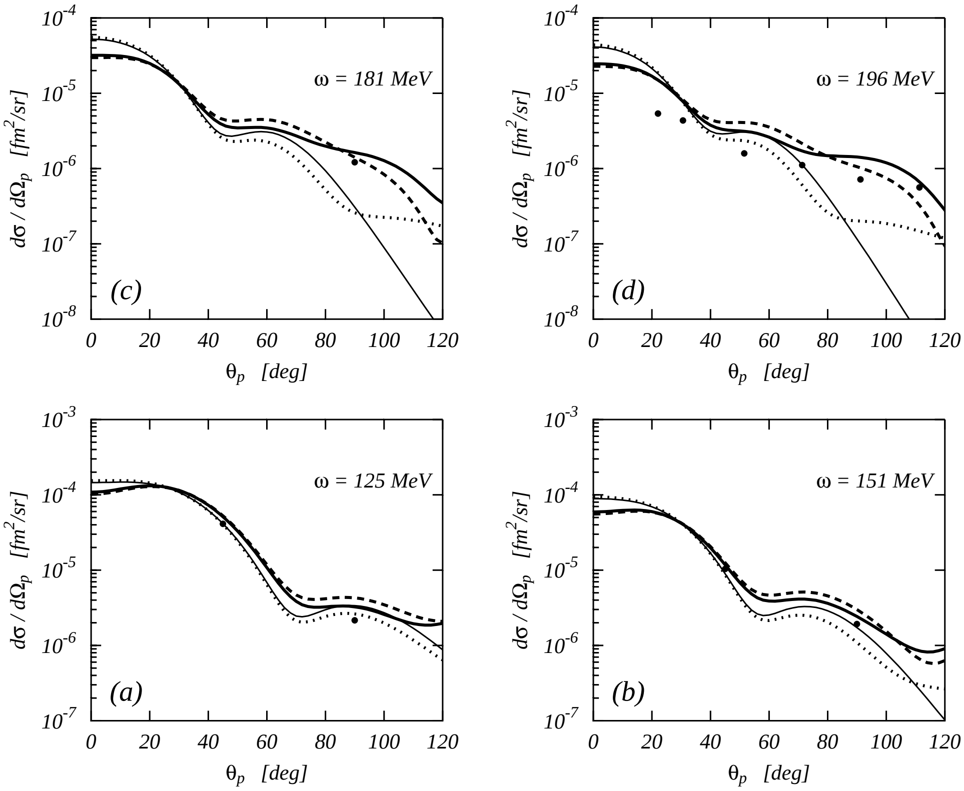

Figure 5.10: The same as in Fig. 5.9 for photon energies above 100 MeV. The data at 126, 151 and 180 MeV are from reference [Lei85] and those at 196 MeV from [Ada88].

The energy dependence of the $^{16}\mathrm{O}(\gamma, p_0)^{15}\mathrm{N}$ cross section for fixed values of the emission proton angle is shown in Fig. 5.11. The meaning of the lines is the same as in Fig. 5.9. For $\theta_p = 45^0$ our calculations show an almost perfect exponential decay. On the other hand the data are not so perfectly aligned. The discrepancy between our calculations and the data is more evident between 50 and 100 MeV. The shapes of the data and of our results for $\theta_p = 90^0$ are characterized by two different trends. An exponential decay up to 100 MeV and an almost flat behaviour at higher energies. This high energy tail is dominated by the *MEC*. We also observe that for $\omega > 100$ MeV the *SRC* effect consists in a reduction of the cross section.

In Fig. 5.12 we compare the results of our calculations with the data relative to the emission of the proton from the $1p_{3/2}$ level [Mil95]. The meaning of the various lines is the same as in Fig. 5.9. Also in this case our calculations slightly overestimate the data at small emission angles and underestimate them at larger angles. The *SRC* reduce the cross section while *MEC* increase it.

5.2.5 Comparison between the Quasielastic $(e, e'p)$ and (γ, p) Reactions

In all the (γ, p) calculations presented so far we did not make use of spectroscopic factors that commonly needed in the analysis of $(e, e'p)$ reaction to scale the experimental data. As we presented for (γ, p) data, by constraining the same theoretical treatment and inputs used to analyze$(e, e'p)$ data, the *DKO* results produce approximately the same size of the data. If

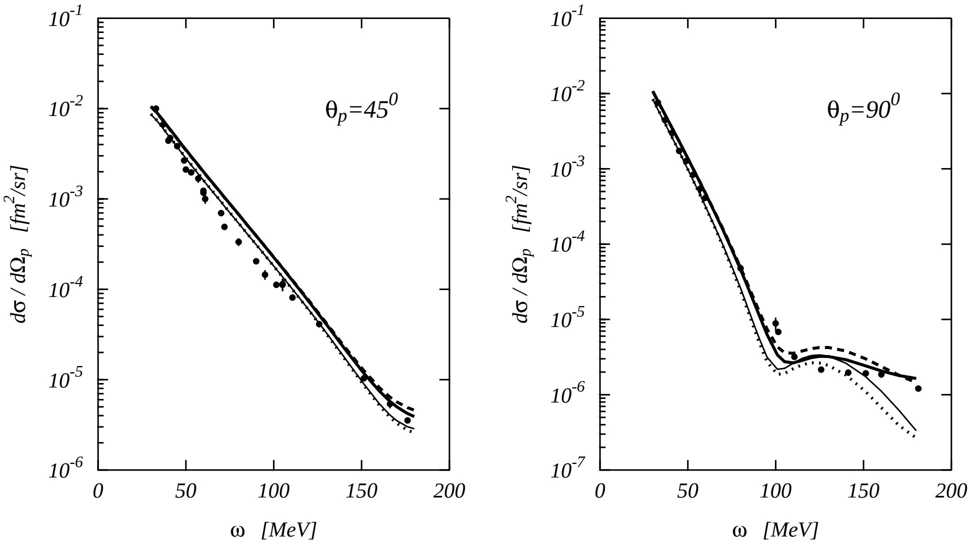

Figure 5.11: Energy dependence of the ^{16}O$(\gamma, p_0)^{15}$N cross section at for various proton emission angles. Like in the previous figures, the thin solid lines are obtained with the *IPM* model, the dotted ones by adding the *SCR* the dashed ones with the *MEC* and the thick solid lines show the total results. Data from [Fin77, Sme93, Mil95, Lei85].

we apply the same spectroscopic factor that we deduced from the $(e, e'p)$ data, which is 0.8 in case of $S3$ input, the *DKO* results will underestimate the data. Thus it is clear that the (γ, p) data can not be understood in a pure *DKO* model and the effects of *SRC* and *MEC* should be considered.

Before making the comparison between (γ, p) and $(e, e'p)$ data, we have to see the effects of adding the *MEC* in the $(e, e'p)$ data. We have already shown in panel (b) of Fig. 5.4 that the effects of *MEC* in quasielastic region are negligible.

In Fig. 5.13 we show our results of quasielastic ^{16}O$(e, e'p_0)^{15}$N in par-

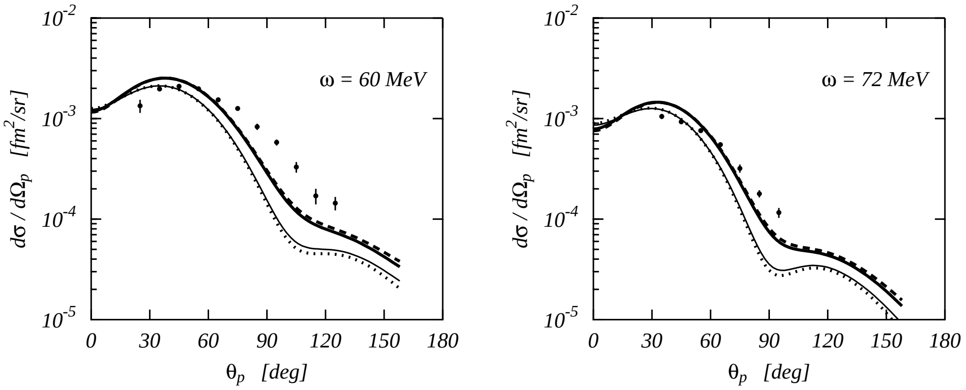

Figure 5.12: Angular distributions for emission of a proton from the $1p3/2$ level. The meaning of the lines is the same as in Fig. 5.9. Data from [Mil95]

allel kinematics for the NIKHEF data [Leu94]. The calculations done by including the effects of both *SRC*, that we done in Chapter 4, and also the effects of *MEC*. The meaning of the lines is the same as in Fig. 5.9. Because the small effects of adding *MEC*, we show in panel (a) of the results in linear scale. The curves are almost overlapped and it is clear the effects of *MEC* in quasielastic $(e, e'p)$ reaction are relatively small. Thus the spectroscopic factor that we deduced in Chapter 4 will not change by adding the effects of *MEC*. In panel (b) of the figure we show the same calculations in logarithmic scale with the experimental data of NIKHEF [Leu94]. All the curves are multiplied by a 0.8 spectroscopic factor to reproduce the data.

After exploring the role of *SRC*, *MEC* and *FSI* in case of $(e, e'p)$ reaction, we now want to compare our results with the experimental data of Mainz [Blo95] where the reduced cross section has been extended to higher missing momentum. In this experiment different kinematic con-

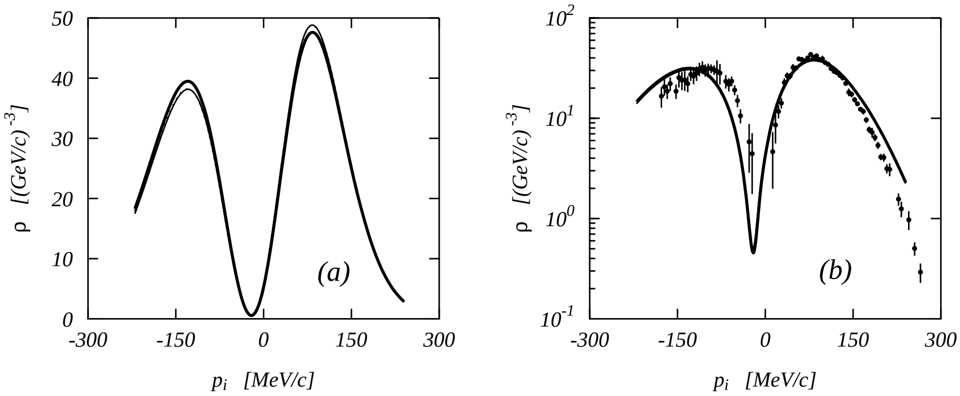

Figure 5.13: ^{16}O$(e, e'p_0)^{15}$N cross section in parallel kinematics with the same conditions presented in Sec. 4.5. The lines have the same meaning of Fig. 5.9. The curves are presented in linear scale in panel (a) and in logarithmic scale in panel (b) compared with experimental data of NIKHEF [Leu94]. All the curves of the panel (b) are multiplied by a 0.8 spectroscopic factor.

ditions have been used. They used parallel kinematics to produce the reduced cross section in the p_i range from 80 to 400 Mev/c. The highest momenta from 400 to 700 MeV/c has been measured in perpendicular kinematics with two different sets of $(\omega, \mathbf{q})$: the first one $(247, 497)$ for the p_i range from 400 to 500 Mev/c and the second one $(252, 318)$ for momenta from 500 to 700 MeV/c. This high missing momentum and possible contribution from *MEC* in addition to *SRC* is the reason of why we delayed the investigation of this data until to include the effects of *MEC* to our calculations.

In Fig. 5.14 we compare the results of our calculations, including multiplying with spectroscopic factor of 0.8, with the $(e, e'p_0)$ data taken at Mainz [Blo95]. The meaning of the lines is the same as in Fig. 5.9 but the

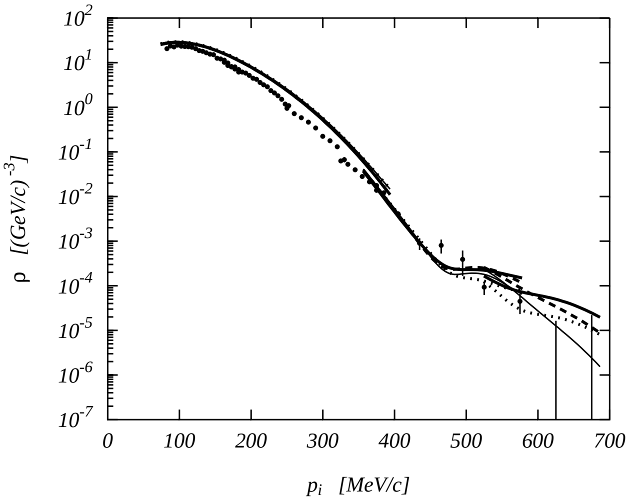

Figure 5.14: ${}^{16}\mathrm{O}(e, e'p_0)^{15}\mathrm{N}$ cross section in different kinematics considered in the experiment of Mainz [Blo95] (see the text). The lines have the same meaning of Fig. 5.9. All the curves are multiplied by a 0.8 spectroscopic factor.

curves are almost overlapped and it is not easy to distinguish them. Only in the p_i range from 500 to 700 Mev/c the calculations start to differ. Although the *IPM* with *OB* currents, thin solid line, is able to reproduce the data in this range, but the need of *SRC* and *MEC* to enhance the high momentum tail is evident. We have to refer that in this region the momentum transfer $\mathbf{q} = 318$ MeV/c is slightly far from the quasielastic peak and it is close from the energy $\omega = 252$ MeV, i.e. we are in a situation very close from the photon point where $q = \omega$ and then the effects of both *MEC* and *MEC* start to be dominant than the *OB* picture as we presented in Figs.5.4 and 5.8.

Using the spectroscopic factor of 0.8, that we deduced from the analysis of $(e, e'p)$ reaction, we compare again the results of our calculations with the (γ, p_0) data in Fig. 5.15. In this figure the dashed lines represent the *IPM* results with *OB* currents only and the solid lines the results of the complete calculations when both *SRC* and *MEC* are included. The agreement with the data is certainly improved with respect to the results shown in Figs.5.9 and 5.10. The inclusion of both *MEC* and *SRC* is necessary to obtain the correct shape of the data and to present both $(e, e'p)$ and (γ, p) reactions in the same scale.

5.3 Conclusions

We have investigated the photonuclear cross section with nuclear model which considers the contributions of both the *SRC* and *MEC*. In our model the *SRC* act only on the *OB* currents while *MEC* are calculated in the *IPM* level. Thus in our computational scheme both *SRC* and *MEC* interact only through the interference terms of the transition matrix elements. We have considered the ^{16}O nucleus.

Since our model can not describe collective excitations, we restricted our investigation to the (γ, p) reaction above the giant resonance in the photon energy range from 60 MeV to 169 MeV where both *IPM* and continuum *RPA* approach for collective states give similar results [Ang02]. At photon energies above 60 MeV the comparison with (γ, p) angular distributions is unsatisfactory by using *IPM* only. Following the treatment commonly adopted to describe the $(e, e'p)$ reactions, the rescattering process between the emitted proton and the rest nucleus has been accounted by using an energy dependent optical potential.

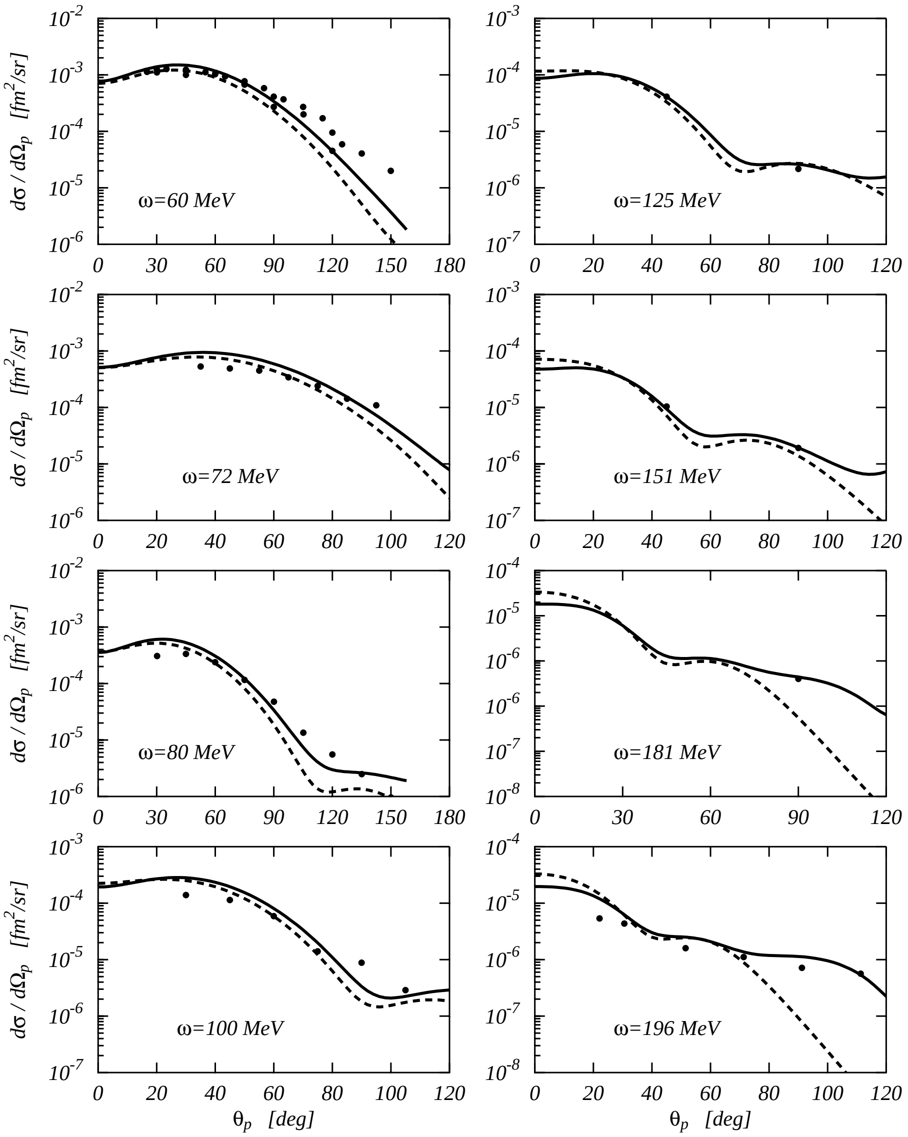

Figure 5.15: $^{16}O(\gamma, p_0)^{15}N$ cross sections for various values of the photon energies. All the curves are multiplied by the spectroscopic factor of 0.8. The dashed lines show the *IPM* results with *OB* currents only and the solid lines the results obtained by including both *SRC* and *MEC*. Data as in Figs. 5.9 and 5.10.

With this model we have investigated the role of the various terms of the electromagnetic current. We studied the difference between electron and photon scattering processes by considering the transverse response at fixed energy for various values of the momentum transfer. We found that at the photon point ($q = \omega$) the response is strongly dominated by the convection current, while with increasing q the magnetization current becomes quickly more important. However, even at the photon point it is not possible to neglect the magnetization current for energies above 100 MeV.

The *MEC* have been analyzed following the model [Ama93b] that considers the π exchange diagrams of Fig. 5.1 where seagull, pionic and Δ currents have been included. The use of the seagull diagram only, as it has been done in Refs. [Ben94, Gai00], overestimates the *MEC* effects. The inclusion of the pion diagram reduces this effect, and the Δ current is important only for photon energies above 100 MeV. At these energies a large difference between cross sections calculated with *OB* currents only and those obtained with the inclusion of the *MEC* is found for large emission angles.

Our *SRC* calculations have been done with three different correlation functions taken from the *FHNC* calculations [Ari96, Fab00]. As already shown in the electron scattering case the effects of two- and three-point diagrams have opposite sign. We observed that the photoemission cross sections show larger sensitivity to the correlations with respect to the electron scattering cross sections. This is due to the different momentum dependences of the transition matrix elements of the *IPM* and of those containing the correlation function. The *IPM* transition matrix elements have a sharp rise, while the other ones are almost flat. At the photon point the difference between the two transition matrix elements is relatively smaller than at higher values of the momentum transfer. This is the source of this relatively high sensitivity.

We found that at excitation energies, above 150 MeV, the cross sections obtained in the *IPM* with *OB* currents, have a sharp decrease for large values of the nucleon emission angle. In this region, the correlations produce cross sections order of magnitude larger than the *IPM* ones. This exactly the same, well known, behaviour of the nucleon momentum distribution. In effect it is possible to translate the emission angle with the initial momentum of the emitted nucleon. One can see that *IPM* and correlated cross section start to separate at about 600 MeV/c, where also the momentum distributions of ^{16}O start to separate. Unfortunately, in these cross sections the *MEC* play an important role, more important than that of the *SRC*. Therefore the effect of *SRC* is overwhelmed by that of the *MEC*.

The comparison with the data improves when a spectroscopic factor is used. We fixed the value of 0.8 for the $1p1/2$ proton emission, by applying our model to the $^{16}\mathrm{O}(e,e'p_0)^{15}\mathrm{N}$ data taken at NIKHEF [Leu94]. The same spectroscopic factor value has been used to describe the coincidence electron scattering data taken at Mainz [Blo95] and the photon emission data available in the literature. The inclusion of this reduction factor greatly improves the agreement with all the data sets, in spite of the fact that the factor was extracted for relatively low values of the missing momentum.

We would like to conclude by mentioning some possible way of improving our model. A first one is related to the treatment of the *MEC*. The energy values of interest is above the pion emission threshold. One may claim that this channel has just open and therefore it is negligible, but one would like to have an estimate of its relevance. A second possible improvement is related to the optical potential at present taken from literature. In a more consistent description the potential should be related to the same nuclear structure model producing the *SRC*.

General Summary and Conclusions

The description of the nucleus as being composed of protons and neutrons moving independently in the mean field potential, leads to the *IPM* where the nucleons occupy the various shells up to the Fermi level. This model contradicts itself in the sense that since the nucleons interact with each other they can not really move independently. The microscopic basis of the *IPM* is the Hartree-Fock theory, where the mean field potential is generated by averaging the interaction between nucleons. Since in the Hartree-Fock theory the many-body states are forced to be Slater determinant, part of the nuclear hamiltonian is neglected. This part, called residual interaction, is the source of collective nuclear phenomena, also called Long-Range correlations. The correlations investigated in this work have a different physical origin. Because the bare *NN* interaction has a strong repulsive core two-nucleons cannot get to close to each other. This produces the Short-Range correlations. In general the correlations lead to a depletion of the occupancy of the levels below the Fermi surface and a non-zero occupancy of states above it. More specifically the best known, and most spectacular, effect produced by the *SRC* is the increase of the nucleon momentum distribution at high momentum values with respect to the *IPM* predictions. Unfortunately, the nucleon momentum distribution is not directly observable, therefore one has to search for phenomena sensitive to this quantity.

The first place to look for these phenomena is the nuclear ground state, the most investigated state from both experimental and theoretical point of view. It has been found that the *SRC* slightly modifies the charge distribution in the nuclear center [Fab00, Co'95]. The size of this effect is however comparable to that produced by the coupling of low-lying collective phonons to the single-particle wave functions [Ang01], therefore difficult to disentangle. There are no other ground state observables showing relevant sensitivity to the *SRC*, therefore one has to search for processes involving the excitation of the nuclear system.

The status of the theory in the description of nuclear excited states is not so well advanced as in the case of the ground state. In this thesis, we have developed a model for the description of nuclear excited states considering the *SRC*. In our model, the correlations act on all the *OB* currents of the charge, magnetization and convection. We have applied the model to the study of processes induced by *EM* probes (electron and γ-photon scattering from nuclei). It is well known that the *EM* probes are particularly suited to study the nuclear structure and hence the correlations between the nucleons in the nucleus.

The description of these processes has been done by using a nuclear model that considers *SRC* up to the first order in the correlation. The basic idea of this model consists in truncating the *CBF* cluster expansion in order to retain only those terms that contain a single correlation line $h(r_{ij}) = f^2(r_{ij}) - 1$. An important property of the expansion in powers of $h(r_{ij})$ is that the normalization of the many-body wave function are exactly preserved at each order. Considering all linked diagrams that contain a single correlation line, we have in addition to the two-point diagrams, commonly calculated in the literature, also three-point diagrams. The inclusion of all these diagrams is necessary to maintain the proper normalization of the many-body wave function.

The calculations have been done using single-particle wave functions and correlations linked together by the same many-body hamiltonian. The single-particle bases have been generated by different sets of mean field Woods-Saxon parameters and linked to the correlation functions through the *FHNC* calculations by minimizing the ground state expectation value of the hamiltonian. In this procedure the Woods-Saxon parameters have been kept fixed and the minimization has been done by changing the correlation function [Ari96, Fab00]. We have tested the need to link both of single-particle basis and correlation by interchanging correlation functions and mean field in our inputs, in this case they are no longer linked with the same hamiltonian.

The presence of collective phenomena is not considered in our model. Thus the application of our model has been limited to situations where collective excitations can be neglected. For this reason we applied our model to the kinematic regimes that are most probably dominated by $1p - 1h$ excitation.

In Chapter 3, we have applied our model to inelastic inclusive electron scattering (e,e') leading to low-lying nuclear excited states below the particle emission threshold. To avoid the collective states we have investigated the excited states that are supposed to be well described as $1p-1h$ pair such as high spin and stretched electric and magnetic states. The investigation extended to values of momentum transfer above 300 MeV/c. We have applied our model to ^{16}O, ^{40}Ca, ^{48}Ca and ^{208}Pb closed shell nuclei. We have tested the collectivity of these states by running discrete *RPA* code with two different residual interactions. According to the results of *RPA* code, we have selected those excited states that are characterized by one (single) or at most two $1p-1h$ pairs. We have used two scalar correlation functions linked to our single-particle basis with the same hamiltonian: the first one labeled $S3$ and the second one of gaussian type labeled G. To test the consistency between our inputs we also used the scalar part of another correlation function labeled $V8$ that not linked with our basis with the same hamiltonian.

Chapter 4 has been devoted to the study of exclusive inelastic $(e,e'p)$ reaction in quasielastic region. The choice of quasielastic region because it is well known that region is dominated by the single particle dynamics and nuclear excitations are dominated by $1p-1h$. We have applied our model to $^{16}\text{O}(e,e'p)^{15}\text{N}$ reaction for the perpendicular and parallel kinematics. We have generated our basis of ^{16}O by using two different mean fields each one linked to the correlation function by the same nuclear hamiltonian. We labeled these inputs as $S3$ and $V8$. The consistency of the input has been tested by interchanged correlation functions and mean field, i.e.

using $S3$ mean field with $V8$ correlation and vice versa. The rescattering processes of the *FSI* between the emitted proton and the rest nucleus have been taken into account by using a complex optical potential taken from proton elastic scattering.

In Chapter 5, the model has been applied to the exclusive photonuclear (γ, p) reaction. Multinucleon mechanisms take place in the photonuclear reactions where not only the *OB* currents contribute but also the *TB* currents due to *MEC*. For specific kinematics the *MEC* may be the dominant mechanism that describe (γ, p) reaction. Thus we have included the *MEC* in our computational scheme by considering that the *SRC* act only on the *OB* currents while *MEC* are calculated in the *IPM*. Again, we restricted our investigation to the (γ, p) reaction above the giant resonance to avoid the presence of collective excitations.

We have applied our model, in Chapter 5, to $^{16}\mathrm{O}(\gamma, p)^{15}\mathrm{N}$ reaction in the photon energy range from 60 MeV to 169 MeV. We have checked the consistency of both $(e, e'p)$ and (γ, p) reactions, under the same theoretical ingredients, i.e. single-particle basis, correlations, spectroscopic factors and consistent optical potentials. Thus we restricted our study to one set of single-particle basis that we labeled as $S3$ since it gives a better description of quasielastic $(e, e'p)$ reaction. We have used three different sets of correlation functions $S3$, G and $V8$ where the first two are linked with our basis while the other one has been taken for the sake of comparison. The *FSI* have been considered with the same optical potential used in the $(e, e'p)$ reaction with taken into account the energy dependent of the potential because the wide range of photon energy under investigation.

From all this investigation we draw the following conclusions:

- For all electron and photon *EM* processes under investigation, the effects of two- and three-point diagrams have opposite sign: the three-point diagrams reduce the effect produced by the two-point diagrams alone, whatever they are. This is the consequence of the correct normalization of the many-body wave function obtained by including two- and three-point diagrams.

- For electron scattering processes under investigation: inclusive electron scattering in the discrete spectrum and semi-exclusive quasielastic electron scattering with emitted proton in continuum, it appears evident that the correlation effects are very small and can not be considered relevant to improve the description of the shape nor the size of the experimental data. In this respect the problem of identifying the physics origin of the required quenching remains open.

- For exclusive $(e, e'p)$ and (γ, p) reactions, the *FSI* between the emitted proton and the rest of the nucleus should be considered. In our work, the *FSI* have been accounted for by using a complex optical potential of Schwandt *et al.* [Sch82] taken from nucleon-nucleus elastic scattering. We have found that the non orthogonality effects between of the basis are not important and do not change the effects of the correlations.

- The effects of *MEC* in quasielastic $(e, e'p)$ reaction are negligible since all the *TB* currents effects diminish at high momentum transfer.

- For photoproton (γ, p) reaction, it is very important to include both *OB* convection and magnetization currents. Although the convection current is strongly dominating at the photon point, with increasing photon energy the magnetization current becomes more important. Also, it is extremely important to include all *TB* seagull, pionic and Δ currents. The destructive interference between seagull and pionic currents reduce the effects of seagull currents. The use of the seagull diagram only, as done in Refs. [Ben94, Gai00], overestimates the *MEC* effects.

- The cross section calculations of photoproton reaction, (γ, p), show larger sensitivity to the different correlation functions than the electron scattering cross sections. We have found that at the photon point this is due to the relatively small difference between the transition matrices of both *IPM* and those containing the correlation function. Thus any small change in the correlation leads to relatively high changes of the cross section.

- The effects of correlations in the (γ, p) reaction at photon energies below 100 MeV are small and produce the same shape of the results of *IPM* with *OB* currents. The role of the correlations increases by increasing the missing momentum of the reaction, i.e. by increasing the photon energy and the values of the proton scattering angles.

- At photon energies above 150 MeV and at large proton scattering angles, both *MEC* and *SRC* play important role on the (γ, p) cross section but the effects of the *MEC* are more sizable.

- The comparison between $(e, e'p)$ and (γ, p) data show that it is possible to reproduce the data for both reactions with the same spectroscopic factor and correlation function only when the *MEC* and *SRC* are included in the (γ, p) reaction.

Finally we would like to discuss some of the limitations of our calculations related to the hypotheses and the approximations of our *SRC* model. One of these limitations is due to the fact that we consider only those diagrams containing a single correlation function. Clearly higher order terms could be important. In the mean time, we have already mentioned that the test of the validity of our model was done [Ama98] for the inclusive nuclear matter charge response. The excellent agreement between our results and those obtained considering an infinite set of diagrams, give us confidence about our approximation, and we trust its validity also in the case of finite nuclear systems and for the *OB* current operators. It would be interesting, in any case, to make other tests about it.

Another limitation of our approach is related to the use of correlation functions of purely scalar Jastrow type. Recent calculations show that the tensor correlations on two-nucleon emission processes [Jan00, Giu99] produce effect comparable, or even larger, than those induced by the scalar correlations. However, these calculations have been done in the single pair approximation, and we have shown how dangerous is to rely on such an approximation which can produce large effects since the three-point counter terms are not present. On the other hand, we know from microscopic calculations [Fab98] that the tensor correlations are essential to bind nuclei. They are also important, together with *MEC* in the nuclear matter transverse quasielastic response [Fab97]. The possible effect of the tensor correlations on nuclear responses is an open problem which should be investigated.

Last, but not least, our model does not take into account those processes beyond the mean field description called *LRC*. These correlations are related to the coupling between the single particle dynamics and the collective excitation modes of the nucleus. Their effects on $(e, e'p)$ processes have been considered in a nuclear matter approach [Ami97], but they do not seem to be relevant. However, one should consider that collective surface vibrations are not present in nuclear matter calculations, and they can be extremely important in finite nuclear systems, as an investigation on the charge density distribution differences of heavy isotones has recently pointed out [Ang01]. As a consequence a calculation of fully correlated responses with including *SRC* and *LRC*, although extremely difficult, would be desirable.

Appendix A

EM Reduced Matrix Elements

In this Appendix, we give the expressions for the $1p-1h$ reduced transition matrix elements given by Eq.(2.39). According to our first order SRC model, we have the contribution from two- and three points diagrams. We will define our multipole expanded operators $O_{J(\eta)}(\mathbf{q})$ in terms of different electromagnetic operators of Eqs. (2.32), (2.33) and (2.34), taking into account $J = \lambda$ and $M = \nu = \eta$ as a result of applying Wigner-Eckart theorem and using the properties of 3j symbol.

A.1 Charge

By inserting the expression of charge operator (2.24) into the multipole expanded charge operator (2.32) and following the definition of Eqs. (2.35) and (2.36), one could get:

$$
\begin{aligned}
O_{J(\eta)} &= \sqrt{2} M_J(q) && \text{(A.1)} \\
&= \sqrt{2}\, j_J(qr_1)\, Y_J(\hat{\mathbf{r}}_1)\ , && \text{(A.2)}
\end{aligned}
$$

for the charge $\eta = 0$. Comparing with our generic expanded operator of Eq. (2.40):

$$F_J(qr_1) \equiv j_J(qr_1) \; , \qquad \mathcal{O}_J(\hat{\mathbf{r}}_1) \equiv Y_J(\hat{\mathbf{r}}_1) \; . \tag{A.3}$$

The matrix $\omega_{\alpha\beta}^{LJ;K}$ of Eq. (2.53) can be evaluated according to the angular operator of Eq. (A.3) as:

$$\begin{aligned} \omega_{\alpha\beta}^{LJ;K} &= \langle\alpha\| \left[Y_J(\hat{\mathbf{r}}_1) \otimes Y_L(\hat{\mathbf{r}}_1)\right]^K \|\beta\rangle \\ &= (-1)^{j_\alpha+j_\beta+K}\widehat{K}\sum_{j_c}\left\{\begin{array}{ccc} j_\beta & j_\alpha & K \\ J & L & j_c \end{array}\right\}\langle\alpha\|Y_J(\hat{\mathbf{r}}_1)\,\|c\rangle\langle c\|Y_L(\hat{\mathbf{r}}_1)\,\|\beta\rangle \, , \end{aligned} \tag{A.4}$$

where usually the intermediate state c will be determined from the properties of the 3j and 6j symbols.

By inserting Eq. (A.3) into the uncorrelated (2.43), two-point (2.46)-(2.51), and three-point (2.56)-(2.61) matrices, we have the final formulae for the charge matrix elements:

$$M_1 = G_E^p(q^2)\,\delta_{t_p,t_h}\,\gamma_{ph}^J\,\mathcal{I}_J^{[ph]}(q) \; , \tag{A.5}$$

$$M_{2.1} = G_E^p(q^2)\,\delta_{t_p,t_h}\,4\pi\,\gamma_{ph}^J\,\mathcal{I}_{J0}^{[ph];[\rho]}(q) \; , \tag{A.6}$$

$$\begin{aligned} M_{2.2} &= G_E^p(q^2)\,\delta_{t_p,t_h}\,\gamma_{ph}^J\sum_{iL}\delta_{t_i,t_p}\,\xi(l_i+l_h+L)\,\widehat{j}_i^2 \\ &\quad\times\left(\begin{array}{ccc} j_i & j_h & L \\ \frac{1}{2} & -\frac{1}{2} & 0 \end{array}\right)^2\mathcal{I}_{JL}^{[pi];[ih]}(q) \; , \end{aligned} \tag{A.7}$$

$$M_{2.3} = \delta_{t_p,t_h}\,4\pi\,\gamma_{ph}^J\,\frac{1}{\widehat{J}^2}\,\mathcal{I}_{JJ}^{[\rho_{\rm ch}];[ph]}(q) \; , \tag{A.8}$$

$$M_{2.4} = G_E^p(q^2)\,\delta_{t_p,t_h}\,\gamma_{ph}^J \sum_{iL} \delta_{t_i,t_p}\,\xi(l_p+l_i+L)\,\widehat{j}_i^2 \times \begin{pmatrix} j_p & j_i & L \\ \frac{1}{2} & -\frac{1}{2} & 0 \end{pmatrix}^2 \mathcal{I}_{JL}^{[ih];[pi]}(q)\ , \tag{A.9}$$

$$M_{3.1} = G_E^p(q^2)\,\delta_{t_p,t_h}\,\gamma_{ph}^J \sum_{ikL} \delta_{t_i,t_p}\,\delta_{t_k,t_p}\,\delta_{j_i,j_p}\,\xi(l_p+l_k+L)\,\xi(l_p+l_i)\,\widehat{j}_k^2 \times \begin{pmatrix} j_p & j_k & L \\ \frac{1}{2} & -\frac{1}{2} & 0 \end{pmatrix}^2 \mathcal{I}_J^{[ih]}(q)\ \mathcal{J}_L^{[pk];[ki]}\ , \tag{A.10}$$

$$M_{3.2} = G_E^p(q^2)\,\delta_{t_p,t_h}\,4\pi\,\gamma_{ph}^J \sum_{i} \delta_{t_i,t_p}\,\delta_{j_i,j_p}\,\xi(l_p+l_i)\ \mathcal{I}_J^{[ih]}(q)\ \mathcal{J}_0^{[pi];[\rho]}\ , \tag{A.11}$$

$$M_{3.3} = G_E^p(q^2)\,\delta_{t_p,t_h}\,\gamma_{ph}^J \sum_{ikL} \delta_{t_i,t_p}\,\delta_{t_k,t_p}\,\delta_{j_i,j_h}\,\xi(l_k+l_h+L)\,\xi(l_i+l_h)\,\widehat{j}_k^2 \times \begin{pmatrix} j_k & j_h & L \\ \frac{1}{2} & -\frac{1}{2} & 0 \end{pmatrix}^2 \mathcal{I}_J^{[pi]}(q)\ \mathcal{J}_L^{[kh];[ik]}\ , \tag{A.12}$$

$$M_{3.4} = G_E^p(q^2)\,\delta_{t_p,t_h}\,4\pi\,\gamma_{ph}^J \sum_{i} \delta_{t_i,t_p}\,\delta_{j_i,j_h}\,\xi(l_i+l_h)\ \mathcal{I}_J^{[pi]}(q)\ \mathcal{J}_0^{[ih];[\rho]}\ , \tag{A.13}$$

$$M_{3.5} = G_E^p(q^2)\,\delta_{t_p,t_h}\,4\pi \sum_{ikL} \delta_{t_i,t_p}\,\delta_{t_k,t_p}\,(-1)^{j_i+j_k+J+L}\,\frac{1}{\widehat{L}^2}\,\gamma_{ik}^J\,\gamma_{pi}^L\,\gamma_{kh}^L \times \begin{Bmatrix} j_p & j_h & J \\ j_k & j_i & L \end{Bmatrix}\ \mathcal{I}_J^{[ik]}(q)\ \mathcal{J}_L^{[pi];[kh]}\ , \tag{A.14}$$

$$M_{3.6} = \delta_{t_p,t_h}\,4\pi\,\frac{1}{\widehat{J}^4}\,\gamma_{ph}^J \sum_{ik} \delta_{t_i,t_k}\,G_E^i(q^2)\ (\gamma_{ik}^J)^2 \mathcal{I}_J^{[ik]}(q)\,\mathcal{J}_J^{[ph];[ki]}\ . \tag{A.15}$$

We get these equations by inserting the operators of Eq. (A.3), thus we should refer to the factor of $\sqrt{2}$ must be multiplied by the above equations to reproduce Eqs. (2.35), (2.36) and (A.2).

In the above equations, the nucleonic internal structure has been considered by folding the pointlike responses with the electromagnetic nucleon form factors of Höhler et.al. [Höh76]. Thus, we have multiplied the above equations by the electric form factor $G_E^{\alpha}(q^2)$ of the nucleon in the single-particle state α.

We have defined the integrals of as:

$$\mathcal{I}_J^{[\alpha\beta]}(q) = \int \mathrm{d}r_1\, r_1^2\, j_J(qr_1)\, R_\alpha^*(r_1)\, R_\beta(r_1) \ , \tag{A.16}$$

$$\mathcal{I}_{JL}^{[\alpha\beta];[\gamma\delta]}(q) = \int \mathrm{d}r_1\, r_1^2\, j_J(qr_1)\, R_\alpha^*(r_1)\, R_\beta(r_1)\, \mathcal{H}_L^{[\gamma\delta]}(r_1) \ , \tag{A.17}$$

$$\mathcal{I}_{J0}^{[\alpha\beta];[\rho]}(q) = \int \mathrm{d}r_1\, r_1^2\, j_J(qr_1)\, R_\alpha^*(r_1)\, R_\beta(r_1)\, \mathcal{H}_0^{[\rho]}(r_1) \ , \tag{A.18}$$

$$\mathcal{I}_{JJ}^{[\rho_{\mathrm{ch}}];[\gamma\delta]}(q) = \int \mathrm{d}r_1\, r_1^2\, j_J(qr_1)\, \rho_{\mathrm{ch}}(r_1)\, \mathcal{H}_J^{[\gamma\delta]}(r_1) \ , \tag{A.19}$$

where $j_J(x)$ is a spherical Bessel function, $\mathcal{H}_L^{[\gamma\delta]}(r)$ is given by Eqs. (2.55), (2.63), $\mathcal{H}_0^{[\rho]}(r)$ is given by Eqs. (2.47), (2.65), and

$$\rho_{\mathrm{ch}}(r) = G_E^{\mathrm{prot}}(q^2)\, \rho_{\mathrm{prot}}(r) + G_E^{\mathrm{neut}}(q^2)\, \rho_{\mathrm{neut}}(r) \ , \tag{A.20}$$

with $\rho_{\mathrm{prot}}(r)$ and $\rho_{\mathrm{neut}}(r)$ the proton and neutron densities, respectively. Finally, the integrals $\mathcal{J}$ are defined in Eqs. (2.62) and (2.64).

A.2 Transverse Electric Current

The transverse electric current has a contribution from both magnetization and convection currents. Thus, we have to define our generic expanded operator individually for both currents.

A.2.1 Electric Magnetization Current

By inserting the expression of magnetization current operator of Eq. (2.27) into the multipole expanded transverse electric excitation of Eq. (2.33) and following the definition of Eqs. (2.35) and (2.36), one could get:

$$\begin{aligned} O_{J(\eta)} &= T^{\mathrm{E}}_{J(\eta);\mathrm{M}}(q) \\ &= q\frac{G_M^\alpha}{2M_\alpha}\, j_J(qr_1)\, \left[Y_J \otimes \boldsymbol{\sigma}\right]^J \,, \end{aligned} \tag{A.21}$$

where $\eta = \pm 1$. We have indicated with $G_M^\alpha(q^2)$ the magnetic form factor [Höh76] of the nucleon in the single-particle state α which we have used instead of anomalous magnetic moment of μ^P and μ^N of Eq. (2.27) and with M_α for the mass of nucleon at this state. Comparing with our generic expanded operator of Eq. (2.40):

$$F_J(qr_1) \equiv q\frac{G_M^\alpha}{2M_\alpha}\, j_J(qr_1)\,, \qquad \mathcal{O}_J(\hat{\mathbf{r}}_1) \equiv \left[Y_J(\hat{\mathbf{r}}_1) \otimes \boldsymbol{\sigma}\right]^J \,. \tag{A.22}$$

The matrices $\omega^J_{\alpha\beta}$ of Eq. (2.44) and $\omega^{LJ;K}_{\alpha\beta}$ of Eq. (2.53) can be evaluated according to the angular operator of Eq. (A.22) as:

$$\begin{aligned} \omega^J_{\alpha\beta} &= \langle \alpha \parallel \left[Y_J(\hat{\mathbf{r}}_1) \otimes \boldsymbol{\sigma}\right]^J \parallel \beta \rangle \\ &= \frac{(-1)^{l_\alpha}}{\sqrt{4\pi}}\, \widehat{j}_\alpha \widehat{j}_\beta \widehat{J} \begin{pmatrix} j_\beta & j_\alpha & J \\ -\frac{1}{2} & -\frac{1}{2} & 1 \end{pmatrix} \xi(l_\alpha + l_\beta + J) \end{aligned} \tag{A.23}$$

and

$$
\begin{aligned}
\omega_{\alpha\beta}^{LJ;K} &= \langle\alpha\| \left[[Y_J(\hat{\mathbf{r}}_1)\otimes\boldsymbol{\sigma}]^J \otimes Y_L(\hat{\mathbf{r}}_1)\right]^K \|\beta\rangle \\
&= \frac{(-1)^{J-L+l_\alpha+1}}{4\pi}\sqrt{6}\,\widehat{j}_\alpha\widehat{j}_\beta\widehat{J}^2\widehat{L}\widehat{K}\widehat{l}_\alpha\widehat{l}_\beta\sum_\kappa \widehat{\kappa}^2 \qquad \text{(A.24)} \\
&\times \begin{Bmatrix} K & L & J \\ J & 1 & \kappa \end{Bmatrix} \begin{pmatrix} J & \kappa & L \\ 0 & 0 & 0 \end{pmatrix} \begin{pmatrix} l_\alpha & \kappa & l_\beta \\ 0 & 0 & 0 \end{pmatrix} \begin{Bmatrix} l_\alpha & \frac{1}{2} & j_\alpha \\ l_\beta & \frac{1}{2} & j_\beta \\ \kappa & 1 & K \end{Bmatrix}
\end{aligned}
$$

By inserting Eq. (A.22) into the uncorrelated (2.43), two-point (2.46)-(2.51), and three-point (2.56)-(2.61) matrices, we have the final formulae for the transverse electric magnetization current matrix elements:

$$
T^{\mathrm{E}}_{1;\mathrm{M}} = -q\,\frac{G_M^p(q^2)}{2M_p}\,\delta_{t_p,t_h}\,\gamma_{ph}^J\,\frac{\chi_p-\chi_h}{\sqrt{J(J+1)}}\,\mathcal{I}_J^{[ph]}(q)\ , \qquad \text{(A.25)}
$$

$$
T^{\mathrm{E}}_{2.1;\mathrm{M}} = -q\,\frac{G_M^p(q^2)}{2M_p}\,\delta_{t_p,t_h}\,4\pi\,\gamma_{ph}^J\,\frac{\chi_p-\chi_h}{\sqrt{J(J+1)}}\,\mathcal{I}_{J0}^{[ph];[\rho]}(q)\ , \qquad \text{(A.26)}
$$

$$
\begin{aligned}
T^{\mathrm{E}}_{2.2;\mathrm{M}} &= q\,\frac{G_M^p(q^2)}{2M_p}\,\delta_{t_p,t_h}\sqrt{\frac{3}{\pi}}\,(-1)^{l_p+j_p+J+\frac{1}{2}}\,\widehat{l}_p\,\widehat{j}_p\,\widehat{j}_h\,\widehat{J} \\
&\times \sum_{iL}\delta_{t_i,t_p}\,\xi(l_i+l_h+L)\,\widehat{l}_i\,\widehat{j}_i^2 \begin{pmatrix} j_i & j_h & L \\ \frac{1}{2} & -\frac{1}{2} & 0 \end{pmatrix} \mathcal{I}_{JL}^{[pi];[ih]}(q) \\
&\times \sum_\kappa \xi(L+J+\kappa)\,\widehat{\kappa}^2 \begin{pmatrix} l_p & l_i & \kappa \\ 0 & 0 & 0 \end{pmatrix} \sum_K \widehat{K}^2 \begin{Bmatrix} L & K & J \\ j_p & j_h & j_i \end{Bmatrix} \\
&\times \begin{pmatrix} 1 & K & \kappa \\ 1 & -1 & 0 \end{pmatrix} \begin{pmatrix} K & J & L \\ 1 & -1 & 0 \end{pmatrix} \begin{Bmatrix} l_p & \frac{1}{2} & j_p \\ l_i & \frac{1}{2} & j_i \\ \kappa & 1 & K \end{Bmatrix}\ , \qquad \text{(A.27)}
\end{aligned}
$$

$$
T^{\mathrm{E}}_{2.3;\mathrm{M}} = 0\ , \qquad \text{(A.28)}
$$

$$
\begin{aligned}
T^{\mathrm{E}}_{2.4;\mathrm{M}} &= q\,\frac{G^p_M(q^2)}{2M_p}\,\delta_{t_p,t_h}\,\sqrt{\frac{3}{\pi}}\,(-1)^{l_p+j_p+j_h}\,\widehat{l}_h\,\widehat{j}_p\,\widehat{j}_h\,\widehat{J}\sum_{iL}\delta_{t_i,t_p}\,(-1)^{j_i-\frac{1}{2}} \\
&\times\xi(l_p+l_i+L)\widehat{l}_i\,\widehat{j}_i^2\begin{pmatrix} j_p & j_i & L \\ \frac{1}{2} & -\frac{1}{2} & 0 \end{pmatrix}\mathcal{I}^{[ih];[pi]}_{JL}(q)\sum_{\kappa}\xi(L+J+\kappa) \\
&\times\widehat{\kappa}^2\begin{pmatrix} l_i & l_h & \kappa \\ 0 & 0 & 0 \end{pmatrix}\sum_K(-1)^K\,\widehat{K}^2\begin{Bmatrix} L & K & J \\ j_h & j_p & j_i \end{Bmatrix} \\
&\times\begin{pmatrix} 1 & K & \kappa \\ 1 & -1 & 0 \end{pmatrix}\begin{pmatrix} K & J & L \\ 1 & -1 & 0 \end{pmatrix}\begin{Bmatrix} l_i & \frac{1}{2} & j_i \\ l_h & \frac{1}{2} & j_h \\ \kappa & 1 & K \end{Bmatrix}, \qquad \text{(A.29)}
\end{aligned}
$$

$$
\begin{aligned}
T^{\mathrm{E}}_{3.1;\mathrm{M}} &= -q\,\frac{G^p_M(q^2)}{2M_p}\,\delta_{t_p,t_h}\,\gamma^J_{ph}\,\frac{\chi_p-\chi_h}{\sqrt{J(J+1)}}\sum_{ikL}\delta_{t_i,t_p}\,\delta_{t_k,t_p}\,\delta_{j_i,j_p} \\
&\times\xi(l_p+l_k+L)\,\xi(l_p+l_i)\,\widehat{j}_k^2\begin{pmatrix} j_p & j_k & L \\ \frac{1}{2} & -\frac{1}{2} & 0 \end{pmatrix}^2\mathcal{I}^{[ih]}_J(q)\,\mathcal{J}^{[pk];[ki]}_L\,, \\
&\qquad \text{(A.30)}
\end{aligned}
$$

$$
\begin{aligned}
T^{\mathrm{E}}_{3.2;\mathrm{M}} &= -q\,\frac{G^p_M(q^2)}{2M_p}\,\delta_{t_p,t_h}\,4\pi\,\gamma^J_{ph}\,\frac{\chi_p-\chi_h}{\sqrt{J(J+1)}}\sum_{i}\delta_{t_i,t_p}\,\delta_{j_i,j_p}\,\xi(l_p+l_i) \\
&\times\mathcal{I}^{[ih]}_J(q)\,\mathcal{J}^{[pi];[\rho]}_0\,, \qquad \text{(A.31)}
\end{aligned}
$$

$$
\begin{aligned}
T^{\mathrm{E}}_{3.3;\mathrm{M}} &= -q\,\frac{G^p_M(q^2)}{2M_p}\,\delta_{t_p,t_h}\,\gamma^J_{ph}\,\frac{\chi_p-\chi_h}{\sqrt{J(J+1)}}\sum_{ikL}\delta_{t_i,t_p}\,\delta_{t_k,t_p}\,\delta_{j_i,j_h} \\
&\times\xi(l_k+l_h+L)\,\xi(l_i+l_h)\,\widehat{j}_k^2\begin{pmatrix} j_k & j_h & L \\ \frac{1}{2} & -\frac{1}{2} & 0 \end{pmatrix}^2\mathcal{I}^{[pi]}_J(q)\,\mathcal{J}^{[kh];[ik]}_L, \\
&\qquad \text{(A.32)}
\end{aligned}
$$

$$
\begin{aligned}
T^{\mathrm{E}}_{3.4;\mathrm{M}} &= -q\,\frac{G^p_M(q^2)}{2M_p}\,\delta_{t_p,t_h}\,4\pi\,\gamma^J_{ph}\,\frac{\chi_p-\chi_h}{\sqrt{J(J+1)}}\sum_{i}\delta_{t_i,t_p}\,\delta_{j_i,j_h}\,\xi(l_i+l_h) \\
&\times\mathcal{I}^{[pi]}_J(q)\,\mathcal{J}^{[ih];[\rho]}_0\,, \qquad \text{(A.33)}
\end{aligned}
$$

$$
\begin{aligned}
T^{\mathrm{E}}_{3.5;\mathrm{M}} &= -q\,\frac{G^p_M(q^2)}{2M_p}\,\delta_{t_p,t_h}\,4\pi\,\frac{1}{\sqrt{J(J+1)}}\sum_{ikL}\delta_{t_i,t_p}\,\delta_{t_k,t_p}\,(-1)^{j_i+j_k+J+L} \\
&\times\frac{\chi_i-\chi_k}{\widehat{L}^2}\gamma^J_{ik}\,\gamma^L_{pi}\,\gamma^L_{kh}\left\{\begin{array}{ccc} j_p & j_h & J \\ j_k & j_i & L \end{array}\right\}\mathcal{I}^{[ik]}_J(q)\,\mathcal{J}^{[pi];[kh]}_L\ , \qquad \text{(A.34)}
\end{aligned}
$$

$$
\begin{aligned}
T^{\mathrm{E}}_{3.6;\mathrm{M}} &= -\delta_{t_p,t_h}\,4\pi\,\frac{1}{\widehat{J}^4\sqrt{J(J+1)}}\,\gamma^J_{ph}\sum_{ik}\delta_{t_i,t_k}\,q\,\frac{G^i_M(q^2)}{2M_i}\,(\chi_i-\chi_k)\,(\gamma^J_{ik})^2 \\
&\times\mathcal{I}^{[ik]}_J(q)\,\mathcal{J}^{[ph];[ki]}_J\ . \qquad \text{(A.35)}
\end{aligned}
$$

In the above equations, the symbol χ_α has been defined as:

$$
\chi_\alpha = (l_\alpha - j_\alpha)\,(2j_\alpha+1)\ . \qquad \text{(A.36)}
$$

A.2.2 Electric Convection Current

By inserting the expression of convection current operator of Eq. (2.26) into the multipole expanded transverse electric excitation of Eq. (2.33) and following the definition of Eqs. (2.35) and (2.36), one could get:

$$
\begin{aligned}
O_{J(\eta)} &= T^{\mathrm{E}}_{J(\eta);\mathrm{C}}(q) \\
&= \frac{1}{2M_\alpha}\sum_{s=\pm1} j_{J_s}(qr_1)\,s\sqrt{(J+\delta_{s,-1})}\left[\mathbf{Y}_{J\,J_s}(\hat{\mathbf{r}}_1)\overrightarrow{\nabla}+\overleftarrow{\nabla}\mathbf{Y}_{J\,J_s}(\hat{\mathbf{r}}_1)\right] \\
&= \frac{1}{2M_\alpha}\sum_{s=\pm1} j_{J_s}(qr_1)\,s\sqrt{(J+\delta_{s,-1})} \\
&\qquad\times\left[\left[Y_{J_s}(\hat{\mathbf{r}}_1)\otimes\overrightarrow{\nabla}\right]^J+\left[Y_{J_s}(\hat{\mathbf{r}}_1)\otimes\overleftarrow{\nabla}\right]^J\right]\ , \qquad \text{(A.37)}
\end{aligned}
$$

where $\eta = \pm1$ and $J_s = J + s$. Comparing with our generic expanded operator of Eq. (2.40):

$$
F_J(qr_1) \equiv \frac{1}{2M_{alpha}}\,j_{J_s}(qr_1)\ , \qquad \text{(A.38)}
$$

$$
\begin{aligned}
\mathcal{O}_J(\hat{\mathbf{r}}_1) &\equiv \mathcal{O}^a_J(\hat{\mathbf{r}}_1) + \mathcal{O}^b_J(\hat{\mathbf{r}}_1) \\
&= \left[Y_{J_s}(\hat{\mathbf{r}}_1) \otimes \overrightarrow{\nabla}\right]^J + \left[Y_{J_s}(\hat{\mathbf{r}}_1) \otimes \overleftarrow{\nabla}\right]^J \ . \qquad \text{(A.39)}
\end{aligned}
$$

In this case, we will not only calculate the angular matrices but also the radial integrals of the diagrams will affect by the presence of the ingredient ∇. Thus the useful matrix element to be evaluated in case of $F_J(qr_1)$ and $\mathcal{O}^a_J(\hat{\mathbf{r}}_1)$ of Eq. (A.39) is:

$$
\begin{aligned}
&\langle \alpha \,\|\, j_{J_s}(qr_1) \left[\left[Y_{J_s}(\hat{\mathbf{r}}_1) \otimes \overrightarrow{\nabla}\right]^J \otimes Y_L(\hat{\mathbf{r}}_1)\right]^K \,\|\, \beta \rangle \\
&\quad = (-1)^{J-L+1}\sqrt{4\pi}\widehat{J}_s\widehat{J}\widehat{L}\sum_{\kappa}\widehat{\kappa}\begin{pmatrix} J_s & \kappa & L \\ 0 & 0 & 0 \end{pmatrix}\begin{Bmatrix} \kappa & L & J \\ J_s & 1 & \kappa \end{Bmatrix} \\
&\qquad \times \langle \alpha \,\|\, j_{J_s}(qr_1) \left[Y_{\kappa}(\hat{\mathbf{r}}_1) \otimes \overrightarrow{\nabla}\right]^K \,\|\, \beta \rangle \ , \qquad \text{(A.40)}
\end{aligned}
$$

where

$$
\begin{aligned}
T^{\mathrm{E}}_{\mathrm{C}}(q) &\equiv \langle \alpha \,\|\, j_{J_s}(qr_1) \left[Y_{\kappa}(\hat{\mathbf{r}}_1) \otimes \overrightarrow{\nabla}\right]^K \,\|\, \beta \rangle \\
&= \frac{(-1)^{l_\alpha+l_\beta+j_\beta+\frac{1}{2}}}{\sqrt{4\pi}}\widehat{j}_\alpha\widehat{j}_\beta\widehat{l}_\alpha\widehat{K}\widehat{\kappa}\begin{Bmatrix} l_\alpha & l_\beta & K \\ j_\beta & j_\alpha & \frac{1}{2} \end{Bmatrix} \\
&\quad \times\Bigg[\widehat{(l_\beta+1)}\sqrt{l_\beta+1}\begin{pmatrix} l_\alpha & \kappa & l_\beta+1 \\ 0 & 0 & 0 \end{pmatrix}\begin{Bmatrix} l_\beta & l_\alpha & K \\ \kappa & 1 & l_\beta+1 \end{Bmatrix} \\
&\qquad \times \int \mathrm{d}r_1\, r_1^2\, j_{J_s}(qr_1) R^*_\alpha(r_1)\left(\frac{\mathrm{d}}{\mathrm{d}r_1} - \frac{l_\beta}{r_1}\right) R_\beta(r_1) \\
&\quad +\widehat{(l_\beta-1)}(-\sqrt{l_\beta})\begin{pmatrix} l_\alpha & \kappa & l_\beta-1 \\ 0 & 0 & 0 \end{pmatrix}\begin{Bmatrix} l_\beta & l_\alpha & K \\ \kappa & 1 & l_\beta-1 \end{Bmatrix} \\
&\qquad \times \int \mathrm{d}r_1\, r_1^2\, j_{J_s}(qr_1) R^*_\alpha(r_1)\left(\frac{\mathrm{d}}{\mathrm{d}r_1} + \frac{l_\beta+1}{r_1}\right) R_\beta(r_1)\Bigg] \ . \\
&\qquad\qquad \text{(A.41)}
\end{aligned}
$$

Using the second operator $\mathcal{O}^b_J(\hat{\mathbf{r}}_1)$ of Eq. (A.39) will give similar equations but with derivation of the radial conjugated function instead.

By inserting Eqs. (A.38) and (A.39) into the uncorrelated (2.43), two-point (2.46)-(2.51), and three-point (2.56)-(2.61) matrices, and taking into account the electric form factor $G_E^{\alpha}(q^2)$ of Höhler et.al. [Höh76], we have the final formulae for the transverse electric convection current matrix elements:

$$T_{1;C}^{\mathrm{E}} = \frac{G_E^p(q^2)}{2M_p}\,\delta_{t_p,t_h}\,\frac{\gamma_{ph}^J}{\widehat{J}^2}\Big[(\chi_{ph}\Big(\frac{\sqrt{J}}{\sqrt{J+1}}\mathcal{I}_{J+1}^{[\frac{1}{r}ph]}(q) - \frac{\sqrt{J+1}}{\sqrt{J}}\mathcal{I}_{J-1}^{[\frac{1}{r}ph]}(q)\Big) + \sqrt{J(J+1)}\Big\{\mathcal{I}_{J+1}^{[ph'-p'h]}(q) + \mathcal{I}_{J-1}^{[ph'-p'h]}(q)\Big\}\Big]\,, \tag{A.42}$$

$$T_{2.1;\mathrm{C}}^{\mathrm{E}} = \frac{G_E^p(q^2)}{2M_p}\,\delta_{t_p,t_h}\,4\pi\,\frac{\gamma_{ph}^J}{\widehat{J}^2} \times\Big[\chi_{ph}\Big(\frac{\sqrt{J}}{\sqrt{J+1}}\mathcal{I}_{J+1,0}^{[\frac{1}{r}ph];\rho}(q) - \frac{\sqrt{J+1}}{\sqrt{J}}\mathcal{I}_{J-1,0}^{[\frac{1}{r}ph];\rho}(q)\Big) + \sqrt{J(J+1)}\Big(\mathcal{I}_{J+1,0}^{[ph'-p'h];\rho}(q) + \mathcal{I}_{J-1,0}^{[ph'-p'h];\rho}(q)\Big)\Big]\,, \tag{A.43}$$

$$\begin{aligned} T_{2.2;\mathrm{C}}^{\mathrm{E}} = {} & \frac{G_M^p(q^2)}{2M_p}\,\delta_{t_p,t_h}\,\frac{\widehat{j}_p\widehat{j}_h}{\sqrt{4\pi}}\sum_{i,L,K,\kappa}(-1)^{j_p+j_h+J+l_p+l_h}\delta_{t_i,t_p}\xi(l_i+l_h+L) \\ & \times\widehat{K}^2\widehat{\kappa}^2\widehat{j}_i^2\left\{\begin{array}{ccc} L & K & J \\ j_p & j_h & j_i \end{array}\right\}\left(\begin{array}{ccc} j_i & L & j_h \\ \frac{1}{2} & 0 & -\frac{1}{2} \end{array}\right)\left\{\begin{array}{ccc} l_p & l_i & K \\ j_i & j_p & \frac{1}{2} \end{array}\right\} \\ & \times\Big[\sqrt{J}(\widehat{J+1})\left\{\begin{array}{ccc} K & L & J \\ J+1 & 1 & \kappa \end{array}\right\}\left(\begin{array}{ccc} J+1 & \kappa & L \\ 0 & 0 & 0 \end{array}\right)X_{2.2;J+1}^{[pi',ip'];[ih]} \\ & -\sqrt{J+1}(\widehat{J-1})\left\{\begin{array}{ccc} K & L & J \\ J-1 & 1 & \kappa \end{array}\right\}\left(\begin{array}{ccc} J-1 & \kappa & L \\ 0 & 0 & 0 \end{array}\right) \\ & \times X_{2.2;J-1}^{[pi',ip'];[ih]}\Big], \end{aligned} \tag{A.44}$$

$$T_{2.3;\mathrm{C}}^{\mathrm{E}} = 0\,, \tag{A.45}$$

$$
\begin{aligned}
T^{\mathrm{E}}_{2.4;\mathrm{C}} &= \frac{G^p_M(q^2)}{2M_p}\,\delta_{t_p,t_h}\,\frac{\widehat{j}_p\widehat{j}_h}{\sqrt{4\pi}}\sum_{i,L,K,\kappa}(-1)^{l_i+l_h+1}\delta_{t_i,t_p}\xi(l_p+l_i+L)\widehat{K}^2\widehat{\kappa}^2\widehat{j}_i^2 \\
&\times\left\{\begin{array}{ccc} K & L & J \\ j_p & j_h & j_i\end{array}\right\}\left(\begin{array}{ccc} j_p & L & j_i \\ \frac{1}{2} & 0 & -\frac{1}{2}\end{array}\right)\left\{\begin{array}{ccc} l_i & l_h & K \\ j_h & j_i & \frac{1}{2}\end{array}\right\} \\
&\times\Bigg[\sqrt{J}(\widehat{J+1})\left\{\begin{array}{ccc} K & L & J \\ J+1 & 1 & \kappa\end{array}\right\}\left(\begin{array}{ccc} J+1 & \kappa & L \\ 0 & 0 & 0\end{array}\right)X^{[ih',hi'];[pi]}_{2.4;J+1} \\
&-\sqrt{J+1}(\widehat{J-1})\left\{\begin{array}{ccc} K & L & J \\ J-1 & 1 & \kappa\end{array}\right\}\left(\begin{array}{ccc} J-1 & \kappa & L \\ 0 & 0 & 0\end{array}\right) \\
&\qquad\times X^{[ih',hi'];[pi]}_{2.4;J-1}\Bigg], \qquad \text{(A.46)}
\end{aligned}
$$

$$
\begin{aligned}
T^{\mathrm{E}}_{3.1;\mathrm{C}} &= \frac{G^p_E(q^2)}{2M_p}\,\delta_{t_p,t_h}\,\frac{\gamma^J_{ph}}{\widehat{J}^2}\times\sum_{ikL}\delta_{t_i,t_p}\,\delta_{t_k,t_p}\,\delta_{j_i,j_p}\xi(l_p+l_k+L)\,\xi(l_p+l_i)\,\widehat{j}_k^2 \\
&\times\left(\begin{array}{ccc} j_p & j_k & L \\ \frac{1}{2} & -\frac{1}{2} & 0\end{array}\right)^2\Bigg[\chi_{ph}\Big(\frac{\sqrt{J}}{\sqrt{J+1}}\mathcal{I}^{[\frac{1}{r}ih]}_{J+1}(q)-\frac{\sqrt{J+1}}{\sqrt{J}}\mathcal{I}^{[\frac{1}{r}ih]}_{J-1}(q)\Big) \\
&\quad+\sqrt{J(J+1)}\Big(\mathcal{I}^{[ih'-i'h]}_{J+1}(q)+\mathcal{I}^{[ih'-i'h]}_{J-1}(q)\Big)\Bigg]\,\mathcal{J}^{[pk];[ki]}_L,
\end{aligned}
$$

(A.47)

$$
\begin{aligned}
T^{\mathrm{E}}_{3.2;\mathrm{C}} &= \frac{G^p_E(q^2)}{2M_p}\,\delta_{t_p,t_h}\,4\pi\,\frac{\gamma^J_{ph}}{\widehat{J}^2}\sum_{i}\delta_{t_i,t_p}\,\delta_{j_i,j_p}\,\xi(l_p+l_i) \\
&\times\Bigg[\chi_{ph}\Big(\frac{\sqrt{J}}{\sqrt{J+1}}\mathcal{I}^{[\frac{1}{r}ih]}_{J+1}(q)-\frac{\sqrt{J+1}}{\sqrt{J}}\mathcal{I}^{[\frac{1}{r}ih]}_{J-1}(q)\Big) \\
&\quad+\sqrt{J(J+1)}\Big(\mathcal{I}^{[ih'-i'h]}_{J+1}(q)+\mathcal{I}^{[ih'-i'h]}_{J-1}(q)\Big)\Bigg]\,\mathcal{J}^{[pi];\rho}_0\,, \qquad \text{(A.48)}
\end{aligned}
$$

$$
\begin{aligned}
T^{\mathrm{E}}_{3.3;\mathrm{C}} &= \frac{G^p_E(q^2)}{2M_p}\,\delta_{t_p,t_h}\,\frac{\gamma^J_{ph}}{\widehat{J}^2}\times\sum_{ikL}\delta_{t_i,t_p}\,\delta_{t_k,t_p}\,\delta_{j_i,j_h}\xi(l_k+l_h+L)\,\xi(l_i+l_h) \\
&\times\widehat{j}_k^2\left(\begin{array}{ccc} j_k & j_h & L \\ \frac{1}{2} & -\frac{1}{2} & 0\end{array}\right)^2\Bigg[\chi_{ph}\Big(\frac{\sqrt{J}}{\sqrt{J+1}}\mathcal{I}^{[\frac{1}{r}pi]}_{J+1}(q)-\frac{\sqrt{J+1}}{\sqrt{J}}\mathcal{I}^{[\frac{1}{r}pi]}_{J-1}(q)\Big) \\
&\quad+\sqrt{J(J+1)}\Big(\mathcal{I}^{[pi'-p'i]}_{J+1}(q)+\mathcal{I}^{[pi'-p'i]}_{J-1}(q)\Big)\Bigg]\,\mathcal{J}^{[kh];[ik]}_L,
\end{aligned}
$$

(A.49)

$$
\begin{aligned}
T^{\mathrm{E}}_{3.4;\mathrm{C}} &= \frac{G^p_E(q^2)}{2M_p}\,\delta_{t_p,t_h}\,4\pi\,\frac{\gamma^J_{ph}}{\widehat{J}^2}\,\sum_i \delta_{t_i,t_p}\,\delta_{j_i,j_h}\,\xi(l_i+l_h) \\
&\quad\times\Big[\chi_{ph}\Big(\frac{\sqrt{J}}{\sqrt{J+1}}\mathcal{I}^{[\frac{1}{r}pi]}_{J+1}(q)-\frac{\sqrt{J+1}}{\sqrt{J}}\mathcal{I}^{[\frac{1}{r}pi]}_{J-1}(q)\Big) \\
&\qquad+\sqrt{J(J+1)}\Big(\mathcal{I}^{[pi'-p'i]}_{J+1}(q)+\mathcal{I}^{[pi'-p'i]}_{J-1}(q)\Big)\Big]\,\mathcal{J}^{[ih];\rho}_0\;, \qquad (\mathrm{A.50})
\end{aligned}
$$

$$
\begin{aligned}
T^{\mathrm{E}}_{3.5;\mathrm{C}} &= \frac{G^p_E(q^2)}{2M_p}\,\delta_{t_p,t_h}\,4\pi\,\frac{\gamma^J_{ph}}{\widehat{J}^2}\,\times\sum_{ikL}\delta_{t_i,t_p}\,\delta_{t_k,t_p}\frac{(-1)^{j_i+j_k+J+L}}{\widehat{L}^2}\,\gamma^J_{ik}\,\gamma^L_{pi}\,\gamma^L_{kh} \\
&\quad\times\left\{\begin{array}{ccc} j_p & j_h & J \\ j_k & j_i & L\end{array}\right\}\Big[\chi_{ik}\Big(\frac{\sqrt{J}}{\sqrt{J+1}}\mathcal{I}^{[\frac{1}{r}ik]}_{J+1}(q)-\frac{\sqrt{J+1}}{\sqrt{J}}\mathcal{I}^{[\frac{1}{r}ik]}_{J-1}(q)\Big) \\
&\qquad+\sqrt{J(J+1)}\Big(\mathcal{I}^{[ik'-i'k]}_{J+1}(q)+\mathcal{I}^{[ik'-i'k]}_{J-1}(q)\Big)\Big]\,\mathcal{J}^{[pi];[kh]}_L\;, \qquad (\mathrm{A.51})
\end{aligned}
$$

$$
\begin{aligned}
T^{\mathrm{E}}_{3.6;\mathrm{C}} &= \delta_{t_p,t_h}\,4\pi\,\frac{\gamma^J_{ph}}{\widehat{J}^6}\sum_{ik}\delta_{t_i,t_k}\,\frac{G^i_M(q^2)}{2M_i}\,(\gamma^J_{ik})^2 \\
&\quad\times\Big[\chi_{ik}\Big(\frac{\sqrt{J}}{\sqrt{J+1}}\mathcal{I}^{[\frac{1}{r}ik]}_{J+1}(q)-\frac{\sqrt{J+1}}{\sqrt{J}}\mathcal{I}^{[\frac{1}{r}ik]}_{J-1}(q)\Big) \\
&\qquad+\sqrt{J(J+1)}\Big(\mathcal{I}^{[ik'-i'k]}_{J+1}(q)+\mathcal{I}^{[ik'-i'k]}_{J-1}(q)\Big)\Big]\,\mathcal{J}^{[ph];[ki]}_J\;. \qquad (\mathrm{A.52})
\end{aligned}
$$

In the above equations, we have indicated:

$$
\chi_{\alpha\,\beta}=(\chi_\alpha-\chi_\beta)(\chi_\alpha+\chi_\beta+1)\,, \qquad (\mathrm{A.53})
$$

and for the two points we have defined:

$$
\begin{aligned}
X^{[(pi)'];[ih]}_{2.2;J_s} &= (-1)^K\widehat{l}_p\Big[(\widehat{l_i+1})\sqrt{l_i+1}\left(\begin{array}{ccc} l_p & \kappa & l_i+1 \\ 0 & 0 & 0\end{array}\right)\left\{\begin{array}{ccc} l_i & l_p & K \\ \kappa & 1 & l_i+1\end{array}\right\}\mathcal{I}^{[p(\mathrm{d}\ell_i)i];[ih]}_{J_s,L}(q) \\
&\quad+(\widehat{l_i-1})(-\sqrt{l_i})\left(\begin{array}{ccc} l_p & \kappa & l_i-1 \\ 0 & 0 & 0\end{array}\right)\left\{\begin{array}{ccc} l_i & l_p & K \\ \kappa & 1 & l_i-1\end{array}\right\}\mathcal{I}^{[p(\mathrm{d}\ell_{i+1})i];[ih]}_{J_s,L}(q)\Big] \\
&\quad+(-1)^\kappa\widehat{l}_i\Big[(\widehat{l_p+1})\sqrt{l_p+1}\left(\begin{array}{ccc} l_i & \kappa & l_p+1 \\ 0 & 0 & 0\end{array}\right)\left\{\begin{array}{ccc} l_p & l_i & K \\ \kappa & 1 & l_p+1\end{array}\right\}\mathcal{I}^{[(\mathrm{d}\ell_p)p\,i];[ih]}_{J_s,L}(q) \\
&\quad+(\widehat{l_p-1})(-\sqrt{l_p})\left(\begin{array}{ccc} l_i & \kappa & l_p-1 \\ 0 & 0 & 0\end{array}\right)\left\{\begin{array}{ccc} l_p & l_i & K \\ \kappa & 1 & l_p-1\end{array}\right\}\mathcal{I}^{[(\mathrm{d}\ell_{p+1})p\,i];[ih]}_{J_s,L}(q)\Big]
\end{aligned}
$$

(A.54)

$$
\begin{aligned}
X_{2.4;J+1}^{[(ih)'];[pi]} = \widehat{l_i}\Bigg[&(\widehat{l_h+1})\sqrt{l_h+1}\begin{pmatrix} l_i & \kappa & l_h+1 \\ 0 & 0 & 0 \end{pmatrix}\begin{Bmatrix} l_h & l_i & K \\ \kappa & 1 & l_h+1 \end{Bmatrix}\mathcal{I}_{J_s,L}^{[i(\mathrm{d}\ell_h)h];[pi]}(q) \\
&+(\widehat{l_h-1})(-\sqrt{l_h})\begin{pmatrix} l_i & \kappa & l_h-1 \\ 0 & 0 & 0 \end{pmatrix}\begin{Bmatrix} l_h & l_i & K \\ \kappa & 1 & l_h-1 \end{Bmatrix}\mathcal{I}_{J_s,L}^{[i(\mathrm{d}\ell_{h+1})h];[pi]}(q)\Bigg] \\
&+(-1)^{\kappa-K}\widehat{l_h}\Bigg[(\widehat{l_i+1})\sqrt{l_i+1}\begin{pmatrix} l_h & \kappa & l_i+1 \\ 0 & 0 & 0 \end{pmatrix}\begin{Bmatrix} l_i & l_h & K \\ \kappa & 1 & l_i+1 \end{Bmatrix}\mathcal{I}_{J_s,L}^{[(\mathrm{d}\ell_i)i\,h];[pi]}(q) \\
&+(\widehat{l_i-1})(-\sqrt{l_i})\begin{pmatrix} l_h & \kappa & l_i-1 \\ 0 & 0 & 0 \end{pmatrix}\begin{Bmatrix} l_i & l_h & K \\ \kappa & 1 & l_i-1 \end{Bmatrix}\mathcal{I}_{J_s,L}^{[(\mathrm{d}\ell_{i+1})i\,h];[pi]}(q)\Bigg].
\end{aligned} \tag{A.55}
$$

The integrals are defined as follow:

$$
\mathcal{I}_{J_s}^{[\frac{1}{r}\alpha\beta]}(q) = \int \mathrm{d}r_1 r_1^2 j_{J_s}(qr_1)\frac{R_\alpha^*(r_1)R_\beta(r_1)}{r_1}\,, \tag{A.56}
$$

$$
\mathcal{I}_{J_s}^{[\alpha\beta'-\alpha'\beta]}(q) = \int \mathrm{d}r_1 r_1^2 j_{J_s}(qr_1)\left[R_\alpha^*(r_1)\frac{\mathrm{d}R_\beta(r_1)}{\mathrm{d}r_1} - \frac{\mathrm{d}R_\alpha^*(r_1)}{\mathrm{d}r_1}R_\beta(r_1)\right], \tag{A.57}
$$

$$
\mathcal{I}_{J_s,0}^{[\frac{1}{r}\alpha\beta];[\rho]}(q) = \int \mathrm{d}r_1\, r_1^2\, j_{J_s}(qr_1)\,\frac{R_\alpha^*(r_1)\,R_\beta(r_1)}{r_1}\,\mathcal{H}_0^{[\rho]}(r_1)\,, \tag{A.58}
$$

$$
\begin{aligned}
\mathcal{I}_{J+1,0}^{[\alpha\beta'-\alpha'\beta];[\rho]}(q) &= \int \mathrm{d}r_1 r_1^2 j_{J_s}(qr_1)\left[R_\alpha^*(r_1)\frac{\mathrm{d}R_\beta(r_1)}{\mathrm{d}r_1} - \frac{\mathrm{d}R_\alpha^*(r_1)}{\mathrm{d}r_1}R_\beta(r_1)\right] \\
&\quad \times \mathcal{H}_0^{[\rho]}(r_1),
\end{aligned} \tag{A.59}
$$

$$
\begin{aligned}
\mathcal{I}_{J_s,L}^{[\alpha(\mathrm{d}\ell_\beta)\beta];[\gamma\delta]}(q) &= \int \mathrm{d}r_1 r_1^2 j_{J_s}(qr_1)\left[R_\alpha^*(r_1)\frac{\mathrm{d}R_\beta(r_1)}{\mathrm{d}r_1} - \frac{l_\beta}{r_1}R_\alpha^*(r_1)R_\beta(r_1)\right] \\
&\quad \times \mathcal{H}_L^{[\gamma\delta]}(r_1)\,,
\end{aligned} \tag{A.60}
$$

$$
\begin{aligned}
\mathcal{I}_{J_s,L}^{[\alpha(\mathrm{d}\ell_{\beta+1})\beta];[\gamma\delta]}(q) &= \int \mathrm{d}r_1 r_1^2 j_{J_s}(qr_1) \\
&\quad \times \left[R_\alpha^*(r_1)\frac{\mathrm{d}R_\beta(r_1)}{\mathrm{d}r_1} + \frac{l_\beta+1}{r_1}R_\alpha^*(r_1)R_\beta(r_1)\right]\mathcal{H}_L^{[\gamma\delta]}(r_1).
\end{aligned} \tag{A.61}
$$

A.3 Transverse Magnetic Current

Again, the transverse magnetic current has both magnetization and convection currents contribution, one should distinguish between them.

A.3.1 Magnetic Magnetization Current

By inserting the expression of magnetization current operator of Eq. (2.27) into the multipole expanded transverse magnetic excitation of Eq. (2.34) and following the definition of Eqs. (2.35) and (2.36), one has:

$$\begin{aligned} O_{J(\eta)} &= T^{\mathrm{M}}_{J(\eta);\mathrm{M}}(q) \\ &= -iq\,\frac{G^{\alpha}_{M}(q^2)}{2M_\alpha}\,\frac{1}{\widehat{J}}\sum_{s=\pm} s\,\sqrt{J+\delta_{s,-1}}\,j_{J_s}(qr_1)\,\left[Y_{J_s}\otimes\boldsymbol{\sigma}\right]^J \end{aligned} \tag{A.62}$$

where $\eta=\pm1$. Comparing with our generic operator of Eq. (2.40):

$$F_J(qr_1)\equiv -iq\,\frac{G^{\alpha}_{M}}{2M_\alpha}\,j_{J_s}(qr_1)\,,\qquad \mathcal{O}_J(\hat{\mathbf{r}}_1)\equiv\frac{1}{\widehat{J}}\,s\,\sqrt{J+\delta_{s,-1}}\,\left[Y_{J_s}(\hat{\mathbf{r}}_1)\otimes\boldsymbol{\sigma}\right]^J\,. \tag{A.63}$$

Then the matrices $\omega^J_{\alpha\beta}$ of Eq. (2.44) and $\omega^{LJ;K}_{\alpha\beta}$ of Eq. (2.53) can be evaluated as:

$$\begin{aligned} \omega^J_{\alpha\beta} &= \langle\alpha\,\|\,\left[Y_{J_s}(\hat{\mathbf{r}}_1)\otimes\boldsymbol{\sigma}\right]^J\,\|\,\beta\rangle \\ &= \frac{(-1)^{l_\alpha+l_\beta+j_\beta+\frac{1}{2}}}{\sqrt{4\pi}}\,\widehat{j}_\alpha\widehat{j}_\beta\,\frac{1}{\widehat{J}}\,s\,\sqrt{\frac{J+\delta_{s,-1}}{J+\delta s,1}}\,(\chi_\alpha+\chi_\beta+sJ+\delta_{s,1}) \\ &\quad\times\begin{pmatrix} j_\alpha & j_\beta & J \\ \frac{1}{2} & -\frac{1}{2} & 0 \end{pmatrix}\xi(l_\alpha+l_\beta+J+1)\,, \end{aligned} \tag{A.64}$$

and

$$
\begin{aligned}
\omega_{\alpha\beta}^{LJ;K} &= \langle\alpha \parallel \left[[Y_{J_s}(\hat{\mathbf{r}}_1)\otimes\boldsymbol{\sigma}]^J \otimes Y_L(\hat{\mathbf{r}}_1)\right]^K \parallel \beta\rangle \\
&= \frac{(-1)^{J-L+l_\alpha+1}}{4\pi}\sqrt{6}\,\widehat{j}_\alpha\widehat{j}_\beta\widehat{J}_s\widehat{J}\widehat{L}\widehat{K}\widehat{l}_\alpha\widehat{l}_\beta\frac{1}{\widehat{J}}\,s\,\sqrt{J+\delta_{s,-1}}\sum_\kappa\widehat{\kappa}^2 \\
&\times\left\{\begin{array}{ccc} K & L & J \\ J_s & 1 & \kappa\end{array}\right\}\left(\begin{array}{ccc} J_s & \kappa & L \\ 0 & 0 & 0\end{array}\right)\left(\begin{array}{ccc} l_\alpha & \kappa & l_\beta \\ 0 & 0 & 0\end{array}\right)\left\{\begin{array}{ccc} l_\alpha & \frac{1}{2} & j_\alpha \\ l_\beta & \frac{1}{2} & j_\beta \\ \kappa & 1 & K\end{array}\right\},
\end{aligned}
\tag{A.65}
$$

By inserting Eq. (A.63) into the uncorrelated (2.43), two-point (2.46)-(2.51), and three-point (2.56)-(2.61) matrices, we have the final formulae:

$$
\begin{aligned}
T^{\mathrm{M}}_{1;M} &= -iq\,\frac{G^p_M(q^2)}{2M_p}\,\delta_{t_p,t_h}\,\eta^J_{ph}\,\frac{1}{\widehat{J}^2} \\
&\times\sum_{s=\pm1} s\sqrt{\frac{J+\delta_{s,-1}}{J+\delta_{s,1}}}\,(\chi_p+\chi_h+sJ+\delta_{s,1})\,\mathcal{I}^{[ph]}_{J_s}(q)\ ,
\end{aligned}
\tag{A.66}
$$

$$
\begin{aligned}
T^{\mathrm{M}}_{2.1;M} &= -iq\,\frac{G^p_M(q^2)}{2M_p}\,\delta_{t_p,t_h}\,4\pi\,\eta^J_{ph}\,\frac{1}{\widehat{J}^2} \\
&\times\sum_{s=\pm1} s\sqrt{\frac{J+\delta_{s,-1}}{J+\delta_{s,1}}}\,(\chi_p+\chi_h+sJ+\delta_{s,1})\,\mathcal{I}^{[ph];[\rho]}_{J_s0}(q)\ ,
\end{aligned}
\tag{A.67}
$$

$$
\begin{aligned}
T^{\mathrm{M}}_{2.2;M} &= -iq\,\frac{G^p_M(q^2)}{2M_p}\,\delta_{t_p,t_h}\sqrt{\frac{3}{2\pi}}\,(-1)^{j_h+j_p}\,\widehat{l}_p\,\widehat{j}_p\,\widehat{j}_h\sum_{iL}\delta_{t_i,t_p}\,(-1)^{j_i+l_i+\frac{1}{2}} \\
&\times\xi(l_i+l_h+L)\,\widehat{l}_i\,\widehat{j}_i^2\left(\begin{array}{ccc} j_i & L & j_h \\ \frac{1}{2} & 0 & -\frac{1}{2}\end{array}\right)\sum_{s=\pm1} s\sqrt{J+\delta_{s,-1}}\,\widehat{J_s} \\
&\times\mathcal{I}^{[pi];[ih]}_{J_sL}(q)\sum_\kappa\widehat{\kappa}^2\left(\begin{array}{ccc} l_p & l_i & \kappa \\ 0 & 0 & 0\end{array}\right)\left(\begin{array}{ccc} L & J_s & \kappa \\ 0 & 0 & 0\end{array}\right)\sum_K(-1)^K\,\widehat{K}^2 \\
&\times\left\{\begin{array}{ccc} L & K & J \\ j_p & j_h & j_i\end{array}\right\}\left\{\begin{array}{ccc} L & J_s & \kappa \\ 1 & K & J\end{array}\right\}\left\{\begin{array}{ccc} l_p & \frac{1}{2} & j_p \\ l_i & \frac{1}{2} & j_i \\ \kappa & 1 & K\end{array}\right\},
\end{aligned}
\tag{A.68}
$$

$$
\begin{aligned}
T^{\mathrm{M}}_{2.3;M} &= 0 \ , && \text{(A.69)} \\
T^{\mathrm{M}}_{2.4;M} &= -iq\,\frac{G^p_M(q^2)}{2M_p}\,\delta_{t_p,t_h}\,\sqrt{\frac{3}{2\pi}}\,(-1)^{j_h+\frac{1}{2}}\,\widehat{l}_h\,\widehat{j}_p\,\widehat{j}_h\sum_{iL}\delta_{t_i,t_p}\,(-1)^{l_i} \\
&\times\xi(l_p+l_i+L)\,\widehat{l}_i\,\widehat{j}_i^2\begin{pmatrix} j_p & L & j_i \\ \frac{1}{2} & 0 & -\frac{1}{2}\end{pmatrix}\sum_{s=\pm1} s\,\sqrt{J+\delta_{s,-1}}\,\widehat{J_s} \\
&\times\mathcal{I}^{[ih];[pi]}_{J_sL}(q)\,\sum_\kappa\widehat{\kappa}^2\begin{pmatrix} l_i & l_h & \kappa \\ 0 & 0 & 0\end{pmatrix}\begin{pmatrix} L & J_s & \kappa \\ 0 & 0 & 0\end{pmatrix} \\
&\times\sum_K\widehat{K}^2\begin{Bmatrix} L & K & J \\ j_h & j_p & j_i\end{Bmatrix}\begin{Bmatrix} L & J_s & \kappa \\ 1 & K & J\end{Bmatrix}\begin{Bmatrix} l_i & \frac{1}{2} & j_i \\ l_h & \frac{1}{2} & j_h \\ \kappa & 1 & K\end{Bmatrix} , && \text{(A.70)} \\
T^{\mathrm{M}}_{3.1;M} &= -iq\,\frac{G^p_M(q^2)}{2M_p}\,\delta_{t_p,t_h}\,\eta^J_{ph}\,\frac{1}{\widehat{J}^2}\sum_{ikL}\delta_{t_i,t_p}\,\delta_{t_k,t_p}\,\delta_{j_i,j_p} \\
&\times\xi(l_p+l_k+L)\,\xi(l_p+l_i)\,\widehat{j}_k^2\begin{pmatrix} j_p & j_k & L \\ \frac{1}{2} & -\frac{1}{2} & 0\end{pmatrix}^2\mathcal{J}^{[pk];[ki]}_L \\
&\times\sum_{s=\pm1} s\,\sqrt{\frac{J+\delta_{s,-1}}{J+\delta_{s,1}}}\,(\chi_p+\chi_h+sJ+\delta_{s,1})\,\mathcal{I}^{[ih]}_{J_s}(q) \ , && \text{(A.71)} \\
T^{\mathrm{M}}_{3.2;M} &= -iq\,\frac{G^p_M(q^2)}{2M_p}\,\delta_{t_p,t_h}\,4\pi\,\eta^J_{ph}\,\frac{1}{\widehat{J}^2}\sum_i\delta_{t_i,t_p}\,\delta_{j_i,j_p}\,\xi(l_p+l_i)\,\mathcal{J}^{[pi];[\rho]}_0 \\
&\times\sum_{s=\pm1} s\,\sqrt{\frac{J+\delta_{s,-1}}{J+\delta_{s,1}}}\,(\chi_p+\chi_h+sJ+\delta_{s,1})\,\mathcal{I}^{[ih]}_{J_s}(q) \ , && \text{(A.72)} \\
T^{\mathrm{M}}_{3.3;M} &= -iq\,\frac{G^p_M(q^2)}{2M_p}\,\delta_{t_p,t_h}\,\eta^J_{ph}\,\frac{1}{\widehat{J}^2}\sum_{ikL}\delta_{t_i,t_p}\,\delta_{t_k,t_p}\,\delta_{j_i,j_h} \\
&\times\xi(l_k+l_h+L)\,\xi(l_i+l_h)\,\widehat{j}_k^2\begin{pmatrix} j_k & j_h & L \\ \frac{1}{2} & -\frac{1}{2} & 0\end{pmatrix}^2\mathcal{J}^{[kh];[ik]}_L \\
&\times\sum_{s=\pm1} s\,\sqrt{\frac{J+\delta_{s,-1}}{J+\delta_{s,1}}}\,(\chi_p+\chi_h+sJ+\delta_{s,1})\,\mathcal{I}^{[pi]}_{J_s}(q) \ , && \text{(A.73)}
\end{aligned}
$$

$$T^{\rm M}_{3.4;M} = -iq\,\frac{G^p_M(q^2)}{2M_p}\,\delta_{t_p,t_h}\,4\pi\,\eta^J_{ph}\,\frac{1}{\widehat{J}^2}\sum_i \delta_{t_i,t_p}\,\delta_{j_i,j_h}\,\xi(l_i+l_h)\,\mathcal{J}_0^{[ih];[\rho]}$$

$$\times\sum_{s=\pm1} s\,\sqrt{\frac{J+\delta_{s,-1}}{J+\delta_{s,1}}}\,(\chi_p+\chi_h+sJ+\delta_{s,1})\mathcal{I}^{[pi]}_{J_s}(q)\ , \qquad \text{(A.74)}$$

$$T^{\rm M}_{3.5;M} = -iq\,\frac{G^p_M(q^2)}{2M_p}\,\delta_{t_p,t_h}\,4\pi\,\frac{1}{\widehat{J}^2}\sum_{ikL}\delta_{t_i,t_p}\,\delta_{t_k,t_p}\,(-1)^{j_i+j_k+J+1}\,\eta^J_{ik}\frac{1}{\widehat{L}^2}$$

$$\times\,\gamma^L_{pi}\,\gamma^L_{kh}\left\{\begin{array}{ccc} j_p & j_h & J\\ j_k & j_i & L\end{array}\right\}\mathcal{J}_L^{[pi];[kh]}$$

$$\sum_{s=\pm1} s\,\sqrt{\frac{J+\delta_{s,-1}}{J+\delta_{s,1}}}\,(\chi_i+\chi_k+sJ+\delta_{s,1})\,\mathcal{I}^{[ik]}_{J_s}(q)\ , \qquad \text{(A.75)}$$

$$T^{\rm M}_{3.6;M} = 0\ . \qquad \text{(A.76)}$$

In the previous equations we have defined

$$\eta^\lambda_{\alpha\beta} = \frac{1}{\sqrt{4\pi}}\,(-1)^{j_\beta+\lambda-\frac{1}{2}}\,\xi(l_\alpha+l_\beta+\lambda+1)\,\widehat{j}_\alpha\widehat{j}_\beta\widehat{\lambda}\left(\begin{array}{ccc} j_\alpha & j_\beta & \lambda\\ \frac{1}{2} & -\frac{1}{2} & 0\end{array}\right), \qquad \text{(A.77)}$$

A.3.2 Magnetic Convection Current

By inserting the expression of convection current operator of Eq. (2.26) into the multipole expanded transverse magnetic excitation of Eq. (2.34) and following the definition of Eqs. (2.35) and (2.36), one could get:

$$O_{J(\eta)} = T^{\rm M}_{J(\eta);{\rm C}}(q)$$
$$= \frac{-i}{2M_\alpha}j_J(qr_1)\left[\left[Y_J(\hat{\mathbf{r}}_1)\otimes\overrightarrow{\nabla}\right]^J+\left[Y_J(\hat{\mathbf{r}}_1)\otimes\overleftarrow{\nabla}\right]^J\right]\ , \qquad \text{(A.78)}$$

where $\eta=\pm1$. Comparing with our generic expanded operator of Eq. (2.40):

$$F_J(qr_1) \equiv \frac{-i}{2M_\alpha}j_J(qr_1)\ , \qquad \text{(A.79)}$$

$$\mathcal{O}_J(\hat{\mathbf{r}}_1) \equiv \mathcal{O}^a_J(\hat{\mathbf{r}}_1) + \mathcal{O}^b_J(\hat{\mathbf{r}}_1) = \Big[Y_J(\hat{\mathbf{r}}_1) \otimes \overrightarrow{\nabla}\Big]^J + \Big[Y_J(\hat{\mathbf{r}}_1) \otimes \overleftarrow{\nabla}\Big]^J . \tag{A.80}$$

Equations similar to (A.40) and (A.41) will obtained but instead of J_s we have here J. By inserting Eqs. (A.79) and (A.80) into uncorrelated (2.43), two-point (2.46)-(2.51), and three-point (2.56)-(2.61) matrices:

$$T^{\mathrm{M}}_{1;C} = -(i)\,\frac{G^p_E(q^2)}{2M_p}\,\delta_{t_p,t_h}\,\eta^J_{ph}\Big[\frac{(\chi_p+\chi_h)(\chi_p+\chi_h+1)-J(J+1)}{\sqrt{J(J+1)}}\Big] \times \mathcal{I}^{[\frac{1}{r}ph]}_J(q)\ , \tag{A.81}$$

$$T^{\mathrm{M}}_{2.1;C} = -(i)\,\frac{G^p_E(q^2)}{2M_p}\,\delta_{t_p,t_h}\,4\pi\,\eta^J_{ph}\Big[\frac{(\chi_p+\chi_h)(\chi_p+\chi_h+1)-J(J+1)}{\sqrt{J(J+1)}}\Big] \mathcal{I}^{[\frac{1}{r}ph];\rho}_{J,0}(q)\ , \tag{A.82}$$

$$\begin{aligned}
T^{\mathrm{M}}_{2.2;C} = {} & -(i)\,\frac{G^p_E(q^2)}{2M_p}\,\delta_{t_p,t_h}\,\frac{1}{\sqrt{2\pi}}(-1)^{j_p+j_h+J+l_p}\widehat{j}_p\widehat{j}_h\widehat{J}\sum_{iLK\kappa}\delta_{t_i,t_p}(-1)^{l_i} \\
& \times\xi(l_i+l_h+L)\xi(L+K+\kappa)\widehat{j}_i^2\widehat{K}^2\widehat{\kappa}^2\left\{\begin{array}{ccc} L & K & J \\ j_p & j_h & j_i \end{array}\right\}\left\{\begin{array}{ccc} l_p & l_i & K \\ j_i & j_p & \frac{1}{2} \end{array}\right\} \\
& \times\left(\begin{array}{ccc} 1 & K & \kappa \\ 1 & -1 & 0 \end{array}\right)\left(\begin{array}{ccc} K & J & L \\ 1 & -1 & 0 \end{array}\right)\left(\begin{array}{ccc} j_i & L & j_h \\ \frac{1}{2} & 0 & -\frac{1}{2} \end{array}\right)\times\Big\{(-1)^L\widehat{l}_p \\
& \Big[(\widehat{l_i+1})\sqrt{l_i+1}\left(\begin{array}{ccc} l_p & \kappa & l_i+1 \\ 0 & 0 & 0 \end{array}\right)\left\{\begin{array}{ccc} l_i & l_p & K \\ \kappa & 1 & l_i+1 \end{array}\right\}\mathcal{I}^{[p(\mathrm{d}\ell_i)i];[ih]}_{J,L}(q) \\
& +(\widehat{l_i-1})(-\sqrt{l_i})\left(\begin{array}{ccc} l_p & \kappa & l_i-1 \\ 0 & 0 & 0 \end{array}\right)\left\{\begin{array}{ccc} l_i & l_p & K \\ \kappa & 1 & l_i-1 \end{array}\right\}\mathcal{I}^{[p(\mathrm{d}\ell_{i+1})i];[ih]}_{J,L}(q)\Big] \\
& +\widehat{l}_i\Big[(\widehat{l_p+1})\sqrt{l_p+1}\left(\begin{array}{ccc} l_i & \kappa & l_p+1 \\ 0 & 0 & 0 \end{array}\right)\left\{\begin{array}{ccc} l_p & l_i & K \\ \kappa & 1 & l_p+1 \end{array}\right\}\mathcal{I}^{[(\mathrm{d}\ell_p)p\,i];[ih]}_{J,L}(q) \\
& +(\widehat{l_p-1})(-\sqrt{l_p})\left(\begin{array}{ccc} l_i & \kappa & l_p-1 \\ 0 & 0 & 0 \end{array}\right)\left\{\begin{array}{ccc} l_p & l_i & K \\ \kappa & 1 & l_p-1 \end{array}\right\}\mathcal{I}^{[(\mathrm{d}\ell_{p+1})p\,i];[ih]}_{J,L}(q)\Big]\Big\},
\end{aligned} \tag{A.83}$$

$$T^{\rm M}_{2.3;C} = 0 \ , \tag{A.84}$$

$$\begin{aligned}
T^{\rm M}_{2.4;C} &= -(i)\,\frac{G_E^p(q^2)}{2M_p}\,\delta_{t_p,t_h}\,\frac{1}{\sqrt{2\pi}}(-1)^{l_h+1}\widehat{j}_p\widehat{j}_h\widehat{J}\sum iLK\kappa\delta_{t_i,t_p}(-1)^{l_i+\kappa} \\
&\times\xi(l_p+l_i+L)\xi(L+K+\kappa)\widehat{j}_i^2\widehat{K}^2\widehat{\kappa}^2\left\{\begin{array}{ccc} K & L & J \\ j_p & j_h & j_i\end{array}\right\}\left\{\begin{array}{ccc} l_i & l_h & K \\ j_h & j_i & \frac{1}{2}\end{array}\right\} \\
&\times\left(\begin{array}{ccc} 1 & K & \kappa \\ 1 & -1 & 0\end{array}\right)\left(\begin{array}{ccc} K & J & L \\ 1 & -1 & 0\end{array}\right)\left(\begin{array}{ccc} j_p & L & j_i \\ \frac{1}{2} & 0 & -\frac{1}{2}\end{array}\right)\Big\{(-1)^L\widehat{l}_i \\
&\times\Big[(\widehat{l_h+1})\sqrt{l_h+1}\left(\begin{array}{ccc} l_i & \kappa & l_h+1 \\ 0 & 0 & 0\end{array}\right)\left\{\begin{array}{ccc} l_h & l_i & K \\ \kappa & 1 & l_h+1\end{array}\right\}\mathcal{I}_{J,L}^{[i(\mathrm{d}\ell_h)h];[pi]}(q) \\
&+(\widehat{l_h-1})(-\sqrt{l_h})\left(\begin{array}{ccc} l_i & \kappa & l_h-1 \\ 0 & 0 & 0\end{array}\right)\left\{\begin{array}{ccc} l_h & l_i & K \\ \kappa & 1 & l_h-1\end{array}\right\}\mathcal{I}_{J,L}^{[i(\mathrm{d}\ell_{h+1})h];[pi]}(q)\Big] \\
&+\widehat{l}_h\Big[(\widehat{l_i+1})\sqrt{l_i+1}\left(\begin{array}{ccc} l_h & \kappa & l_i+1 \\ 0 & 0 & 0\end{array}\right)\left\{\begin{array}{ccc} l_i & l_h & K \\ \kappa & 1 & l_i+1\end{array}\right\}\mathcal{I}_{J,L}^{[(\mathrm{d}\ell_i)i\,h];[pi]}(q) \\
&+(\widehat{l_i-1})(-\sqrt{l_i})\left(\begin{array}{ccc} l_h & \kappa & l_i-1 \\ 0 & 0 & 0\end{array}\right)\left\{\begin{array}{ccc} l_i & l_h & K \\ \kappa & 1 & l_i-1\end{array}\right\}\mathcal{I}_{J,L}^{[(\mathrm{d}\ell_{i+1})i\,h];[pi]}(q)\Big]\Big\},
\end{aligned} \tag{A.85}$$

$$\begin{aligned}
T^{\rm M}_{3.1;C} &= -(i)\,\frac{G_E^p(q^2)}{2M_p}\,\delta_{t_p,t_h}\,\eta^J_{ph}\sum_{ikL}\delta_{t_i,t_p}\,\delta_{t_k,t_p}\,\delta_{j_i,j_p}\xi(l_p+l_k+L)\,\xi(l_p+l_i) \\
&\times\widehat{j}_k^2\left(\begin{array}{ccc} j_p & j_k & L \\ \frac{1}{2} & -\frac{1}{2} & 0\end{array}\right)^2\Big[\frac{(\chi_p+\chi_h)(\chi_p+\chi_h+1)-J(J+1)}{\sqrt{J(J+1)}}\Big] \\
&\times\mathcal{I}_J^{[\frac{1}{r}ih]}(q)\,\mathcal{J}_L^{[pk];[ki]},
\end{aligned} \tag{A.86}$$

$$\begin{aligned}
T^{\rm M}_{3.2;C} &= -(i)\,\frac{G_E^p(q^2)}{2M_p}\,\delta_{t_p,t_h}\,4\pi\,\eta^J_{ph}\sum_{i}\,\delta_{t_i,t_p}\,\delta_{j_i,j_p}\,\xi(l_p+l_i) \\
&\times\Big[\frac{(\chi_p+\chi_h)(\chi_p+\chi_h+1)-J(J+1)}{\sqrt{J(J+1)}}\Big]\mathcal{I}_J^{[\frac{1}{r}ih]}(q)\,J_0^{\rho;[pi]}\ ,
\end{aligned} \tag{A.87}$$

$$
\begin{aligned}
T^{\mathrm{M}}_{3.3;C} &= -(i)\,\frac{G_E^p(q^2)}{2M_p}\,\delta_{t_p,t_h}\,\eta^J_{ph}\sum_{ikL}\delta_{t_i,t_p}\,\delta_{t_k,t_p}\,\delta_{j_i,j_h}\,\xi(l_k+l_h+L)\,\xi(l_i+l_h) \\
&\quad\times\widehat{j}_k^2\begin{pmatrix} j_k & j_h & L \\ \frac{1}{2} & -\frac{1}{2} & 0 \end{pmatrix}^2\Big[\frac{(\chi_p+\chi_h)(\chi_p+\chi_h+1)-J(J+1)}{\sqrt{J(J+1)}}\Big] \\
&\qquad\times\mathcal{I}_J^{[\frac{1}{r}pi]}(q)\,\mathcal{J}_L^{[kh];[ik]}\,, \qquad \text{(A.88)}
\end{aligned}
$$

$$
\begin{aligned}
T^{\mathrm{M}}_{3.4;C} &= -(i)\,\frac{G_E^p(q^2)}{2M_p}\,\delta_{t_p,t_h}\,4\pi\,\eta^J_{ph}\sum_{i}\delta_{t_i,t_p}\,\delta_{j_i,j_h}\,\xi(l_i+l_h) \\
&\quad\times\Big[\frac{(\chi_p+\chi_h)(\chi_p+\chi_h+1)-J(J+1)}{\sqrt{J(J+1)}}\Big]\mathcal{I}_J^{[\frac{1}{r}pi]}(q)\,\mathcal{J}_0^{[ih];\rho}\,, \qquad \text{(A.89)}
\end{aligned}
$$

$$
\begin{aligned}
T^{\mathrm{M}}_{3.5;C} &= -(i)\,\frac{G_E^p(q^2)}{2M_p}\,\delta_{t_p,t_h}\,4\pi\sum_{ikL}\delta_{t_i,t_p}\,\delta_{t_k,t_p}\,(-1)^{j_1+j_k+J+L}\eta^J_{ik}\frac{1}{\widehat{L}^2}\gamma^L_{pi}\,\gamma^L_{kh} \\
&\quad\times\begin{Bmatrix} j_p & j_h & J \\ j_k & j_i & L \end{Bmatrix}\Big[\frac{(\chi_i+\chi_k)(\chi_i+\chi_k+1)-J(J+1)}{\sqrt{J(J+1)}}\Big] \\
&\qquad\times\mathcal{I}_J^{[\frac{1}{r}ik]}(q)\,\mathcal{J}_L^{[kh];[pi]}\,, \qquad \text{(A.90)}
\end{aligned}
$$

$$
T^{\mathrm{M}}_{3.5;C} = 0\,. \qquad \text{(A.91)}
$$

A.4 Useful Relations

Through the derivation of the equations one may use the help of some important relations of the 3j, 6j and 9j symbol. Here, we give a few relations which are used to solve and simplify our formulae.

$$\begin{pmatrix} j_p & j_h & J \\ \frac{1}{2} & \frac{1}{2} & -1 \end{pmatrix} = -(-1)^{j_h+l_h+\frac{1}{2}} \frac{\chi_h + (-1)^{l_p+l_h+J+1}\chi_p}{\sqrt{J(J+1)}} \begin{pmatrix} j_p & j_h & J \\ \frac{1}{2} & -\frac{1}{2} & 0 \end{pmatrix} \tag{A.92}$$

$$\begin{aligned} \begin{Bmatrix} \lambda & L & J \\ J & 1 & \alpha \end{Bmatrix} \begin{pmatrix} J & \alpha & L \\ 0 & 0 & 0 \end{pmatrix} &= \begin{Bmatrix} L & J & \alpha \\ 1 & \lambda & J \end{Bmatrix} \begin{pmatrix} L & J & \alpha \\ 0 & 0 & 0 \end{pmatrix} \\ &= (-1)^{\lambda+1} \frac{\sqrt{2}}{\widehat{J}} \begin{pmatrix} 1 & \lambda & \alpha \\ 1 & -1 & 0 \end{pmatrix} \\ &\quad \begin{pmatrix} \lambda & J & L \\ 1 & -1 & 0 \end{pmatrix} \xi(L+\lambda+\alpha) \end{aligned} \tag{A.93}$$

$$\begin{aligned} \begin{pmatrix} l_\alpha & J-1 & l_\beta+1 \\ 0 & 0 & 0 \end{pmatrix} \begin{Bmatrix} l_\beta & l_\alpha & J \\ J-1 & 1 & l_\beta+1 \end{Bmatrix} &= \frac{1}{\widehat{l_\beta}\widehat{(l_\beta-1)}\widehat{J}\widehat{(J-1)}} \\ \times \Bigg[\sqrt{l_\beta}\sqrt{J+1} \begin{pmatrix} l_\beta & J & l_\alpha \\ 1 & -1 & 0 \end{pmatrix} &+ \sqrt{l_\beta+1}\sqrt{J} \begin{pmatrix} l_\beta & J & l_\alpha \\ 0 & 0 & 0 \end{pmatrix} \Bigg] \\ \times\, \xi(l_\alpha+l_\beta+J) & \end{aligned} \tag{A.94}$$

$$\begin{aligned} \begin{pmatrix} l_\alpha & J+1 & l_\beta+s \\ 0 & 0 & 0 \end{pmatrix} \begin{Bmatrix} l_\beta & l_\alpha & J \\ J+1 & 1 & l_\beta+s \end{Bmatrix} &= \frac{1}{\widehat{l_\beta}\widehat{(l_\beta+s)}\widehat{J}\widehat{(J+1)}} \\ \times \Bigg[\sqrt{l_\beta+\delta_{s,-1}}\sqrt{J} \begin{pmatrix} l_\beta & J & l_\alpha \\ 1 & -1 & 0 \end{pmatrix} &- s\sqrt{l_\beta+\delta_{s,1}}\sqrt{J+1} \begin{pmatrix} l_\beta & J & l_\alpha \\ 0 & 0 & 0 \end{pmatrix} \Bigg] \\ \times\, \xi(l_\alpha+l_\beta+J) & \end{aligned} \tag{A.95}$$

$$
\begin{aligned}
&\begin{pmatrix} l_\alpha & J-1 & l_\beta+s \\ 0 & 0 & 0 \end{pmatrix} \begin{Bmatrix} l_\beta & l_\alpha & J \\ J-1 & 1 & l_\beta+s \end{Bmatrix} = \frac{1}{\widehat{l_\beta}(\widehat{l_\beta+s})\widehat{J}(\widehat{J-1})} \\
&\times\Big[\sqrt{l_\beta+\delta_{s,-1}}\sqrt{J+1}\begin{pmatrix} l_\beta & J & l_\alpha \\ 1 & -1 & 0 \end{pmatrix} + s\sqrt{l_\beta+\delta_{s,1}}\sqrt{J}\begin{pmatrix} l_\beta & J & l_\alpha \\ 0 & 0 & 0 \end{pmatrix}\Big] \\
&\qquad \times \xi(l_\alpha+l_\beta+J) \qquad\qquad (A.96)
\end{aligned}
$$

where $s = \pm 1$

$$
\begin{aligned}
\begin{Bmatrix} l_\alpha & \frac{1}{2} & j_\alpha \\ l_\beta & \frac{1}{2} & j_\beta \\ J_s & 1 & J \end{Bmatrix} \begin{pmatrix} l_\alpha & J_s & l_\beta \\ 0 & 0 & 0 \end{pmatrix} &= \frac{(-1)^{l_\beta+j_\beta+\frac{1}{2}}}{\sqrt{6}} \frac{1}{\widehat{l_\alpha}\widehat{l_\beta}\widehat{J_s}\widehat{J}} \\
&\quad \frac{\chi_\alpha+\chi_\beta+sJ+\delta_{s,1}}{\sqrt{J+\delta s,1}} \begin{pmatrix} j_\alpha & j_\beta & J \\ \frac{1}{2} & -\frac{1}{2} & 0 \end{pmatrix} \\
&\qquad \times \xi(l_\alpha+l_\beta+J+1) \qquad (A.97)
\end{aligned}
$$

List of Abbriviations

CBF	Correlated Basis Function
DKO	Direct Knock-Out
DWIA	Distorted Wave Impulse Approximation
EM	Electromagnetic
FHNC	Fermi Hypernetted Chains
FSI	Final State Interactions
GFMC	Green Function Monte Carlo
IA	Impulse Approximation
IPM	Independent Particle Model
LRC	Long-Range Correlations
MEC	Meson Exchange Currents
NN	Nucleon-Nucleon
OB	One-Body
PWBA	Plane Wave Born Approximation
QCD	Quantum Chromodynamics
QED	Quantum Electrodynamics
RPA	Random Phase Approximation
SOC	Single Operator Chain
SRC	Short-Range Correlations
TB	Two-Body
VMC	Variational Monte Carlo

Bibliography

[Ada88] G.S. Adams, E.R. Kinney, J.L. Matthews, W.W. Sapp, T. Soos, R.O. Owens, R.S. Turley and G. Pignault *Phys. Rev.* **C38**(1988) 2771.

[Afn68] I.R. Afnan and Y.C. Tang, *Phys. Rev* **175** (1968) 1337.

[Ama92a] J.E. Amaro, and A.M. Lallena, *Nucl. Phys.* **A537** (1992) 585.

[Ama92b] J.E. Amaro and A.M. Lallena, *Mod. Phys. Lett.* **A7** (1992) 3029.

[Ama93a] J.E. Amaro and A.M. Lallena, *J. Phys.* **G19** (1993) 99.

[Ama93b] J.E. Amaro, G. Co', and A.M. Lallena, *Ann. Phys.* (N.Y.) **221** (1993) 306; J.E. Amaro, *Ph. D. Thesis*, Granada University, (Granada, Spain), (1993) unpublished.

[Ama94] J. E. Amaro, G. Co', and A. M. Lallena, *Nucl. Phys.* **A578** (1994) 365.

[Ama98] J.E. Amaro, A.M. Lallena, G. Co' and A. Fabrocini, *Phys. Rev.* **C57** (1998) 3473.

[Ama99a] J.E. Amaro, F. Arias de Saavedra, A.M. Lallena, G. Co', A. Fabrocini and S. R. Mokhtar, in *Proceedings of the 4th Workshop on Electromanetically Induced Two-Hadron Emission* (G. Garcia-Recio, P. Grabmayr, A.M. Lallena and R.O. Owens, Eds.), Granada (Spain) 1999, p. 112.

[Ama99b] J.E. Amaro, A.M. Lallena and J.A. Caballero, *Phys. Rev.* **C60** (1999) 014602.

[Ama01] J.E. Amaro, G. Co' and A.M. Lallena, in book *Electromagnetic response functions of nuclei* (R. Cenni Ed.), Nova Science Publishers 2001.

[Ami96] K. Amir-Azimi-Nili, H. Müther, L.D. Skouras and A. Polls, *Nucl. Phys.* **A604** (1996) 245.

[Ami97] K. Amir-Azimi-Nili, J.M. Udias, H. Müther, L.D. Skouras and A. Polls, *Nucl. Phys.* **A625** (1997) 633.

[Ang01] M. Anguiano and G. Co', *J. Phys.* **G27** (2001) 2109.

[Ang02] M. Anguiano, G. Co', A.M. Lallena and S.R. Mokhtar, *Ann. Phys.* (NY) **296** (2002) 235.

[Ari94] F. Arias de Saavedra and A.M. Lallena, *Phys. Rev.* **C50** (1994) 2384.

[Ari96] F. Arias de Saavedra, G. Co', A. Fabrocini and S. Fantoni, *Nucl. Phys.* **A605** (1996) 359.

[Ari97] F. Arias de Saavedra, G. Co' and M.M. Renis, *Phys. Rev.* **C55** (1997) 673.

[Bal91] M. Baldo, I. Bombaci, L.S. Ferreira, G. Giansiracusa and U. Lombardo, *Phys. Rev.* **C43** (1991) 2605.

[Ben89] O. Benhar, A. Fabrocini and S. Fantoni, *Nucl. Phys.* **A505** (1989) 267.

[Ben90] O. Benhar, A. Fabrocini and S. Fantoni, *Phys. Rev.* **C41** (1990) R24.

[Ben94] G. Benenti, C. Giusti and F.D. Pacati, *Nucl. Phys.* **A574** (1994) 716.

[Ber82] M. Bernheim, A. Bussière, J. Mougey, D. Royer, D. Tarnowsky, S. Turk-Chièze, S. Frullani, S. Boffi, C. Giusti, F.D. Pacati, G.P. Capitani, E. De Sanctis and G.W. Wagner, *Nucl. Phys.* **A375** (1982) 381.

[Bjo64] J.D. Bjorken and S.D. Drell, *Relativistic Quantum Mechanics*, (McGraw Hill, New York, 1964).

[Blo95] K.I. Blomqvist, W.U. Boeglin, R. Böhm, M. Distler, R. Edelhoff, J. Friedrich, R. Geiges, M. Kahrau, M. Korn, H. Kramer, K.W. Krygier, V. Kunde, M. Kuss, J. Lác, A. Liesenfeld, K. Merle, R. Neuhausen, E.A.J. M. Offermann, Th. Pospischil, M. Potokar, A.W. Richter, A. Rokavec, G. Rosner, P. Sauer, S.

Schardt, A. Serdarević, Th. Veit, B. Vodenik, A. Wagner, Th. Walcher and S. Wolf, *Phys. Lett.* **B344** (1995) 85.

[Bob94] I. Bobeldijk, M. Bouwhuis, D.G. Ireland, C.W. de Jager, E. Jans, N. de Jonge, W-J. Kasdorp, J. Konijn, L. Lapikás, J.J. van Leeuwe, R.L.J. van der Meer, G.J.L. Nooren, E. Passchier, M. Schroevers, G. van der Steenhoven, J.J.M. Steijger, J.A.P. Theunissen, M.A. van Uden, H. de Vries, R. de Vries, P.K.A. de Witt Huberts, H.P. Blok, H.B. van den Brink, G.E. Dodge, M.N. Harakeh, W.H. A. Hesselink, N. Kalantar-Nayestanaki, A. Pellegrino, C.M. Spaltro, J.A. Templon, R.S. Hicks, J.J. Kelly and C. Marchand, *Phys. Rev. Lett.* **73** (1994) 2684.

[Bof81] S. Boffi, C. Giusti and F.D. Pacati, *Nucl. Phys.* **A359** (1981) 91.

[Bof82] S. Boffi, F. Cannata, F. Capuzzi, C. Giusti and F.D. Pacati, *Nucl. Phys.* **A379** (1982) 509.

[Bof84] S. Boffi, R. Cenni, C. Giusti and F.D. Pacati, *Nucl. Phys.* **A420** (1984) 38.

[Bof93] S. Boffi, C. Giusti and F.D. Pacati, *Phys. Rep.* **226** (1993) 1.

[Bof96] S. Boffi, C. Giusti, F.D. Pacati and M. Radici, *Electromagnetic Response of Atomic Nuclei* (Clarendon Press, Oxford, 1996).

[Cav82] M. Cavinato, M. Marangoni, P.L. Ottaviani and A.M. Saruis, *Nucl. Phys.* **A373** (1982) 445.

[Cav84] M. Cavinato, M. Marangoni and A.M. Saruis, *Nucl. Phys.* **A422** (1984) 237.

[Cio80] C. Ciofi degli Atti, *Prog. Part. Nucl. Phys.* **3** (1980) 163.

[Cio91] C. Ciofi degli Atti, E. Pace and G. Salmè, *Phys. Rev.* **C43** (1991) 1155.

[Cla79] J.W. Clark, *Prog. Part. and Nucl. Phys.*, **2** (1979) 89.

[Co'85] G. Co' and S. Krewald, *Nucl. Phys.* **A433** (1985) 392.

[Co'87] G. Co' and J. Heisenberg, *Phys. Lett.* **B197** (1987) 489.

[Co'88] G. Co', K. F. Quader, R. Smith and J. Wambach, *Nucl. Phys.* **A485** (1988) 61.

[Co'90] G. Co' and A.M. Lallena, *Nucl. Phs.* **A510** (1990) 139.

[Co'92] G. Co', A. Fabrocini, S. Fantoni and I. E. Lagaris, *Nucl. Phys.* **A549** (1992) 439.

[Co'94] G. Co', A. Fabrocini and S. Fantoni, *Nucl. Phys.* **A568** (1994) 73.

[Co'95] G. Co', *Nuov. Cim.* **A108** (1995) 623.

[Co'98] G. Co' and A. M. Lallena, *Phys. Rev.* **C57** (1998) 145.

[Co'01] G. Co' and A.M. Lallena, *Ann. Phys.* (NY) **287** (2001) 101.

[Con92] J.P. Connelly, D.J. DeAngelis, J.H. Heisenberg, F.W. Hersman, W. Kim, M. Leuschner, T.E. Milliman, J. Wise and C.N. Papanicolas, *Phys. Rev.* **C45** (1992) 2711.

[Dec81] J. Dechargè, L. Sips and D. Gogny, *Phys. Lett.* **B98** (1981) 229.

[Deh85] J.S. Dehesa, S. Krewald, A.M. Lallena and T.W. Donnelly, *Nucl. Phys.* **A436** (1985) 573.

[Die75] A.E.L. Dieperink and T. de Forest Jr., *Ann. Rev. Nucl. Sc.* **25** (1975) 1.

[Don75] T. W. Donnely and J. D. Walecka, Ann. Rev. Nucl. Sci. 25 (1975) 329.

[Edm57] A.R. Edmonds, *Angular momentum in quantum mechanics*, (Princeton University Press, Princeton, 1957).

[Fab97] A. Fabrocini, *Phys. Rev.* **C55** (1997) 338.

[Fab98] A. Fabrocini, F. Arias de Saavedra, G. Co' and P. Folgarait, *Phys. Rev.* **C57** (1998) 1668.

[Fab00] A. Fabrocini, F. Arias de Saavedra and G. Co', *Phys. Rev.* **C61** (2000) 044302.

[Fab01] A. Fabrocini and G. Co', *Phys. Rev.* **C63** (2001) 044319.

[Fan74] S. Fantoni and S. Rosati, *Lett. Nuovo Cimento* **10** (1974) 545.

[Fan75] S. Fantoni and S. Rosati, *Nuovo Cimento* **A25** (1975) 593.

[Fan79] S. Fantoni and S. Rosati, *Nucl. Phys.* **A328** (1979) 45.

[Fan87] S. Fantoni and V.R. Pandharipande, *Nucl. Phys.* **A473** (1987) 234.

[Fet71] A.L. Fetter and J.D. Walecka, *Quantum Theory of Many-Particle Systems*, (McGraw-Hill, New York, 1971).

[Fin77] D.J.S. Findlay and R.O. Owens, *Nucl. Phys.* **A279** (1977) 385.

[For66] T. de Forest Jr. and J.D. Walecka, *Adv. Phys.* **15** (1966) 1.

[For67] T. de Forest Jr., *Ann. Phys.* (NY) **45** (1967) 365.

[For83] T. de Forest Jr., *Nucl. Phys.* **A392** (1983) 232.

[Fru84] S. Frullani and J. Mougey, *Advances in Nuclear Physics* **14**, Eds. J.W. Negele and E. Vogt, (Plenum Press, New York, 1984).

[Gai00] M.K. Gaidarov, K.A. Pavlova, A.N. Antonov, M.V. Stoitsov, S.S. Dimitrova, M.V Ivanov and C. Giusti, *Phys. Rev.* **C61** (2000) 014306.

[Gar99] In *Proceedings of the 4^{th} Workshop on Electromanetically Induced Two-Hadron Emission* (G. Garcia-Recio, P. Grabmayr, A.M. Lallena and R.O. Owens, Eds.), Granada (Spain) 1999.

[Gia85] M. M. Giannini and G. Ricco, *Riv. Nuovo Cim.* **8** (1985) 1.

[Giu87] C. Giusti and F.D. Pacati, *Nucl. Phys.* **A473** (1987) 717

[Giu91] C. Giusti and F.D. Pacati, *Nucl. Phys.* **A535** (1991) 573.

[Giu94] C. Giusti and F.D. Pacati, *Nucl. Phys.* **A571** (1994) 694.

[Giu99] C. Giusti, H. Müther, F.D. Pacati and M. Stauf, *Phys. Rev.* **C60** (1999) 054608.

[Ham80] I. Hamamoto, J. Lichtenstadt and G. Bertsch, *Phys. Lett.* **B93** (1980) 213; *ibidem* **B96** (1980) 249.

[Har82] R. De Haro, S. Krewald and J. Speth, *Nucl. Phys.* **A388** (1982) 265.

[Hin92] N.M. Hintz, A.M. Lallena and A. Sethi, *Phys. Rev.* **C45** (1992) 1098.

[Höh76] G. Höhler, E. Pietarinen, I. Sabba-Stefanescu, F. Borkowski, G.G. Simon, V.H. Walther and R.D. Wendling, *Nucl. Phys.* **B114** (1976) 505.

[Hyd87] C.E. Hyde-Wright, W. Bertozzi, T.N. Buti, J.M. Finn, F.W. Hersman, M.V. Hynes, M.A. Kovash, J.J. Kelly, S. Kowalski, J. Lichtenstadt, R.W. Lourie, B.E. Norum, B. Pugh, C.P. Sargent, B.L. Berman, F. Petrovich and J.A. Carr, *Phys. Rec.* **C35** (1987) 880.

[Ire94] D.G. Ireland and G. van der Steenhoven, *Phys. Rev.* **C49** (1994) 2182.

[Jan00] S. Janssen, J. Ryckebusch, W. Van Nespen and D. Debruyne, *Nucl. Phys.* **A672** (2000) 285.

[Jas55] R. Jastrow, *Phys. Rev.* **98** (1955) 1479.

[Kel96] J.J. Kelly, *Advances in Nuclear Physics* **23**, Eds. J.W. Negele and E. Vogt, (Plenum Press, New York, 1996).

[Kie93] A. Kievsky, M. Viviani and S. Rosati, *Nucl. Phys.* **A551** (1993) 241.

[Kle83] W.E. Kleppinger and J.D. Walecka, *Ann. Phys.* (NY) **146** (1983) 349.

[Kre80] S. Krewald and J. Speth, *Phys. Rev. Lett.* **45** (1980) 417.

[Kre86] S. Krewald, A.M. Lallena and J.S. Dehesa, *Nucl. Phys.* **A448** (1986) 685.

[Lal88] A. M. Lallena, *Nucl. Phys.* **A489** (1988) 70.

[Lal93] A. M. Lallena, *Phys. Rev.* **C48** (1993) 344.

[Lap99] L. Lapikás, J. Wesseling and R.B. Wiringa, *Phys. Rev. Lett.* **82** (1999) 4404.

[Lei85] M.J. Leitch, J.L. Matthews, W.W. Sapp, C.P. Sargent, S.A. Wood, D.J.S. Findlay, R.O. Owens and B.L. Roberts, *Phys. Rev.* **C31** (1985) 1633.

[Leu94] M. Leuschner, J.R. Calarco, F.W. Hersman, E. Jans, G.E. Kramer, L. Lapikás, G. van der Steenhoven, P.K.A. de Witt Huberts, H.P. Block, N. Kalantar-Nayestanaki and J. Friedrich, *Phys. Rev.* **C49** (1994) 955.

[Lic79] J. Lichtenstadt, J. Heisenberg, C.N. Papanicolas, C.P. Sargent, A.N. Courtemanche and J.S. McCarthy, *Phys. Rev.* **C20** (1979) 497; J.Lichtenstadt, Ph.D. thesis, MIT 1979 (unpublished).

[Ma91] Z.Y. Ma and J. Wambach, *Phys. Lett.* **B256** (1991) 1.

[Mah91] C. Mahaux and R. Sartor, *Adv. Nucl. Phys.* **20** (1991) 1.

[Mig67] A.B. Migdal, *Theory of Finite Fermi Systems and Applications to Atomic Nuclei*, (Wiely, New York 1967).

[Mil95] G.J. Miller, J.C. McGeorge, J.R.M. Annand, G.I. Crawford, V. Holliday, I.J.D. MacGregor, R.O. Owens, J. Ryckebusch, J.-O. Adler, B.-E. Andersson, L. Isaksson and B. Schrøder, Nucl. Phys. A586 (1995) 125.

[Mor95] K. Mori, P.D. Harty, Y. Fujii, O. Konno, K. Maeda, I. Nomura, G.J. O'Keefe, J. Ryckebusch, T. Suda, T. Terasawa, M.N. Thompson and Y. Torizuka, *Phys. Rev.* **C55** (1995) 2611.

[Müt94] H. Müther and W. H. Dickhoff, *Phys. Rev.* **C49** (1994) R17.

[Müt99] H. Müther in *Proceedings of the 4th Workshop on Electromanetically Induced Two-Hadron Emission* (G. Garcia-Recio,

P. Grabmayr, A.M. Lallena and R.O. Owens, Eds.), Granada (Spain) 1999, p. 1.

[Ord81] J.W. Van Orden and T.W. Donnelly, *Ann. Phys.* (N.Y.) **131** (1981) 451.

[Pan79] V.R. Pandharipande and R.B. Wiringa, *Rev. Mod. Phys.* **51** (1979) 821.

[Pan84] V.R. Pandharipande, C.N. Papanicolas and J. Wambach, *Phys. Rev. Lett.* **53** (1984) 1133.

[Pan90] V.R. Pandharipande and S.C. Pieper, *Nucl. Phys.* **A507** (1990) 167c.

[Pin88] D. Pines, K.F. Quader and J. Wambach, *Nucl. Phys.* **A477** (1988) 365.

[Pol97] A. Polls, M. Radici, S. Boffi, W.H. Dickhoff and H. Müther, *Phys. Rev.* **C55** (1997) 810.

[Ram89] A. Ramos, A. Polls and W.H. Dickhoff, *Nucl. Phys.* **A503** (1989) 1.

[Rin78] G.A. Rinker and J. Speth, *Nucl. Phys.* **A306** (1978) 360.

[Ris84] D.O. Riska, *Prog. Part. Nucl. Phys.*, **11** (1984) 199.

[Ros82] S. Rosati, in *From nuclei to particles*, Proc. Int. School E. Fermi, course LXXIX, (A. Molinari, Ed.), North Holland (Amsterdam) 1982, p73.

[Ros00] G. Rosner, *Prog. Part. Nucl. Phys.* **44** (2000) 99.

[Ryc87a] J. Ryckebusch, *Ph. D. Thesis*, Gent University, (Gent, Belgium), (1987) unpublished.

[Ryc87b] J. Ryckebusch, M. Waroquier, K. Heyde and D. Ryckbosch, *Phys. Lett.* **B194** (1987) 453.

[Ryc88] J. Ryckebusch, M. Waroquier, K. Heyde, J. Moreau and D. Ryckbosch, *Nucl. Phys.* **A476** (1988) 237.

[Ryc95a] In *Proceedings of the Second Workshop on Electromanetically Induced Two-Nucleon Emission* (J. Ryckebusch and M. Waroquier, Eds.), University of Gent, Gent (Belgium), 1995.

[Ryc95b] J. Ryckebusch, V. Van der Sluys, K. Heyde and M. Waroquier, *Phys. Lett.* **B350** (1995) 1.

[Ryc97] J. Ryckebusch, V. Van der Sluys, K. Heyde, H. Holvoet, W. Van Nespen and M. Waroquier, *Nucl. Phys.* **A624** (1997) 581.

[Ryc00] J. Ryckebusch, S. Janssen, W. Van Nespen and D. Debruyne, *Phys. Rev.* **C61** (2000) 021603.

[Sar93] A.M. Saruis,*Phys. Rep.* **235** (1993) 57.

[Sch82] P. Schwandt, H.O. Meyer, W.W. Jacobs, A.D. Bacher, S.E. Vigdor, M.D. Kaitchuck and T.R. Donoghue, *Phys. Rev.* **C26** (1982) 55.

[Slu97] V. van der Sluys, K. Heyde, J. Ryckebusch and M. Waroquier, *Phys. Rev* **C55** (1997) 1982.

[Sme93] F. De Smet, H. Ferdinande, R. Van de Vyver, L. Van Hoorebeke, D. Ryckbosch, C. Van den Abeele, J. Dias and J. Ryckebusch, *Phys. Rev.* **C47**(1993) 652.

[Spa93] C.M. Spaltro, H.P. Blok, E. Jans, L. Lapikás, M. van der Schaar, G. van der Steenhoven and P.K.A de Witt Huberts, *Phys. Rev.* **C48** (1993) 2385.

[Spe77] J. Speth, E. Werner and W. Wild, *Phys. Rep.* **33** (1977) 127.

[Spe80] J. Speth, V. Klemt, J. Wambach and G.E. Brown, *Nucl. Phys.* **A343** (1980) 382.

[Sta91] A. Stadler, W. Glöckle and P.U. Sauer, *Phys. Rev.* **C44** (1991) 2319.

[Ste86] G. van der Steenhoven, H.P. Blok, J.F.J. van der Brand, T. de Forest Jr., J.W.A. den Herder, E. Jans, P.H.M. Keizer, L. Lapikás, P.J. Mulders, E.N.M. Quint, P.K.A. de Witt Huberts, J. Mougey, S. Boffi, C. Giusti and F.D. Pacati, *Phys. Rev. Lett.* **57** (1986) 182.

[Ste87] G. van der Steenhoven, A.M. van den Berg, H.P. Blok, S. Boffi, J.F.J. van der Brand, R. Ent, T. de Forest Jr., C. Giusti, J.W.A. den Herder, E. Jans, G.J. Kramer, J.B.J.M. Lanen, L.

Lapikás, J. Mougey, P.J. Mulders, F.D. Pacati, E.N.M. Quint, and P.K.A. de Witt Huberts, *Phys. Rev. Lett.* **58** (1987) 1727.

[Ste88] G. van der Steenhoven, H.P. Blok, E. Jans, M. de Jong, L. Lapikás, E.N.M. Quint and P.K.A. de Witt Huberts, *Nucl. Phys.* **A480** (1988) 547.

[Suz83] T. Suzuki and H. Hyuga, *Nucl. Phys.* **A402** (1983) 491.

[Udi93] J.M. Udías, P. Sarriguren, E. Moya de Guerra, E. Garrido and J.A. Caballero, *Phys. Rev C* **48** (1993) 2731.

[Wil87] C.F. Williamson, J.K. Wong, M. Deady, Kamal K. Seth, D. Barlow, S. Iverson, M. Kaletka and A. Saha, *Abst. subm. to PANIC (JAPAN)* 1987.

[Wir88] R.B. Wiringa and V. Fiks and A. Fabrocini, *Phys. Rev.* **C38** (1988) 1010.

[Wir91] R.B. Wiringa, *Phys. Rev.*, **C43** (1991) 1585.

[Wir95] R.B. Wiringa, V.G.J. Stoks, R. Schiavilla, *Phys. Rev.* **C51** (1995) 38.

[Wir00] R.B. Wiringa, S.C. Pieper, J. Carlson and V.R. Pandharipande, *Phys. Rev.* **C62** (2000) 014001.

[Wis85] J.E. Wise, J.S. McCarthy, R. Altemus, B.E. Norum, R.R. Whitney, J. Heisenberg, J. Dawson and O. Schwentker, *Phys. Rev.* **C31** (1985) 1699.